Combinatorial Exploration of Non-Platinum Catalysts for Oxygen Reduction at Low Temperatures

by Jonathan Raymond Petrie

COMBINATORIAL EXPLORATION OF NON-PLATINUM CATALYSTS FOR OXYGEN REDUCTION AT LOW TEMPERATURES

A Dissertation

Presented to the Faculty of the Graduate School

of Cornell University

In Partial Fulfillment of the Requirements for the Degree of

Doctor of Philosophy

by

Jonathan Raymond Petrie

August 2010

COMBINATORIAL EXPLORATION OF NON-PLATINUM CATAYSTS FOR OXYGEN REDUCTION AT LOW TEMPERATURES

Jonathan Raymond Petrie, Ph. D.

Cornell University 2010

Fuel cells present an intriguing method of transforming stored chemical energy into electricity. In PEM fuel cells that operate near room temperature, kinetic limitations in the oxygen reduction reaction (ORR) limit efficiencies. This study attempted to increase the ORR rate by replacing the platinum traditionally used to catalyze it at the cathode. Despite the high cost, platinum has had the lowest kinetic overpotential of any metal for the ORR, in addition to good conductivity and superior chemical/mechanical resistance.

This study used a high-throughput method to investigate possible non-platinum ORR catalysts. Multiple elemental targets were simultaneously sputter deposited to produce thin film combinatorial spreads covering a range of elemental compositions. By including a fluorescent indicator dye into the testing solution, an optical sweep technique could determine local regions of high ORR activity. Such regions corresponded to unique compositions that were examined in further detail using cyclic voltammetry and a battery of other characterization steps.

The ORR kinetics of palladium was increased through ligand and strain effects on its electronic structure. It was hot sputtered with tungsten to generate $Pd_{90}W_{10}$, which dealloyed at the surface to form a skeletal/skin layer of 4-5% W. Its activity was increased even further by adding a compressive strain of less than 0.1% through room temperature sputtering. A 3rd element was added into the $Pd_{90}W_{10}$ bulk to replace the sputtered compressive strain. In aerated 0.05 M H_2SO_4, $Pd_{87}W_6V_6$ had a

current density at 850 vs. RHE mV at least 30 times greater than that of platinum, along with much better resistance to methanol crossover.

Conductive Pb-Ru pyrochlores were studied using both composition and temperature gradients. An optimal concentration of $Pb_2(Ru_{1.5}Pb_{.5})O_{6.5}$ had a binary Pb:Ru ratio of 50:50 on the surface. The high activity likely came from a weakened $Pb\text{-}O_b$ bond favoring the displacement reaction of O_bH in $Pb\text{-}O_bH\text{-}Ru$ by HO_2. With a ternary Pb:Ru:Pd ratio of 25:50:25 on the surface, the activity was increased above platinum at low overpotentials in aerated 0.05 M H_2SO_4. In all cases, continuous gradients were leveraged with a general understanding of ORR catalysis to more easily and quickly focus on promising materials.

.

BIOGRAPHICAL SKETCH

Jon Petrie was born in San Diego in 1981. It was a sunny, dry day. His fraternal brother, Tim, came into the world minutes later, ensuring that his older sibling would remain minutes wiser in life…supposedly. Jon hit the jackpot by having parents, Tom and Marlene, who encouraged him in his endeavors and taught him to value ideas like hard work, common sense, and curiosity of the world around him. They remain the two people he admires most.

Jon remained in San Diego until he was 17. He attended public education in University City and La Jolla. Most of his teachers excelled in both creating and quenching a desire to learn. Memorable among them include Mrs. Homm, Mrs. Rodenrys, Ms. Posen, Mr. Stansell, Mr. Teachworth, Dr. Mac, and Mrs. Ickstadt.

In 1999, he graduated from high school. Taking advantage of one of the few benefits of being a California citizen, he moved up the coast to UC Berkeley. It was an interesting place. On the academic side, he received a B.S. in Materials Science & Engineering and a B.A. in Physics, with minors in Chemistry and Business Administration from departments with excellent teachers. All this meant was that he had a few slips of paper, a head full of concepts, and a head start on where to find information he had forgot. When looking back, he feels that it was definitely worth it.

After graduating in 2003, Jon headed across the country to Cornell University in Ithaca, NY. While it was rumored that the allure of snow was a strong component in this decision, the official rationale only mentioned the outstanding academics and research associated with the MSE department. In particular, he was blown away by the opportunity to try high-throughput sputtering research. Besides the tremendous amounts of knowledge and experience he has gained in Ithaca, he has also learned that there is a reason slush is never seen on a Christmas card.

dedicated

to all those who

seek catalysts in their lives

or are catalysts in the lives of others

ACKNOWLEDGEMENTS

The work presented here would not have been possible without the guidance and support of many talented individuals who have my sincere appreciation. First, many thanks to my advisor, Professor Bruce van Dover, for just about everything. Whether it was theory, fabrication, testing, characterization, or as a sounding board for crazy ideas, he could either provide help from experience or point me in the right direction. Basically, Bruce was like a friendly GPS system for navigating the high seas of research. Professors Frank diSalvo, Kit Umbach, and Héctor Abruña were bedrocks of help on just about everything as well, and were extremely generous in their time. Sometimes I think that professors are more interested in unexpected results, and I hope that they were satisfied throughout this research.

Many others have my thanks for contributing to this noble (metal) study. John Gregoire was invaluable as the point man for much of the scientific apparatus – in fact, he built it. Michele Tague brought her chemistry skills to the bench, not the least of which was umbelliferone. Paul Bishop and John Sinnott worked wonders in the basement. Jon Shu, John Hunt, Maura Weathers, and Steve Kriske could make X-rays dance with electrons, and then tell you which waltz was played. Mark Dreibelbis employed magic in making multi-composition nanoparticles. David Finkelstein and Eric Rus were tour guides on the wonders of electrochemistry. Carol, Vicki, Patti, Joseph, Michele, and Verne were always helpful upstairs. Group members, department members, and others in Ithaca who were supportive and have never sued me include Mr. P., Bear, Karen, Steve, Hitesh, Noble, John, Maxim, Totka, Rob, Henry, Jeremy, Hanjong, Taro, Joe, Jon, Harry, and those I was a shmegege not to mention. My parents and brother, Tim, will always have my gratitude. Finally, I'd like to thank the American people for their tax dollars in support of this research.

TABLE OF CONTENTS

LIST OF FIGURES

LIST OF TABLES

CHAPTER 1

1 INTRODUCTION

1.1 Motivation

Fuel cells will be a major currency in the changing energy economy. Fossil fuels, long used to satisfy a majority of the world's energy needs, are being phased out over a combination of supply, efficiency, and environmental concerns. These fuels store radiative energy captured millions of years ago from the sun. Renewable processes (i.e. solar, geothermal, wind, etc.) and nuclear energy are expected to increase our capture of more recent energy sources. While these should supply and surpass the output of disappearing fossil fuels, there are concerns over the ability to store this energy in a usable format not related to fossilized plant and animal material. Until society reaches the high echelons imagined by science fiction writers, such as Robert Heinlein's 'solid-state quantum Shipstones', batteries and fuel cells remain the likeliest prospects to accomplish this [1]. By relying on chemical storage through an oxygen-reduction reaction, they are able to circumvent low efficiencies (~20-30%) from Carnot-type heat transfer and the 2nd Law of Thermodynamics associated with combustion and turbine engines. As seen in Figure 1, both batteries and fuel cells have storage capabilities in the range of heat transfer systems, but with much higher efficiencies [2]. In addition, when compared to batteries, fuel cells have a much greater storage capacity at present since their reactants can be continuously supplied from some outside reservoir rather than being limited by the size of the battery. However, they are kinetically limited for applications that require a high rate of electricity; hybrid systems with capacitors can attempt to overcome this deficiency with mixed success [3]. Theoretically, fuel cells would combine high efficiency with

longetivity. In practice, and just like that other type of green currency that stores (human) work, this system has challenges that must be met for fuel cells to receive greater acceptance in society.

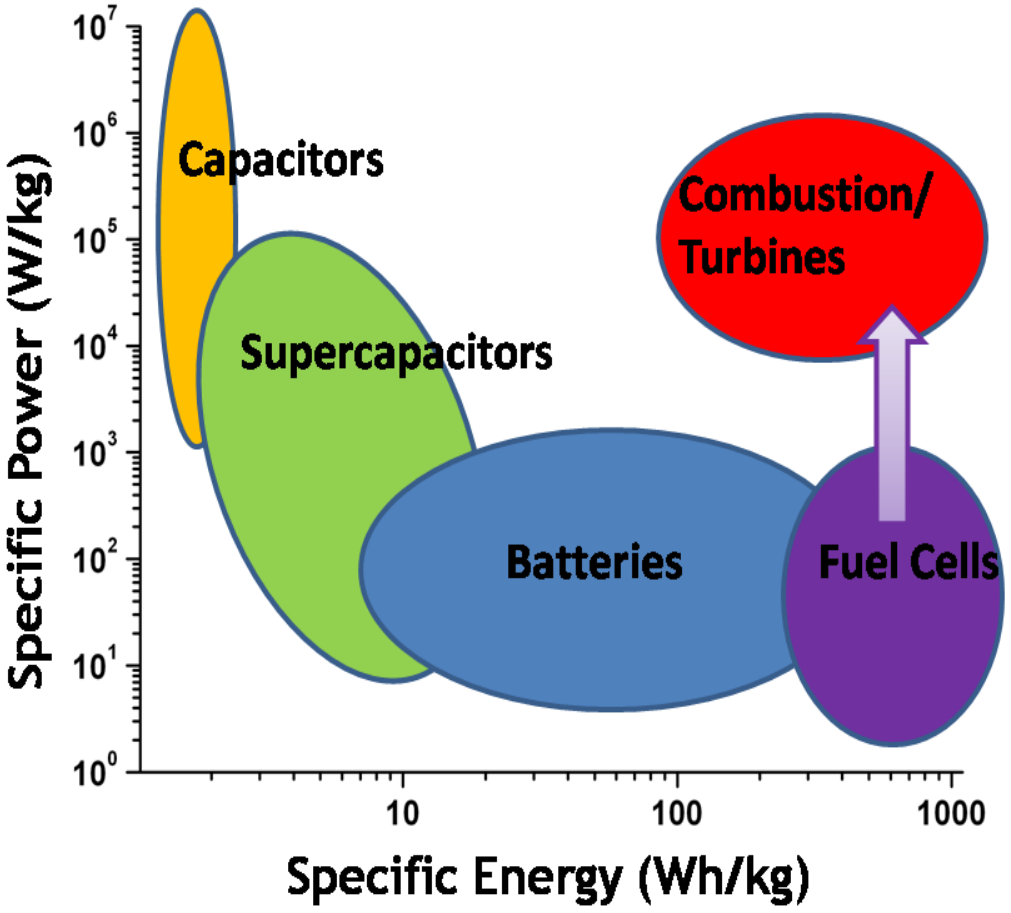

Figure 1. Ragone Plot of known energy storage systems showing large capacity for fuel cells (reproduced from [2]).

1.2 Fuel Cell Basics

At their most basic, fuel cells work by oxidizing one reactant at the anode while reducing another at the cathode. The electrons from the oxidized reactant are forced into a circuitous path that travels through whatever device is using it, such as an automobile shaft, to the cathode. To balance charge at either end, the anode and cathode are separated by an electrolyte that is insulative to electrons but permeable to ions. Sir William Grove invented one of the first fuel cells in 1843, which he called a bovine-free 'gas battery' [4]. His cell used Pt as both the anode and cathode with dilute sulfuric acid as the electrolyte. Hydrogen gas was oxidized at the anode to H^+ and oxygen gas (O_2) was reduced at the cathode that, when combined with the H^+ that drifted across the sulfuric acid electrolyte, produced water. Electrons 'flowed down' the potential gradient, due to the difference in reduction potential between anode and cathode, and were measured with a voltmeter. In terms of the half-reactions at each site:

Anode: $2H_2 \leftrightarrow 4e^- + 4H^+$	$E° = 0V$	(1.1)
Cathode: $O_2 + 4H^+ + 4e^- \leftrightarrow 2H_2O$	$E° = 1.229V$	(1.2)
Overall: $O_2 + 4H^+ + 4e^- \leftrightarrow 2H_2O$	$\Delta E° = 1.229V$	(1.3)

Thus, the thermodynamic voltage, or the approximate open-circuit potential, under standard temperature and pressures should be 1.229V, meaning this reaction is producing a favorable potential difference that moves electrons through a load (i.e. electricity). Using the equation $\Delta G° = -nFE°$, where n = # electrons involved and F = 96485 C/mol, or the charge of electrons in a mole, $\Delta G° = -235.8$ KJ/mol. This denotes a highly favorable reaction. As with many reactions, there is an activation energy

barrier, resulting in slow kinetics. For the previous reaction, it is most explosively demonstrated when mixing hydrogen and oxygen gas in a balloon and bringing a lit match nearby to thermally overcome the activation energy. This barrier to oxidation and/or reduction can be due to a few different processes, which will be discussed later. Of course, many other types of fuel cells were developed with varying fuels, electrolytes, and operating conditions, as seen in Figure 2. All of these seem to oxidize some variant of hydrogen or hydrocarbon while reducing oxygen, resulting in environmentally friendly water.

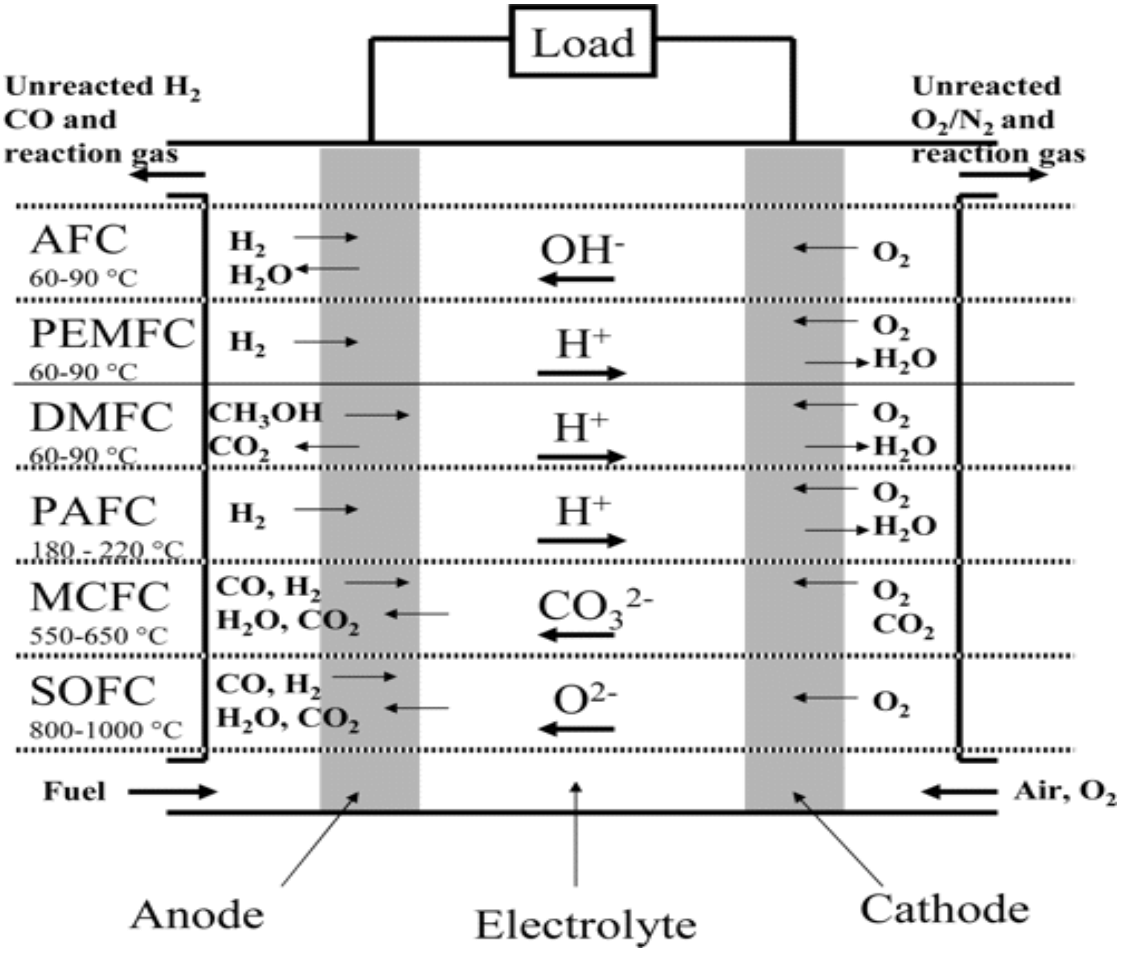

Figure 2. Classes of known fuel cells [3].

As fuel cells operate at higher temperatures, the added thermal energy (e.g. lit match) makes it easier to overcome the activation barrier for the reaction to take place, increasing their efficiency. For instance, some SOFCs (solid-oxide fuel cells) have efficiencies bordering into the 70% range, which can be increased into 90% if the heat is recycled back into the system [5]. For lower temperature cells (<200°C), efficiencies are subsequently lower, and without a catalyst to speed up the reaction could not take place at measureable rates. A mere score from celebrating its bicentennial in the fuel cell business, Pt still remains the main catalyst to both oxidize hydrogen, or some variant of it, and reduce oxygen. If these lower temperature fuel cells are to be used commercially (e.g. automobiles), improvements in the Pt catalyst must be considered.

As mentioned previously, a theoretically perfect fuel cell operating with hydrogen and oxygen gas at STP will produce 1229 mV RHE. A direct methanol fuel cell (DMFC), which the group the author is associated with has studied, will theoretically yield a potential of 1186 mV due to a small additional potential for oxidizing a C-H bond. However, under real operating conditions, these cells yield a potential of only 500-600mV due to overpotential shifts at the anode and cathode, as seen in Figure 3 [6]. Anode shifts, often due to poisoning of the Pt catalyst by CO, sulfates, and other impurities, introduce a loss of is 100-200 mV. At the cathode side, the shift is more disturbing, acting almost immediately around 400 mV due to the slow kinetics of oxygen reduction on the Pt electrodes while gradually increasing from ohmic and diffusive polarizations as the current increases. The oxygen reduction half-reaction should yield a potential close to 1229 mV, or 1170 mV at a pH ~ 1 and STP. Instead, it only reaches a potential from 800-900mV [7].

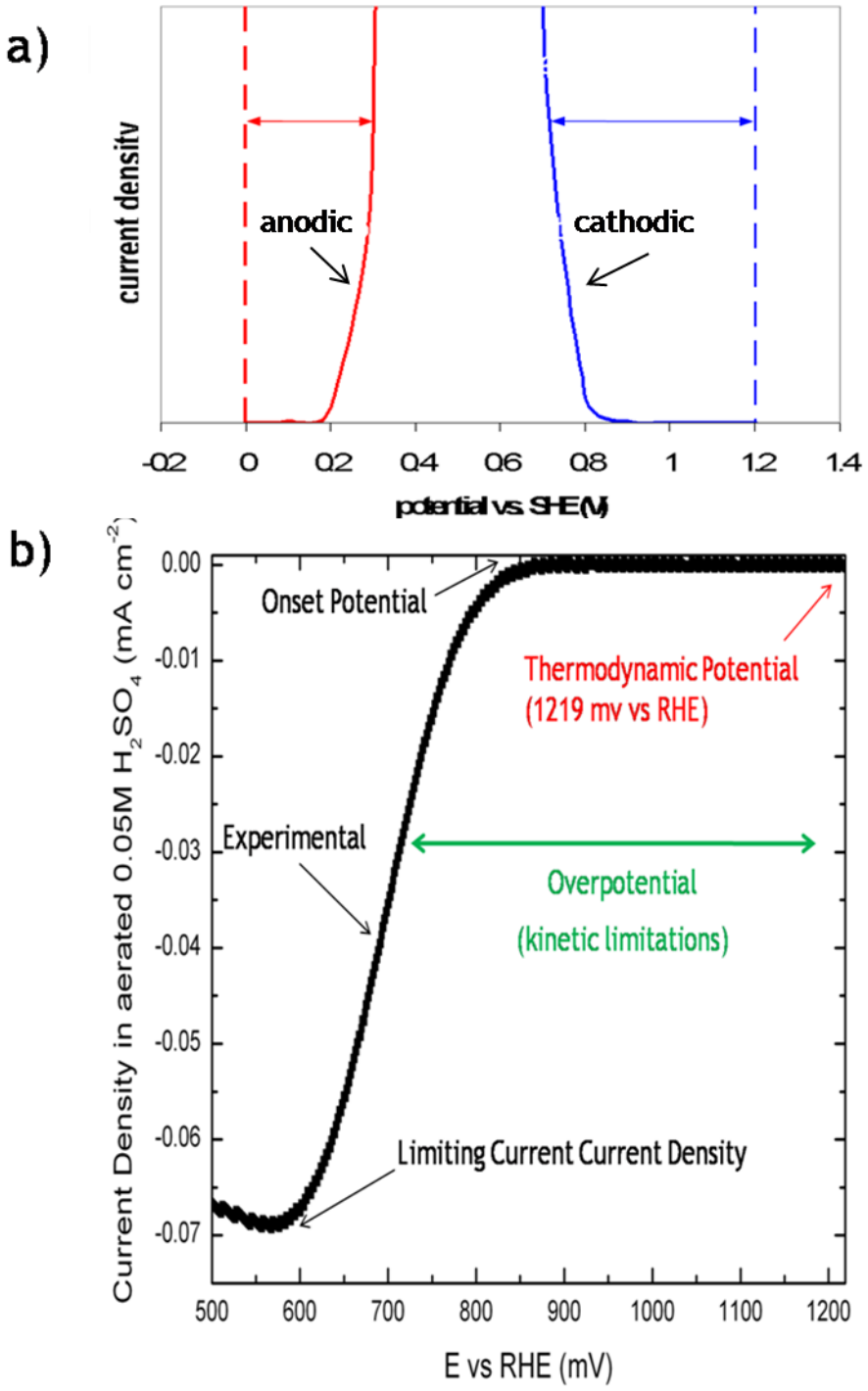

Figure 3. Experimental data on Pt-catalyzed fuel cell. In a), theoretical potentials of half-cell reactions are given by dashed lines and real potentials by solid lines (reproduced from [6]). In b), the cathodic oxygen reduction reaction (ORR) on a sputtered Pt thin film is shown.

1.3 Goals of Study

The purpose of this thesis is to find cathodic materials that can replace Pt as the cathode for direct methanol fuel cells (DMFCs). These materials must satisfy several criteria:

1) Improved kinetics in the oxygen reduction reaction is required to lower the overpotential.

2) In addition to the traditional $4e^-$ cathodic half-cell reaction ($O2 + 4H^+ + 4e^- \leftrightarrow 2H_2O$), there is also an undesirable $2e^-$ half-cell reaction that lowers the theoretical half-cell voltage and produces peroxide as an intermediate before its reduction to water($H_2O_2 + 2H^+ + 2e^- \leftrightarrow 2H_2O$). This peroxide can attack and damage the cathode and electrolyte. We would like a material, which either limits this reaction or immediately consumes the peroxide.

3) High Protonic/Electronic conductivity is necessary to allow the transfer protons and electrons to oxygen without adding a separate conductive element.

4) Stability in acidic environments (e.g. .1-1M H_2SO_4) is essential so that the catalyst could coexist in aqueous environment containing nafion© used as the electrolyte.

5) Resistance to poisoning from inadvertent methanol crossover through the nafion© would decrease the overpotential compared to Pt.

6) A lower cost than Pt would be ideal. This should not be incredibly difficult, as Pt is one of the most expensive elements already in circulation at ~$1600/ounce due to a combination of monetary and industrial value (e.g. catalytic converters).

1.4 Alternatives to Pure Pt Cathodes

1.4.1 Platinum Group Metal (PGM) Alloys

Despite the previous concerns, Pt is still the most widely used catalyst for ORR. A first step towards improvement has been to look at alloying this metal with other transition metals. This strategy has given enhancements in ORR activity although comparative measurements differ. An early study by Mukerjee in 1993 on PtM alloys supported on carbon (where M = Cr, Mn, Co, or Ni) showed activity enhancements of several times compared to pure Pt [8]. Another by Toda and Watanabe in 1999 showed higher current densities with up to 30% Fe, Ni, or Co alloyed to Pt [9]. However, these results all vary widely, depending on preparation and testing conditions, with nanocrystallites [10] giving different values than polycrystalline thin films [11] for the same composition due to surface effects. Still, improvements in methanol poisoning reduction were seen [12] as well as significant reductions in the Pt overpotential [13-16]. The main reason for this increase in kinetics is still under debate, but the consensus seems to have moved from Pt-Pt interatomic distance or surface area effects towards the electronic effects of these alloying atoms under a protective Pt ‘skin layer’ [17-19]. Such reports have proposed that these elements have increased the 5d vacancies in Pt, leading to higher 2π back-bonding from the O_2(ads), increasing the adsorption rate and decreasing the strength of the oxygen double bond, all leading to a higher ORR rate. Others argued that the alloying

element's effect on the Pt 5d vacancies led to a decrease in OH(ads), which would free up catalytic sites and thus increase the kinetics of ORR [20]. In most cases, a noble Pt 'skin layer' a few monolayers thick from surface segregation, or a Pt 'skeletal layer' a few monolayers thick where most of the less noble element had dealloyed or were contained in a Pt 'cage', were pursued in both thin film and nanoparticle structures. Groups, such as those headed by Adzic, have even developed this idea into core/shell nanoparticles with the more noble element on the outer 'skin' protecting some less noble composition inside [21].

A potential replacement for Pt could be Pd, another Platinum group metal (PGM). As seen in Figure 4, its price mirrors that of Pt at a lower price level during non-strike years. It also has the largest annual PGM production (albeit half come from mines controlled by Russian interests), and has many similar properties to Pt, even replacing it in applications from jewelry to catalytic converters [22]. While it also has good stability in acidic fuel cell conditions (Figure 5) and is less susceptible to methanol poisoning, it has slightly worse kinetics than Pt towards oxygen reduction reactions (ORR) [23]. However, there are reports that by alloying it with other elements, such as the 3d transition series, the activity both with and without methanol might be increased even higher than that of Pt [24-27]. Groups, including the one headed by Adzic, have transitioned from Pt into this area. In most cases, the same skin or skeletal layer rationale translates from Pt to Pd. Some, such as Fernandez and Bard, postulated that the alloying element(s) might help split the oxygen double bond [28]. Nevertheless, this study will start from the assumption of the alloying element(s) influencing the electronic properties of the 4d state in surface Pd.

.

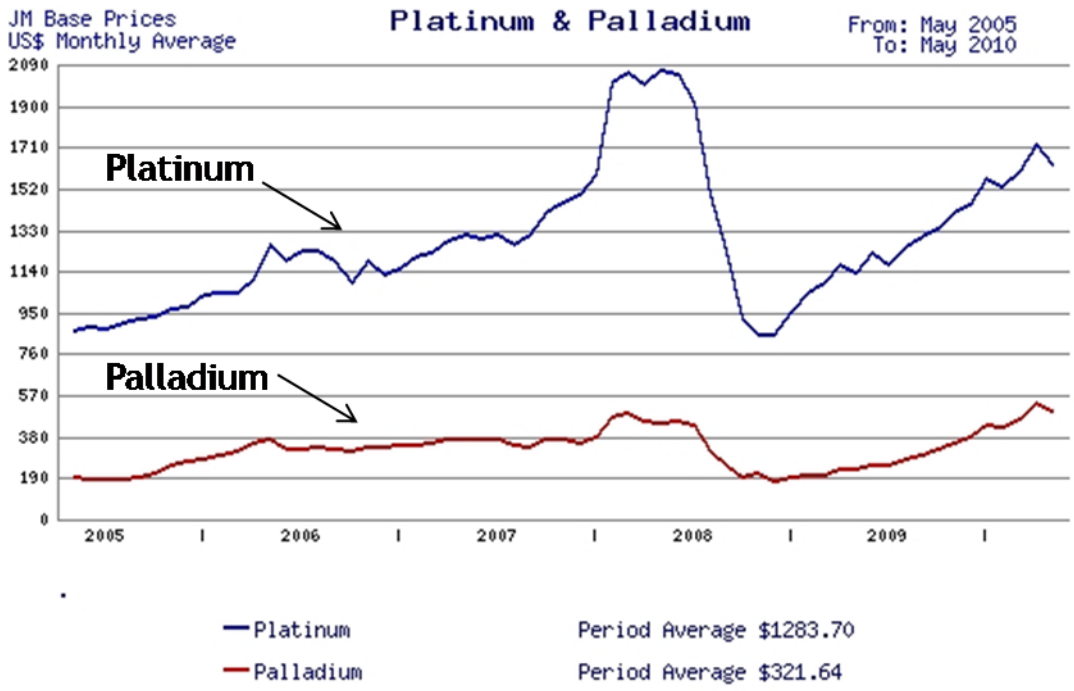

Figure 4. Market Prices of Pt and Pd for the past 5 years, according to the Johnson-Matthey Platinum Metals Report [29].

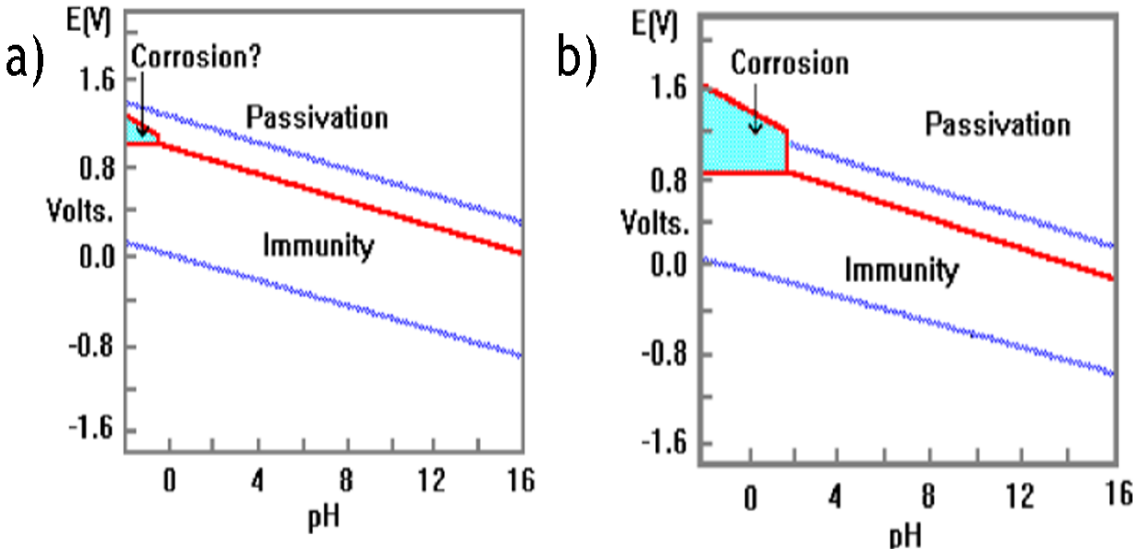

Figure 5. Pourbaix Diagrams of a) Pt and b) Pd. Pd is slightly more corrosive at low potential [30].

1.4.2 Pyrochlores and Other Cathodic Materials

While PGM alloys remain a major field of study, these metals are by no means the only possible ORR catalysts under study. Transition metal oxides are tolerant to many types of poisoning (i.e. methanol in DMFCs) and have multiple valencies that present intriguing possibilities for oxygen reduction. Some examples include spinels (i.e. Co_3O_4 and $NiCo_2O_4$), doped lanthanum cobaltites, lanthanum manganites, and Pb-Ru pyrochlores ($Pb_2Ru_2O_7$) [31-34]. Of these, only the pyrochlores seem to have any kind of stability in acidic solutions in addition to possessing the unique property of conductivity in the defect state. Horowitz and his group, who discovered the relatively high ORR activity of this material, proposed it was due to surface vacancies and disorder on the surface [35]. By doping increasing amounts of Pb^{4+} on the Ru B-site of the pyrochlore to form $Pb_2(Ru_{1.95}Pb_{0.05}O_{7-\gamma}$ with increased surface Pb and likely oxygen vacancies, Goodenough and his group were able to increase the catalytic activity [36]; unfortunately, even by binding it to Vulcan carbon-72, this activity remained less than that of Pt [37]. Raghuveer tried making nanoparticles of this pyrochlore and reached even higher activities comparable with that of Pt, perhaps through differing defect states on the nanoparticulate surface [38]. Other groups have doped various 3d transition metal elements into the B-site [39] of Pb-Ru pyrochlores, such as Mn, with mixed results not yet sufficiently explained [40]. The author of this study has himself doped some differing elements into these pyrochlores with varied success.

Other exotic alternatives include nitrides, sulfides, carbides, and other reactively-formed compounds. For instance, pyrolyzed macrocyclic Fe compounds has shown intriguing catalytic activity [41]. Co and Ni-based nitrides and sulfides have also garnered sufficient interest due to the relative abundance of the raw materials

[42]. Even such compounds as W_2C has shown good resistance to CO and methanol poisoning, with some potential cathodic activity by itself and combined with Pt [43, 44].

1.5 ORR Reaction Mechanism

To better understand the rationale behind a catalyst choice, it might be instructive to more closely examine the oxygen reduction reaction (ORR) at the molecular level. This study incorporates both a noble metal surface, on which aqueous molecules are weakly bound, and a hydroxylated pyrochlore oxide surface. For oxygen adsorption on noble metals, three possible configurations include end-on, side-on, and bridge adsorption, respectively characterized by Pauling, Griffith, and Yeager models. The Pauling model involves lower overlap between the oxygen π bonds and d orbitals, making it less energetically favorable to break the molecular oxygen bonding; this leads to a preponderance of peroxide. The most widely accepted model for noble metal catalysts, such as Pt and Pd, are the Griffith or Yeager 'bridge-bonding' model [45]. As seen in Figure 6 for the bridge model, an oxygen molecule must first be adsorbed onto the catalyst surface. With some degree of π^* back-bonding weakening the double bond before a first electron/proton transfer, the adsorbed oxygen (O_{2ads}) can be broken up into separate oxygen atoms. Each can be reduced to form hydroxide and/or water molecules in a $4e^-$ process; peroxide from a Pauling adsorption model results in a $2e^-$ process. There is still some debate on whether the first electron transfer leads to the immediate breakage of the O_2 double bond or results in the first proton bond [46]. In either case, one can collapse the initial electron transfer and final O-O bond breakage into the rate-determining step:

$$O_{2ads} + H^+ + e^- \leftrightarrow O_{ads} + OH_{ads} \qquad (1.4)$$

Through experimentation with different materials, it was found that the best catalysts had an optimal binding energy range for oxygen species. It had to be large enough to bind and reduce oxygen that came into contact but low enough that these same species would not poison the catalytic sites with bound –OH and –O groups. Materials with low binding energies, as typified by Au, result in either weakly bound oxygen or intermediate peroxide production from not being able to catalyze the breaking of the O-O bond. Such production would be both deleterious for the fuel cell and inefficient in the release of electricity. Higher binding energies than optimum, as seen in Pd and Pt, have slower kinetics primarily from –OH and –O species, due to reduced oxygen or water molecule interaction, blocking valuable catalytic sites. Numerous graphs of catalytic current densities associated with the ORR reduction kinetics show the Sabatier 'volcano curve' relationship typified by Figure 7 from the catalysts group at Brookhaven [47]. In addition, Nørskov and co-workers discovered a relationship between the d-band center (i.e. middle of integrated d-orbital density of states) of these catalytic materials and their binding energies, which has to do with orbital overlap between the d orbitals of the catalysts and p orbitals of the oxygen species. In order to reach the optimal point on the Sabatier curve for enhanced ORR kinetics, one must be able to tune this d-band center.

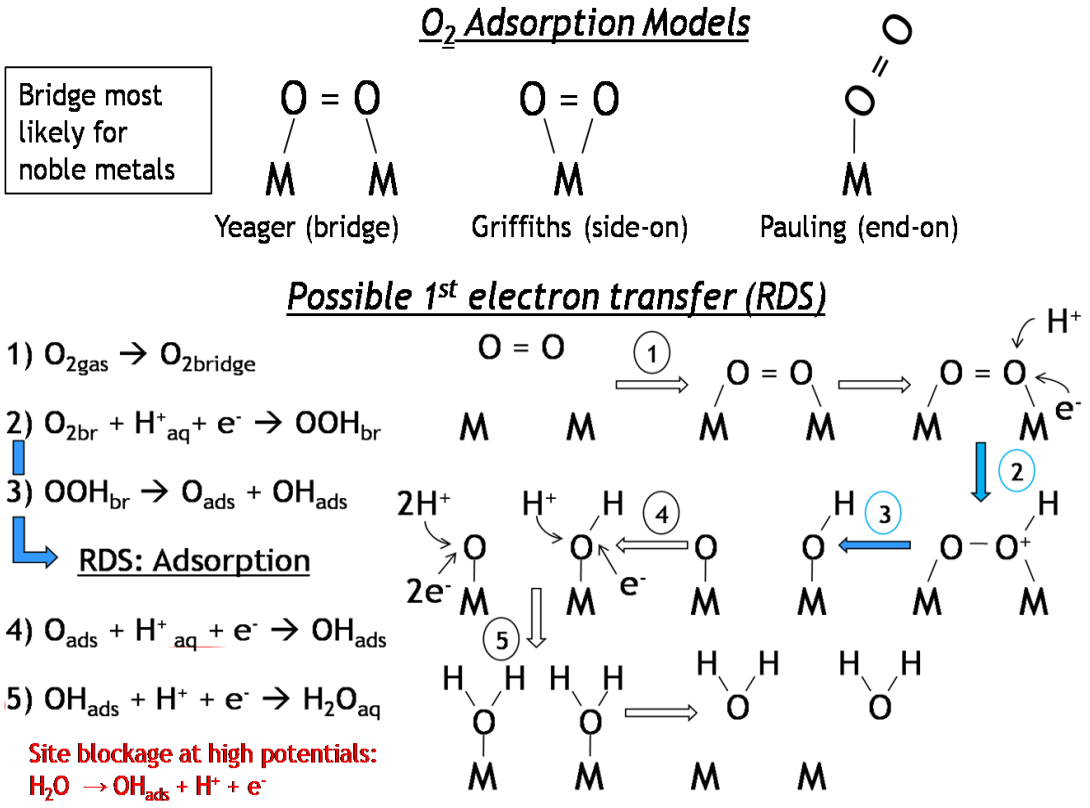

Figure 6. Different O_2 adsorption models. Reaction mechanism using Yeager Model for the 4-electron oxygen reduction reaction (ORR). Mechanistic equations are on the left and descriptive model on the right [48]. The rate determining step (RDS) involves the first electron/proton transfer and breaking of oxygen bonds.

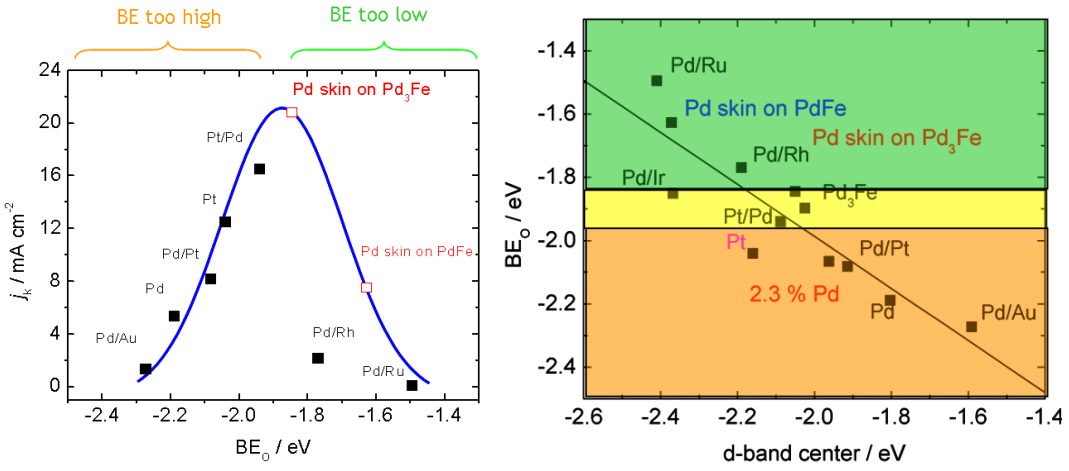

Figure 7. Sabatier Curve for Pt and Pd-alloys and linear relationship between this binding energy and the d-band center of the catalyst (Adzic group).

1.5.1 Tuning the d-band center

Some particularly interesting work has appeared over the past few years, which have speculated on the effects of ligand atoms and strain on noble-metal d-band centers. The interest focuses on using these two effects as a 'tinker-box' to shift the d-band center and increase ORR kinetics. For instance, Hyman and Medlin, have looked at the relationship between d-band centers in Pt alloys and their overlap with the bonding and anti-bonding states of various adsorbates during the redox reactions [49]. Their DFT calculations, which are in rough agreement with others in the field for both Pt and possibly Pd, imply that there is an optimum point for the d-band center with respect to the Fermi energy of the valence d-electrons. For many of the oxygen-based adsorbates involved in the system, particularly OH and O_2, there are anti-bonding 2p electron states located just above the Fermi energy of the Pd or Pt. The greater the interaction between unoccupied d-states and these anti-bonding states, the stronger the bond between the Pt or Pd and adsorbate becomes, as expanded upon in much greater quantum depth by Hammer and Nørskov [50].

To reduce the binding energies of noble metals with these oxygen adsorbates, one must weaken the metal-oxygen bond by decreasing the amount of unoccupied d-states above the Fermi level. One can see the interaction causing this strong bond best for Pt in a) of Figure 8 for O, OH and OOH, where there is a large unoccupied density of states above the Fermi level associated with the grey-shaded anti-bonding O 2p states. This weakening of the bond is accomplished by shifting the d-band center down to lower energies to reallocate away from the Fermi level the large 'bulge' of unoccupied states just above this center. The two most common mechanisms of doing this are through 1) strain and 2) ligand effects. As seen in b) for the pure Pt density of states (DOS) with differing lattice constants (a_{Pt} = 3.92 Å), tensile strain the Pt

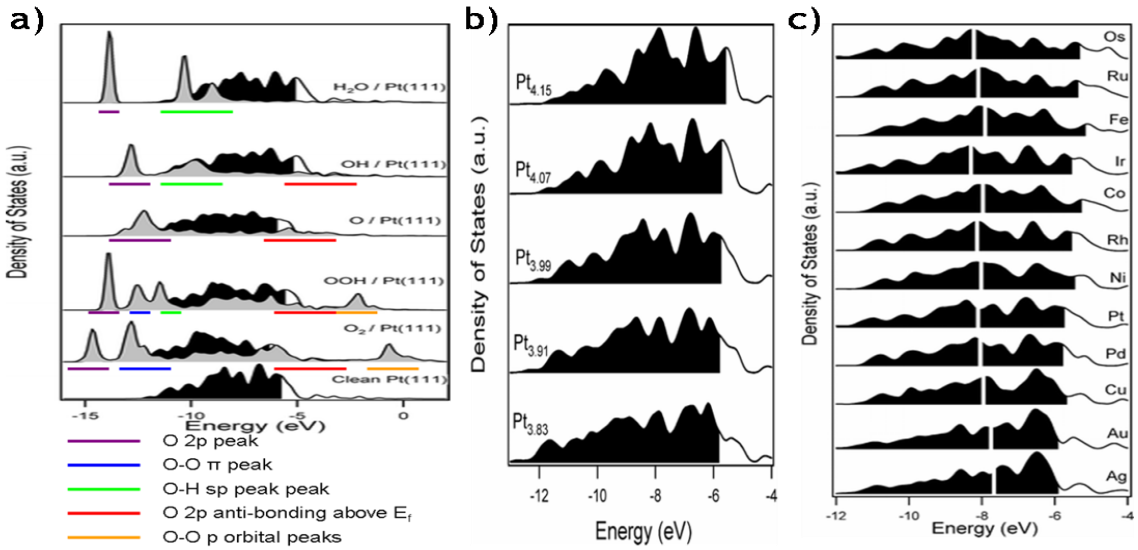

Figure 8. DOS vs. Energy Diagrams for adsorption on Pt (111). The dark-shaded regions are occupied Pt states while the lighter regions are the s and p states of the oxygen-based adsorbate whose peaks in a) are indicated by the underlined colors. The Pt lattic is compressed as one goes down in b), expanding the d-band. When M = X is computed for a PtMPt 'sandwich', c) is plotted with the vertical white line indicating the d-band center. It is most negative with respect to the fermi energy at top and least at bottom, but since the ligand effect also shifts the Fermi energy the redistribution seems rather unpredictable (Hyman and Medlin).

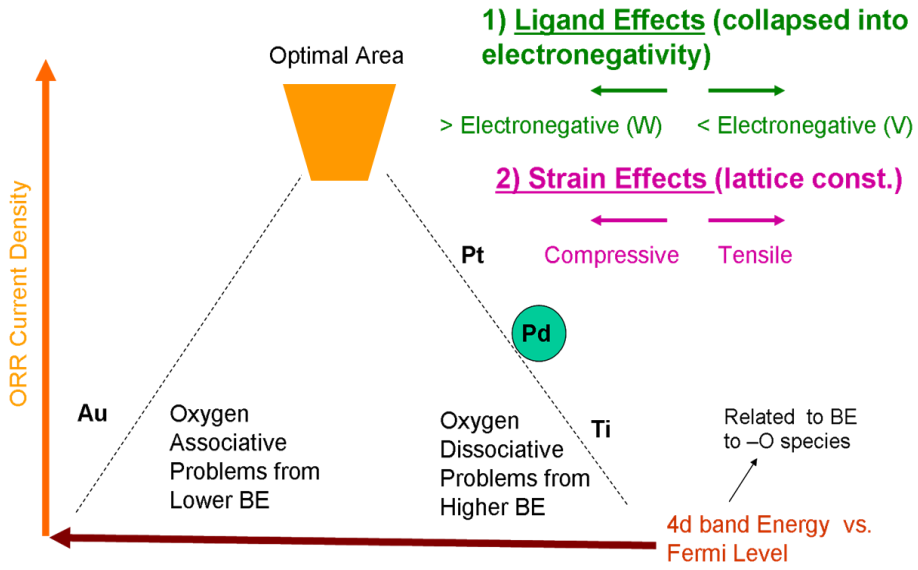

Figure 9. Simplistic representation of ORR activity as related to ligand and strain effect.

constricts the d-band as the atom becomes more like a separate atom (localized states), shifting the bulk of the d-states towards the Fermi level. Conversely, compressing the Pt expands the d-band into a more delocalized state, shifting the d-band center away from the Fermi level as desired. However, overly compressing it lowers the bond energy of not only deleterious –OH that would poison the sites, but also O_2 and OOH that are needed for the 1st electron transfer and superoxide O-O bond breaking of the RDS. Thus, there is an optimal compression (a_{Pt} = 3.91 Å), where the –OH poisoning is severely lessened without having a major effect on the other adsorbates.

As opposed to expanding or contracting the d-band to change the DOS in relation to the Fermi level, ligand effects directly change the distribution of the electrons in the d-band themselves. Using the simple rationale that the revised Pauling electronegativity is a measure of the relative tendency of an atom to transfer charge to another, a more electropositive atom should fill a noble metal's DOS, shifting it toward the Fermi level. A more electronegative atom should do the opposite. This is essentially the case, but due to the 'uneven distribution of electrons' from this process, it is extremely unpredictable for different alloying atoms and their concentrations, as seen in c) of Figure 8.

A simplistic approach to the expected relationship between ORR activity and d-band center is presented in Figure 9. Strain effects are relatively straightforward while ligand effects, due to alloying with different elements of dissimilar Fermi energies and valence electrons, are collapsed into the revised Pauling electronegativities of the elements.

CHAPTER 2

2 EXPERIMENTAL METHODS

2.1 Combinatorial Technique

A combinatorial co-sputtering method was employed to quickly and efficiently examine a wide variety of possible compositions for ORR catalysis. Such a setup encourages high-throughput scanning of composition space to identify valuable trends [51]. Up to three guns placed in different conformations around a 3" wafer create deposition-rate gradients when their targets are individually sputtered. If multiple targets are sputtered simultaneously (i.e. co-sputtering), these gradients can translate into composition gradients with intimate intermixing of the sputtered atoms on the substrate. For instance, van Dover et al. have used this technique to show that a certain composition space on an amorphous zirconium tin titanate (ZTT) thin film had a surprisingly high dielectric constant [52]. Such a survey would have taken years to independently synthesize (e.g. sinter) and test each composition; in their study, they were able to do it in just days. Others approaches use sequential sputtering with shutters to obtain thickness wedges, but these do must be further processed for atomic intermixing, and, even so, can be heavily dependent on diffusivity between the layers [53]. The co-sputtering technique was chosen for this study to ensure that the Pd would segregate into a Pd-rich surface layer and bypass the problems associated with diffusion through an overlying film. After sputtering, the thin films were first examined for catalytic properties using an optical/voltammetric cell screening technique and then characterized in an AFM/SEM for surface roughness/bulk concentration, XPS for surface concentration and binding energy, and XRD/Raman -

for structure. Computer modeling would be an additional information source, but has not yet been pursued.

2.2 Introduction to Sputtering

In a sputter deposition system, a high flux of ions is deliberately accelerated towards a target material. Depending on a variety of variables and environmental conditions, a number of events can occur [54]. These ions can reflect elastically with little kinetic energy lost and possibly neutralized. Often of use in the semiconductor industry, they can penetrate into the near-surface or bulk in a technique known as ion implantation. These implanted ions, often with kinetic energies in the thousands of eV, can change the structure of the target as well by knocking other atoms off lattice positions. Of more interest for this study are two other main processes that can occur and are not mutually exclusive: secondary electron generation and target atom ejection. The former occurs when the impacting ion imparts just enough energy (typically a few eV) to surface atoms so that one or more of their valence electrons can escape into vacuum. The latter, and what is most useful for actual deposition, occurs when the impacting ion imparts enough energy (often in the tens to hundreds of eV) in its collision with the target to overcome the binding energy of one or more target atoms, allowing them to leave the surface. In addition, enough energy can be left over for the emission of secondary electrons and re-arrangement of the near-surface structure of the target. The ejected target atoms in this study usually leave the surface with kinetic energies of up to tens of eV, allowing them to travel some distance away to deposit on a substrate near the target. At pressures in the millitorrs, this distance would be in the cm regime.

Both sputtering systems in this study use Ar^+ as their source of ions. Ar, as a noble gas, acts more like a 'billiard ball' than other ionized gases in transferring momentum to target atoms and is less likely to form compounds with them. Heavier noble gases are sometimes used to impart more momentum transfer to transition metal targets for a higher sputtering yield, but Ar is more readily available. Initially, only a few ppm Ar is actually ionized from cosmic rays [55]. To accelerate these ions towards the target, magnetron sputtering guns are used. As seen in Figure 10, these consist of a coaxial cable buried within the metallic stem with the active lead electrically attached to a metal base plate. The target, in this study a disk 2" in diameter and not more than 3/8" thick, is firmly attached to this plate by either a bolted or a screwed-in faceplate. A 'ground' shield is attached above and around the side of the target and faceplate. This ground shield, while electrically connected to the rest of the chamber, is not conductive to the target. When an external power source applies a negative voltage to the target, the difference in potential between the two creates a gradient that accelerates the Ar^+ towards the target. During the sputtering process, the secondary electrons created ionize more Ar atoms to create a cascade effect within the plasma and retain the glow discharge of the plasma.

Normally, a sustainable sputtering plasma would require Ar pressures in the hundreds of millitorrs to ensure sufficient Ar ionization. However, this would result in too little target atoms reaching the surface of a substrate because of collisions. A typical rule-of-thumb (derived for atoms with energies below an eV but still of use here) is that the mean free path (mfp) of the target atoms is ~ 4.7 mtorr*cm/$Ar_{pressure}$[mtorr] [56]. Since substrates are often within tens of cm from the target must have enough energy to reach a substrate and stick, lower gas pressures were needed. The magnetron gun has magnets placed just under the base plate that are arranged pole-to-pole to create a magnetic field able to influence the movement of

secondary electrons near the surface. It causes them to travel in a helical motion that curves around in circle, almost tracing out a toroid. This confinement of secondary electrons near the surface increases the chance of Ar being ionized and reduces the high gas pressure requirement of Ar within the chamber to a more manageable 2-50 mtorr for reasonable sputtering rates. In addition, it results in most of the sputtered target atoms coming from a 'racetrack' ring above the magnets, where the majority of Ar^+ is now localized. This ring, a few mm inside the boundary of the 2" targets, erodes at a noticeably higher rate than the rest of it.

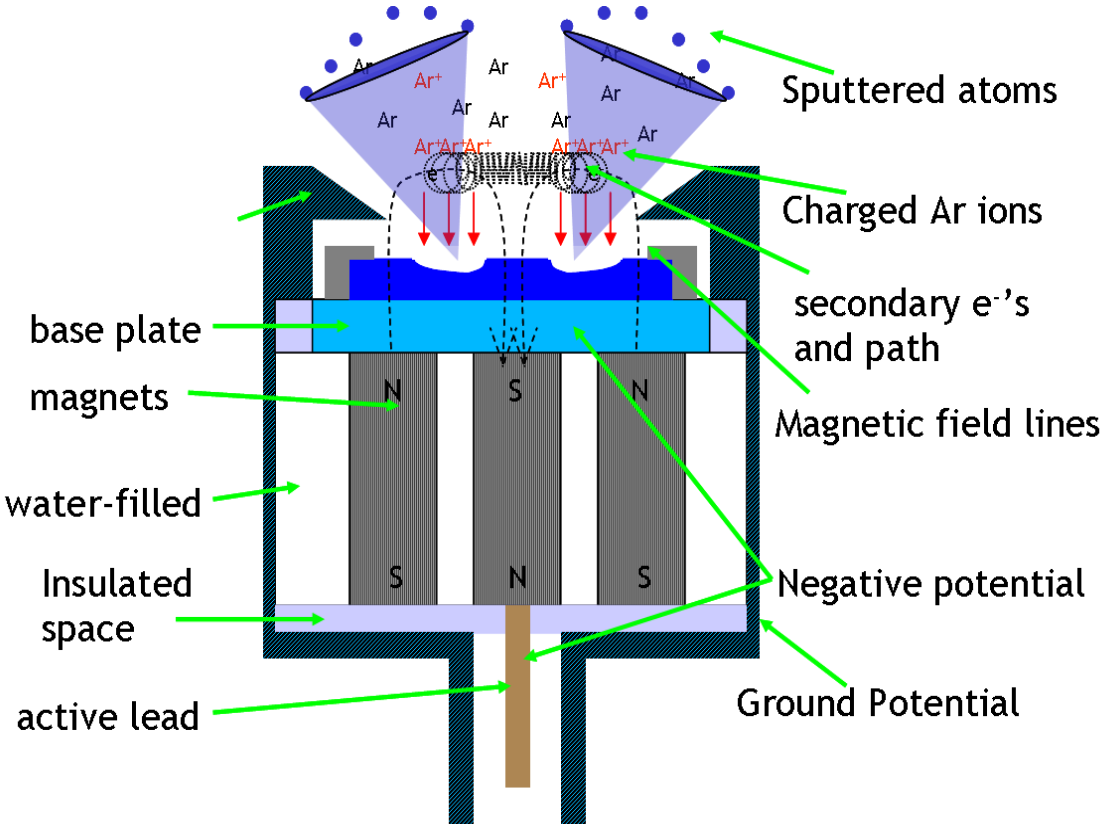

Figure 10. Diagram of US Gun II magnetron sputter gun. Adapted from Downey dissertation [57].

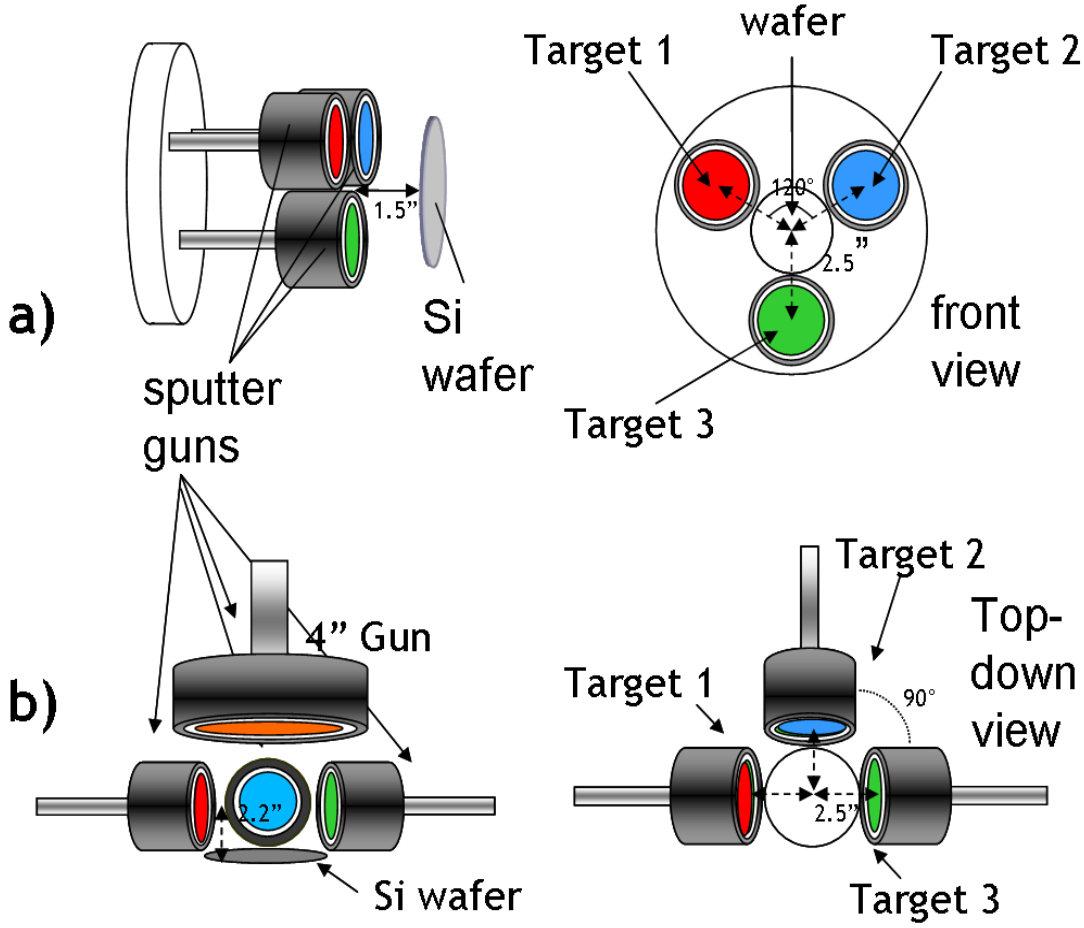

Figure 11. Schematic Diagrams of a) Gilgamesh on-axis system and b) Fenris off-axis system, as seen from both perpendicular to substrate plane (i.e. from sides of each chamber) and parallel to substrate plane. The 4th and 5th guns for Gilgamesh are not pictured.

2.2.1 Gilgamesh On-Axis Sputtering System

The Gilgamesh system, as seen in Figure 11a), combinatorially sputtered three guns (US Gun II, US Inc., San Jose, Ca) with 2” targets placed in a triangular arrangement on-axis to a 3” substrate holder. The distance from the center of each target to the center of the substrate was 2.5” in the plane of the substrate and ~1.5”

perpendicular to this plane. Base pressure were at least 2 microtorrs and sputtering pressures of Ar usually 10 millitorrs. For underlayer and single-layer deposition, two other guns were employed. A 4th gun of similar make was located 60° clockwise of this flange and a 5th S-gun (Sputtered Films, Inc. Santa Barbara, CA), which utilized ring-like targets, was 120° counter-clockwise of the flange. Both the 4th and 5th gun were ~5" from the substrate holder to ensure as uniform a film thickness as possible. All guns were water-cooled. Four dc power supplies, one connected to each gun, could control the power, current, and voltage to each gun. In most cases, current was adjusted to change the sputtering rate.

The substrate holder was suspended from the lid and had 4 sides at right angles to each other. Two of the sites held slots for 3" wafer placement so that they would be directly facing the guns. Halogen bulbs could radiatively heat these substrates up to 700°C with the temperature monitored by type-K thermocouples. Most of the films were hot-sputtered at 500°C to reach thermodynamic equilibrium on the surface and in the bulk before cooling down. The cool-down time to a removal temperature of 50°C was approximately 2-3 hours. A third site held a quartz-crystal monitor (QCM) fixed in a position corresponding to the middle of a 3" wafer when placed in one of the substrate holders. By sensing the change in mass depositing on the crystal through detecting changes in its resonant frequency vibrations, the QCM could give a real-time reading of the sputter rate. This was used to adjust the sputtering rates of each gun in the same pumpdown as the deposition. The 4th site had a DC motor attached to an un-heated substrate holder for constant composition sputtering from multiple guns.

The 3-gun arrangement was the workhorse of the system, depositing films that covered at least 60% of the composition space of a ternary diagram. As mentioned before, each gun was centered 2.5" off the center of the substrate. When sputtered separately, each would deposit a film whose rate of deposition decreased the farther

away from the gun. This decreasing rate could be fit to a decaying exponential of form y = A*exp(-R/d), where A and d were constants related to sputtering conditions and R the distance from the center of the target in the plane of the substrate. A sample plot for Pd, with a desired rate of 0.5 Å/s in the middle of the substrate, is shown in Figure 12a). The rate often decreases towards the edge of each the substrate closest to the gun due to a combination of shadowing from the substrate holder and a temporary node from the 'racetrack' configuration of sputtering on the target. However, areas this near the edge were not used in testing and disregarded. As follows from this simple modeling, the rate translated to a 2-D fit would be:

$$\text{Rate}_{gun}(x, y) \sim A*\exp(-\sqrt{[(x - x_c)^2 + (y - y_c)^2]}/d) \qquad (2.1)$$

where x_c and y_c were the coordinates of the center of each gun. Geometrically, one could think of a sputtering cone of exponential slant perpendicular to the substrate plane. Its intersection would produce exponentially decaying rates in a circular pattern centered around each target in the plane of the substrate, as demonstrated by Figure 12b). Of course, the decay of these rates was not identical for each deposition. They varied according to the atoms in each target, current and voltage used, pressure of the Ar gas, and so forth. In addition, re-sputtering from Ar reflecting off heavier targets before knocking off atoms on the substrate has been known to decrease the experimental rate of loosely bound atoms [58].

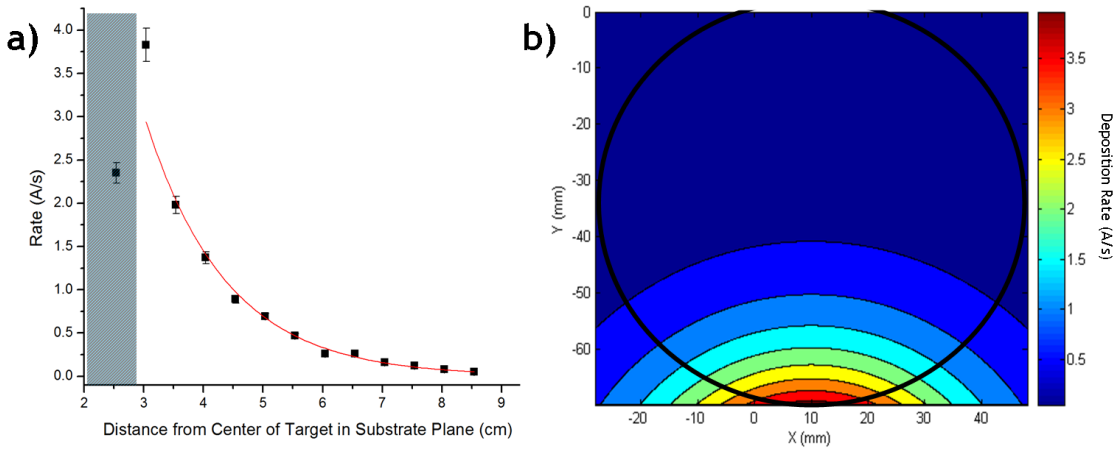

Figure 12. Pd Deposition rate in Gilgamesh system from one of the US Guns for a QCM-predicted rate of 0.5 A/s and current of 60 mA in the middle of the wafer. In a), the rate is compared vs. a direct line from the target. A ~ 27.4 Å/s and d ~ 13.6 mm. The highlighted area is either off of the 3" wafer or an edge region that is not used in testing or characterization. In b), this thickness is generalizaed to the 2D wafer surface (borders in black) from the bottom gun in the ternary setup. Since this involves on-axis sputtering, the rate can be approximated as coming from a point source cone perpendicular to the substrate intersecting its plane in circular rate contours.

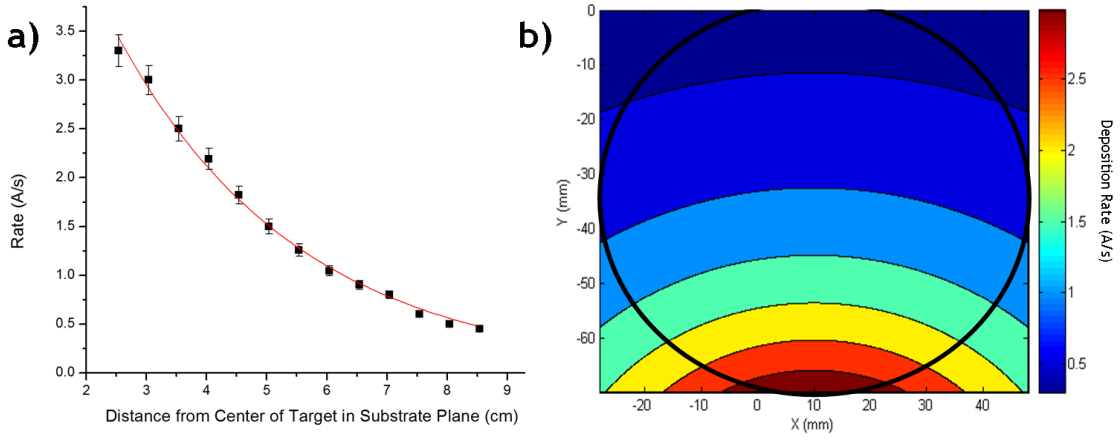

Figure 13. W Deposition rate in Fenris system from one of the US Guns for a QCM-predicted rate of 1 A/s in the middle. In a), the rate is compared vs. a direct line from the target. A ~ 7.94 Å/s and d ~ 30.3 mm. In b), this rate is generalizaed to the 2D wafer surface (borders in black) from the bottom gun in the ternary setup. Since this involves off-axis sputtering, the rate can be approximated as coming from a point source cone parallel to the substrate intersecting it in elliptical rate contours with c, or the added factor to the axis perpendicular to the target, hovering around 0.8.

2.2.2 Fenris Off-Axis Sputtering System

The Fenris system (diagrammed in Figure 11b)) combinatorially sputtered three facing guns (US Gun II, US Inc., San Jose, Ca) with 2" targets in a triangular off-axis arrangement around a 3" substrate holder. The distance from the center of each target to the center of the substrate was 2.5" in the plane of the substrate and ~2.2" perpendicular to this plane. The off-axis system allowed for less oxygen bombardment during reactive oxygen sputtering and perhaps Ar reflection as well. Cross-contamination would have been a problem at lower sputtering pressures, but since 30 millitorr was the standard operating regime, with a mean free path into the tenths of cm, this was not deemed a significant problem. The off-axis and high-pressure arrangement compared to the Gilgamesh sputtering system resulted in atoms impacting the substrate with much less kinetic energy and in a slightly different exponential decay model. However, at least according to XRD, the standard 500°C hot-sputtering seemed to minimize structural changes (such as higher texturing from off-axis deposition). Higher base pressures of 6 microtorrs may have resulted in greater oxygen and water incorporation into metallic films, but these were visually lacking, with oxide and partial-oxide XRD peaks in sputtered metallic films not noticed.

For underlayer and single-layer deposition, a top 4" US Gun II gun was employed. This 4" gun was pulled as far back from the substrate as possible when the other three 2" guns were in use due to the strong magnetic fields associated with its magnetron sputtering system influencing the plasma of the other guns, changing such variables as their dc biases and yields. In addition, when the 4" gun was in use, it was still pulled as far back as possible to give a reasonable deposition rate. Although the 4" target was larger than the 3" substrate, the majority of material sputtered still came

from the typical magnetron ‘racetrack’ centered over the magnets buried in the gun. This ‘racetrack’, where the majority of secondary electrons that ionize the Ar responsible for sputtering were located, had a diameter slightly smaller than 3”. As such, placing the gun too close to the substrate would result in an unacceptable thickness variation. Also, reflected Ar and other ions coming from the gun could cause unwanted changes in the deposited film. A typical sputtering distance for depositing many types of metallic underlayers at 100 W in 10 millitorr Ar was ~16 cm, which seemed to produce a thickness variation of at most 10% between the center and edge of the substrate while leaving the deposited film with compressive ‘bulk-like’ properties.

Four rf power supplies, operating at a standard 13.6 MHz, were connected to each gun. An alternating power supply was not needed for the Gilgamesh system, since it mainly dealt with metallic targets. The metallic target could usually compensate for any positive charge from Ar^+ impacts by e^- compensation from the negatively charged base-plate electrically connected to this surface through the metal. In some cases of dc reactive sputtering (with a small amount of reactive gas) in which the author was involved, a thin non-metallic (i.e. oxide) layer would form on the surface. It would be thin enough to still allow a compensating charge from the base e^-, but thick enough to show up as an increased voltage when under current control, requiring greater power to sputter. However, the Fenris system’s main emphasis was oxides. The higher oxygen reactive gas partial pressures produced surface oxides with thicknesses too high for charge compensation through the base plate. To provide this compensation, an rf power supply alternated the potential of the target between the standard dc negative voltage to attract Ar^+ and a new positive voltage to attract e^- from the plasma. These electrons were able to compensate for the positive charge from surface Ar instead of e^- traveling through bulk target to the surface. In fact, since these

e^- in the plasma travel so much faster than the Ar^+, a negative bias developed on the target inherent to the plasma conditions. For metallic sputtering, it stayed constant, but for oxide sputtering, this inherent bias could increase as the thickness increased. Since the applied potential is alternated, Ar^+ ions were not always sputtering the target, resulting in reduced rates in comparison to dc systems.

To overcome this rate reduction dilemma when a target had to absolutely, positively be sputtered at higher rates in the Fenris system, a 5^{th} power source used pulsed dc generation. It usually applied square waves that had a much longer duration at negative than positive voltages. Compensation from plasma electrons could still occur due to their much faster movement, but the larger negative potential would allow greater Ar^+ bombardment for a higher sputtering rate. An added bonus was that any impedance mismatch at dc (even at the maximum 250 KHz operating regime of the pulse source) between the source and gun was much less than at rf, allowing a much higher power for sputtering without worrying as much about the resultant heat dissipation in the rf cable and target.

The substrate holder was connected to a rotating rod connected to a motor on the bottom of the chamber. Wafers could simply be held onto it by gravity, as opposed to the Gilgamesh slot arrangement. Only one film could be sputtered at a time on the single holder. This holder could be heated resistively up to ~500°C with the temperature monitored by type-K thermocouples. The lower temperature was indicative of both a more thermally connected substrate holder combined with a smaller more easily radiatively-heated than in Gilgamesh. Higher temperatures than 500°C could result in damage to the Viton O-ring seals, ruining the vacuum. A QCM switched in place of the substrate holder would determine rates in a prior pumpdown, with elements lighter than Si giving unreliable measurements, either from oxide formation, unreliable sticking coefficients to the crystal, or other effects [59].

Similar to Gilgamesh, each of the triangular off-axis guns in this system could separately deposit a film whose rate exponentially decayed from the edge of the 3" substrate closest to it. If a 2-D axis on the film were defined with the origin at the target center, the x-axis perpendicular and the y-axis parallel to the gun, a typical equation for the deposition rate would be:

$$Rate_{gun}(x, y) \sim A*\exp(-\sqrt{[(x - x_c)^2 + c(y - y_c)^2]}/d) \quad (2.2)$$

where b and d were fudge-factors related to the rate and sputtering conditions (e.g. power, pressure, bias, etc.). An example for Pd at 30 W is seen in Figure 13. The main difference from on-axis sputtering was the 'c' factor, which related to the off-axis nature of the previously-described 'sputter cone' intersecting the substrate plane at an oblique angle. In most cases for metal targets, 'c' hovered around .8 while it was lower for oxides. This more elliptical pattern from the metal atoms may have been due to the higher rates and kinetic energies of target atoms translating to less scattering events before deposition.

With the conditions most often used for metallic films, the on-axis Gilgamesh sputtering system could reach ~60% of the composition space of a ternary alloy compared to ~40% for the Fenris off-axis system, as seen in the diagrams in Figure 14 for an A:B:C metallic alloy with a desired 1:1:1 ratio in the middle of the substrate. Since the hot-sputtered structures of the two systems were similar, this made the Gilgamesh system particularly appealing for covering a wide swath of composition space and the Fenris system interesting for zeroing in on a smaller portion. For instance, Gilgamesh could sputter compositions that atomistically changed by ~1%/mm while Fenris could decrease that to ~0.5%/mm.

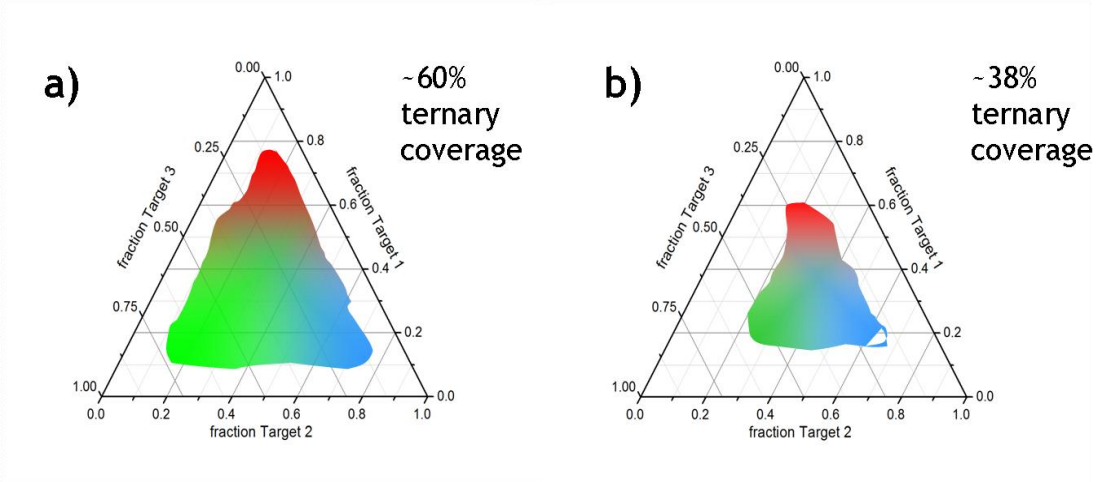

Figure 14. Phase diagram coverage at the sputtering conditions used in this study for a) Gilgamesh on-axis system and b) Fenris off-axis system when each gun is calibrated to produce a 1:1:1 atomic mixture in the middle of the substrate.

2.3 Fluorescence Optical Screening

2.3.1 Introduction to Fluorescence Screening Technique

An optical screening technique, first developed by Reddington and Mallouk, was adapted to identify highly catalytic compositions on sputtered films suitable for further investigation [60]. In their combinatorial search for a better DMFC anode, they realized that in the half-cell reaction for the oxidation of methanol:

$$CH_3OH + H_20 \leftrightarrow CO_2 + 6H^+ + 6e^- \qquad (2.3)$$

there was an excess of H^+ ions produced within the diffusion layer close to the anode. A dye mixed into the electrolyte with methanol that would only fluoresce in an acidic environment, such as Quinine, could identify regions of high H^+ concentration. As the

pH was stepped up on substrates to promote methanol oxidation, localized regions that had high catalytic activity would reduce the pH within their diffusion layer, leading to high fluorescent intensity within that area. This intensity could be detected with a camera, allowing regions that fluoresced at lower overpotentials, or lower applied potentials, to be easily seen both literally and figuratively.

This study was interested in catalysts that would promote the oxygen reduction reaction (ORR), whose half-cell equation is:

$$O_2 + 4H^+ + 4e^- \leftrightarrow 2H_2O \qquad (2.4)$$

Consequently, the dye used would need to fluoresce more intently under UV light as the pH increased to indicate a local increase of this reaction on the substrate. Umbelliferone, a dye found in sunscreen and ceramics, was chosen. As seen in Figure 15, it fluoresces under UV light. However, in acidic solutions under pH ~ 6 its center of absorbance is ~320 nm, in the UVB regime. Above this, to approximately a pH of 8.5, it becomes deprotonated, changing the electronic structure of its fluorophores and moving its center of absorbance to ~360 nm [61]. By using a typical UVA black light with a center of emittance ~360 nm, one could detect an increase in umbelliferone fluorescence as the pH of its solution increased above 6. However, there would still be some initial fluorescence from the protonated umbelliferone below pH ~ 6 since the black light source had a fairly broad spectrum that fell into the 320 nm regime at low levels.

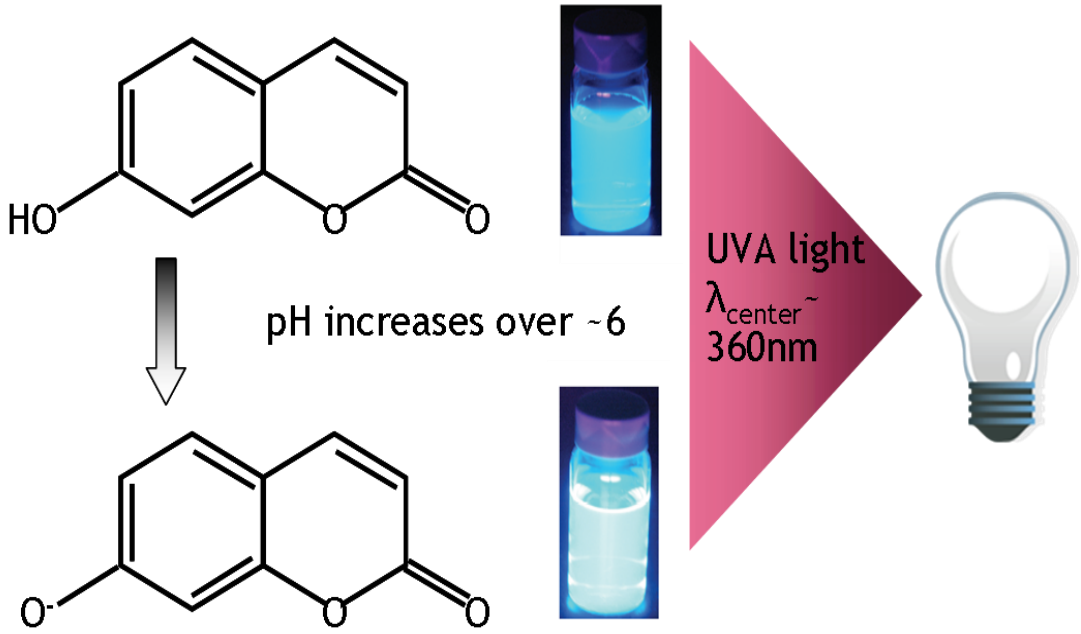

Figure 15. Deprotonated umbelliferone from pH 6 – 8.5 fluoresces more strongly under UVA light than acidic umbelliferone.

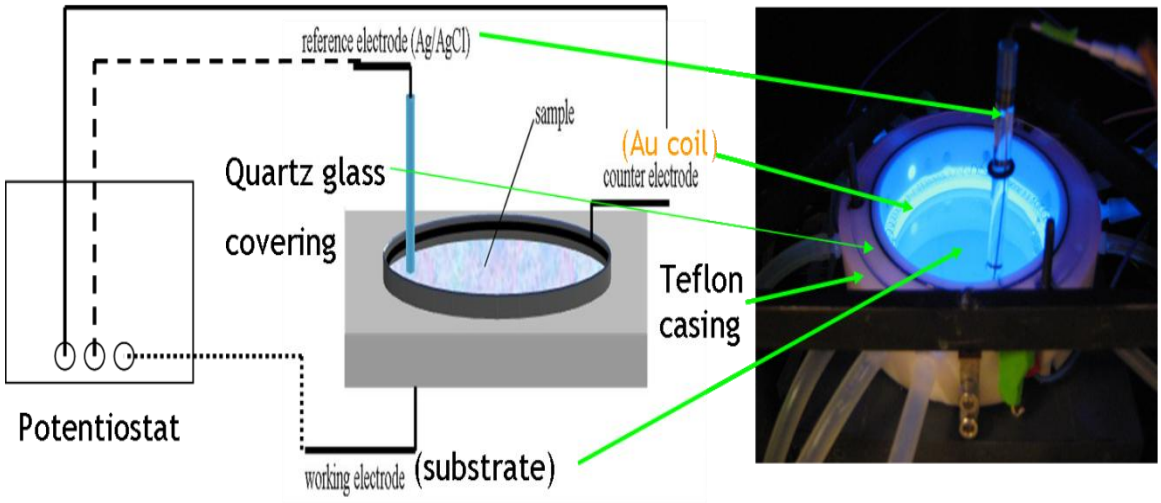

Figure 16. E-chem Setup to characterize sputtered films for ORR fluorescence intensity. Picture on right is e-chem setup in use.

2.3.2 Fluorescence Setup

To characterize the sputtered substrates for activity, a three-electrode 'e-chem setup' was employed. As seen in Figure 16, the substrate itself (i.e. doped Si bulk, Ta underlayer, and sputtered thin film) was the working electrode, a gold wire placed well away from the diffusion layer of the substrate was the counter-electrode, and an Ag/AgCl couple acted as the reference electrode. Teflon© casing, with an inner diameter of 67.8 mm and an O-ring on the bottom, was clamped down upon the substrate to hold in the electrolyte. A quartz glass covering, transparent to UV light, was placed on top of the cell. To apply the potential and measure current coming into and out of working electrode substrate, a Pine AFRDE5 potentiostat was used.

The ~50 ml electrolyte for fluorescence testing consisted of 0.1M sodium sulfate and 0.3mM umbelliferone in deionized water naturally at pH~5.6 from dissolved carbon dioxide. This translated into ~1.5 x 10^{-5} moles of umbelliferone, or 9 x 10^{18} molecules in the solution. Even before expending any of the $10^{-5.6}$ M H^+, or ~7.56x10^{16} H^+ ions in the ORR reaction , that would still leave a greater number of umbelliferone molecules than the 1.2 X 10^{14} hydroxide molecules (or water) likely to deprotonate the umbelliferone. A dense (111) FCC surface of 2 Pd atoms/unit cell surface (3.89 X 3.89 Å dimension) would result in 1.50 X 10^{15} atoms/cm^2, or 5.42 X 10^{16} atoms/fluorescent cell. If all the Pd atoms catalyzed a separate reaction, there would still be orders of magnitude greater umbelliferone in solution, more than sufficient to indicate ORR activity.

Initially, a 0.1M sodium sulfate 'background' solution, deaerated for at least 30 minutes with N_2 gas, was added to the cell. N_2 gas continued to flow through the cell, with the quartz covering ensuring little O_2 introduction to interfere with this purging. The working potential applied to the substrate was decreased from 1000 mV → 800

mV → 600mV, each step taken when the current coming into or out of the substrate stabilized close to zero. This ensured that any dealloying or oxidation state changes did not affect the fluorescence testing. It was stopped at 600 mV since this would be the beginning of the potential sweep. This potential was chosen since it was close to the thermodynamic potential for ORR at a near-neutral pH and was above the ORR open-circuit potential of the films undergoing testing. Once this was done, the background electrolyte was flushed and the same electrolyte, only aerated and mixed with .3mM umbelliferone, was introduced. The cell was swept from an initial potential of 600mV to -100 mV vs. Ag/AgCl at a rate of 5 mV/s. Pictures were taken with a CCD camera every 20 mV.

As stated previously, the starting potential of 600 mV should have been close to the thermodynamic potential of the ORR reaction at near-neutral pH due to the Nernst equation for increasing pH. None of the catalysts should have had a driving potential for ORR above 600 mV and none appeared to, as seen in the open-circuit potential taken before testing (albeit the value included the entire film and not just one region). As the applied potential was swept downward, this potential opposing the ORR reaction decreased. Once it decreased below the driving potential of ORR for any catalytic site, that site would begin to reduce dissolved oxygen gas, use up H^+, and increase the local pH in that region. This increase in pH above 6 would result in the deprotonation of umbelliferone and cause it to fluoresce. The potential at which an increase in fluorescence was first noticed indicated the threshold, or onset, potential for ORR at that site. The increasing pH would initiate a 'cascade effect', as the increase in pH would lower the overpotential for ORR even further, resulting in an increased reaction rate and even brighter fluorescence. The onset potential was seen to correlate fairly well with the potential at which ORR activity was initiated.

An example of this optical screening mechanism can be seen in Figure 17 for Pd-Ti. As the potential was scanned downward, a) the Pd site, which is more catalytic and has a lower overpotential than Ti, started to fluoresce first. To eliminate background fluorescence from protonated umbelliferone and reflected UV light off the cell surface, b) the 500 mV picture, where no ORR activity occurred, was subtracted from the others. A Labview® program sifted through the images for the blue-green intensity indicating fluorescence and determined the onset potential in c) by finding the first dramatic increase in slope from background intensity. This onset potential was graphed with millimeter-scale resolution to reveal the relative catalytic activity of the substrate in a fluorescence map figure. As expected, the near-pure Pd showed the highest signs of catalytic activity.

Assuming there is minimal oxidation occurring and a Nernstian behavior for the oxygen reduction reaction (fast enough charge transfer and diffusion on the surface to maintain concentration levels of reactant determined by the Nernst potentials), its potential should be described by:

$$E = E_{1/2} + (RT/nF)\ln((j_l - j))/j) \qquad (2.5)$$

where $E_{1/2}$ is the half-wave potential at $j = \frac{1}{2}(j_l)$, $RT/F \sim 59.1$ mV under testing conditions, n = # electrons in the reduction (4), j is the reduction current, and j_l is the limiting reduction current due to mass transport limitations. Rearranging for the reduction current gives:

$$j = j_l/(1 + e^{((59.1mV)\text{-}1n(E_{1/2} - E))} \qquad (2.6)$$

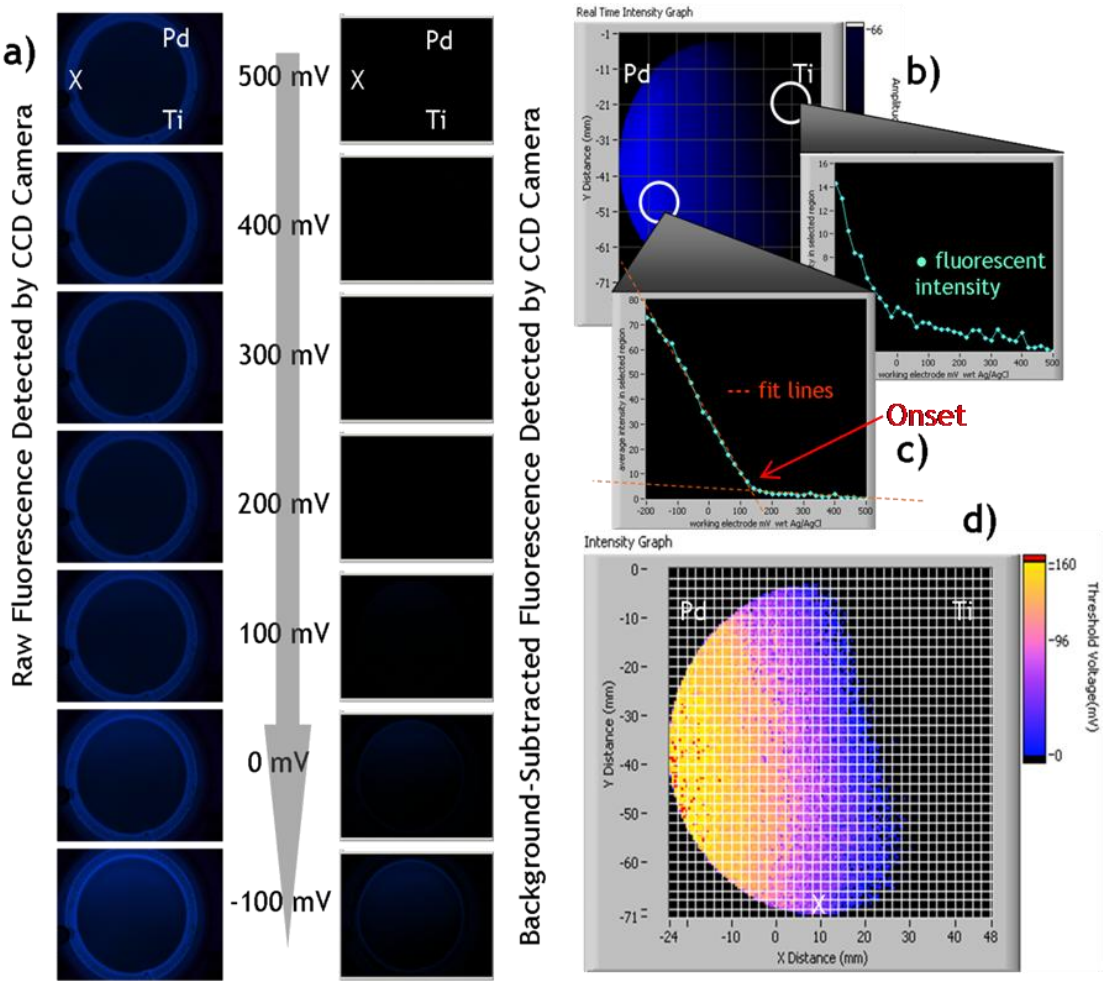

Figure 17. Sample fluorescence scan for an on-axis Pd-Ti-X spread sputtered on the on-axis Gilgamesh sputtering system, where 'X' stand for 'no target'. In a), as the potential to the substrate is scanned downward from 500mV, the CCD camera picks up fluorescence from the umbelliferone ,which is separated from UV light reflection from the sides of the cell by subtracting a background (500mV picture). A Labview® program filters out red light and obtains a numerical value up to 256 for the blue-green intensity over the wafer, as seen for the two sample regions that are b) Ti-rich and c) Pd-rich. Onset potential is determined from steep increases in the intensity and d) plotted in real-space. For this sample, one can see that the highest potential, or greatest ORR catalytic activity, occurs in the Pd-rich region, as expected.

As described in a recently published paper by J. Gregoire and M. Kostylev, by assuming the limiting current is related to the catalyst surface area, one can integrate this equation for the coulombic charge density (Q) from the reduction reaction, where v is the sweep rate, and determine that:

$$Q \alpha j_l v^{-1} \ln(1 + e^{[(E - E1/2)/(59.1mV)]}) \qquad (2.7)$$

Since the fluorescent intensity increases as the number of H^+ ions decrease in the ORR, it is related to the charge density passed for such a reaction [62]. This would make fluorescence an integrative method of detecting ORR. Other groups employing high-throughput optical techniques have used electrochromic material to determine the charge generated [63].

In either case, a film with a higher surface area (i.e. a rougher or dealloyed surface) would have a much higher fluorescence at all stages of the reaction. In fact, it might indicate a higher detectable onset potential than a smoother film. To resolve this and obtain a current measurement that might give a more specific measurement of the ORR, a smaller test cell was used to better identify catalytic composition regimes that showed high activity in the fluorescence test.

2.4 Cyclic Voltammogram Cell

This test cell design was very similar to the previously described fluorescence cell. The major differences were size and reference electrode. It had an inner diameter of 1 cm compared to the previous 6.78 cm. In addition, a Pt RHE electrode replaced the Ag/AgCl since the confined space would increase the chance of Cl^- poisoning from

the electrode. Once regions of high catalytic activity were identified in the fluorescence testing, this smaller test cell would be clamped over it. An air-saturated 0.05 M sulfuric acid solution, or a 0.05 M sulfuric acid + .1 M Methanol solution, was most commonly used. Gas, consisting of either nitrogen, oxygen, or air, could be bubbled into the cell, agitating the solution. The pH = 1 solution was relatively similar to the acidic environment of a PEM cathode due to bordering on the nafion electrolyte. Added methanol simulated poisoning commonly encountered in DMFC fuel cells from methanol crossover.

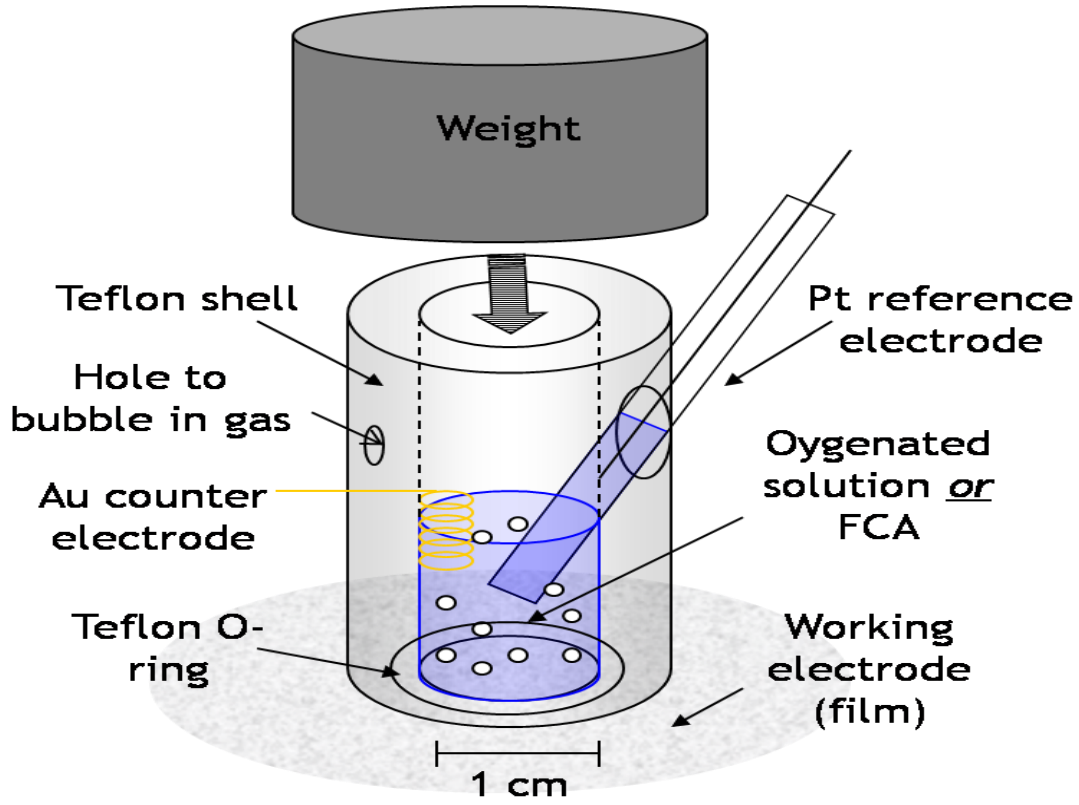

Figure 18. Diagram of testing cell used for cyclic voltammetry

2.4.1 Cyclic Voltammogram of Pt

A cyclic voltammogram on nanometer-level smooth Pt film aerated 0.05 M sulfuric acid can be seen in Figure 19. Its onset potential as well as its Tafel slope regions correlated with known data [64]. Activation overpotential determined by an ORR rate-limiting step dominated to ~720 mV. At higher overpotentials, diffusion (e.g. mass transport) of the oxygen gas limited the reaction rate to a limiting current density of ~.07 mA/cm^2, which was about 4 to 7 times lower than for other studies of Pt with a fully oxygenated circulating (RDE) solution in the cell [65]. Such low values may have been due to a combination of low oxygen concentrations and rotation rate. As known, air holds roughly 5x less O_2 than pure oxygen and thus an O_2-saturated electrolyte would have a saturation concentration roughly 5x higher that the aerated one used in this study. Since the ORR reaction has an experimentally determined reaction order of 1 with respect to dissolved oxygen, this should correspond to a five-fold decrease in current [66]. These studies also find a lower diffusion constant and higher Henry's Law constant for dissolved oxygen in air than a pure oxygen atmosphere, further decreasing the current. Also, a lack of rotation in the cell may have increased the O_2 diffusion layer close to the film, resulting in a smaller limiting current. However, the repeatability of scans indicated that the diffusion layer remained constant with time. Such Nernstian, as opposed to Cottrell, diffusion is similar to that found in RDE scans, and suggested that as long as future films were swept at the same conditions as the sputtered Pt film, valid comparable results could be obtained. Such fortuitous results may have been due to the slow scan rate of 5 mV/s, inherent convection in the cell from aeration agitation, or some other process.

Two other significant redox peaks appear in the voltammogram at lower potentials. One set, at ~60 mV vs. RHE, were the peaks associated with hydrogen gas

adsorption on the (111) facets that dominate the texture of the sputtered Pt. The peak areas have been used to approximate specific surface areas on Pt; however, due to the unique adsorption properties of hydrogen into bulk Palladium, this does not work well for that metal [67]. The second set of peaks occurred ~250mV, and were indicative of (bi)sulfate reduction and oxidation on the surface. The adsorption of this anion on the surface plays a strong role in ORR kinetics due to site-blocking and electronic effects [68].

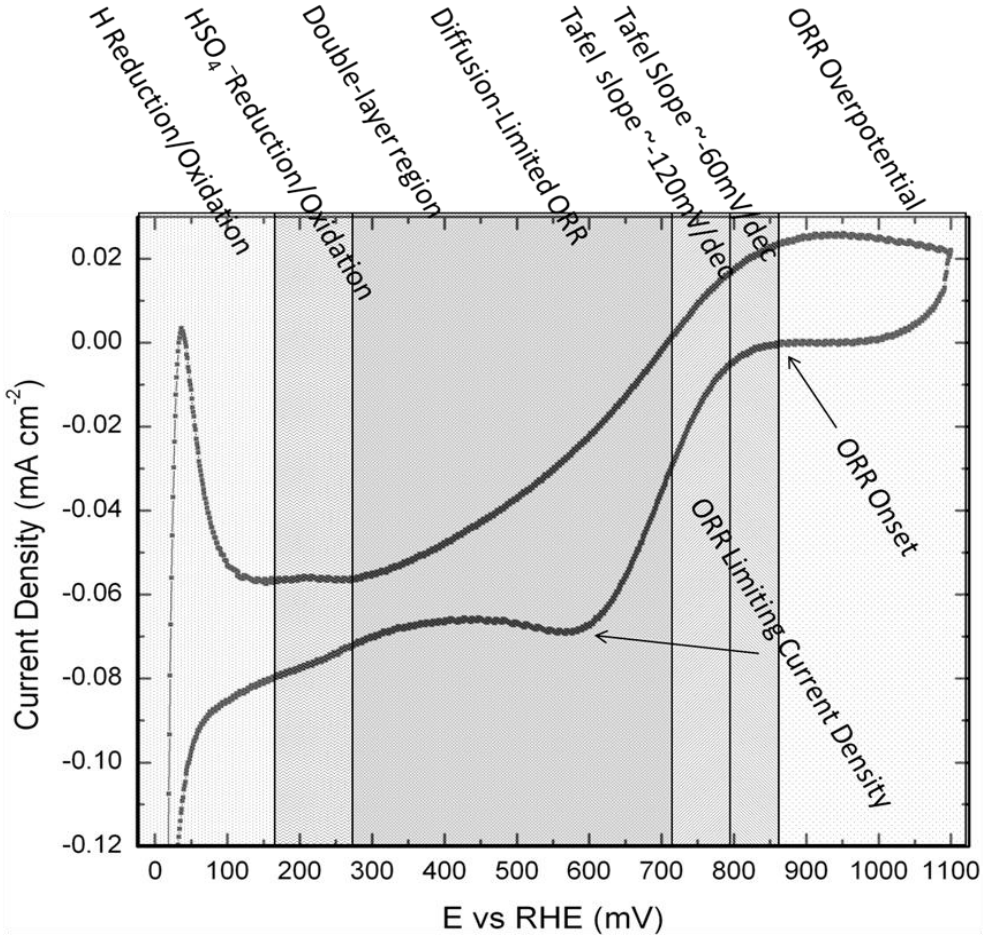

Figure 19. Pt (~1000 Å thick) tested with 1 cm diameter cell in 0.05 M Sulfuric acid. Since Pt had a surface roughness in the nm regime, the current was approximately equal to the current density. Regions for pH = 1 correspond to what is known about Pt, including overpotential of 300-400.

2.4.2 Polarization Curve of Pt

A Tafel plot can help analyze the oxygen reduction reaction in the activation polarization region. As long as the reaction is controlled by such charge-transfer kinetics, it can be described by a variant of the Butler-Volmer equation:

$$j_c = j^o_{O_2}\left(e^{n\alpha_O F\eta_c/RT} - e^{-n\alpha_O F\eta_c/RT}\right) \qquad (2.8)$$

where j_c is the oxygen reduction reaction (ORR) current density , $j^o_{O_2}$ is the ORR exchange current density, n is the number of electrons in the rate-determining step (RDS), α_O is the transfer coefficient, F is the Faraday constant, η is the ORR overpotential, R is the gas constant, and T is the temperature in Kelvin. At the large overpotentials for this reaction, the second term, representing the reverse reaction, becomes negligible:

$$j_c = j^o_{O_2} e^{n\alpha_O F\eta_c/RT} \qquad (2.9)$$

By taking the log of both sides, the overpotential η can be plotted versus the current density j_c according to:

$$\eta_c = (2.3RT/n\alpha_0 F)(\log j_c - \log j^o_{O_2}) \qquad (2.10)$$

where the prefactor ($2.3RT/n\alpha_O F$) is the Tafel slope (b) of η vs. j_c. For the room-temperature 4-electron ORR on Pt, the transfer coefficient $\alpha_O \sim ½$ and the apparent n equals 1 or 2 for the number of electrons in the RDS. Hence, b has values near either 60 mV/dec or 120 mV/dec. In this study, the RHE potential rather than the

overpotential was plotted vs. the current density; and these slopes became, respectively -60 mV/dec and -120 mV/dec. The plot for sputtered Pt can be seen in Figure 20. More recent studies have suggested that the inherent Tafel slope derives from only an intrinsic 1-electron RDS (i.e. -120 mV/dec Tafel slope) involving the Langmuirian adsorption of oxygen:

$$O_{2ads} + H^+ + e^- \leftrightarrow O_{ads} + OH_{ads} \qquad (2.11)$$

It is difficult to determine how exactly this reaction occurs. The favored model for the RDS in the bridge-bonding model (e.g. Pt, Pd) is:

$$2M + O_{2ads} + H^+ + e^- \rightarrow M\text{-}OOH_{ads}\text{–}M \qquad (2.12)$$

$$M\text{-}OOH_{ads}\text{-}M \rightarrow M\text{-}O_{ads} + M\text{-}OH_{ads} \qquad (2.13)$$

where M is the catalyst metal and OOH is a superoxide intermediate before the final O-O bond is broken [69, 70]' . Griffiths model side-on interactions involving only one M atom can be substituted in some cases. The lower slope at -60 mV/dec has been proposed due to the site-blocking and electronic effects of anion adsorption, in particular OH and other oxygen species [71]. The deviation in the Tafel slope (b) from -120 mV/dec for Pt and related metals in an aqueous solution is then mainly due to the site-blocking effects of these chemisorbed oxygen species according to:

$$b = (2.3RT / n\alpha_0 F)(1 - \frac{1}{1-\theta}\frac{d\theta}{d\log j_c}) \qquad (2.14)$$

where θ is the fractional coverage of catalytic sites by the site-blocking oxygen species. Of these, the adsorbed OH is a part either of the ORR process or from water adsorption:

$$M + H_2O \rightarrow M\text{-}OH + H^+ + e^- \qquad (2.15)$$

Therefore, the lower apparent slope is experimentally indicative of the ORR under Temkin conditions, in which these oxygen species hinder the activity by binding too strongly to potential catalytic sites. Since a Langmuirian adsorption of oxygen is desired to create more catalytic sites, one would like to increase the transition potential at which the slope changes from -60 mV/dec to -120 mV/dec. This 'transition potential' has been shown to occur when the coverage by reduced surface oxygen decreases below $\theta = ½$. [72]

Exchange current densities can be determined by extrapolating the Tafel plot to an ohmic-loss corrected zero overpotential, or the thermodynamic open-cell potential (OCP). For the 1 cm cell with aerated 0.05 M sulfuric acid (pH = 1), the potential would be 1219 mV vs. RHE, 10 mV below the OCP at standard 1 atm O_2 pressures. This exchange current density indicates intrinsic ORR electron transfer rates in the material where the forward and reverse reactions are in dynamic equilibrium; a higher current density is often associated with a better catalyst. If the extrapolation occurs from the intrinsic -120 mV/dec slope region, it will determine how rapidly the reaction can occur without the site-blocking effects of chemisorbed species like OH. Since the extrapolation is only for a 1-electron RDS, it must be multiplied by 4 to obtain the exchange current density for the 4-electron ORR. The exchange current density can be defined as:

$$j_0 = nFC_{O_2}k \qquad (2.16)$$

.

where the only new terms are the concentration of O_2 at the surface, C_{O_2}, and the electrochemical rate constant k [73]. This rate constant is proportional to an Arrhenius expression involving exp(-ΔG(ϕ)/RT), where ΔG(ϕ) is the activation energy for the rate-limiting electron transfer at some potential ϕ. Therefore, a higher exchange current suggests a lower, more favorable activation energy for the ORR.

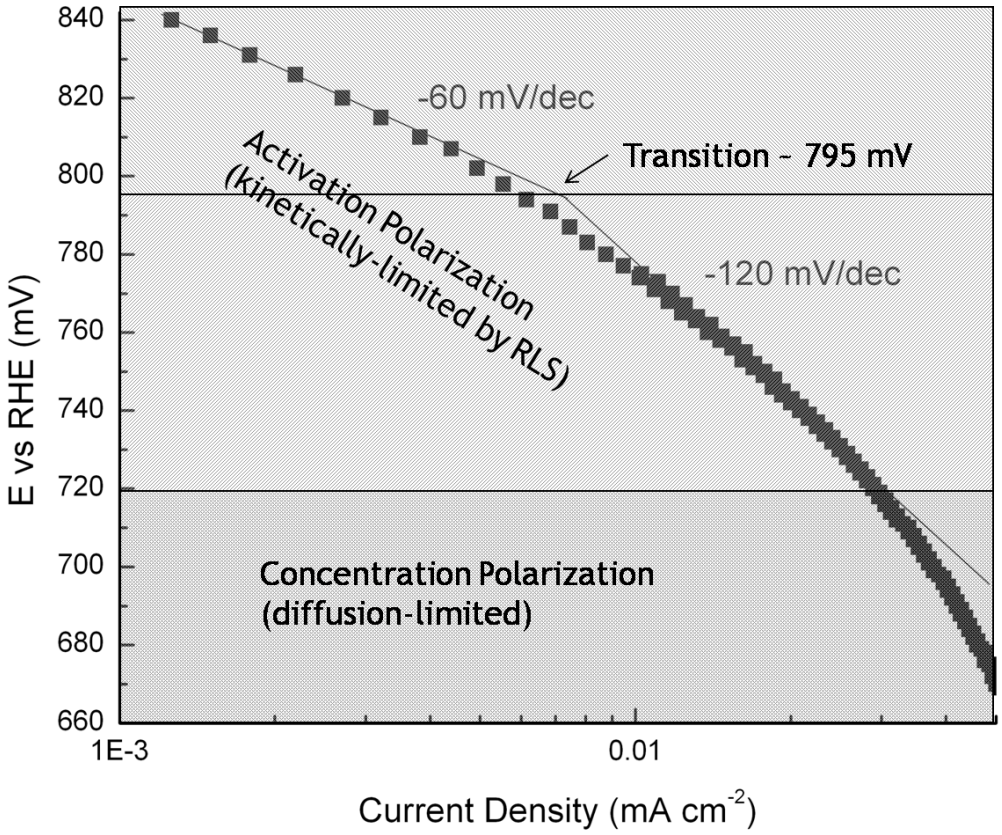

Figure 20. Polarization curve of Pt in aerated 0.05 M sulfuric acid. Above 720 mV, the reaction is mainly kinetically limited by the rate-determining step (RDS). A change in the Tafel slope implies a change in the RLS from Temkin to Langmuir-like O_2 adsorption. Below, 720 mV, mass transport limitations become predominant.

2.4.3 Surface Area Measurement with Ferrocene

As with the fluorescence test, the current measured in the cyclic scans was dependent on surface area. Many of the alloys were expected to become less smooth than the sputtered Pt due to dealloying, surface segregation, and other roughening events [74]. With a higher surface area leading to a probable increase in the number of catalytic sites, the ORR current, and thus the activity, could be overestimated. To measure this surface area and determine a current density (mA cm^{-2}), the study used a linear sweep voltammetry with a ferrocene redox couple previously developed to determine the surface area in a dealloyed Pt-Zn composition spread [62].

This technique scanned the potential of the working electrode substrate in the 1 cm cell using a new solution consisting of 0.2 mM ferrocene monocarboxylic acid (FCA) and the standard 0.1 M sodium sulfate supporting electrolyte. The key ingredient was the Fe in the ferrocene while the monocarboxylic acid functional group primarily existed to keep the molecule more polar solubility purposes. As the potential was increased from 100mV to 700mV, a peal ~200-400mV indicated that the Fe^{2+} in the FCA oxidized to Fe^{3+}. This produced an oxidation peak, i_p [mA], which, when the background current was zeroed out, gave a rough estimate of the surface area, A[cm^2]:

$$A = (3.72 \times 10\text{^-}6) \times i_p \times v^{-1/2} \times D\text{-}^{1/2} \times C^{-1/2} \times n^{-3/2} \quad (2.17)$$

where v was the scanning rate of 5 mV/s, D was the diffusion constant of FCA, C the bulk concentration of FCA, and n the number of electrons in the redox half-reaction, which was '1' in this case for Fe^{2+}/Fe^{3+}. By taking the average of i_p with the Fe^{3+} reduction on the scan back down, a more accurate reading could sometimes be achieved. The surface area figure was normalized to that of Pt, which it

underestimated, by adding a fudge factor of ~3. While the FCA molecule was larger than O_2 and could likely not diffuse as well into smaller pores, the Nernstian dynamics should have been relatively close, as such small areas would quickly deplete in O_2 leading to little activity. Towards the end of this study, ferrocene methanol at higher concentrations of 1 mM was used to observe the redox peaks more easily. Additionally, only conductive sites would have been able to oxidize and/or reduce both species. Other techniques to measure the current density, such as H_2 production by scanning past 0 RHE in the 1 cm cell with sulfuric acid, would have given dubious results due to high degrees of H absorption into the bulk by the catalysts sputtered, notably Pd [75].

2.5 Composition Characterization

2.5.1 Energy Dispersive Spectroscopy (EDS)

Thin film atomic concentrations were characterized using two main techniques: (1) Energy Dispersive Spectroscopy (EDS) and X-ray Photoelectron Spectroscopy (XPS). The former analyzes the bulk concentration down to at least 100 nm while the latter measures the elemental concentration down to ~2 nm, or the first few surface monolayers. A diagram of the principles involved can be seen in Figure 21.

EDS measures atomic concentration by subjecting the sample to high-energy electrons in an SEM (~5 – 30 KeV). These excite X-ray lines characteristic of the elements in the material. The initial high-energy electrons generated in the SEM are accelerated towards the sample, impacting with high enough velocities to transfer sufficient energy for inner shell electrons up to a few microns deep to leave their

respective atoms. Once these inner-shell electrons are ejected, electrons from the outer shells drop down to fill up the now-empty states. The difference in energy between the former outer electrons and the now-inner electrons is released at wavelengths in the X-ray regime, which are characteristic of the atoms. A solid-state detector can measure the intensity of these X-rays over a range of wavelengths, translating the data into an estimate of the bulk atomic concentration in a thin film.

This particular study used a JEOL 8900 Scanning Probe SEM with a Beryllium window in front of a SiL detector. The scanning area was typically a square, ~ 1mm on a side, and at the 100x magnification level. Due the low-energy X-ray absorbance properties of the detector and window, elements with atomic numbers below that of Mg had trouble being measured. In addition, carbon contamination on the window reduced resolution. Other problems impacting accuracy include secondary electrons generated from X-rays coming from deep within the sample (although initial impacting electron energies were always kept above 2x the expected energy needed to knock out inner electrons to reduce this problem), charging on the surface (although most were metallic), overlap between peaks within 100 meV of each other (wavelength dispersive spectroscopy, with a crystal such as LiF diffracting wavelengths close to each other for easier analysis, could be used), and a non-standard calibration applied to convert the characteristic X-ray lines to composition. In all scans, the author collected X-ray lines for at least 60 seconds using initial electron energies from 7 to 20 KeV, resolving atomic composition data within 1-2% precision. It was estimated that the accuracy of this technique to determine bulk thin film composition was +/- 5%.

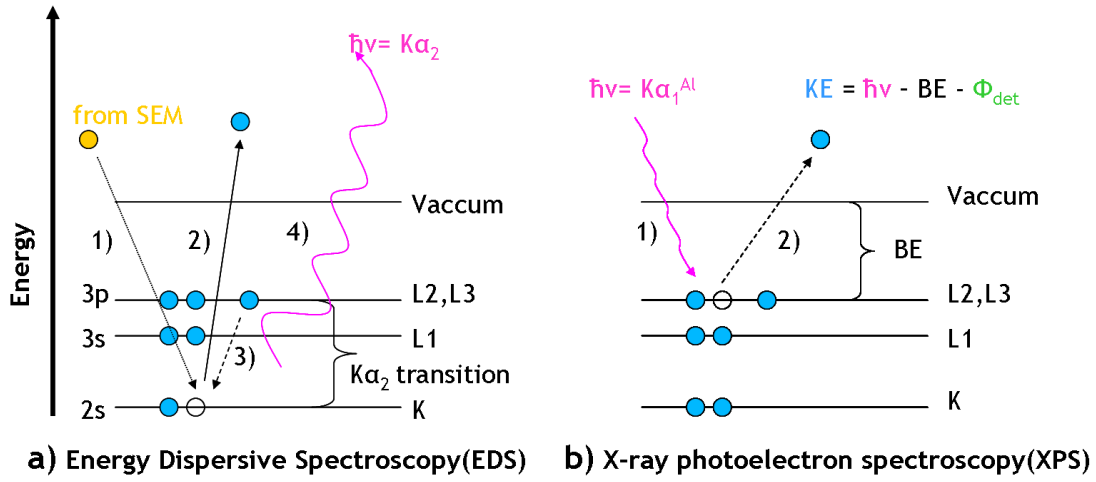

Figure 21. Principles of a) EDS and b) XPS for a P atom. For EDS, 1) a high-energy electron 2) knocks an inner shell electron out, resulting in 3) a more energetic outer shell electron falling into its spot and 4) releasing X-ray radiation characteristic of the atom. For XPS, 1) X-rays from an Al source 2) knock (usually valence) electrons out, with a kinetic energy (KE) calculated from the energy of the initial X-ray (ħν) – the binding energy of the electron (BE) – the work function of the detector (Φ) [76].

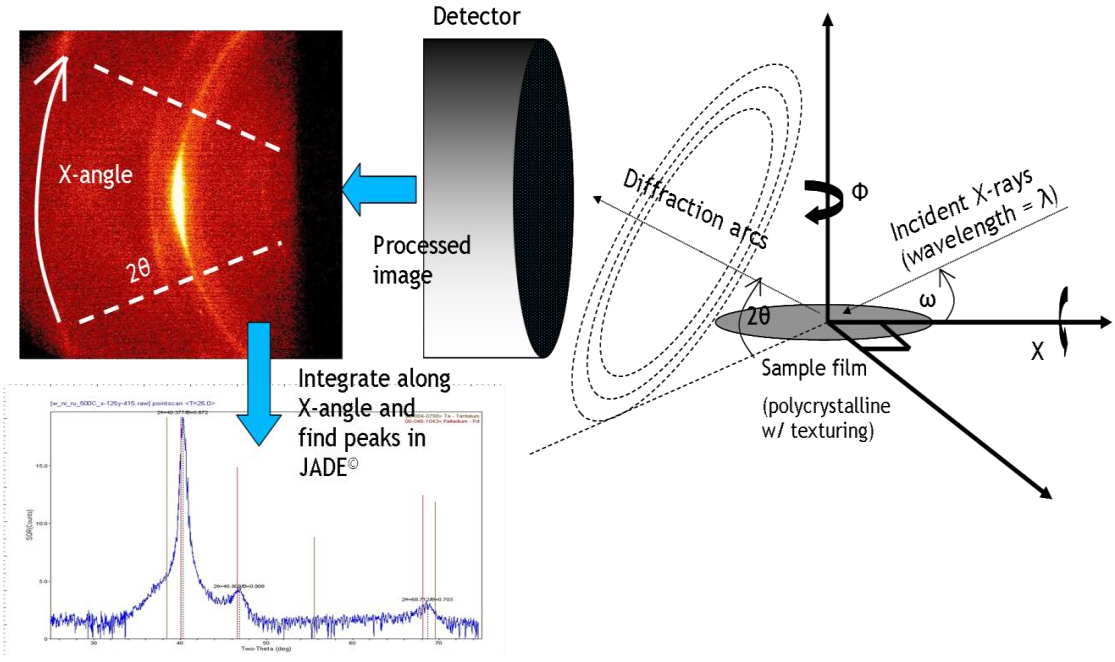

Figure 22. Basic principles of operation of the GADDS XRD System.

2.5.2 X-Ray Photoelectron Spectroscopy (XPS)

XPS was used to analyze compositions typically 1 – 4 nm from the surface. As such, it could only exploit a technique where characteristic properties were detected from atoms near the surface. In order to do this, it probes the samples with X-rays. The X-rays (typically around 1 KeV) penetrate through much of the bulk, knocking off electrons with binding energies less than this. The kinetic energy of such 'photoelectrons', equal to the incident energy of the X-ray minus the binding energy, is read by a detector that applies a magnetic field to separate the negatively-charged electrons around a turn; more kinetically energetic photoelectrons travel faster and have less time to bend in a field before striking a solid state detector. By backing out the initial X-ray energy and known work function of the detector, the intensities of photoelectrons coming off at different binding energies could be tabulated. Using a few 'fudge factors' (e.g. the relative sensitivity factor), this can be converted into atomic percentages based on binding energies characteristic to the constituents. Since the kinetic energies of these photoelectrons can reach up to approximately 1 KeV, photoelectrons produced down in the bulk do not have sufficiently kinetic energy to escape to the surface. Thus, even though the initial X-rays travel through much of the bulk, only signal within the first few nanometers is actually picked up by the detector. In addition to determining the composition, XPS can also be used to estimate the oxidation states and neighboring environment of the constituent atoms since the binding energies of photoelectrons are somewhat dependent on them. For instance, a photoelectron coming from a Ti^{4+} ion will have had a higher binding energy than that from Ti^{3+} ion due to less electron shielding from the attraction of the atomic nucleus. Some ions, such as Pb^{+4} and Pb^{+2}, do not follow this trend due to relativistic effects.

In this study, a Surface Science Instruments (SSI) model SSX-100 was used, with an Al Kα source generating X-rays having an energy of 1.4866 KeV over a spot size with a diameter ~ 800 μm. The hemispherical analyzer which 'bends' the photoelectrons to separate them into bins can operate over ~50 to 1100 eV. Operating pressures are at UHV pressures ~2 x 10^{-9} torr, about a few orders of magnitude greater than the EDS microprobe so the photoelectrons generated have a large mean free path to the detector. The listed detection limits were from .1 to 1% with accuracies within a few percent. Possible sources of error include sample and photoelectron charging leading to intensity peak broadening, plasmons and auger electrons introducing unwanted peaks, and contamination having a much greater effect on the low-intensity photoelectron signal compared (usually) to the much higher count ratio seen in EDS. Efforts at 'cleaning' the surface by sputtering off unwanted atoms (e.g. carbon-base molecules) with Ar^+ ions beforehand were limited when oxidation states were desired. Theses Ar^+ had a tendency to change the oxidation states of some atoms (e.g. Ru, Pb) noticeably after impact.

2.6 X-Ray Diffraction using GADDS

X-Ray Diffraction (XRD) makes use of the wavelength of X-rays (Angstroms, or Å) being on the same length scale as atomic spacing in many materials. This fortuitous (in this case!) circumstance leads to diffraction from the interaction of the X-rays with the electrons of periodic crystalline structures, such as the metal alloys the author intended to sputter. A simple relationship between the wavelength of the X-rays (λ), spacing between similar atomic planes in a crystal (d), angle of diffraction (θ), and

order of the pattern (n, which is most often 1 for these measurements) is known as Bragg's law, or:

$$n\lambda = 2d\sin\theta \qquad (2.18)$$

To determine the lattice constant (a_0) from cubic (e.g. FCC) alloys, which will be primarily examined in the study on Pd alloys, another geometrically-defined relationship involving the peaks from Miller-indices defines planes is:

$$d_{hkl} = a_0/\sqrt{(h^2 + k^2 + l^2)} \qquad (2.19)$$

Without significant texturing and using structure-factor calculations, the FCC (111) peaks will have the highest intensity, followed by the (200), and (220) peaks. If all three main peaks in this cubic crystal can be measured, one can use Cohen's method to take out any systematic errors shifting the peaks by plotting the derived lattice parameters vs. $1/2(\cos^2\theta/\theta + \cos^2\theta/\sin\theta)$ and extrapolating θ to 90° [76].

The primary X-ray instrument used in this study was the Bruker AXS General Area Detector Diffraction System, known as GADDS, with a $\lambda_{Cu\ K\alpha} = 1.5406$ Å. Its basic principle of operation is defined in Figure 22. A 2-dimensonal detector is able to analyze a range of 2θ and X-angles from the primarily polycrystalline samples examined. If they were single crystalline without multiple plane orientations, the arcs the detector processes would transform to single points. Texturing, as shown in the sample GADDS image, produces regions of brighter intensity along the X-arcs. By varying ϕ in the sample, a pole figure can be taken. By varying the ω-angle, rocking curves can show crystallinity. For most of the XRD scans done, X was kept at 90°, ϕ was 0°, ω was centered at 20°, and the detector was centered at 2θ = 40°. Once the

images were integrated along some X-angle range to determine the peaks along 2θ, the file with a .raw extension was transferred to the JADE© data analysis program, where θ-angles of the peaks were determined through Lorentzian/Gaussian peak fitting to find the lattice constants. In some cases for particle sizes small enough to make strain-broadening insignificant, an average grain size was determined from the FWHM calculations (Δ) and the Debye-Scherrer formula [77], or:

$$d \text{ (grain size)} \sim 0.9*\lambda/(\Delta\cos\theta) \qquad (2.20)$$

In most of the metallic sputtered films, the grain size from Debye-Scherrer analysis was ~10 nm.

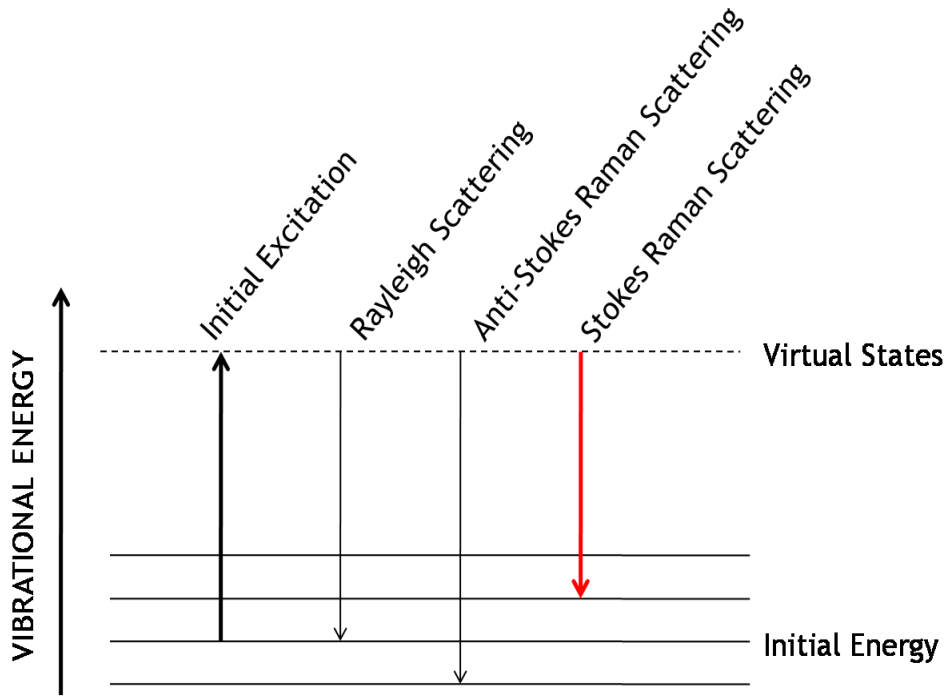

Figure 23. Different types of scattering that can occur upon excitation of the vibrational modes. The most relevant phenomena for this study are the Stokes Raman shift.

2.7 Raman Spectroscopy

Raman spectroscopy was used to obtain vibrational bonding information on the thin films. When photons of light from a laser are shone onto a molecule, they will excite vibrational and rotational states in the bonds from their initial energy state to virtual states. Once these states relax to their final states, they will re-emit these photons in a process known as scattering. If the final and initial energy states are equal, the photons will have the same energy, and thus wavelength, leaving the sample. This is called Rayleigh, or elastic scattering. However, if the final and initial energy states are different, the photons leaving the sample will have different wavelengths than before to conserve energy. This shift due to changes in the final vibrational states is called a Stokes shift if the scattered photons are less energetic and anti-Stokes if they are more, as seen in Figure 23. By resolving the shifts of these scattered photons, displayed in inverse wavelength, or wavenumbers (cm^{-1}), one can fingerprint the Raman active modes in a sample to determine the nature of chemical bonds, crystallization structures, and so forth.

This study used a Renishaw Invia Confocal Microscope with a spatial resolution of 1 μm, spectral resolution of ~ 0.1 cm^{-1}, and laser excitation wavelength of 785 nm with a power of ~ 1 mW/cm^2. Only Stokes shifts were collected from 100 to 4000 cm^{-1}. Peaks in the spectrum indicated Raman active modes, meaning the bonds either changed polarization, the shape of the electron density, or there were characteristic inelastic scattering modes in a solid state sample. Infrared spectroscopy would provide complementary information for bonds that changed dipole moment or IR-active modes in a solid sample. In all cases, a Si substrate peak at ~520 cm^{-1} revealed that the scattered photons were coming from the entire thickness of the film.

CHAPTER 3

3 PALLADIUM ALLOY COMPOSITION SPREAD

3.1 Verification of Fluorescence Screening Technique

To verify that the fluorescence setup using umbelliferone was working, 1000 Å Pt was sputtered onto 100 Å Ta at 500°C. Most of the films were sputtered at this thickness and relative homologous temperature to avoid the Zone 1 region of the Zone Boundary Model and eliminate surface effects (such as roughness) as much as possible [78]. As mentioned previously, the theoretical potential of such a system is +1219mV at room temperature in a pH = 0 solution. Since the sodium sulfate/umbelliferone solution had an expected (and meter-measured) pH starting in the pH ~ 6 regime, the theoretical potential would be shifted by 59mV/decade, or 59mV/dec * 6 dec = 354mV, to a lower potential of +875mV. With an Ag/AgCl reference electrode having an offset of ~223 mV from the SHE, this theoretical onset voltage would drop to +652mV. The initial slow kinetics of Pt result in reported overpotentials in the 300-400mV regime for sputtered thin films, so if the setup was valid the expected onset would occur in the 250-350mV range, depending on both preparation and testing conditions [79]. As seen in Figure 24, this was the onset range obtained for Pt.

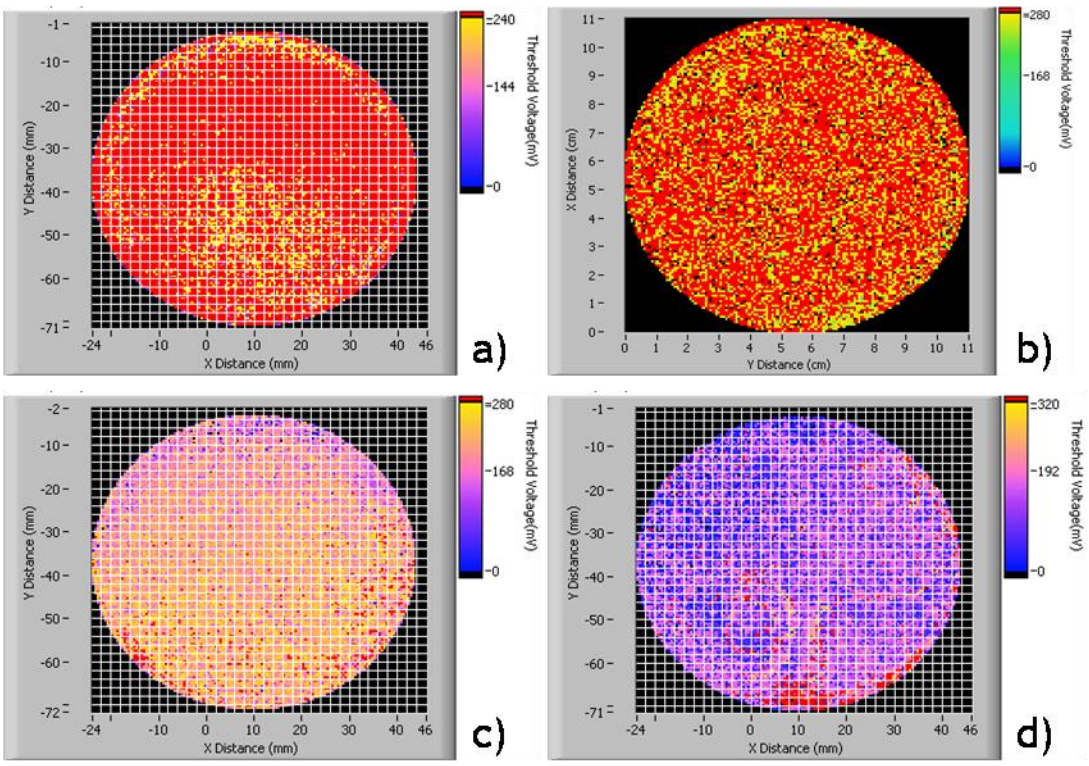

Figure 24. Fluorescence Onset Maps of Pt at prepared at various times. From top left, they are a) Tubby August 2007 b) Fenris Gun 4 April 2008 c) Gilgamesh Gun 3 August 2008 d) Gilgamesh Gun 4 August 2008

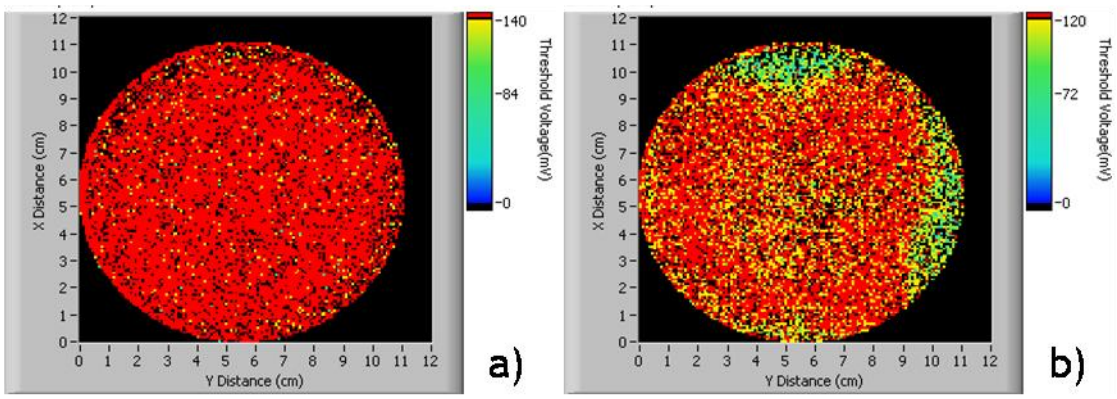

Figure 25. Fluorescence Onset Maps for a) Pd and b) Ir sputtered from Fenris Gun 4 March 2008.

A representative of the fluorescence intensity of Pt in Figure 24 is compared to its current density in aerated 0.05M sulfuric acid in Figure 26. The onset potential at 300 mV vs. Ag/AgCl corresponded to an onset of 820 mV vs. RHE at pH = 1, or an overpotential of ~344 mV for Pt, similar to other studies. By integrating the current density from 1100 mV to 854 mV RHE, a total charge density of .010 mV*mAcm^{-2} / (5mV/s) = 2.0 μC cm^{-2} resulted in the first noticeable fluorescent onset.

Since other non-Pt alloys were desired, pure Pd and Ir were deposited under the same conditions as the Pt. Because Pd and Ir both have overpotentials 100-200mV greater than Pt, one would expect the onset to occur 100-200mV lower [80, 81]. This is observed in Figure 25. A representative of the Pd fluorescence intensity in the previous figure is compared to the current density in aerated 0.05 M sulfuric acid in Figure 27. The onset potential is ~120 mV lower than Pt, which is upheld by other studies [82]. By integrating the current density from a start of 1100 mV to the onset potential at 700 mV RHE, a total charge density of .160 mV*mAcm^{-2} / (5mV/s) = 32 μC cm^{-2} results in the first noticeable fluorescent onset. If the local fluorescence were dependent on the local pH, this would imply that greater charge was needed for a comparable change in pH to Pt. A lower onset potential signified a lower ORR activity, which would create a smaller concentration gradient of protons to the Pd surface. Protons outside the depletion layer would have more time to replenish it, resulting in a greater cumulative depletion of protons (from the ORR reaction) to shift the local pH into the onset mode in the non-agitated fluorescent test.

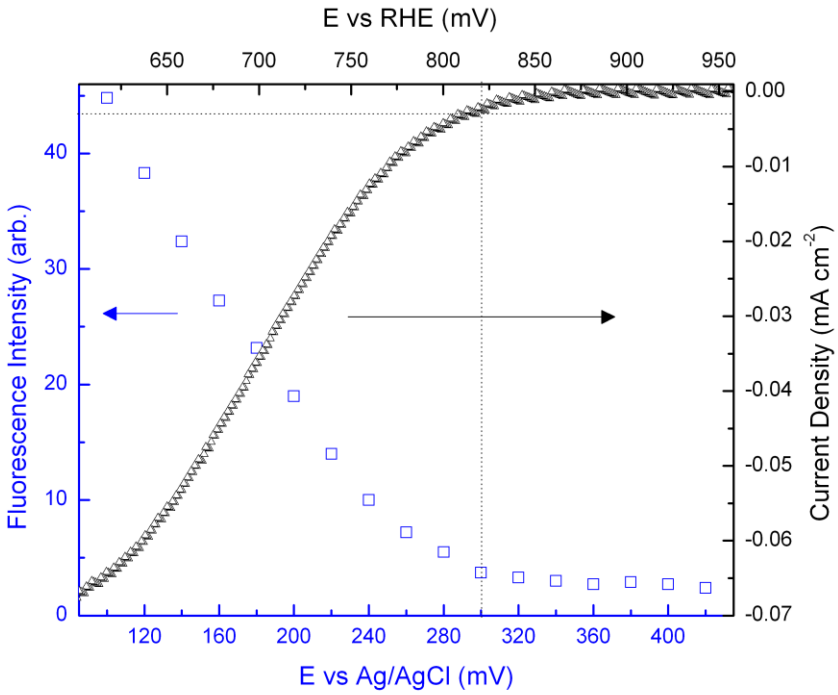

Figure 26. Fluorescent onset of Platinum in aerated 0.05M sulfate solution compared to current density in 0.05 M aerated sulfuric acid.

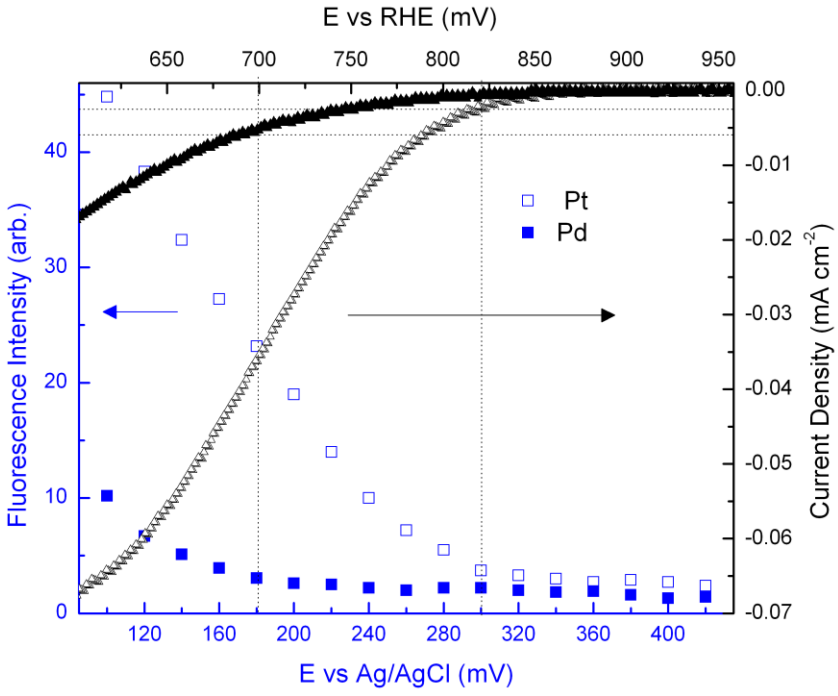

Figure 27. Fluorescent onset of Palladium and Platinum in aerated 0.1M sulfate solution compared to current density in 0.05 M aerated sulfuric acid.

3.2 An Initial Study Using the Gilgamesh On-Axis Sputtering System: A Meandering Path

Once the onsets were known for the pure noble metals, alloys and intermetallics could be sputtered. Any onset close to that of Pt would be worth investigating. The element widely regarded as having redox properties closest to Pt is Pd, where binary and ternary searches have started accelerating in number [83]. Whether fortuitously or not, the author decided that an element more electronegative than Pd would 'pull' electrons away from the d-level and increase ORR kinetics comparably to ongoing studies on Pt alloys. The two elements initially chosen after consideration of the phase diagrams and literature were Au and W. A main factor in this were the recent papers by the Bard group at the University of Texas, whose ternary composition spreads involving Pd-Mo-Co and Pd-Au-Co were among the major ternary spreads cited in literature reviews [84]. Although they used a chemical calcining synthesis rather than sputtering technique, the temperatures involved (~500°C) were approximately the same as those planned in this study, with a ratio of 7:1 Pd:Au,Mo always giving the best results. Nevertheless, since the combinatorial sputtering technique employed in the Gilgamesh on-axis system could cover over 60% of the ternary diagram, it was decided to aim for a centered 3:1 Pd:X ratio in the binary and 2:1:1 ratio in the ternary spreads to incorporate a larger composition space rather than just having large areas of near-pure elemental compositions. Right from the start, when a binary spread was sputtered of both Pd-Au and Pd-W, the W-based films seemed to produce higher onsets, as seen in Figure 28. This was further confirmed by a ternary spread consisting of W-Au-Pd, where the composition area farthest from the Au seemed to have the higher onset. One could also see enhanced fluorescence from increased surface area due to W leaching, a continued problem with this integrative high-throughput method

that helps make the onsets so approximate and more useful for trend development than concrete statements.

A series of rather haphazard ternary composition spreads containing Pd-Au or Pd-W were sputtered with the same Ta underlayer, 1000 Å thickness, 500°C temperature, and 2 microtorr base pressure. The highest onset potentials on each film can be found in Figure 29. The author wishes he could ascribe this to the lack of targets at the periods he was scheduled to sputter, but more likely than not it was due to a scattershot technique at trying to find the 'perfect composition' without really knowing anything yet. However, even with the differences in the 3rd element for the respective spreads, the W-X-Pd compositions had a higher median and lower standard deviation of onset potentials than the Au-X-Pd, whose composition onsets were both above and below that of the binary spread, indicating at times an undesirable impact of a third element, something never encountered for the Pd-W based alloys. A closer examination of some of the higher onset spreads was undertaken.

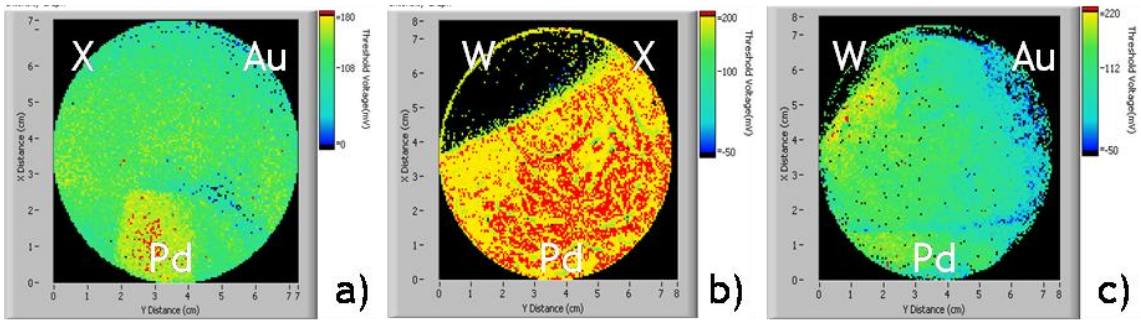

Figure 28. Pd-based composition spreads sputtered in Gilgamesh at 500C in the regular Gun 1-2-3 formation, with a) X-Au-Pd, b) W-X-Pd, and c) W-Au-Pd.

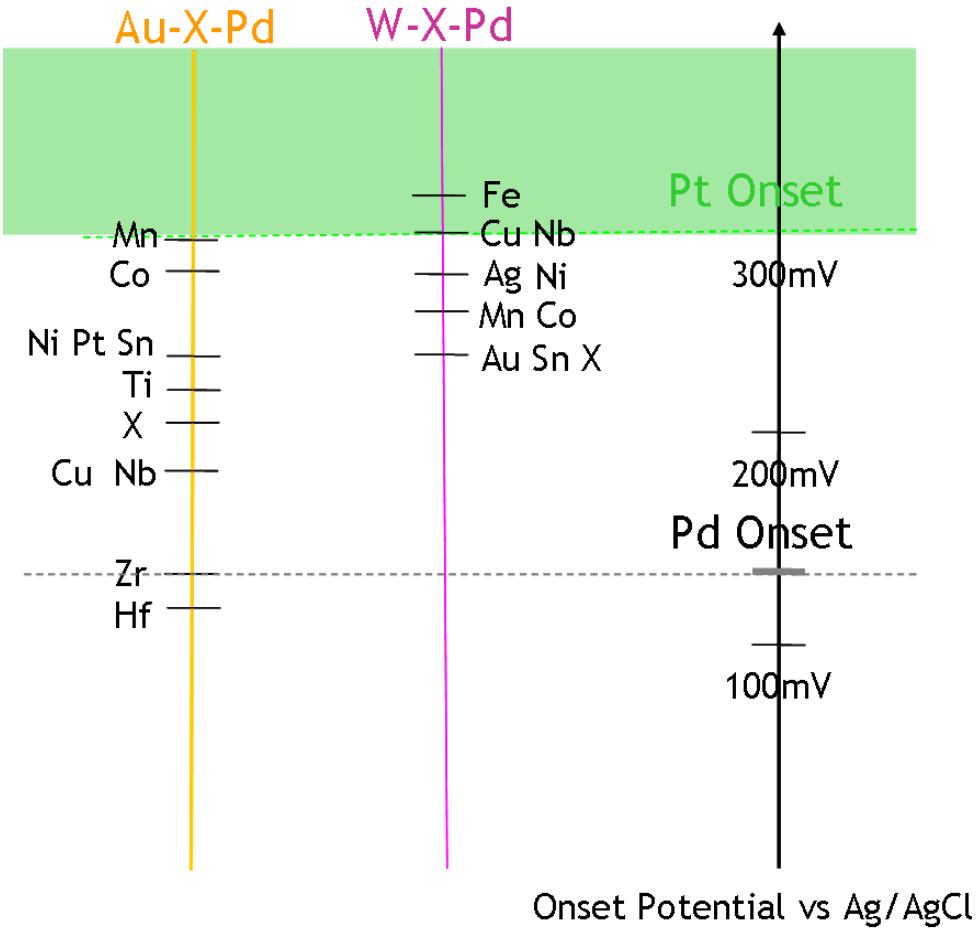

Figure 29. Onset Potentials of the Au and W-based Pd alloys. While interesting in themselves, composition spreads with onset voltages not near the values for Pt were disregarded.

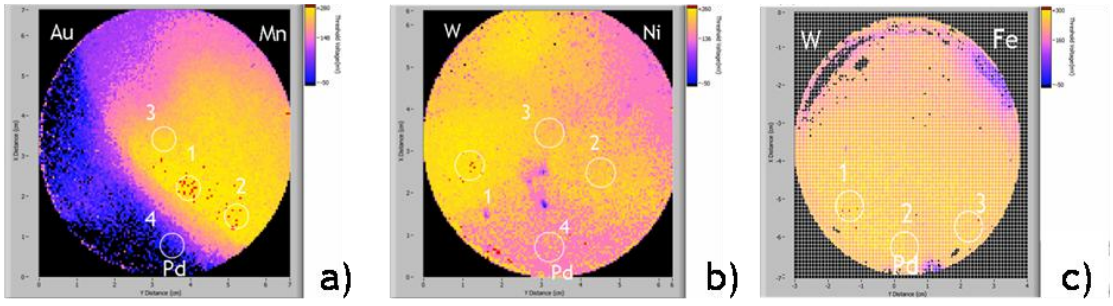

Figure 30. Fluorescence onset maps for three of the ternary spread-s whose points provided the highest onsets and were examined in more detail: a) Au-Mn-Pd, b) W-Ni-Pd, and c) W-Fe-Pd.

3.2.1 Au-Mn-Pd Composition Spread

3.2.1.1 Results

For Au-X-Pd class, X = Mn resulted in a spread with the highest onset potential, similar to that of the best Pt sputtered. Conversely, while the added Co to the W-X-Pd spread did not attain as high an onset, the X = Ni showed points on the wafer with an onset just about as high as the Au-Co-Pd composition discussed in the previously-mentioned Bard group paper. Even more exciting, X = Fe had an onset greater than Pt. Each of these will be discussed in more detail using the JEOL microprobe for bulk composition, GADDS system for XRD, and Zeiss Ultra-SEM for high-magnification scans of the surface.

The highest onset X-Au-Pd spread sputtered had X = Mn. One of the first things one cold notice from either looking at the fluorescence map in Figure 31, the table with compositions at certain points, or the EDS-confirmed ternary diagram was that the highest onset potential occurs on a near iso-concentration line where the atomic Pd:Mn ratio was ~60-70:40-30. As the percentage of Au passed ~13% of the total composition, the high onset started to level off, drastically decreasing after the 25% bulk Au level. All points showed a rough surface in the high-resolution SEM image, with the most coarsened grains appearing where there was the least amount of Mn. Curiously, there was no appreciable onset at almost pure Pd with a touch of Au.

By examining the shift in the (111) Pd peak, the lattice constant increased with increasing Au. This made sense since Au is a larger atom than Pd, which has an FCC bulk lattice parameter of 3.889 Å, rounded off to 3.89 Å. The GADDS arc for (111) was highly textured, showing a preferred orientation. A secondary peak ~42.3° for points 1-3 was indicative of either a very strained (200) Pd plane or a combination of

$PdMn_2$ and Au. Since this peak disappeared at point 4, where there was even more bulk Au but less Mn than at point 2, it most likely implied a segregated $PdMn_2$ structure. Applying Vegard's Law for a solid solution of Au/Mn/Pd and using metallic radius values for an FCC 12-nearest neighbor structure, the lattice constants should be $2\sqrt{2}$*radius = 3.837, 3.793, 3.875, and 3.882A for points respective from 1 through 4. As compared to the actual lattice parameters from XRD, these values were more than 1% larger than experimental values, except for point 4. Since the lattice constant for the distorted tetragonal face-centered $PdMn_2$ was 3.82A and the c/a ratio ~ 4.05A, the formation of this Pd-Mn precipitate likely reduced the amount of smaller Mn available for alloying to the rest of the Pd and Au, increasing the alloy lattice constant for points 1-3, as seen in the GADDS diffraction patterns [85]. Point 4, with little to no Mn, seemed to be a solid solution of Pd and Au, which are almost completely soluble in each other according to binary phase diagrams [86].

Point	Au/Mn/Pd Atomic % (EDS-rel.)	Onset Pot.(mV)	a_0 for Pd(111) Peak (Ang)
1	21/28/51	300	3.971
2	6/33/61	300	3.957
3	33/23/44	280	3.993
4	8/3/89	0	3.911

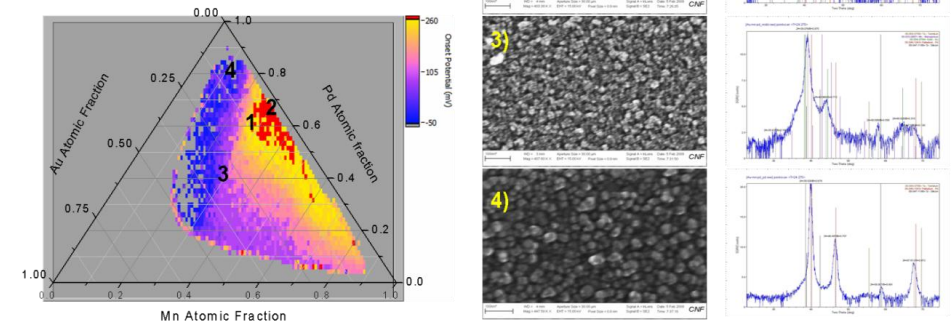

Figure 31. Toolbox of data for Au-Mn-Pd points where a) is a table of associated values, b) EDS-verified ternary diagram, c) Zeiss Ultra SEM pictures at 200nm scale, and d) XRD diagrams from GADDS with chi-arc for Point 1.

3.2.1.2 Discussion

The author interpreted this composition spread to show that ~30-40% Mn in Pd produced a good catalyst for ORR. The Au, rather than helping, looked like it was detrimental to the process. This could have been due to either 1) Au on the surface taking away spots for catalysis or 2) beneath the surface hindering it through other means. Supporting the first case, (111) FCC Au has a lower surface energy than (111) FCC Pd, being respectively ~90 and 140 microjoules/cm^2 [87]. When hot sputtering at 500°C in vacuum, one would expect the lower surface energy metal to dominate on the surface unless diffusing into the bulk. One could obtain conclusive proof from either XPS or back-scattered measurements on an SEM due to the difference in atomic scattering factors. This was not done here. Supporting the 2nd case for the hindering effect of Au was the decreasing onset potential with increasing lattice constant but relatively constant Pd:Mn ratio. An implication here is that too high a tensile strain on the Pd interrupts its catalytic effect, either through some electronic means or through physically stretching out the Pd so far apart that the Yeager bridging mechanism for oxygen reduction could not efficiently occur. In either case, previous work had shown that Pd on Au bound oxygen-based species so well that they would poison the Pd sites; Au on Pd had the opposite effect [88]. This would have explained the low onset of the Pd at point 4 with a small amount of Au.

While the results seemed to dissuade the author from further research into Pd-Au based alloys, it did support the use of Mn with Pd. In fact, about this time he found a paper by Kunchan Lee, et al. from 2005 where they sputtered Pd-X (X=Co, Ni, Cr) alloys of differing compositions by varying the area of the 3d transition metal target surface covered by Pd, as seen in Figure 32 [89]. The highest catalytic activities of the binary catalysts were found in the 30-40% regime, which fit with the Mn data. Their

explanation was that: *The partially filled Pd d-band shows a strong chemisorption of O and/or OH, and their chemisorption bonds get weaker as the d-band is filled by electrons donated by the electropositive elements. It is considered that the decreased DOS at the Fermi level of the Pd sites in the Pd alloys might weaken the chemisorption of O and/or OH on the Pd sites in aqueous solution.* The implication here was that the author should have been focusing on more electropositive elements, not electronegative elements, to shift the d-band center of the Pd towards the Fermi level, not away, to decrease poisoning of active sites by oxygen species. Mn, with a Pauling electronegativity of 1.550 compared to Palladium's 2.200, would make sense as a Pd-alloy catalyst enhancer [90].

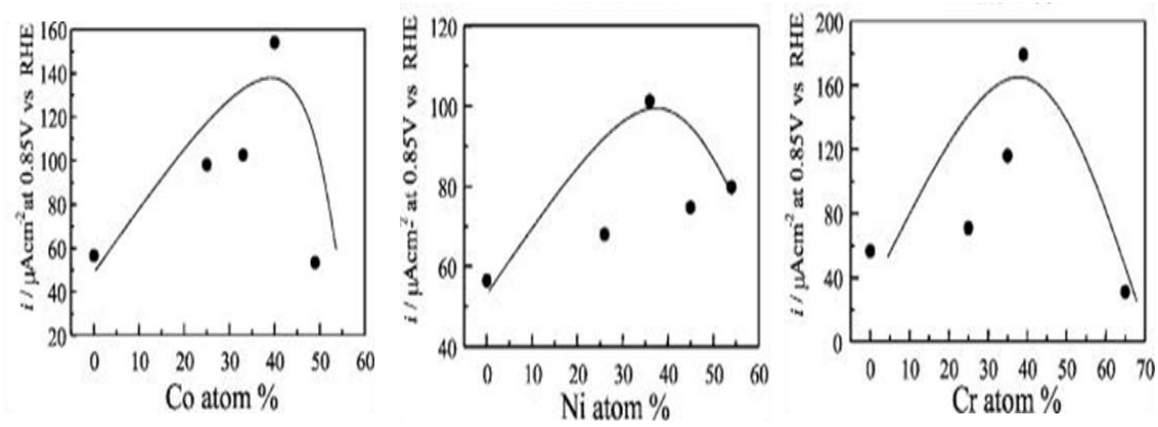

Figure 32. ORR current density in .1M sulfuric acid for sputtered Pd-X (X = Co,Ni,Cr) alloys from K. Lee et al. (reproduced from [79]).

At the same time as the d-band theory predicting slow kinetics from Pd-O species formation, particularly influential in the literature was the simple thermodynamic model proposed by Fernandez and Bard that a step slowing the kinetics would be the cleavage of the double bond in oxygen before being reduced. As such, Pd would be more catalytic when paired with a metal with a high negative free

energy for metal oxide formation, allowing the oxygen double bond to be more easily cleaved according to the Yeager model of 2 M + O_2 ↔ 2MO before 'migrating' to a Pd site to be reduced [28, 91]. Assuming Mn were still left on the surface of the sample, this would imply the Mn, with a high affinity for oxide formation (Figure 33), would make the entire alloy more catalytic by serving as the 'bond-breaker' for Pd-Mn. Both these theories made some sense, and, along with the increased surface area, could account for the lower onset. To be frank, the author was somewhat confused at this point.

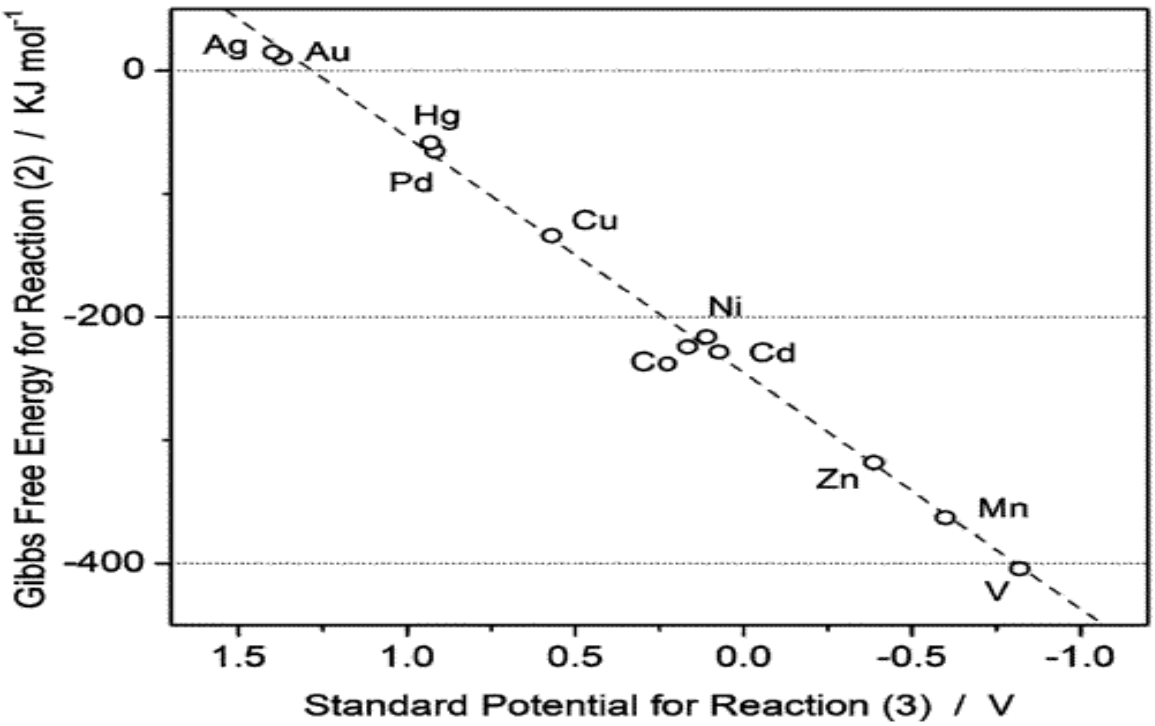

Figure 33. Fernandez and Bard's Graph of Gibbs free energy for 2M + O2 ↔ 2MO formation vs. potential for 2MO + H^+ + $4e^-$ ↔ 2M + $2H_2O$.

3.2.2 W-Ni-Pd Composition Spread

3.2.2.1 Results

Having soured on Pd-Au based alloys from the previous case study, the author turned to W-X-Pd alloys. One of the higher onset composition spreads used Ni as the 3rd element, seen in Figure 34. Due to an oversight in using the QCM rate monitor, the Ni rate was greater than expected for a 1:1:2 W:Ni:Pd atomic ratio in the middle of the wafer. As with the Au-Mn-Pd alloy, there was an iso-concentration line for Pd:Ni of ~1.3:1, or ~43% for a binary solution of the two, which according to phase diagrams are completely soluble in each other [92]. This roughly corresponded to Lee's ~40% maximum catalytic activity for Ni in Pd, as seen in Figure 32. Unlike the addition of Au, adding more W to this iso-concentration line did not change the relatively high onset potential much. In addition, the onset at point 4 of the almost-pure Pd, with some small amount of W, was close to that of pure Pd. Perhaps most intriguing, though, was the semi-iso-concentration line on the other side of the wafer with a 1:3.7 ratio of W:Pd and a peak at ~24% Ni, a phenomenon completely missing in the Au-Mn-Pd spread. When viewed in the SEM, compositions with more than ~60% Pd had a 'nano-smooth' Pd skin layer, whereas minor roughness from dealloying occurred at all other points.

The chi-arc for the (111) peak showed even greater texturing than the Au-Mn-Pd, consistent with a more-ordered Pd surface layer, as confirmed in the 'smoother' SEM pictures. A secondary peak at ~38.6° for points 1-3 was indicative of another alloy or intermetallic forming outside of the Pd-based solid solution. Peak location and EDS composition suggested tetragonal Ni_4W. Applying Vegard's Law for a solid solution of W/Ni/Pd and using metallic radius values for an FCC 12-nearest neighbor

structure, the lattice constants should have been $2\sqrt{2}$*radius = 3.796, 3.727, 3.734, and 3.889A for points respective from 1 through 4. Points 1 through 3 had higher-than-expected parameter values whose degree difference from a pure Pd solid solution positively correlated with the intensity of the peak showing Ni_4W, further verifying its presence. Point 4 appears to be a purely Pd-skin on top of a solid solution.

Point	W/Ni/Pd Atomic % (EDS)	Onset Pot.(mV)	a_0 for Pd(111) Peak (Ang)
1	17/24/59	280	3.87
2	5/41/54	260	3.77
3	10/40/50	260	3.89
4	2/7/91	140	3.86

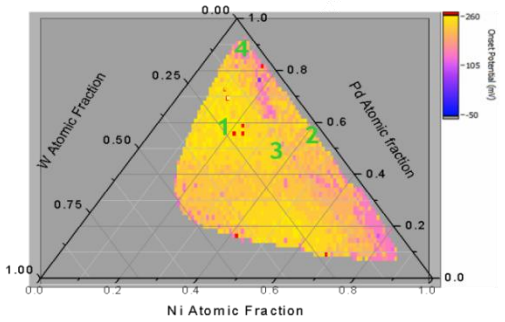

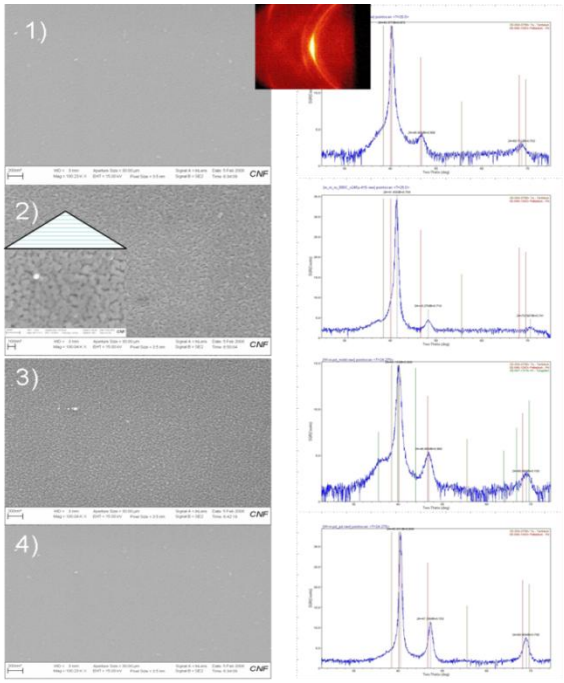

Figure 34. Toolbox of data for W-Ni-Pd points where a) is a table of associated values, b) EDS-verified ternary diagram, c) Zeiss Ultra SEM pictures at 200nm scale, and d) XRD diagrams from GADDS with chi-arc for Point 1.

3.2.2.2 Discussion

After the Pd-Au sample, the author found this one even more complex and interesting. The onset potential of the near pure-Pd point 4 was approximately the same as pure Pd. This would suggest that the W, unlike the Au, did not have a deleterious effect on Pd ORR and that the Pd (111), with a lower surface energy than

W (111), was most likely segregated on the surface as its 'skin', as seen in the SEM pictures. In addition, there was some activity in the Ni-W section of the wafer, due to a combination of inherent catalytic material and enhanced surface area from its porous nature. Starting at point 2, the same type of iso-concentration Pd-X (X = Ni with ~40%) line seemed to corroborate the study by Lee as adding W did not appreciably change the onset. This would further have supported the debatable need for electropositive, oxide-forming elements in Pd alloys if taken by itself. However, other evidence questioned that line of reasoning. First, the GADDS data seemed to imply that most, if not all, of the W in the region studied was already incorporated into the Ni_4W and likely not available for alloying with Pd. For that matter, the lattice constant of the region never reached a lattice parameter that put the Pd-alloy in tension, as happened in the Au-Mn-Pd, although extrapolation of this line showed a lower onset at higher W concentrations. Third, the iso-concentration onset line for Pd:Ni was lower than that for Pd:W. Finally, besides having a higher onset, it reached a peak at a certain Ni concentration. This surface concentration of Ni and W was suspected to be inflated since some would undoubtedly be incorporated into bulk Ni_4W (with a lower surface energy than Pd) first seen in the GADDS XRD scans.

In fact, by assuming that the sputtering at high temperature would result in intimate intermixing and that the heat of formation of Ni_4W was greater than either W or Ni substitution into a Pd alloy, one could estimate the amount of Ni and W present in the Pd alloy. In the middle of the wafer at point 3, there was approximately a 4:1 ratio of Ni:W and the highest intensity Ni_4W peak, showing that most of the Ni and W were incorporated into this alloy. In addition, the lattice constant was close to that of pure Pd, implying either that the lattice constant of Ni_4W was close to matching Pd or that the alloy that precipitated out had little to no strain effect on the Pd. This could be tested at point 2, where there was a 41:5 Ni:W ratio. Assuming all the 5%W is used up

with 20% of the 41% aggregate Ni, that would leave 21% of the Ni free to alloy with the Pd in which it is almost completely soluble in binary phase diagrams. This would correspond to a 1:0.39 Pd:Ni ratio in agreement with Lee's previous results for the same binary system. If Vegard's law was applied to the Pd:Ni alloy at respective radii of 1.375 Å and 1.24 Å, a lattice parameter of 3.78 Å would occur, which is very close to the experimental value. If the Ni_4W appreciably contributed to this constant while having a parameter similar to pure Pd ~3.89Å, the experimental constant would have a noticeably larger value. Since it did not, and with the Scherrer broadness of its peaks, one could conclude that the Ni_4W appeared as nanoparticulate inclusions in the Pd alloy. Looking at the literature, one notices similar occurrences, as with Fe in Pd [93]. In this particular study, they found that while the optimum ORR concentration ratio of a Pd:Fe alloy was ~3:1, only 12% of the Fe actually alloyed with the Pd while the rest formed Fe nanoparticulates. While this may have some relevance to the Pd:Mn and Pd:Ni ratios and will be brought up later, in this case it lends credence to the particulate theory. Finally, when applying this to the optimal onset potential at point 1, one could conclude that all the Ni was in the Ni_4W and an excess of 11%W was alloyed with Pd. It would account for a lattice parameter much closer to that of Pd, with little Ni available to compress the Pd, as in point 3. It would also show that a Pd/W alloy could have a higher onset potential than a Pd/Ni and restore the author's hope in finding a catalytic system founded on a more electronegative atom alloyed to Pd (e.g. W) rather than a more electropositive one (e.g. Mn or Ni). As a side note, it would also entail that a Pd alloy with ~11% W was more catalytic than a ternary Pd/W/Ni alloy since it had a higher onset potential than the same Pd/W composition with a Ni input high enough to leave Ni free to alloy (e.g. opposite side of wafer from point 1).

3.2.3 W-Fe-Pd Composition Spread

3.2.3.1 Results and Discussion

Having gotten encouraging results out of the W-Ni-Pd composition spread, the author turned to W-Fe-Pd, with data covered in Figure 35. Like the previous two composition systems, there was a binary iso-concentration line of high onset around 40% Fe in Pd on the lower right side of the wafer. This line seemed to persist with increasing W until ~13% W as part of the total atomic concentration. On the other side, there was an iso-concentration line of 18% W in Pd that stayed at a high onset until ~22% Fe in the total concentration and peaked at 9% Fe. The wafer surface above ~60% Pd seemed 'nano-smooth' while leeching occurred in those regions with a lower amount of Pd.

As with the W-Ni-Pd sample, there were shoulder peaks to the (111) Pd in the GADDS spectrum that indicated the formation of a non-Pd based alloy in the bulk. Matching this up to known data and phase diagram for W-Fe, one could speculate that this was due to nanoparticulates of Fe_2W. If accounted for in point 2, this would leave 0% W and 21% Fe available to alloy with the 67% Pd, or a 3.19:1 ratio of Pd:Fe. Interestingly, this would correspond with Lee's study for the Pd:Fe binary alloy where an approximately 3:1 ratio yielded the best ORR catalyst. On the side nearer the W, the peak at a W:Fe:Pd ratio of 16:9:75 would transform to 11.5:0:75 with all the Fe used up forming Fe_2W. As with the W-Ni-Pd, a Pd alloy with ~11% W gave the best ORR catalyst for this system with a 20 mV higher onset than that of Pt. The lattice parameter from the (111) Pd peak indicated a lack of alloying with the much smaller Fe atom and perhaps a small degree of incorporation of W, which fit this model.

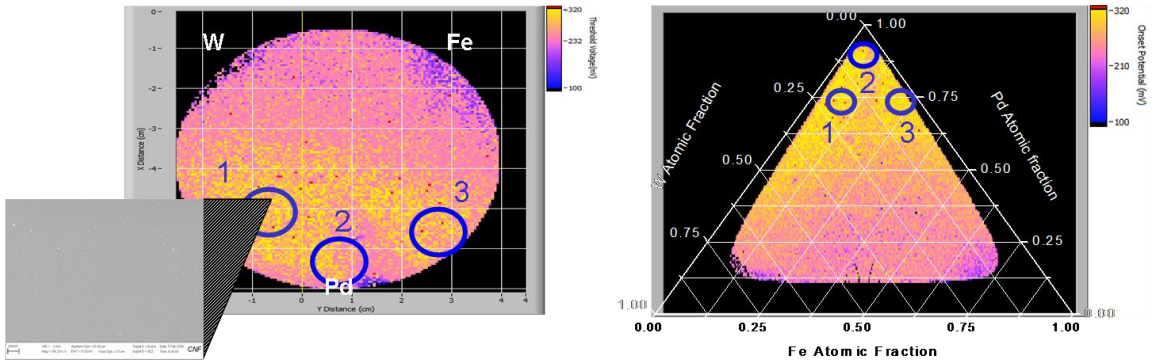

Point	W/Fe/Pd Atomic %	Onset Pot.(mV)	a0 for Pd(111) Peak (Ang)
1	16/9/75	320	3.88
2	4/29/67	280	N/A
3	6/4/90	220	3.87

Figure 35. Data for W-Fe-Pd showing a) the onset fluorescence of the wafer, b) the onset fluorescence on the ternary phase diagram, and c) a table of values relating to characterization and potential.

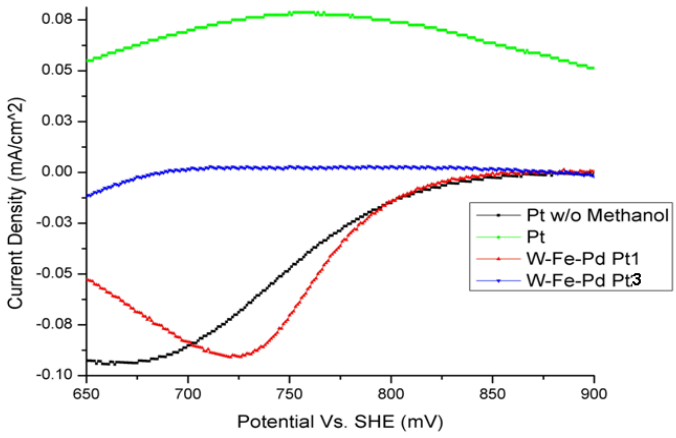

Figure 36. Current densities from the 1 cm cell at points on the Pd alloy and a sputtered Pt wafer in 0.05 M sulfuric acid and in 0.05 M sulfuric acid with 5 M methanol. The Pd alloy had similar curves in both solutions.

3.2.3.2 Initial Testing for ORR Current Density

Further testing with the 1 cm cell confirmed the catalytic properties of the $W_{.16}Fe_{.09}Pd_{.75}$ composition with similar current densities in both aerated 0.05 M sulfuric acid and aerated 0.05 M sulfuric acid + 5M methanol solution, as seen in Figure 36. Point 3, which was mainly pure Pd, had a similarly lower onset in both solutions. When compared to Pt in sulfuric acid, the $W_{.16}Fe_{.09}Pd_{.75}$ composition had a similar onset but higher current densities at lower potentials. With the added methanol, Pt performed significantly worse, as expected from the poisoning of its catalytic sites. The Tafel slopes were closer to -120 mV/decade, indicating that the rate-determining step (RDS) could be related to the initial electron transfer from the metal to the bound oxygen molecule. With the system only initially saturated with air (~20% O_2), the Pt w/o methanol should have had at least 5x less O_2 than one saturated with pure oxygen. Previous studies have found ~0.1 mA/cm^2 for Pt in a 0.05M sulfuric acid solution saturated with pure oxygen at 850 mV as opposed to ~0.02 mA/cm^2 in this study [94]. Fortunately, this study is only comparing possible catalysts to each other at the same conditions, not finding absolute current densities at possible working conditions.

Concurrently, the author found in a literature search that this particular composition was covered by a rather broad patent by Ilika Technologies LTD, which mentioned all W-Fe-Pd compositions as being catalytic [95]. Since this was obviously not the case from fluorescence testing, it would not have likely stood in the way of this particular composition being patented. However, with the electronegative W again adding the catalytic 'kick' to the Pd, the author officially excluded the electropositive theory and wondered what exactly the 3rd element was doing to make the alloy more conducive to ORR. Was the Fe anywhere near the surface or was it bound up in the bulk? XPS measurements on the surface were used to answer this.

Indeed, XPS results probing these first several monolayers found no statistical evidence for Fe near the surface and roughly 2-4% W alloyed to Pd. From bulk EDS and GADDS results, the lack of Fe could be explained away by bulk alloy formation; however, the discrepancy in W from ~11% to 2-3% could only come from a non-homogeneous distribution either caused occurring during the sputtering or the leeching during testing. Taking into account the surface smoothness to within the tens of nanometers in the SEM, the most likely thing that happened was a segregation of Pd on the surface as well as a small amount of W that may have partially dealloyed, leaving a skeletal layer only a few monolayers thick. Interestingly, this corresponded relatively closely to the 10% Mo Bard and Fernandez noticed produced the best catalyst in their Mo-Co-Pd alloys. With Mo in the same periodic group as W, perhaps they have similar properties when mixing with Pd. The dearth of Fe near the surface pointed to some electronic influence on the catalytic properties (d-band center) of Pd due to the angstrom-level distances required for significant electronic effects.

3.3 W-X-Pd Composition Spreads Using the Fenris Off-Axis Sputtering System: A Publishable Path

To understand how the 2nd and 3rd elements affected the W-X-Pd system, the author sputtered composition spreads centered at a respective 1:0:8 or 1:1:8 ratios. This would reflect the optimal ~10-11% W component exhibit in this and other studies as well as some small 3rd element influence. The ‘X’ included the entire top row transition metals in addition to Zr and In to investigate possible strain and ligand d-band interactions. Mg, Al, and Si were included to isolate possible size/strain effects. To cover a smaller composition space that would not involve the same steep gradients

of 1%/mm given in the Gilgamesh on-axis sputtering system, the Fenris off-axis system was used. This would essentially zoom in on the desired concentrations, ensuring easier identification during fluorescence testing and verification that more of the optimal concentration was being tested in the 1 cm cell. Target ions would strike the substrate indirectly and with less energy than in Gilgamesh. To ensure that sputtered atoms had enough surface energy to intermix and relax any intrinsic strains, the substrate was heated at 500°C. This hot-sputtered setup was used successfully to deposit pure Pt and Pd. No evidence of significant bulk oxide or hydride formation, as seen through XRD, was seen at the higher base pressure for Fenris. To confirm that the structural deposition results from the two systems would be similar, special attention was paid to the highest onset W-Ni-Pd and W-Fe-Pd spots on the Fenris-sputtered wafers.

3.3.1 W-Pd Binary Alloy

To begin, W and Pd were sputtered from facing guns along a Si wafer at an approximate 1:8 atomic ratio of W:Pd in the middle. This wafer was held at 500°C and had previously been sputtered with 100Å $Ta_{.96}Al_{.04}$ from the 4-inch on-axis gun. There was no other reason for the unique composition of the underlayer other than the lack of availability of a 4-inch pure Ta wafer. A strip of Kapton tape covered the equatorial region of the wafer. Removal of the Kapton tape left a clean Si surface with little to no polymeric residue. Figure 37 reveals a fluorescent onset map of the binary spread with aerated solution. The nitrogen pre-bubbled map (not seen) had onset potentials under 0 mV vs. Ag/AgCl, as did the area covered by Kapton tape in both instances. A cut across the aerated map from the W to Pd-rich side is seen in the accompanying graph

with the distance scale converted into an EDS-determined bulk atomic percentage of W in the alloy. A pure Pd alloy (e.g. 0% W) has an onset in the 160-180 mV range. As W was added, the onset increased, implying an increase in ORR activity. This activity peaked around a 10% bulk W window at 340 mV before gradually decreasing to 310mV near 20% W. The further addition of W resulted in a more drastic drop in onset potential, although it still appeared higher than pure Pd. An anomalous region of high onset occurred at the top left of the wafer, which was attributed to a high surface area in an area visibly rougher than the rest of the treated film surface.

Voltammograms (Figure 38) were taken with the aerated 1 cm cell at selected W percentages along this binary composition line. Due to the size of the cell, the given W percentages were the compositions at which the cell was centered; they may have varied radially by up to 2%. Data for both nitrogen-bubbled and aerated cells were taken from a 5mV/s sweep after 10 cycles swept at 50 mV/s to stabilize the cell. Relevant nitrogen-bubbled data, when significant, was subtracted from aerated current data for the sections above 500 mV. As seen in the following figure, Pd (0 % W) had a much higher overpotential than Pt. The inclusion of up to 3% W bettered the ORR activity, but still had produced only 25% of the current density j_{O2} of Pt at 850 mV vs. RHE. This was consistent with the onset potential data, where the 3% W region had an onset potential below the 300 mV level of Pt. However, there was an even larger increase in activity between 3% and 6% W, with the current at 850 mV now 25% greater than Pt at the same potential. The current at 850 mV further increased to almost 3x that of Pt at the 10% W window. Interestingly, all the points above 15% W, as represented by the 22% W curve in the voltammogram plot, had current densities far exceeding any of the other Pd alloy or Pt points, even though the fluorescent map did not suggest higher ORR activity at these compositions. All current densities at 850 mV along these points were more than 10x that of Pt.

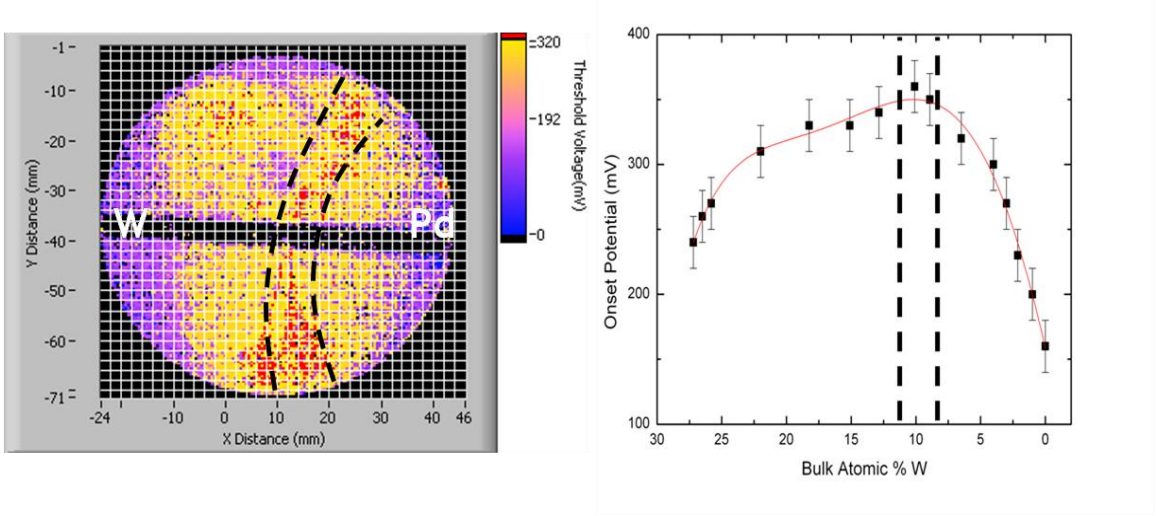

Figure 37. W-Pd fluorescent onset map with W sputtered from the left and Pd from the right on top of 100 Å Ta at 500C. The black strip in the middle was covered with Kapton tape, indicating that the Si wafer not very catalytic to ORR reactions. High catalytic activity between dashed lines on binary cut curve was around a bulk 10% W in the binary W-Pd composition spread. Bulk W percentages have an error of +/-5%.

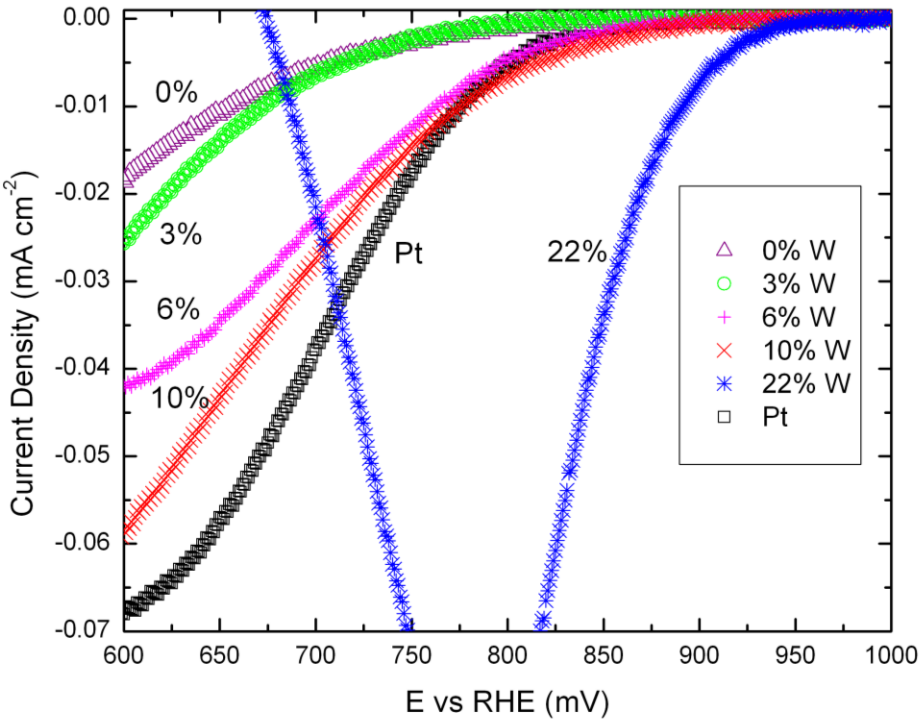

Figure 38. Voltammogram measurements of various bulk W % in W-Pd alloys in aerated 0.05 M sulfuric acid.

By plotting the data in a format similar to a polarization curve, pseudo-Tafel plots could be derived in Figure 39. The term 'pseudo' was used to convey the caveat that the current density in this case was the total current density, not just the RDE-derived kinetic component. Current ranges were limited in the plots to considerably smaller values than the limiting currents to keep the kinetic components of these currents as high as possible. In most cases, the maximum current in the Tafel plots were kept to within 10% of the limiting current values. Relevant data from these plots indicated Tafel slopes, potentials where there was a transition in Tafel slope, and exchange currents by extrapolating plots to 1219 mV vs. RHE, the thermodynamic potential of the ORR at pH = 1 and a p_{O2} near 0.2 atm.

As discussed for the sputtered Pt, Tafel slopes near -60 mV/dec indicate Temkin adsorption conditions, where OH and O species block Pd catalytic sites. An increase to the inherent -120 mV/dec slope for the ORR indicates a switch to a more Langmuirian adsorption as these site-blocking species decrease in surface coverage. The higher the transition potential between these two adsorption models, the lower the overpotential and the more likely the catalyst will have a higher activity towards the ORR. In this study, Pt transitioned from -60 mV/dec to -120 mV/dec at 795 +/- 5 mV. Pd with less than 3% W had lower transitions while those above 3% had higher potential transitions. $Pd_{90}W_{10}$ had a transition more than 70 mV higher than that of Pt, further demonstrating its promising catalytic activity.

By extrapolating the current to the thermodynamic (open circuit) potential of 1219 mV, one could find the exchange current determined by the 1^{st} electron transfer/oxygen bond-breaking RDS. This allowed a relative valuation of the phenomena leading to increased ORR activity at 850 mV, which would either be due to a decrease in deleterious θ adsorption or increase in 1^{st} electron transfer/superoxide bond-breaking in the RDS. For instance, the $Pd_{94}W_6$ alloy had a lower inherent

exchange current density j^o_{O2} but a higher current density j_{O2} at 850 mV, which was due to it having an almost 60 mV higher transition to its inherent Tafel slope. The $Pd_{90}W_{10}$ alloy, with a transition potential and exchange current higher than the previous alloy, had a j_{O2} almost 3x higher than that of Pt. Since j^o_{O2} was comparable to Pt in this alloy, the higher current density at 850 mV was almost wholly due to the decrease in blocking-site species rather than a higher RDS than Pt. This can also be graphically portrayed in the Tafel plots of Pt and $Pd_{90}W_{10}$; both had similar plots anodically approaching the OCP until, due to site-blocking kinetics, the Pt transitioned at a lower potential to a lower slope.

The Tafel plots also suggested a different reaction than the 4-electron ORR was contributing to the current density at and above 10% W. The slope transitioned from -60 to -90 mV/dec, indicating that the inherent rate-limiting reaction was different than the 'simultaneous' H^+/e^- transfer and superoxide bond-breaking previously described for Pt and Pd alloys. The difference from -120 mV/dec implied the Tafel slope factor $n\alpha_O \sim 2/3$. One circumstance in which this could occur would have the electrons in the limiting reaction n ~4/3 while α_O remained close to ½. The n ~ 4/3 electrons would suggest a complex limiting reaction or a combination of n = 1 and n = 2 limiting reactions. No ORR limiting step in the literature has n = 4/3 electrons. On the other hand, if it was a combination of n = 1 and n = 2 limiting steps, there would likely be some significant change in slope as W was added to the alloy above the 10% level; in this case, all of these points had the same -60 mV/dec to -90 mV/dec transition. The more likely circumstance for $n\alpha_O \sim 2/3$ would have n = 1 electrons in the limiting step, but an increase of the transfer coefficient α_O to ~ 2/3. This would probably have involved the production of peroxide, which would either reduce again to water or decompose to water and oxygen gas:

$$O_2 + 2H^+ + 2e^- \rightarrow H_2O_2 \qquad E^\circ = 695 \text{ mV} \qquad (3.1)$$

$$H_2O_2 + 2H^+ + 2e\text{-} \rightarrow 2H_2O \qquad E^\circ = 1770 \text{ mV} \qquad (3.2)$$

$$H_2O_2 \rightarrow 2H_2O + O_2 \qquad E^\circ = 1770 \text{ mV} \qquad (3.3)$$

First, peroxide production through the ORR 2-electron pathway has been known to have transfer coefficients exceeding 0.5. [96] The RDS in the peroxide pathway is similar to the n = 1 direct 4-electron ORR, with the major difference being the Pauling model's end-on bonding of the oxygen molecule. Low interaction between the superoxide oxygen bond and catalyst metal would result in:

$$M + O_2 + H^+ + e^- \rightarrow M - OOH_{ads} + H^+ + e^- \rightarrow M\text{-}HOOH \qquad (3.4)$$

Secondly, the reduction current above 500 mV vs. RHE significantly decreased across the entire sample for the background N_2 scans, indicating a dependence on oxygen reduction. However, since one local H^+ proton was used up for every e^- in the 4-electron pathway, attributing all the current to this particular ORR reaction would have been inconsistent with the fluorescent data's peak at ~10% W. This implied that oxygen was being reduced, but through a different pathway involving significant peroxide formation and partial reduction. After repeated scans, the surface of the wafer above ~15% W appeared much more damaged than the rest of the sample, again suggesting destructive peroxide formation.

Thirdly, initial evidence pointed to enhanced (bi)sulfate adsorption at W compositions above 10%. As seen in Figure 40 for the representative >10% W sample (e.g. 22% W), a large redox peak became more noticeable around ~250 mV with an increasing percentage of W. According to the literature, this redox peak was located at a similar potential as (bi)sulfate anion adsorption peaks on Pd and Pt [97]. Such anion

adsorption could stimulate peroxide production by blocking possible bridge sites of the direct 4-electron pathway proposed by Yeager [98]. Such steric and/or electrostatic hindrance could make it more energetically favorable for O_2 to bind end-on, as described by the Pauling model [99]. With the π bonds in the oxygen molecule perpendicular to the surface rather than parallel, possible overlap with the d orbitals and any backbonding would have been limited. This would have increased the difficulty in the disassociation of the molecular oxygen bond, leading to an increase in peroxide formation, as seen in Au catalysts [100]. In addition, some current could be due to a reduction reaction on the sulfate itself. Another possible explanation for this peak was hydrogen adsorption at low-index (100) facets. No evidence of significant (100) texturing appeared in XRD measurements as the amount of W in the bulk increased.

Table 1. ORR current densities and slope transition points for W-Pd alloy thin films in aerated 0.05 M sulfuric acid

Bulk Composition (EDS)	Surface Composition (XPS)	Tafel slope transition (mV) -60 → -120 mV/dec (*) -60 → -90 mV/dec (^)	j_{O_2} @ 850 mV (mA cm^{-2})	$j^0_{O_2}$(mA cm^{-2})
Pt	Pt	795*	1.00×10^{-3}	8.20×10^{-6}
Pd	Pd	735*	1.00×10^{-4}	0.624×10^{-6}
$Pd_{97}W_3$	$Pd_{97.3}W_{2.7}$	768*	2.50×10^{-4}	1.23×10^{-6}
$Pd_{94}W_6$	$Pd_{96.8}W_{3.2}$	854*	1.28×10^{-3}	6.20×10^{-6}
$Pd_{90}W_{10}$	**$Pd_{95.6}W_{4.4}$**	**868***	**2.71×10^{-3}**	**8.40×10^{-6}**
$Pd_{85}W_{15}$	$Pd_{94.3}W_{5.7}$	854^	1.09×10^{-2}	3.60×10^{-6}
$Pd_{78}W_{22}$	$Pd_{93.8}W_{6.2}$	880^	3.37×10^{-2}	10.0×10^{-6}
$Pd_{73}W_{27}$	$Pd_{93.4}W_{6.6}$	869^	3.08×10^{-2}	10.2×10^{-6}

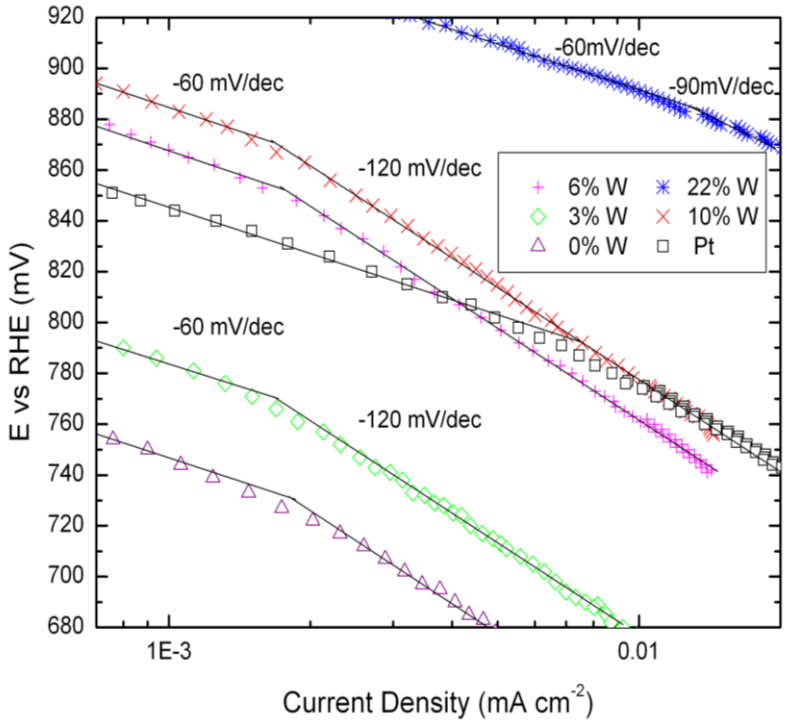

Figure 39. Polarization curves of various bulk W % in W-Pd alloys in aerated 0.05 M sulfuric acid. The majority of current is assumed kinetic.

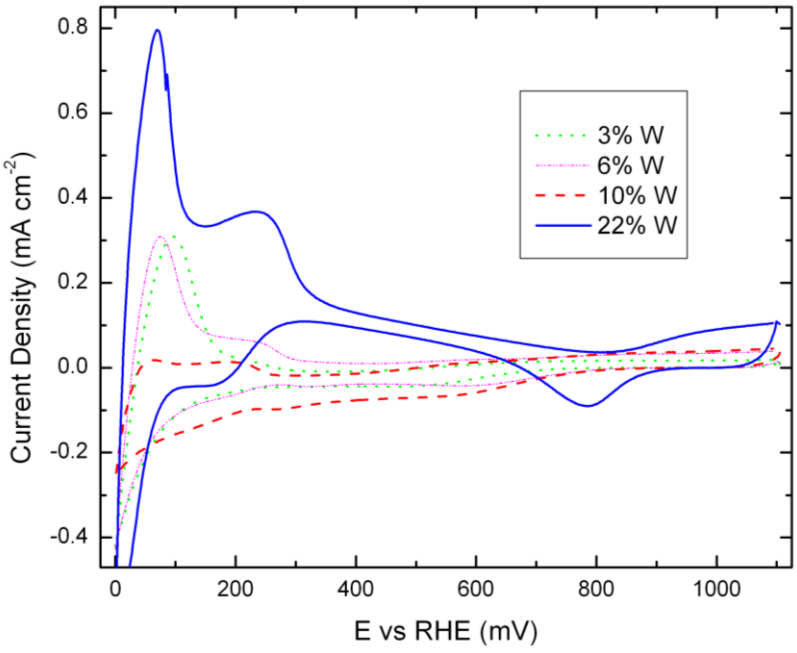

Figure 40. Cyclic voltammograms of selected W-Pd alloys in aerated 0.05 M sulfuric acid, showing differences between $Pd_{78}W_{22}$ and lower W concentrations.

While the bulk concentration ~10% W indicated a high ORR activity, the ligand effect of the W is short-range, with electronic interactions within one or two nanometers of the surface. At the high test potentials here, unprotected W would likely form an oxide and dissolve into the solution, reducing the concentration of W on the surface. As determined by X-ray photoelectron spectroscopy (XPS) before and after testing, such a disparity did in fact exist between the bulk and near-surface atomic concentration of W. As seen in the Figure 41, after ~2% W, the amount of W at the post-tested surface was diminished compared to the bulk. Any W still left was either protected by a Pd skin layer or 'caged' near the surface in a skeletal structure. Most W concentrations near the surface diminished by 40-50% after undergoing sulfuric and nitric acid testing, as seen in Figure 42. At the optimal ~10% bulk level of W, 4-5% W was left near the surface. The lattice constant in the bulk, as determined by XRD in Figure 43, slowly increased in accordance with larger W substitution into an FCC Pd structure of pure Pd lattice constant a_{pd} = 3.889 Å. The Debye-Scherrer grain size decreased with increasing amounts of W, likely due to slower diffusion of the larger W into this crystalline structure. After ~15% bulk W, the surface concentration of the W started to level off while the strain in the thin film exhibited a sharp uptick. As seen in phase diagram for the Pd-W binary alloy in Figure 44, W begins to saturate in the FCC Pd structure in the 15-20% atomic percentage range at high temperatures [101]. This implied saturation of the columnar Pd-W alloy grains by additional W above 15% bulk W, which may have started forming its own nanocrystalline/amorphous structure not readily apparent by XRD. Such W appeared to have added a tensile strain component to the rest of the solid solution, likely through a lattice mismatch with the Ta underlayer or interaction between columnar grains. In addition, saturated W was unprotected during electrochemical testing, resulting in its dissolution near the surface.

This created a ‘rougher’, more cauliflower-like surface seen in Figure 43 with increasing tensile strain.

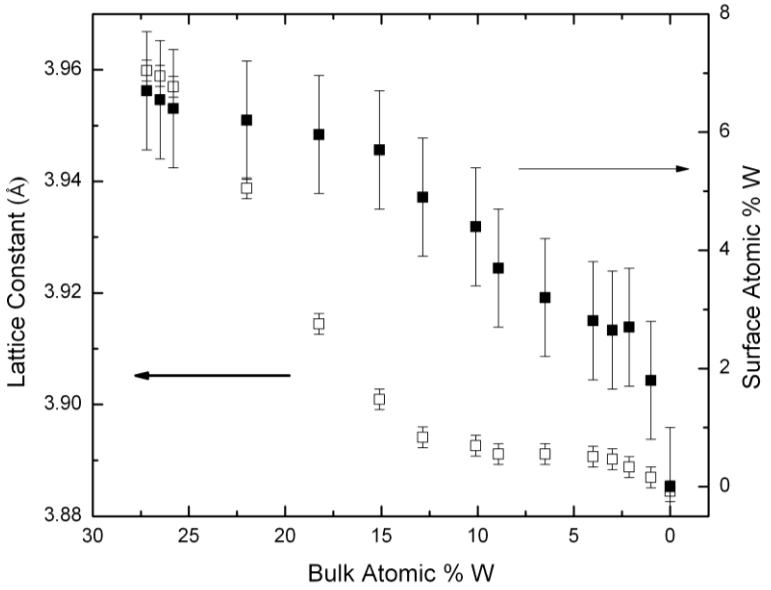

Figure 41. Lattice constant and W surface concentration vs. bulk surface concentration in W-Pd thin film.

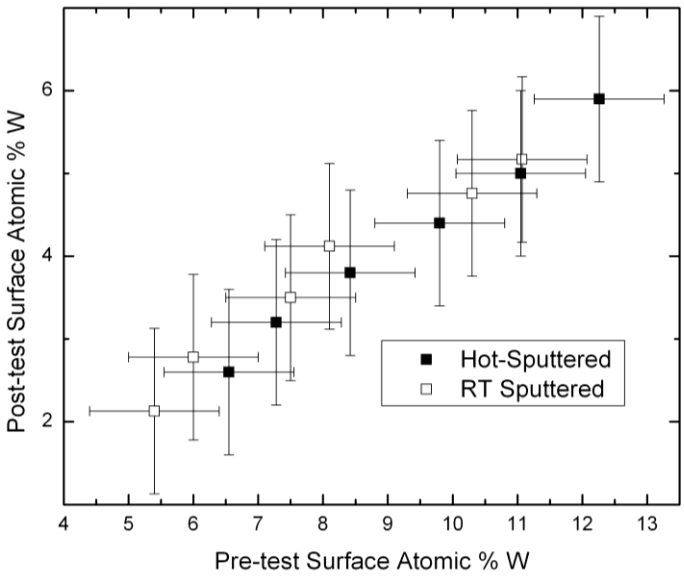

Figure 42. Comparison between pre- and post-test W surface concentration for either hot-sputtered or room temperature sputtered W-Pd thin films.

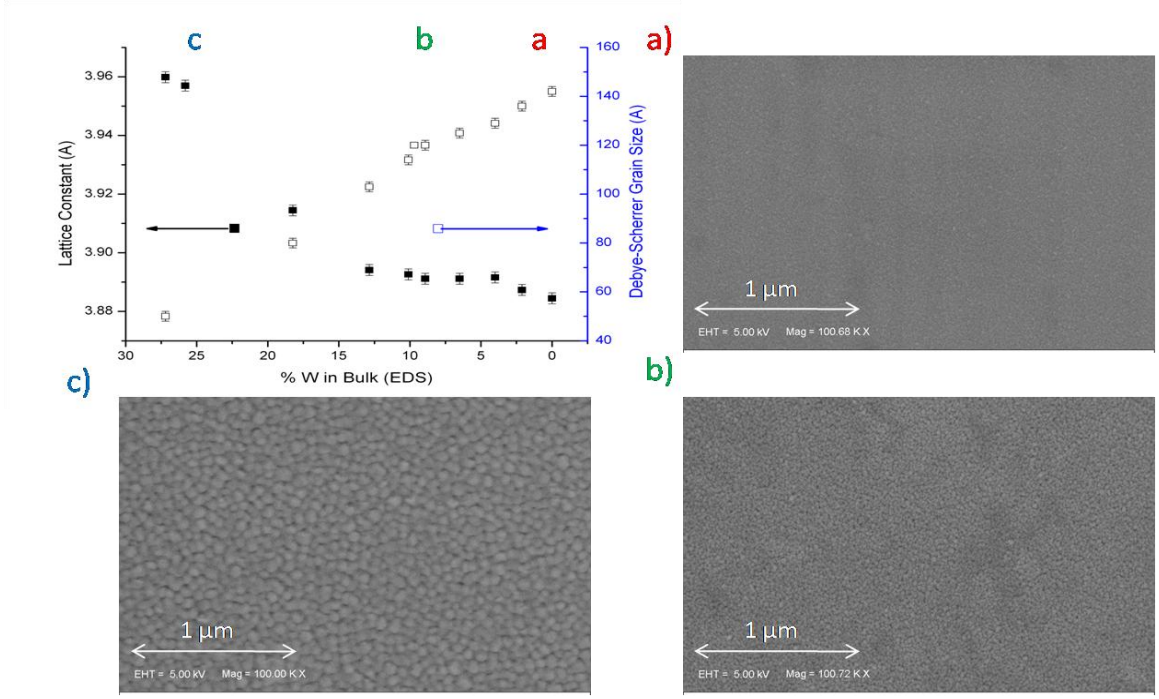

Figure 43. W-Pd lattice constant and Debye-Scherrer grain size determined by XRD. SEM figures at a) 3%, b) 10%, and c) 25 bulk atomic % W.

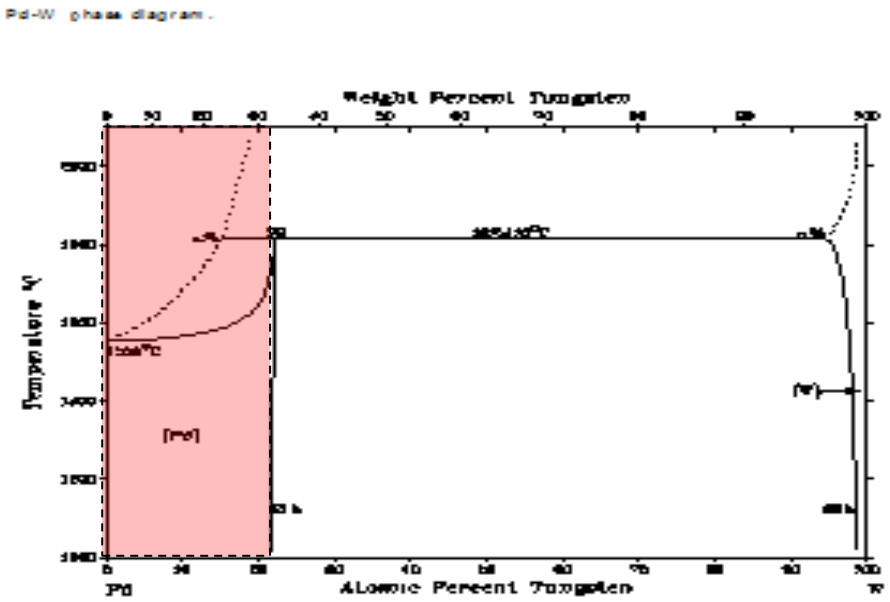

Figure 44. W-Pd binary phase diagram shows ~20% solid solubility W in Pd above 1000C, as shown by the highlighted region [102].

The high-resolution XPS Pd 3d5/2 peak can be deconvoluted into separate peaks dependent on the oxidation state at the surface. Approximate binding energy intervals in this study were 334.9-335.5, 335.5 – 337, and 337-338.5 eV for, respectively, Pd^{0}, Pd^{+2}, and Pd^{+4}. By observing the Pd^{0} 3d5/2 peak shift with added W in Figure 45, one saw how initially adding the more electronegative W near the surface increased the binding energy of the Pd 3d core levels. Since the shift in the 3d levels mimics a shift in the valence 4d levels, this indicated a valence d-band center shift to a lower energy compared to a relatively stationary Fermi level [102]. Such a shift would decrease the overlap between unoccupied d-orbitals and O antibonding orbitals, decreasing the binding energy. This progressively lower interaction between Pd and O species likely led to a decrease in blocking sites that hindered the ORR. The highest ORR activity at ~10% bulk and ~4.4% surface W was associated with a binding energy of 335.16 eV, having errors within a tenths of an eV. The addition of W above this level appeared to decrease the fluorescence-determined ORR activity. After ~15% bulk and ~5% surface W, the binding energy decreased as the strain effect from tension in the bulk shifted the d-band center back towards the Fermi level. While a simple correlation between the d-band center and catalytic activity would anticipate a higher ORR activity, it actually decreased according to the fluorescence test and changed intrinsic Tafel slopes to -90 mV/dec in the cell tests. These implied the impact of some mechanism other than the 4-electron ORR. Both ligand and strain effects could result in complex interactions near the Fermi level not represented by the peak shift, since the d-band center movement is only a representation of the movement of the 4d energy band.

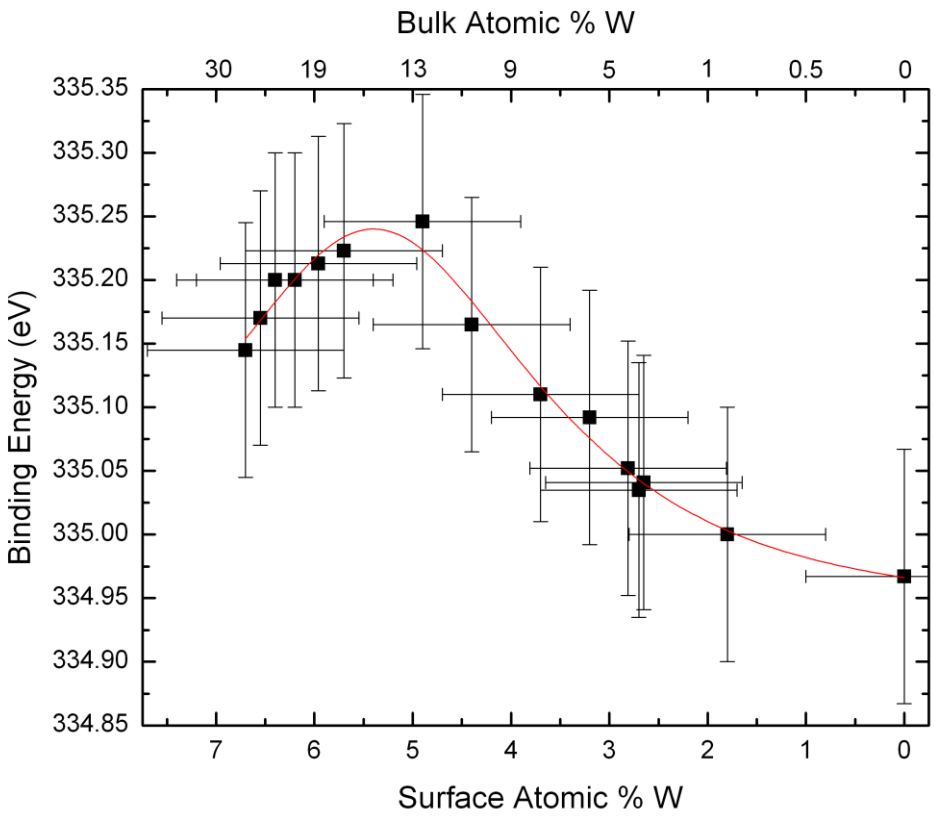

Figure 45. Peak location of the Pd 3d5/2 binding energy vs. W surface concentration for W-Pd alloy.

High-resolution XPS was done after the thin film was repeatedly cycled in a pH = 1 solution of either sulfuric acid or nitric acid and stopped on the cathodic scan at 850 mV vs. RHE. The 850 mV value was picked as a reasonable comparison to the standard overpotential used by other research groups and industrial studies. While sulfuric acid could produce insoluble sulfate complexes on the surface, nitrates from the nitric acid would have dissolved into the solution before the film was taken out for XPS, leaving a 'cleaner' surface for examination. The area under each deconvoluted peak was used to determine the percentage of supposed 0, +2, and +4 Pd oxidation states on the alloy surface in Figure 46. Such oxidation states could possibly help determine the adsorbed molecules on the surface in addition to the reduction state of

dissolved oxygen. Since this was an ex-situ characterization in vacuum, some of these states could have changed, with Pd^{+4} in particular known as highly variable. No Argon bombardment was used to clean the surface for fear of further changes to the oxidation state.

From 0 to 4% W in both the sulfuric and nitric acid at 850 mV, the +4 state decreased and the pure metal state increased. The most likely explanation for this was a decrease in PdO_2 as the binding energy interaction for such oxide formation declined with added W. The +2 state decreased in the sulfuric acid and increased in the nitric acid. As PdO_2 formed during the anodic scans above 850 mV grew thinner, the exposed surface was left free for hydroxyl groups from the reaction of Pd with H_20. Such hydroxyl groups (or their deprotonated state in vacuum) may have led to the +2 increase in the nitric acid solution; sulfonated hydroxyl groups may have been more loosely bonded to the surface, resulting in a decrease in the sulfuric acid solution.

In the ~4 to 10% W range, the +4 state increased while both the pure and +2 states fell in both solutions. With the oxygen binding energy still decreasing, the decrease in the +2 state from reduced blocking-site species (e.g. –O, OH) was expected. However, due to increasing ORR kinetics from the intermediate superoxide bond-breaking RDS, the pure Pd was diminished and +4 state increased to reach a peak at ~10% in the sulfuric acid solution. The rationale behind the +4 state corresponding to ORR activity was unknown.

From ~10 to 27% W, differences were apparent between the oxidation states in the two solutions. The +2 state had reached a minimum at ~10% in the sulfuric acid before rising again while it had approached a valley at ~15% in the nitric acid solution. The latter could be explained by the d-band center (XPS binding energy) encountering a minimum at ~15% W from the ligand effect before increasing from added tensile strain. The +4 state in nitric acid, corresponding to the likely ORR

activity, also peaked at this percentage as a result of the minimum d-band center energy. However, the oxidation state in sulfuric acid proved more complicated. After ~10% W, there were discontinuities in the pure and +4 states, which implied some species other than reduced oxygen may have been bonding to the surface. Previous studies of pure Pd in sulfuric acid have identified $PdO(HSO_4^-)$ complexes at potentials below 700 mV that could be responsible for binding energies comparable to the +4 state of Pd in PdO_2 [103]. Furthermore, differences with the +4 state in nitric acid implied some sulfate complex had shifted the binding energy. Interestingly, the startling shift in pure and +4 states occurred just after ~10% W and not at the minimum binding energy point described by ~15%W. This may have indicated that the ligand-based shift in the d-band above 10% introduced a higher degree of interaction with the bisulfate (HSO_4^-); tensile strain only increased the bonding interaction. As previously mentioned, these shifts are only a measure of the changing conformation in the d-band. While strain-based effects can lead to an easily interpretable shift depending on the narrowing or broadening of the d-band, ligand-based effects can introduce added complexities in the conformation of the d-band.

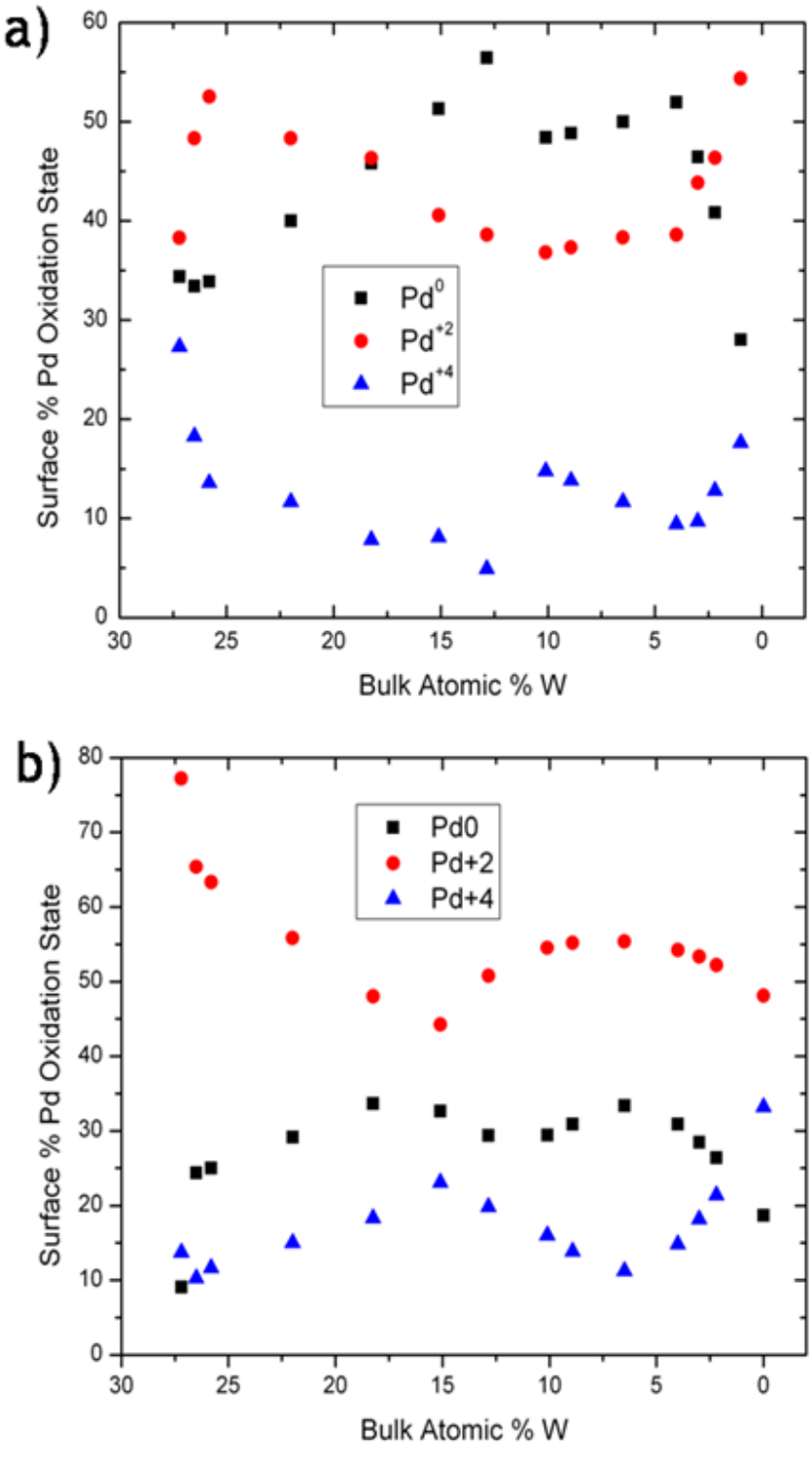

Figure 46. XPS-determined oxidation states of Pd on ex-situ Pd-W alloy surface after cathodic scan to 850 mV in a) 0.05 M H_2SO_4 and b) 0.1 M HNO_3.

Ex-situ Raman spectra were taken 10-15 minutes after the scan in sulfuric acid had been stopped at 850 mV vs. RHE. It was hypothesized that any blocking-site species or reactant/product in the RDS identified by the Raman characterization would be the predominant species at that potential. Figure 47 shows normalized peak intensities centered around 3300, 1338, 865, and 1190 cm^{-1}, which corresponded respectively to the vibrations of O-H, O-O of O_2(ads), O-O of O_2H, and the symmetric S-O stretch mode of HSO_4^-. [104, 105]' Due to the roughness of the film after ~25% W, intensities may have been unreliable in that region. The OH peak appeared to verify the ~10% W minimum that was earlier seen in the XPS oxidation states, with a low level of hydroxide after this due to a lower oxygen binding energy for such site-blocking species. Adsorbed O_2, corresponding to PdO_2 with a weakened double bond between the oxygen molecules, markedly decreased from 0 to 4% W while the wavenumber decreased from 1340 to a low of 1336 cm^{-1} cm Again, this fit the expectations of a faster RDS and fewer O species available on the surface to further oxidize to PdO_2. Along the same W percentage range, the peak due to superoxide (OOH) rose to a maximum. Since the superoxide is an intermediate in the RDS after the first electron transfer, this represented an increase in the RDS from 1^{st} electron transfer to greater amounts of newly-adsorbed oxygen.

From ~4 to 10% W, the superoxide peak declined and its wavenumber shifted downward from 885 to 868 cm^{-1}. These were indicative of a weaker superoxide bond being easier to break, resulting in an increase in the kinetics of the second part of the RDS to form O_{ads} and OH_{ads}. At 10% W, where the kinetics of the 4-electron ORR should have been greatest, the amount of superoxide had still not plateaued to its lowest level. In fact, the lowest level was reached at ~15% W, where the binding energy, and hence the d-band center, had shifted to its lowest level. There was no Raman characterization from a nitric acid solution, but by relating ORR activity to the

Pd^{+4} increase in its XPS scan, the minimum plateau in the OOH level should have corresponded to the highest reaction rate.

A possible explanation for this discrepancy was the rise of the peak due to the S-O stretch in (bi)sulfate after 10%. The (bi)sulfate peak dropped from 0 to 4%W as PdO_2, onto which it could easily bind, disappeared; on a Pd surface devoid of PdO_2, it reached its lowest point. However, after ~10% W, the HSO_4^- intensity rose again. The spread of tridentate (bi)sulfate, with each oxygen atom bound to a Pd atom, likely took up potential 4-electron ORR catalytic sites. Such obstruction to bridging or side-on adsorption of oxygen molecules would favor an increase in end-on interaction, which made breaking the superoxide bond even more energetically unfavorable. The most probable product from any oxygen adsorption would then be some form of peroxide (e.g. HOOH), degenerating to H_2O and O_2. This model would explain the oxidation state jump in Pd^0 after unstable peroxide production as well as the increase in Pd^{+4} after 10%W from sulfate interaction. Therefore, adding >10-15% bulk W to Pd would increase the superoxide interaction and O-O bond-breaking, but the complicated band diagram change would also increase (bi)sulfate interaction and deleterious peroxide production. A simple model can be seen in Figure 48. Since sulfate-containing electrolytes, such as nafion©, are prevalent in current PEM and DMFC fuel cells, an additional phenomena other than the ligand effect of W was needed to increase the O-O bond-breaking mechanism in the RDS.

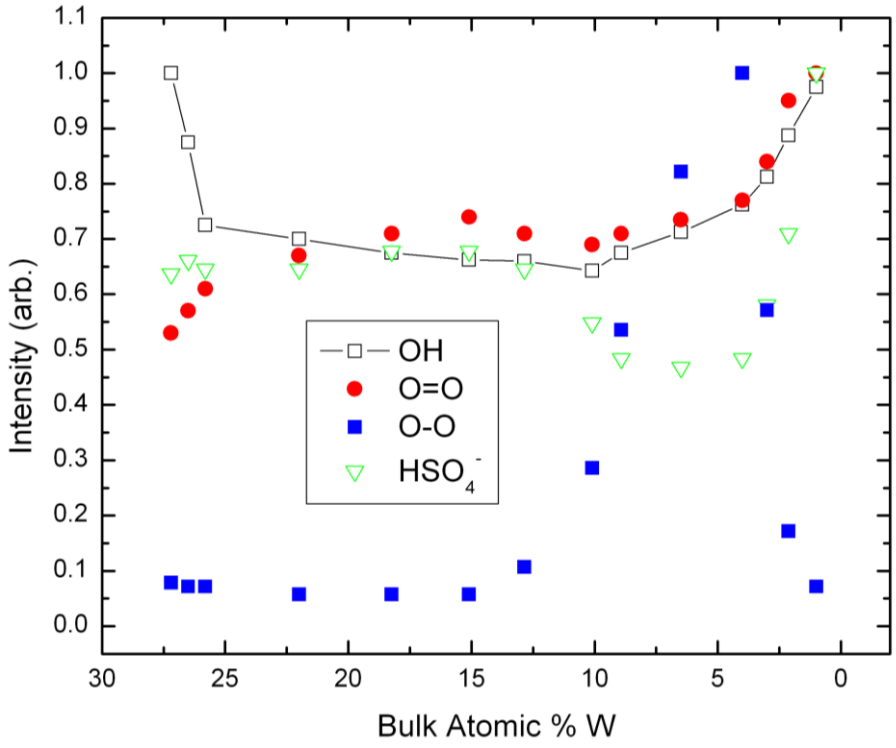

Figure 47. Normalized Raman peak intensities for adsorbed molecules on Pd-W alloy surface after ex-situ scan to 850 mV RHE.

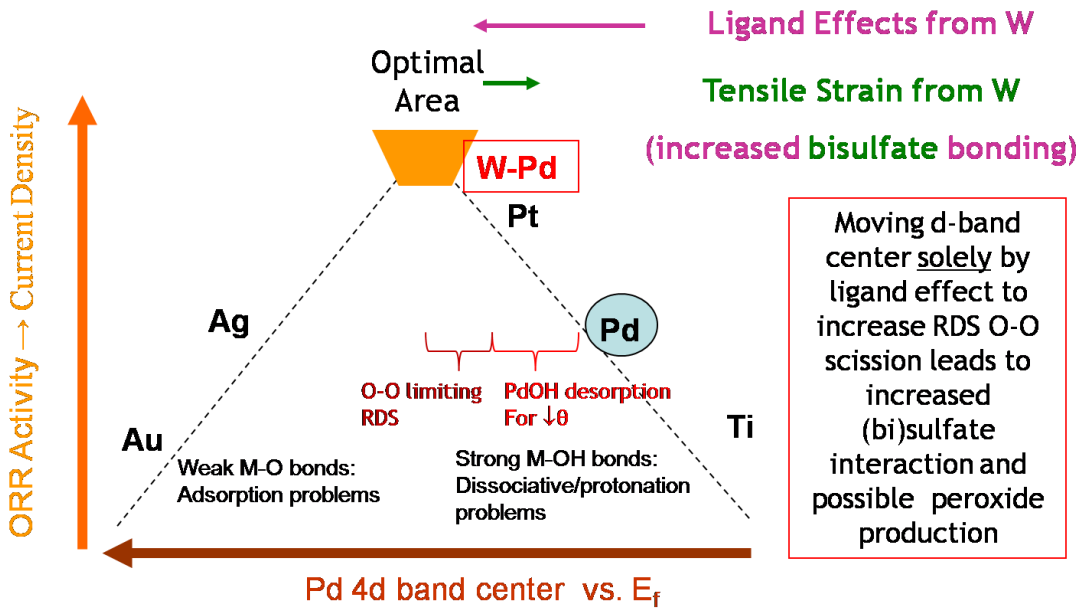

Figure 48. Pictorial representation of binary W-Pd ORR activity hypothesis for a Sabatier 'volcano curve' model.

3.3.2 W-X-Pd Composition Spreads

3.3.2.1 Results

Next, a third element 'X' was sputtered off-axis at the same conditions from the bottom of the wafer, at right angles from the other two guns. The desired atomic ratio in the middle for W:X:Pd was 1:1:8 and the power of the guns were separately calibrated by a quartz crystal monitor (QCM) to obtain this, although due to re-sputtering and other effects this ratio may have been slightly off-target [106]. Nevertheless, the approximate composition coverage in each case was about the same. As shown in the following fluorescence maps in Figure 49, the areas of greatest catalytic activity for the ternary spreads appeared somewhere near the bulk 10% W region seen in the binary spread. A few, such as Ni and Cu, appeared outside this trend, most likely due to the discussed Ni-W alloy formation for the former and strong segregation, along with re-sputtering, between Zn and W in the latter. The compositions with the highest onsets had X = Ti to Cr, Mg, Al, and Si. This was intriguing since there was a mix of 3d-transition metals and 2p elements, suggesting something other than a ligand effect was leading to enhanced catalytic activity. To reduce the possibility of a false positive ORR catalyst due only to a greater dealloyed surface area, the 1 cm^2 cell was used to find not only ORR currents but also ferrocene-derived surface areas. Current densities for 0.05 sulfuric acid both with and without 0.1 M methanol were derived.

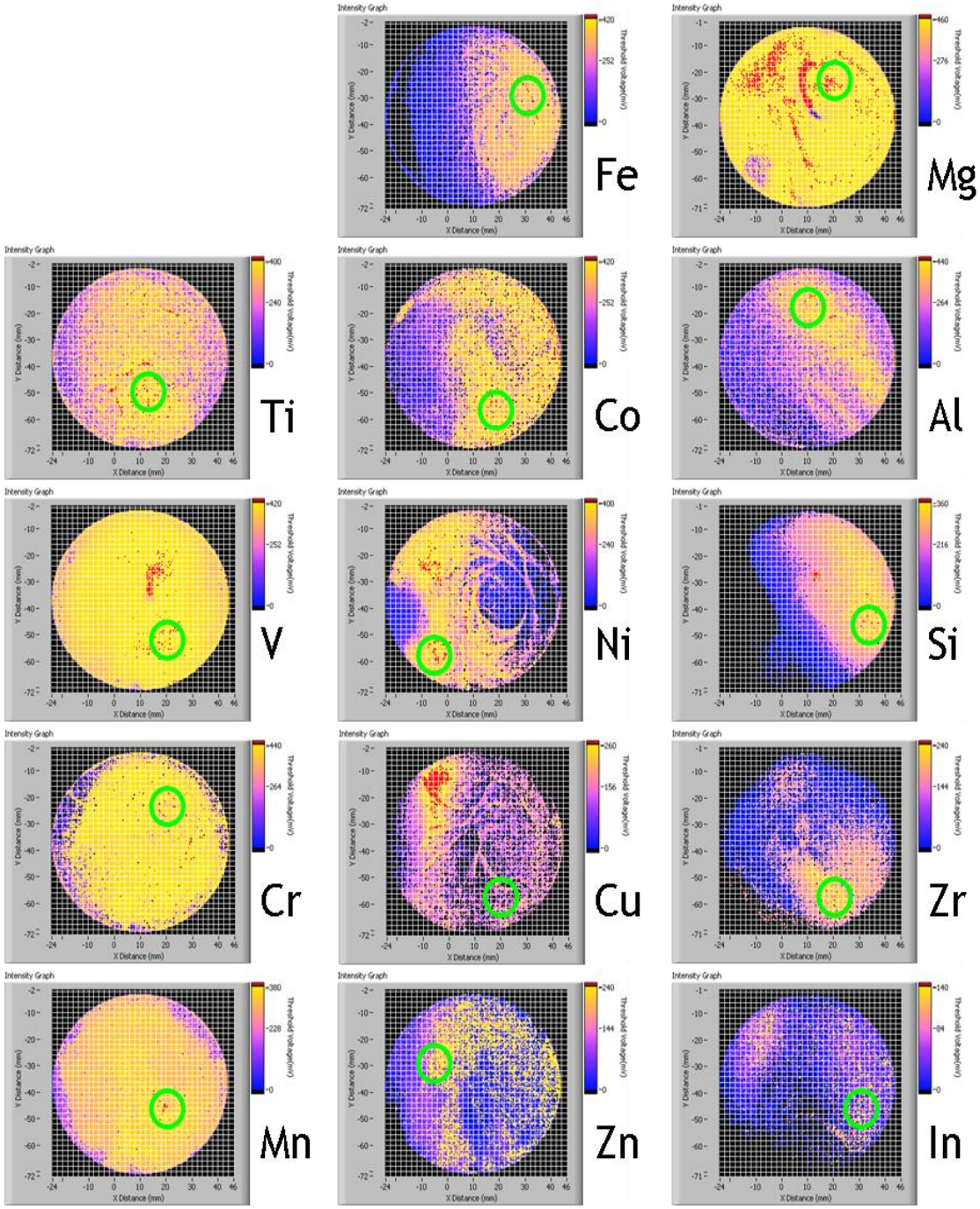

Figure 49. Fluorescence Map of W-X-Pd Sputtered off-axis on Fenris at 500C on 100A Ta where X=element symbol in bottom left corner. Keep in mind W sputtered directly from left, X from bottom, and Pd from right. Green circles represent region of highest onset. In some cases, there was more than one region, which was narrowed after ORR current density testing with the 1 cm^2 cell.

The current densities at 850mV RHE were plotted vs. X valence electron number for W-X-Pd in a pH = 1 aerated sulfuric acid solution both with and without 0.1M methanol in Figure 50. This potential appeared to be close to the limit of a viable onset for Pt, with its known 300-400mV overpotential from 1219 mV, the thermodynamic potential for ORR in an aerated solution. Dashed lines showed the current density on pure Pt, Pd, and on the $W_{10}Pd_{90}$ alloy. One could immediately see the low current density for Pd and Pt compared to the W-Pd and many W-X-Pd alloys. As expected, pure Pd had a low current density at such high potentials in both solutions. The current density of Pt was greater than that of Pd in the sulfuric acid solution, but the addition of methanol almost halved it, a result of the aforementioned methanol poisoning which plagues Pt cathode DMFCs [107]. Pd and Pd-based alloys were not as troubled by such carbon-based oxidation, as seen in Figure 51, since it is known that its 4d-band has a smaller amount of interaction with CO, leading to lower absorption [108].

More exciting, the $W_{10}Pd_{90}$ alloy reached current densities an order of magnitude higher than Pt in both the sulfuric acid and added methanol solutions. By adding a 3d transition element, an interesting trend developed. In both solutions, current densities increased to a peak from Ti to V and then decreased almost exponentially compared to valence electron number to Ni before picking up again when Cu and Zn were included. There were some notable outliers, such as W-Mn-Pd having a higher current density than W-Cr-Pd, but these were within experimental error. The inclusion of other elements outside transition metals failed to show any significant relationship between valence electron number and current density. Comparing the W-V-Pd current density in the following figure to the Pt and W-Fe-Pd gotten earlier in Figure 51, one could see a significant improvement.

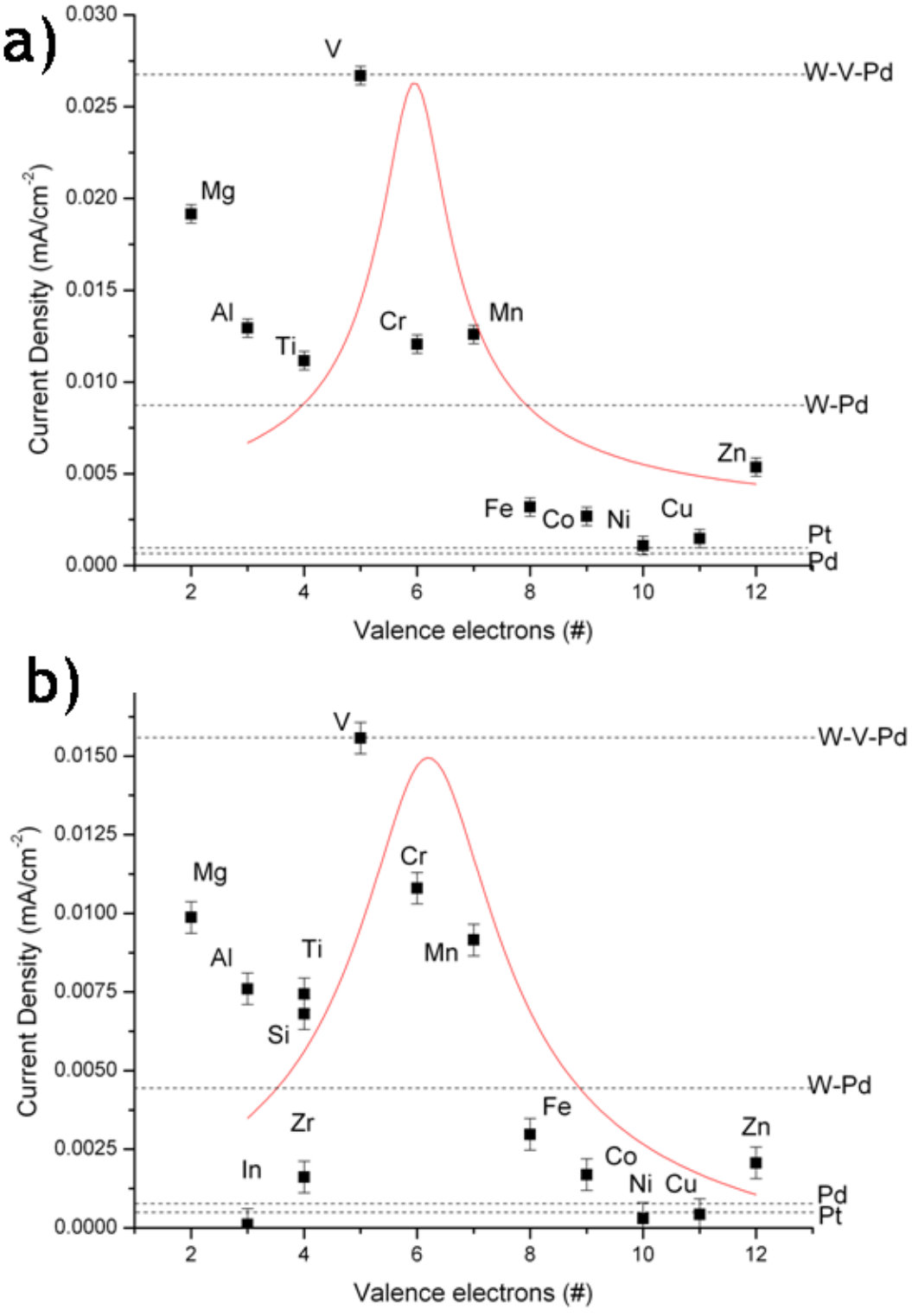

Figure 50. ORR current density @ 850mV RHE for W-X-Pd, where X = 3rd element, for a) .1M sulfuric acid and b) 0.05M sulfuric acid + .1M methanol.

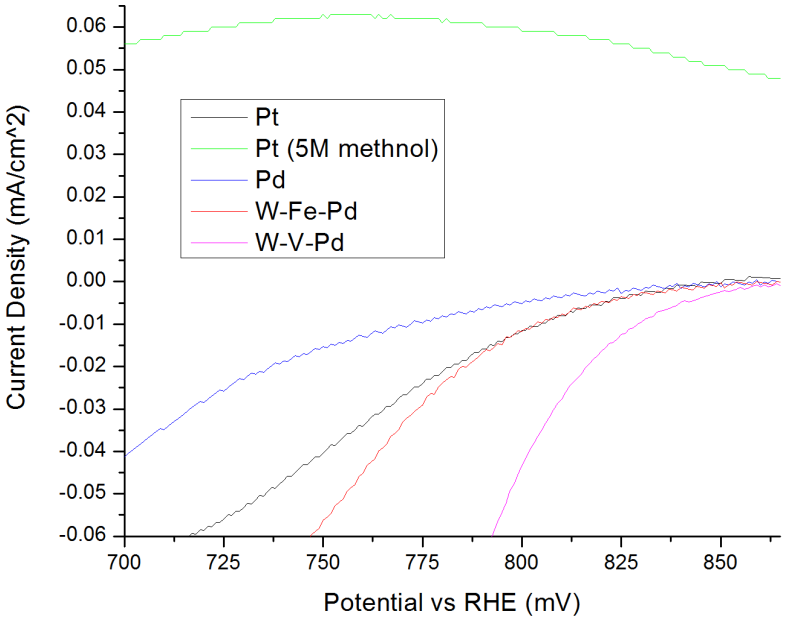

Figure 51. ORR current density for pure metal and alloy surfaces in aerated 0.05 M sulfuric acid/.1M methanol.

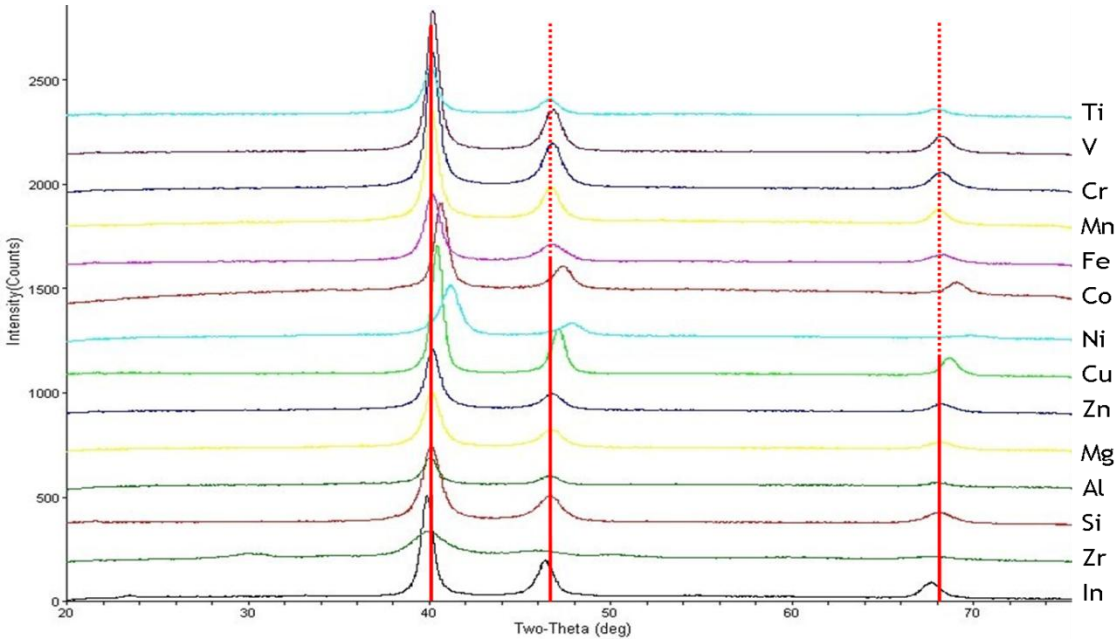

Figure 52. XRD of W-X-Pd Sputtered off-axis on Fenris at 500C on 100A Ta where X=element symbol at right of each spectrum. Peaks to left of red Pd reference lines represent larger and those to right smaller lattice constants than pure Pd.

XRD spectrums of the most catalytic regions for W-X-Pd were taken with the GADDS system, as seen in Figure 52. Visual inspection of the peaks for the 3d transition metal series alloys showed a shift toward higher angles from Ti to Ni, which reversed for Cu to Zn. Other elements shifted the peaks either towards higher or lower angles. Since the majority of spectrums appeared to represent solid solution of Pd, this shift could be converted to a lattice constant for the FCC Pd alloy by using the (111), (200), and (220) peaks with a Cohen analysis to help limit systematic error when possible. Other peaks besides those corresponding to Pd could be easily seen for Zr, In, and Mn.

These same catalytic spots were exposed to energy dispersive spectroscopy (EDS) in the Leo SEM. All of them had some amount of incorporated W, with a range ~4-15% of the total bulk concentration. They also had ~5-25% of the 3rd element mixed in, except for Mg, where there was close to nothing left in the bulk. The bulk concentration of the most catalytic spot was close to $W_{.06}V_{.06}Pd_{.88}$. In addition to EDS, these points all featured XPS scans that would present the composition within the first couple of monolayers of the surface, where the ORR reaction was actually occurring. With the exception of Ti, none of the 3rd element was detected. Further, the Ti d-level peak was observed at an energy level indicating it was Ti^{+4}, or oxidized TiO_2, which has been shown to have little to no ORR catalytic activity comparable to Pt [109]. Similarly, ~2-5% W repeatedly occurred for most of the alloys. A couple of the spots may have had part of the bulk examined due to a misalignment in the instrument. The bulk and XPS concentrations, expected lattice constants from Vegard's Law for solid solutions, XRD-determined lattice constants, surface areas from ferrocene tests, and ORR current densities in both solutions are seen in Table 2. As could be guessed from the SEM picture of W-X-Pd, where X = V, Zr, and Si, in Figure 53, the surface areas for all the alloys were greater than the Pt surface of 0.79 cm^2. The probable cause was

dealloying to form a skeletal surface layer of Pd with some small amount of W. The dealloying increased respectively among these three alloys, with the X = Si having a 3x larger surface area than X = V, according to ferrocene tests.

Table 2. Characterization data corresponding to Pd, Pt, and Pd alloys.

Pure Metal or Pd-W-X	EDS %W (+/-5%)	EDS %X (+/-5%)	XPS %W (+/-1%)	XPS %X (+/-1%)	Pred. a_0 from EDS solid solution (+/- .07 Å)	Exp. a_0 from XRD (+/- .002 Å)	FAA Exp. Surface area (+/- .01 cm^2)	Aerated 0.05M H_2SO_4 j_c @ 850 mV vs RHE (+/- .002 mA cm^{-2})	Aerated 0.5M H_2SO_4/.1MeOH j_c @ 850 mV vs RHE (+/- .002 mA cm^{-2})
Pt	0	0	0	0	3.920	3.910	.79	9.43E-4	6.00E-4
Pd	0	0	0	0	3.890	3.890	.79	7.52E-4	8.15E-4
X	10	0	4.4	0	3.894	3.893	.91	.00724	.00443
Ti	12.9	10.5	4.7	27.49	3.923	3.894	1.05	.0112	.00743
V	6.0	5.7	3	0	3.886	3.890	1.26	.0267	.0156
Cr	6.8	6.4	3.2	0	3.875	3.889	1.21	.0121	.0108
Mn	5.3	21.4	1.9	0	3.828	3.892	1.10	.0126	.00915
Fe	4.0	3.5	3.4	0	3.880	3.882	1.02	.00320	.00298
Co	11.3	17.8	3.0	0	3.832	3.842	1.05	.00270	.00170
Ni	11.7	26.5	8.4	0	3.793	3.790	1.60	.00109	2.98E-4
Cu	6.8	12.3	7.3	0	3.860	3.862	1.15	.00147	4.30E-4
Zn	15.2	12.2	6.7	0	3.884	3.887	1.09	.00537	.00207
Mg	4.7	.1	1.5	0	3.892	3.892	1.87	.0192	.00987
Al	7.9	8.4	6.3	0	3.906	3.889	1.21	.0129	.00761
Si	4.2	14.2	3.5	0	3.893	3.895	3.16		.00680
Zr	10.0	23.4	7.6	0	4.043	3.918	1.75		.00162
In	10.3	14.9	5.8	0	3.981	3.920	1.05		1.14E-4

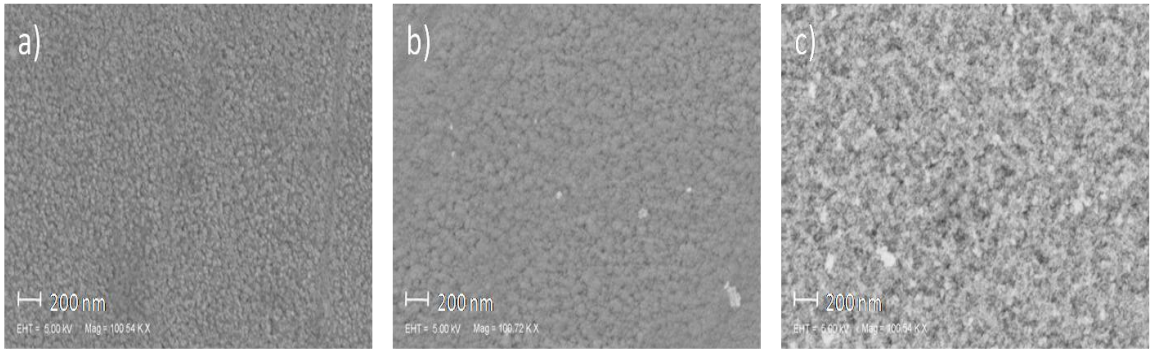

Figure 53. SEM pictures from secondary electron and backscattered mixing for catalytic a) W-V-Pd, b) W-Zr-Pd, and c) W-Si-Pd spots on increasingly dealloyed, roughened surface.

3.3.2.2 Discussion

When examining the binary W-Pd alloy fluorescent map for the 500°C spread, one saw a band of onset potential above that of even Pt at approximately 10% W. High onsets occurred on either side of this composition band between ~20%W and ~3%W. As seen in the previous W-Ni-Pd and W-Fe-Pd alloys sputtered on-axis, W added to Pd in a solid solution increased the ORR catalytic activity, mainly through a ligand effect at the surface related to the tungsten's higher revised Pauling electronegativity. The optimal surface concentration was ~4.4% +/- 1% W. This increased 'appetite for electrons' resulted in the W shifting some of the d-band electron density away from the Fermi level, electronically causing a smaller overlap between the empty d-states of the Pd and anti-bonding states of oxygen species. This smaller overlap would decrease the binding energy of such blocking-site species (e.g. OH), leading to more sites open for oxygen reduction and an increase in the kinetics of ORR. Close to the optimum W surface percentage, there would also be a significant increase in the RDS for O-O bond breakage, resulting in an added increase in the ORR. In addition, as previously

discussed, Pd has a lower surface energy than W and, in a sputtered alloy with enough energy to thermodynamically relax, should have form a surface skin/skeletal layer consisting of mainly Pd. This is likely what happened below ~17% W, with increasing amounts of W segregated into a eutectic solution not as well protected by Pd. Likewise, too little bulk W would result in too little W near the surface, trending toward the lower ORR activity of Pd as W diminished.

Adding a 3rd element to the W-Pd binary alloy both increased and decreased its ORR current density in either acidic solution. Due to site competition with methanol, the current densities in the .1M methanol solution were lower by close to a factor of two. As seen in Figure 50, there was a maximum at $W_{.06}V_{.06}Pd_{.88}$ and a higher current density than W-Pd for 3d transition elements X=Mn and below. This current density decreased below that of the binary W-Pd for Fe and kept on decreasing to Ni before increasing again with X = Cu to Zn. Adding non-3d elements, and even elements without d-level valence electrons, showed both higher and lower current densities than W-Pd, with X = In having a lower current density than even Pd or Pt for the methanol solution. Such a wide variety of results associated with valence electrons at all different valence orbitals and Pauling electronegativities initially lent doubt to any ligand effect on the system. In addition, the XPS results showed a dearth of any 3rd element alloyed on the surface of the Pd alloy. Since studies have shown that 3d atoms more than a few layers away from the surface have little to no effect on the valence d-electrons of Pd, this could almost substantively rule out any ligand effect on the Pd or W [110].

If this were indeed the case, the only variable this 3rd element could add would have been a bulk strain felt on the surface. As noticed in the XRD scans, the Pd peaks did shift in a way that seemed to mirror the current density of the two solutions. Plotting the current densities of the alloys with respect to their lattice constants from

the XRD scans produced Figure 54. By collapsing the data from all the 3rd elements into this lattice constant variable, a clear trend could be seen relating current density in both solutions to the bulk lattice constant in Figure 54. Fitting the data to a Lorentzian curve exhibited a peak centered at ~ 3.890 A with R^2 ~ .94 and R^2 ~ .84 for 0.05 M sulfuric acid with and without methanol, respectively. This corresponded with the experimental lattice constant for W-V-Pd of 3.890A. It is suspected that this lattice constant was slightly overstated, with a predicted constant using Vegard's Law on the bulk solid solution closer to 3.887 A No peaks in the XRD scan showing anything else but a solid solution. Interestingly, the binary W-Pd lattice constant of 3.893 Å intersected the ternary Lorentzian curve at very near the current density of .0075 - .01 mA/cm^2 seen in both binary and ternary scans at 850 mV, further providing evidence for a strain effect on the ORR activity.

When the current density was plotted against the 3d5/2 binding energy (an indicator of the 4d band center shift) from high-resolution XPS, a peak similar to the one involved in the lattice constant plot was observed in Figure 55. The peak was centered at the W-V-Pd alloy with a binding energy ~335.26 eV. Such a peak implied a transitive relation between the lattice constant and ORR activity based on the binding energy (d-band center) of the palladium at the surface. A compressive strain would move the d-band center away from the Fermi level for a lower palladium-oxygen interaction (higher binding energy) and a tensile strain toward the Fermi energy. When binding energy was plotted against lattice constant in Figure 56, a slope similar to that for the strained RT W-Pd, -14.3 eV/Å, was detected. Above a binding energy of ~335.32 eV, or on the outliers of the ORR activity peak for both binding energy and lattice constant, this linear relationship appeared to break down. This may have been due to W levels near the surface outside of the optimal binary range of 3-5% W, a ligand effect from the third element trapped in a skeletal structure near the

surface, or some artifact involved from the dealloying. In any case, these points were on the lower end of the ORR activity and did not warrant immediate consideration for possible catalyst candidates.

The hypothesis for ternary activity can be seen in Figure 57, adapted from the simplistic picture in the binary W-Pd sections relating the ligand and strain effects to the ORR activity. Essentially, the more electronegative W would move the d-band center of Pd away from the Fermi energy and anti-bonding O- species states, resulting in weaker bonding with such blocking species, such as –OH, which reduce the kinetics of the ORR by taking up valuable catalytic sites. However, the tension from the incorporation of the larger W atom into the Pd would counteract this effect, resulting in a smaller ORR activity than expected if both atoms were the same size. Adding a smaller 3rd element did not contribute through any sort of charge transfer; instead, its main involvement was a bulk compressive strain to move this d-band back towards an optimal area for the ORR slightly less than the lattice constant of pure Pd. Here, the blocking-site species were sufficiently low at 850 mV to allow the 1st electron transfer in the RDS to occur, and the interaction between superoxide and Pd large enough to break the O-O bond of the superoxide in the RDS. If the d-band center were shifted back too far by compressive strain (e.g. W-Fe-Pd), the interaction (e.g. binding energy) with O-species would be too low for sufficient π-backbonding and the 1st electron transfer to O_2, reducing the ORR current density again. A recent presentation by Nørskov in Figure 58 makes a similar case relating binding energy to ORR activity for various elements, although it may present a few differences in the RDS steps [111].

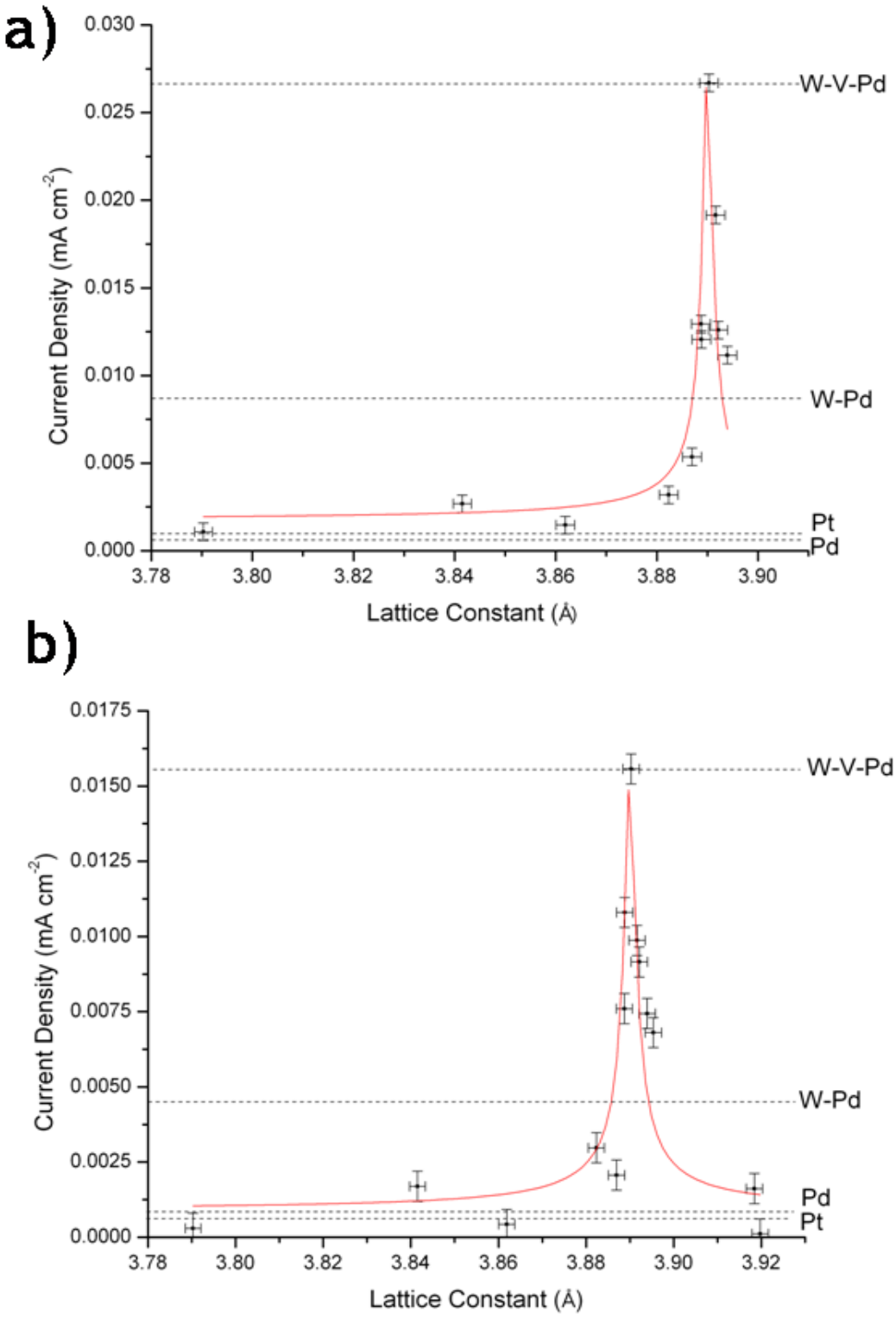

Figure 54. ORR current density plotted versus the bulk lattice constant of W-X-Pd ternary alloys at 850 mV RHE for aerated 0.05M sulfuric acid both a) without and b) with 0.1 M methanol.

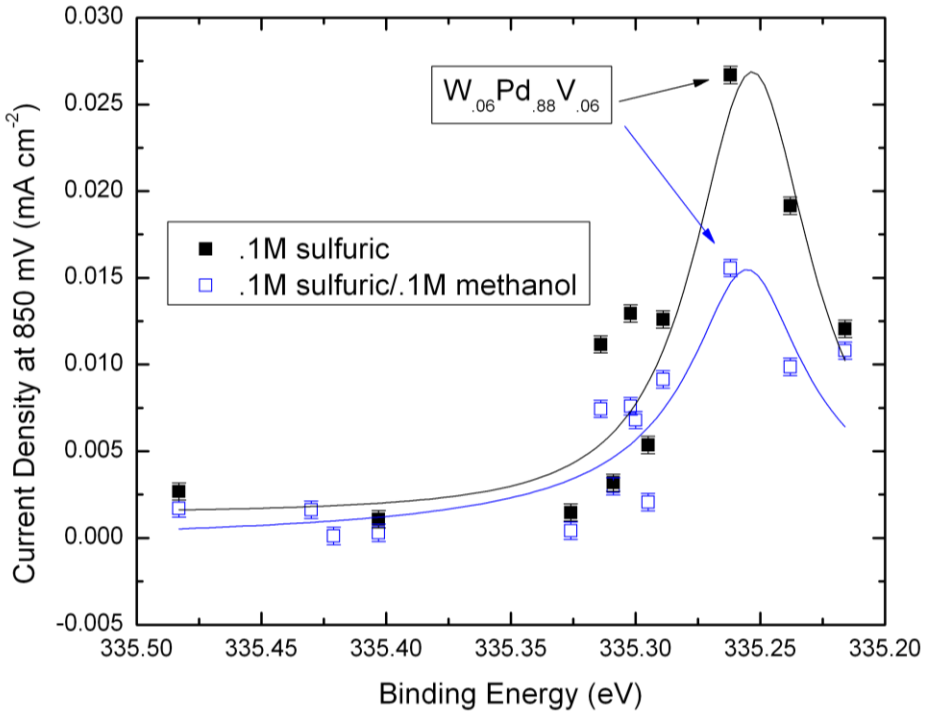

Figure 55. ORR current density plotted versus the XPS binding energy of W-X-Pd ternary alloys at 850 mV RHE for aerated 0.05 M sulfuric acid both with and without 0.1 M methanol.

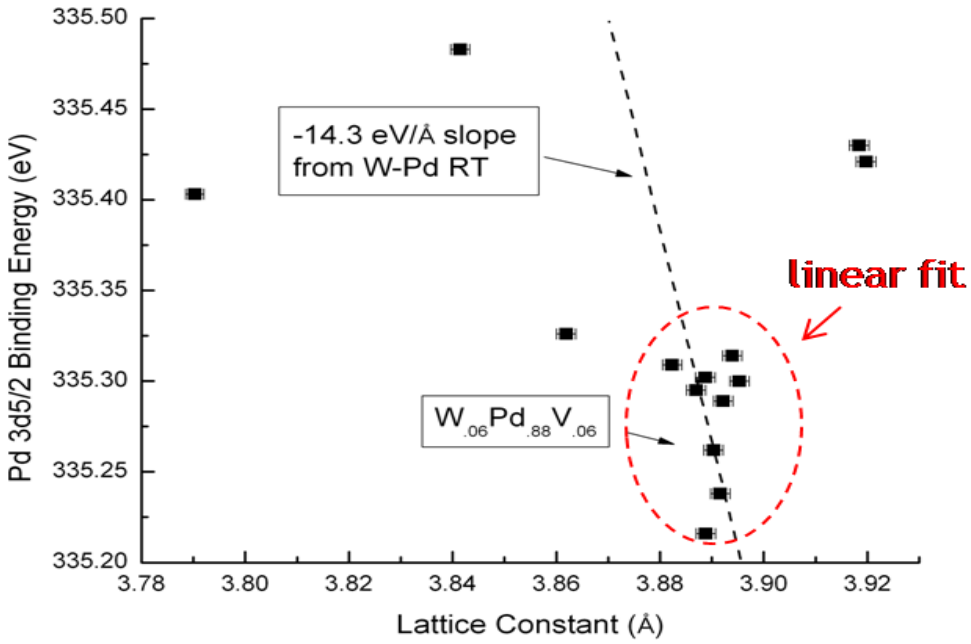

Figure 56 W-X-Pd ternary alloy binding energy plotted versus the lattice constant.

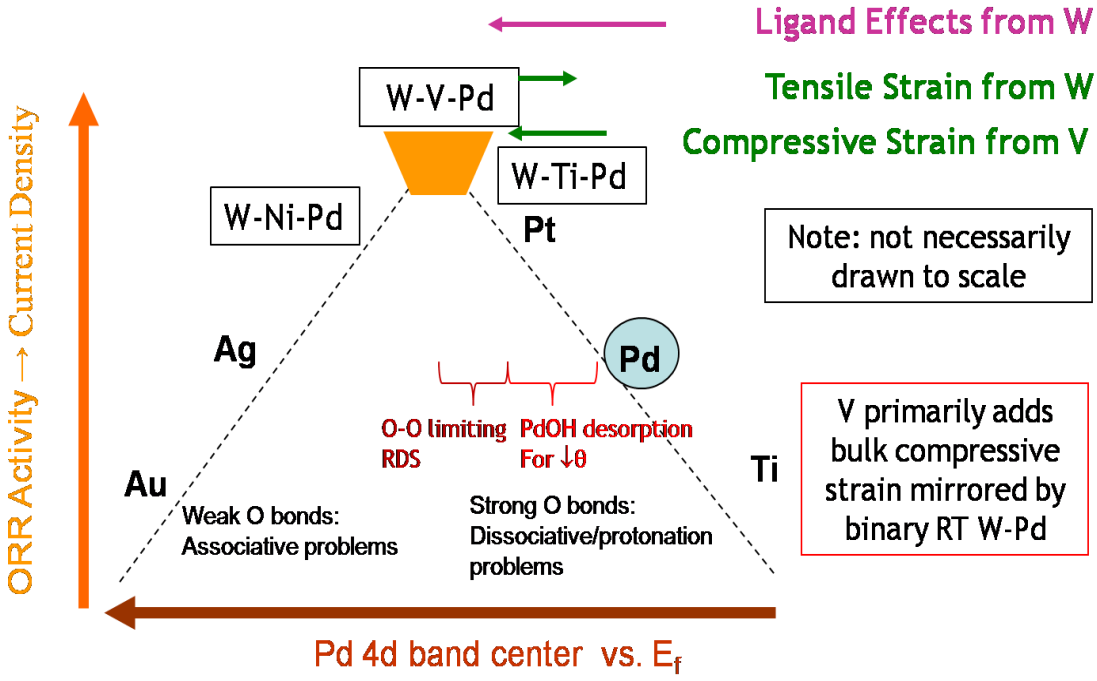

Figure 57. Pictorial representation of ternary W-X-Pd ORR activity hypothesis for a Sabatier 'volcano curve' model.

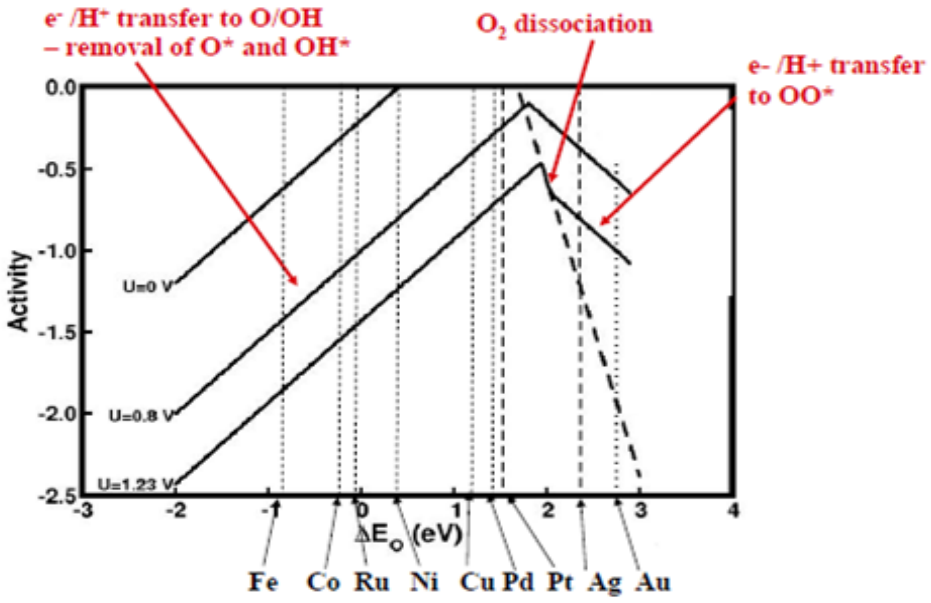

Figure 58. Diagram from Nørskov talk relating ORR activity to O binding energies. The W-X-Pd alloys, including W-V-Pd, with the highest current densities appear to be located in the O_2 disassociation region related to the highest activity.

According to Pourbaix diagrams, while the 3rd element should have de-alloyed (except Ti, where some formed a non-reactive oxide) and did, the entire W component should have dissolved at an experimental pH = 1 sulfuric/nitric acid solution at RHE potentials up to the 1100 mV range [112]. While some of the W must have de-alloyed, as in the 10% bulk binary and some of the ternary alloys, some significant fraction usually remained. Such evidence supported the contention, supported by other studies, that the Pd (or Pt) formed a skeletal surface that 'cages' the ~2-8% W from de-alloying [19, 113]. In fact, perhaps alloying Pd with W may have increased the corrosion resistance of the Pd itself, with evidence pointing to enhanced sulfide corrosion resistance when Ni (in the same group as Pd) was alloyed with W [114]. In addition, the surface area of the W-Pd binary alloy determined from the ferrocene tests was similar to that of many of the ternary alloys, including the bulk $W_{.06}.V_{06}Pd_{.88}$. This could lend some evidence to the theory that the much of the de-alloying during testing came primarily from W near the surface while most of the 3rd element was protected within the bulk. In a few cases, such as when the 3rd element was Zr, Si, or Mg, such an observation did not hold. Kinetically, this could come from the larger W diffusing less into the bulk than the smaller 3rd element during sputtering. Thermodynamically, in many of these ternary alloys, including V, the enthalpy of mixing the 3rd element with W was greater than mixing with Pd, leaving Pd near the surface [115].

CHAPTER 4

4 PALLADIUM ALLOY COMPOSITION/STRAIN SPREAD

4.1 Introduction to Technique

Further experimentation to provide evidence relating the ligand effect of W and compression from a 3rd element to a higher ORR catalytic activity resulted in a novel sputtering technique able to combine a composition and strain gradient onto a single substrate. Essentially, two of the guns in the on-axis ternary sputtering system were used, as seen in Figure 59. One gun sputtered Pd and the other W onto a substrate with a 100 Å Ta underlayer, as in the previous spreads. The sputtering was done at a low rate of 1 Å /s and expected thickness of 1000 Å in the middle of the wafer, as measured by a quartz crystal monitor (QCM). The end closest to the guns had a thickness ~3000 Å and the end farthest away ~300 Å. Since this sputtering was done at room temperature, as opposed to the previous 500°C hot sputtering, any intrinsic strains from the sputtering would more likely be kinetically locked into the spread. Compressive strains should increase at similar compositions farther from the wafer with decreased thickness. This would occur as the thinner layers composed of less energetic sputtered atoms on the mismatched Ta HCP lattice would experience the compressive effects of atomic peening and interfacial stress much more readily than the bulk-like thicker layers nearer to the guns [116]. Areas closer to the guns might be influenced by other factors, such as reflected Ar ions. Onset potential maps from fluorescent scans would help initially identify regions of high ORR activity.

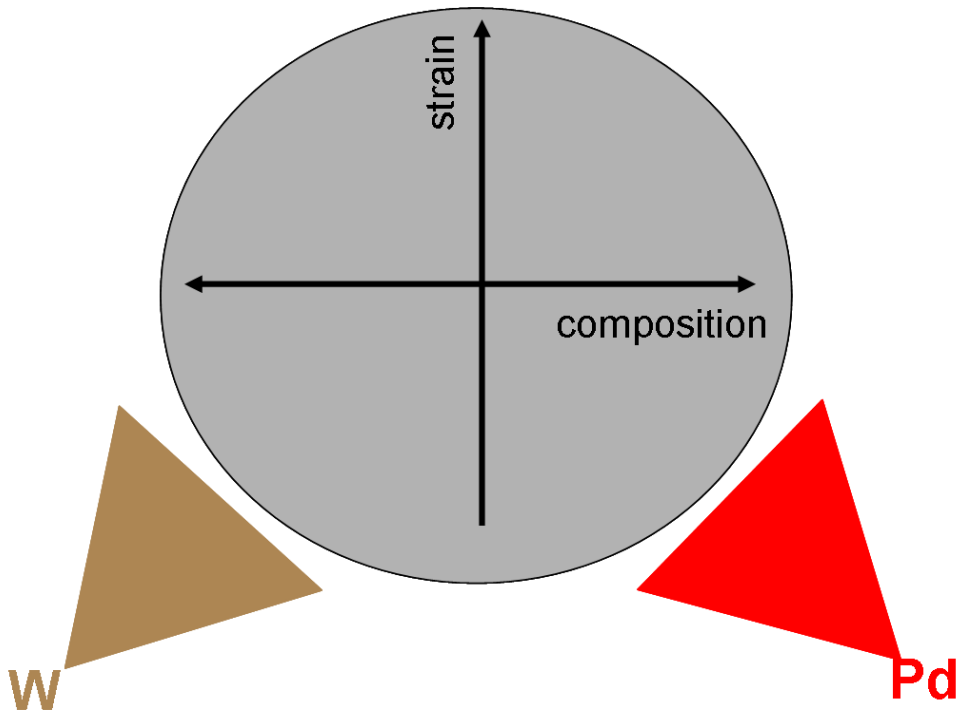

Figure 59. Representation of on-axis sputtering system where two guns, holding a W and Pd target, sputter from one side at room temperature. This creates a composition spread in one direction and possible strain gradient in the other.

4.2 W-Pd Spread

This composition/strain spread technique was first used for a binary W-Pd spread, as seen in Figure 60 for sputtering done at both room temperature and ~300°C. Onset potentials, bulk Pd percentages, and lattice constant maps were derived for each temperature. Compositions were taken from EDS readings and lattice constant from XRD scans on 21 points plus any with high activity. Maps were interpolated using a thin plate spline (TPS) method found in the Origin© graphing program in which a 2-d graph was formulated by 'deforming' the z-data between the given data points using a spline interpolation, much like a circus tent is deformed between the poles supporting it.

The Pd composition maps had a similar trend for both temperatures while the lattice constants were dramatically different at lower thicknesses. As expected, the room temperature (RT) substrate showed a much greater degree of compression farther away from the guns than the higher temperature sputtered substrate. The most likely cause for this was the decreasing thickness coupled with the smaller translated lattice constant of the HCP Ta underlayer. Higher velocity sputtered material may have also been able to relax the sputtered structure closer to the guns. This resulted in completely different onset potentials for each sample.

In the RT-sputtered W-Pd spread, the higher onset region seemed centered around the bulk Pd percentage ~90%, or 10% W, which corresponded to the previous investigation on the hot-sputtered W-Pd film. XPS studies put the surface W at ~4%, again similar to the hot-sputtered binary. As seen in Figure 60, the pink region of relatively high onset ranged from ~3% - 20%, which also was similar to the W-Pd previously discussed. Along the 10% composition curve in Figure 61, the lattice constant ranged from 3.897 to 3.868 Å, with the highest onset at 3.885 +/- .002 Å. Surprisingly, this was fairly close to the experimental value of 3.890 Å for W-V-Pd and even closer to the EDS-predicted lattice constant of 3.887 Å for W-V-Pd, adding evidence that a slight compressive strain for W-Pd from the pure Pd lattice constant of 3.890 Å provided the optimum ORR activity.

Additionally in Figure 61, side-on SEM pictures showed a texturing of the columnar grains toward the guns. Indeed, the XRD scans seen in Figure 62 almost mirrored each other, except for the greater texturing of the binary RT-sputtered film due to atoms on the growing surface of the substrate having less diffusive energy than in the hot-sputtered W-V-Pd alloy. This was again reflected in the Debye-Scherrer grain size, which decreased away from the guns due to less energy available for grain coarsening. As also seen in the previous study, W did de-alloy to increase the surface

roughness, but only in the first few monolayers. Surface area increases associated with layer thickness did not significantly affect the integrative effects of the fluorescence scans.

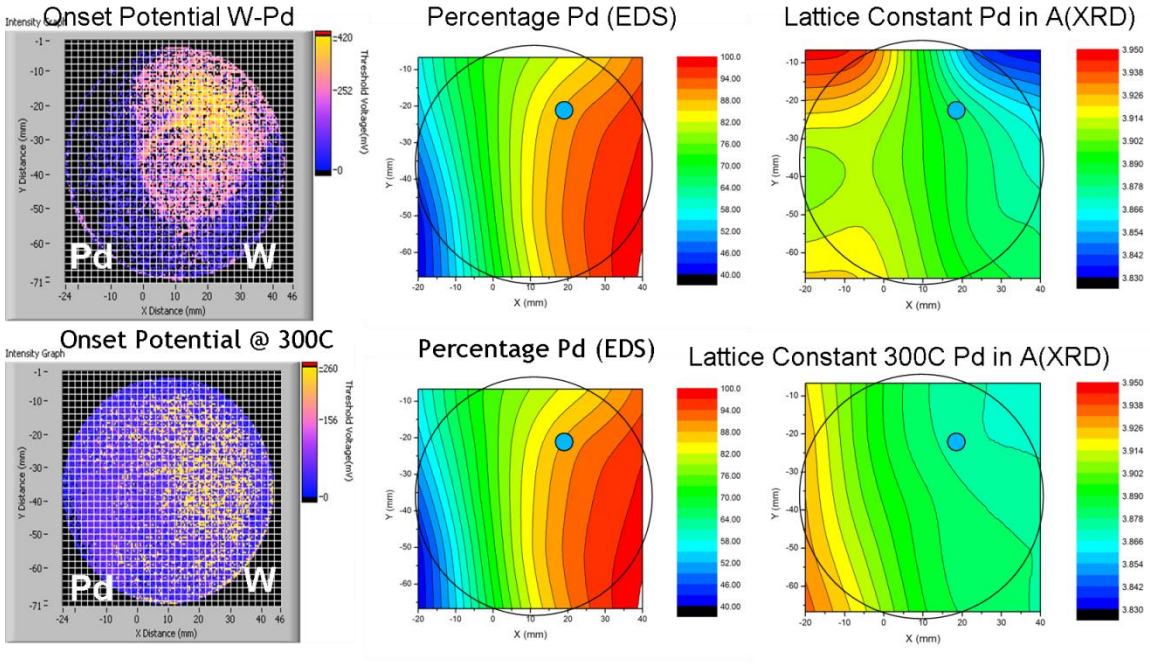

Figure 60. Onset Potentials, bulk Pd percentages, and lattice constants for W-Pd. The first row is for room temperature and the second row for 300°C. The blue dots represent the region of highest onset foe the RT-sputtered substrate.

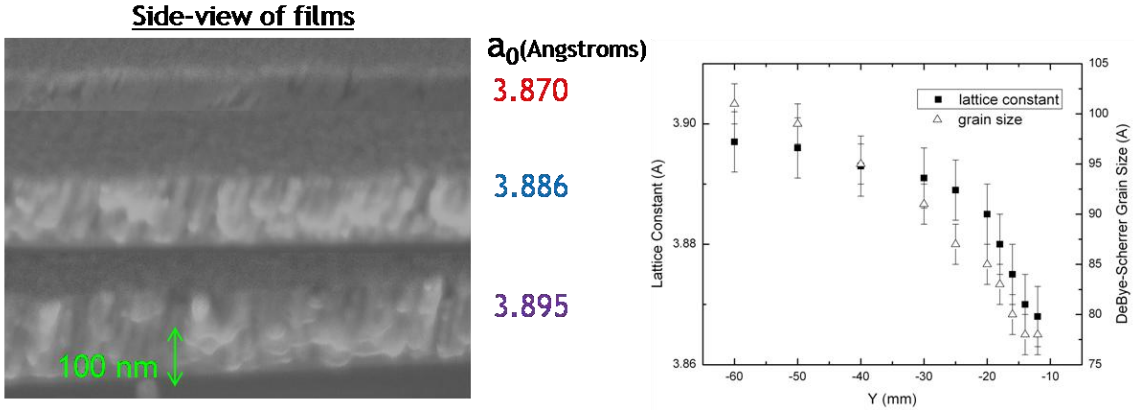

Figure 61. SEM and XRD data along room temperature sputtered $Pd_{90}W_{10}$ thin film.

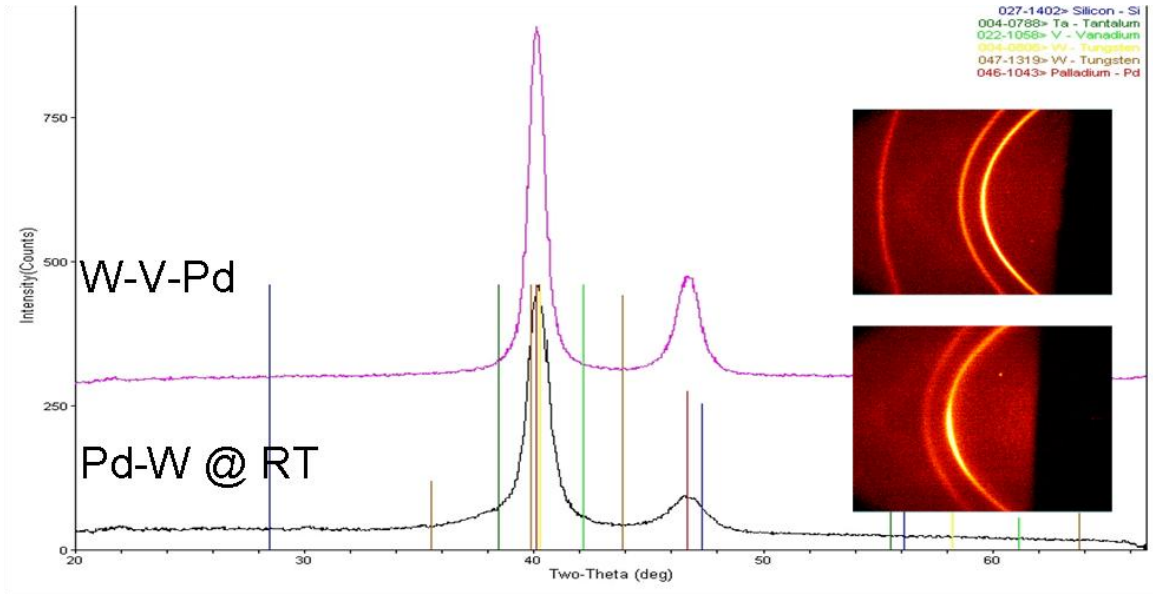

Figure 62. XRD scans from GADDS for the highest onset potential in the W-Pd binary spread at RT as compared to the highest onset W-X-Pd alloy, where X = V. Chi-arcs are also included for each scan, which show a higher degree of texturing in the RT-sputtered binary alloy.

Three main points were tested with the 1 cm cell. They were centered around 3.895, 3.885, and 3.870 Å. In terms of 3.889 Å, the pure lattice constant of Pd (a_{Pd}), these were at 1.002, 0.999, and $0.995a_{Pd}$. Cyclic voltammograms in aerated 0.1M H_2SO_4 were scanned in Figure 63 while pseudo-Tafel plots were drawn in Figure 64. Table 3 lists relevant characterization data. Both the current density at 850 mV and the intrinsic exchange current density were ~4.5 times higher at the 3.895 Å ($0.995a_{Pd}$) point than in the ~10% bulk W region of the hot-sputtered binary. Since this point most closely resembled the expected hot-sputtered lattice constant of 3.894 Å, the two sets of data did not quite corroborate each other. Possible reasons for this included greater activity at (111) texturing, different lattice constants on the surface in un-relaxed RT alloys, or some other variable (e.g. sunspots) involving the different times that the different substrate were tested over different time period. However, the most

likely scenario involved the optimal 10% bulk/4% surface W region being larger in the RT-sputtered alloy. Even though the cell was centered over this region in both sputtered alloys, the composition varied as one got closer to the edge. This variation must have been lower in the RT-sputtered alloy, increasing the area of the optimal composition region by a factor of ~4.5.

As the lattice constant decreased, the Tafel slope transition from -60 mV/dec to the intrinsic -120 mV/dec increased. Such an increase would be expected as the oxygen binding energy decreased due to compression. This would decrease the attachment for hydroxide ions mainly caused by the interaction of water with the Pd surface at high potentials. The transition potential for 3.895 Å was slightly lower than the expected ~870 mV for hot-sputtered W-Pd; such differences may have been due to the difference in texturing, as the (111) faces of Pd are known to attach anions more strongly than others [117]. There was no suggestion of an intrinsic slope different from -120 mV/dec, implying that any sulfate bonding was not occurring in significant levels to affect the oxygen reduction.

Interestingly, both the 850 mV current density and the intrinsic exchange current density of the slightly compressed 3.885 Å were three times greater than either more positively or negatively strained points. Since the increase in 850 mV current varied with the exchange current and not the Tafel slope transition, the increase in ORR activity was most likely due to an increase in the RDS and not a significant change in blocking site coverage. Such coverage modification would have further been incompatible with a Tafel slope transition for all the points above the 850 mV current benchmark. The increase in the RDS from the 3.895 Å to 3.885 Å spot could have resulted from either a more energetically favorable first electron transfer to O_{2ads} or ability to break the O-O bond of the superoxide intermediate $O_2^-{}_{ads}$. A subsequent decrease at 3.870 Å could have been attributed to either process as well, although the

continued decrease in OH blocking species pointed to a decrease in the rate of the first electron transfer step on O_{2ads}. Both points on either side of 3.885 Å had similar limiting current densities in addition to similar exchange current densities, which could be expected given similar oxygen diffusion constants and RDS rates.

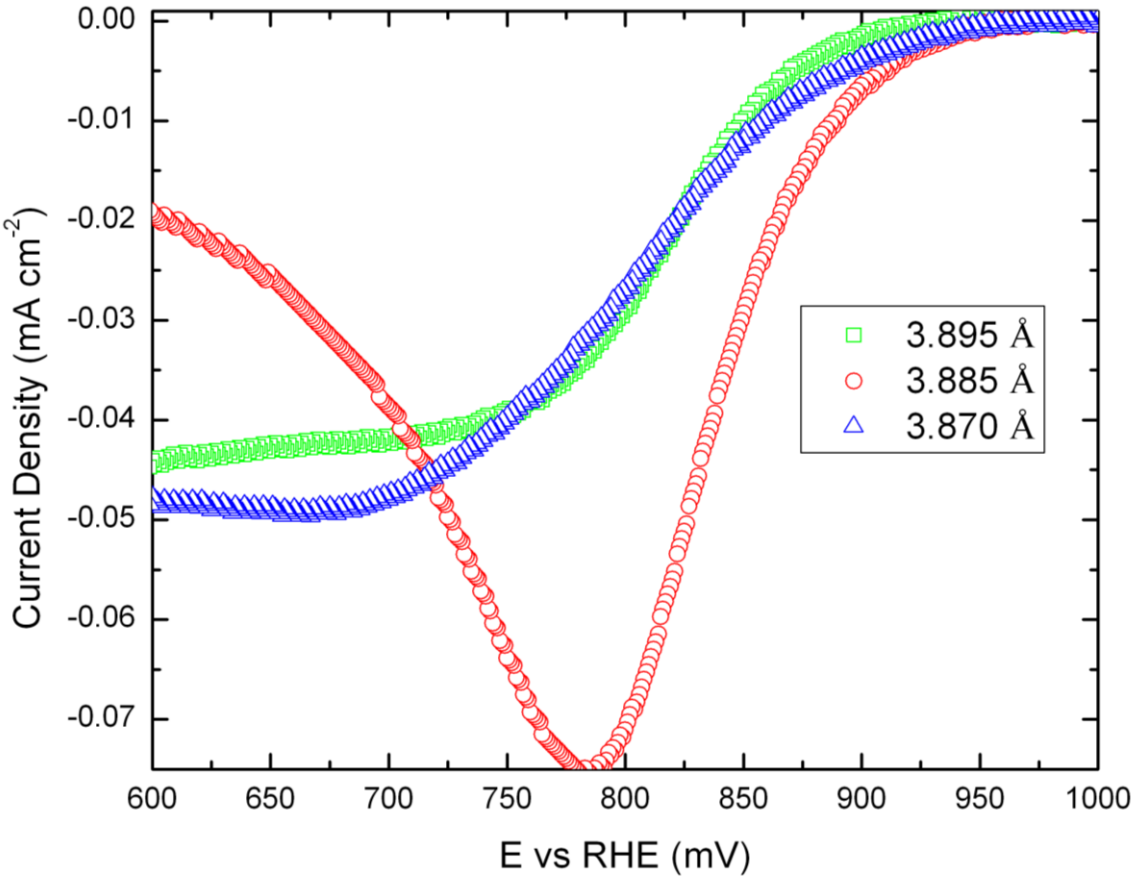

Figure 63. Voltammogram measurements of ~10% W alloy at various levels of strain. Pure Pd has a lattice constant of 3.889 Å.

Table 3. ORR current densities and slope changes for progressively constrained $Pd_{90}W_{10}$ thin films.

Bulk $Pd_{90}W_{10}$ Lattice constant (Å)	Bulk $Pd_{90}W_{10}$ Lattice constant (a_{Pd})	Tafel slope transition (mV) -60 → -120 mV/dec (*)	j_{O_2} @ 850 mV (mA cm^{-2})	$j^0_{O_2}$ (mA cm^{-2})
3.895	1.002	854*	1.00×10^{-2}	38.0×10^{-6}
3.885	**0.999**	**873***	**3.00×10^{-2}**	**102×10^{-6}**
3.870	0.995	903*	1.16×10^{-2}	38.3×10^{-6}

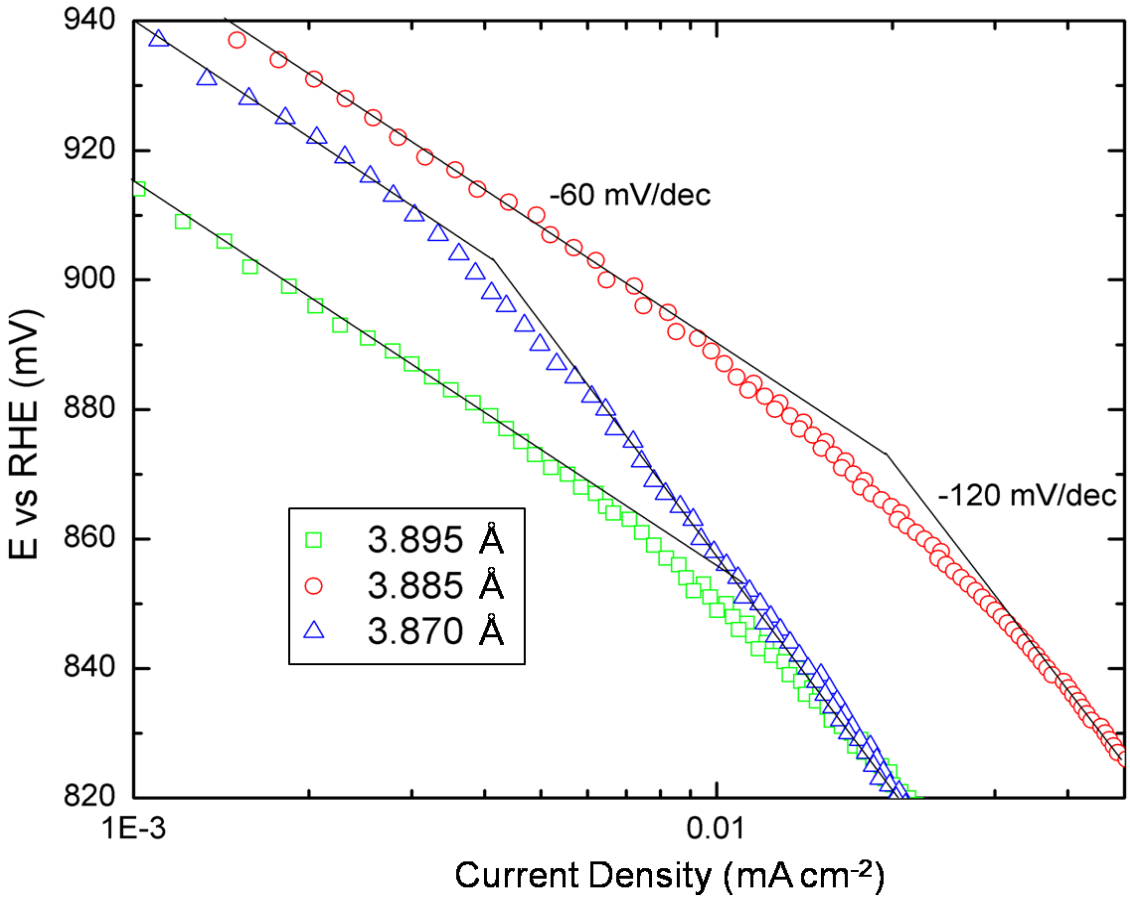

Figure 64. Polarization curves of ~10% W alloy at various levels of strain.

XPS data, as seen in Figure 65, produced a linear correlation of approximately -14.3 eV/ Å between the lattice constant and d-band peak (e.g. d-band center) for the core Pd 3d band. Since the d-band center shift in the 4d band is proportional to that in the 3d, such data supported a linear relationship between lattice constant and 4d band center noticed in other studies for noble metals [118]. This shift away from the Fermi level would have weakened the interaction with oxygen and increased the interaction with superoxide, supporting the hypothesis proposed from the current density observation. These processes would have been optimized at a binding energy of ~335.3 eV, approximately 140 meV above the optimal point and 50 meV from the lowest binding energy point of the hot-sputtered W-Pd binary. The optimal energy was therefore greater than any seen using only the ligand effect of the W before significant tensile strain. Pd oxidation levels could not be accurately determined from high-resolution XPS scans due to baseline problems.

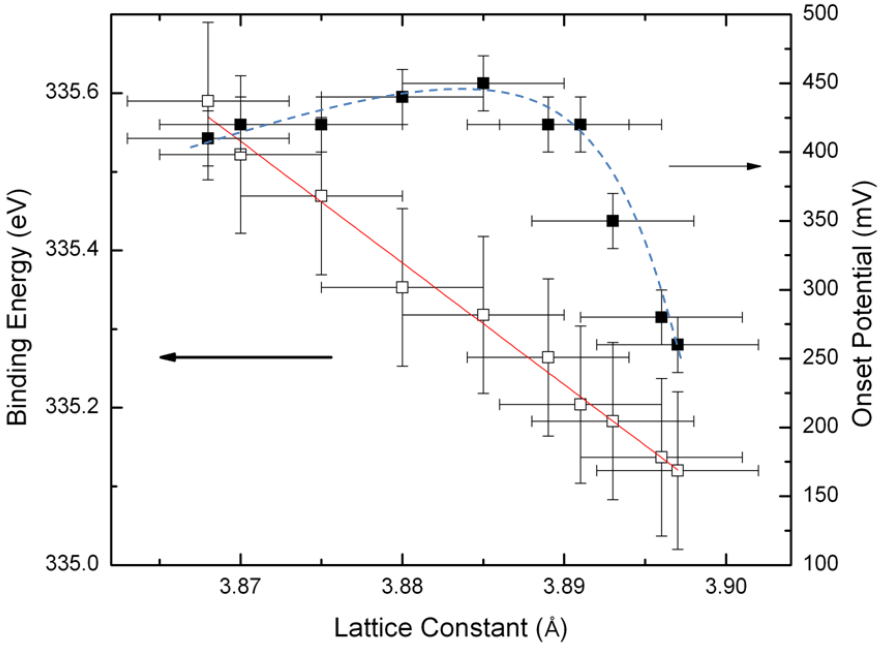

Figure 65. ORR onset potential and Pd $3d_{5/2}$ binding energy peak location as a function of lattice constant along the $Pd_{90}W_{10}$ thin film.

Ex-situ Raman characterization seen in Figure 66 augmented the previously ascribed theories. Site-blocking hydroxide appeared to decrease continually with a lower d-band center from added compression, resulting in a higher Tafel slope transition Most importantly for the RDS, instead of only a minimum of O_{2ads} at the optimum point, both O_{2ads} and OOH were at a minimum. The superoxide (either $O_2^-{}_{ads}$ or HO_{2ads}) appeared to have a greater interaction with the skeletal palladium surface at a lower d-band center, making the O-O bond-breaking mechanism more favorable. After the optimal d-band center point, the adsorbed oxygen interaction with palladium became too low for π-backbonding to weaken the double bond effectively, resulting in a higher amount of O_{2ads} as greater difficulty was encountered in the 1st electron transfer. Because of either this or a weakened interaction with the superoxide and its final O-O bond, the amount of superoxide also increased after the optimal point. Bisulfate, while increasing from its previously seen 'valley' regime for the 3.894 Å W-Pd alloy, did not rise to levels significant to change the overall reaction to a more peroxide-based product. As opposed to the hot-sputtered binary W-Pd, an added compressive strain was able to lower the d-band center sufficiently to increase the O-O bond-breaking in the RDS without increasing (bi)sulfate interaction. A simple pictorial representation of the 'volcano curve' is seen in Figure 67.

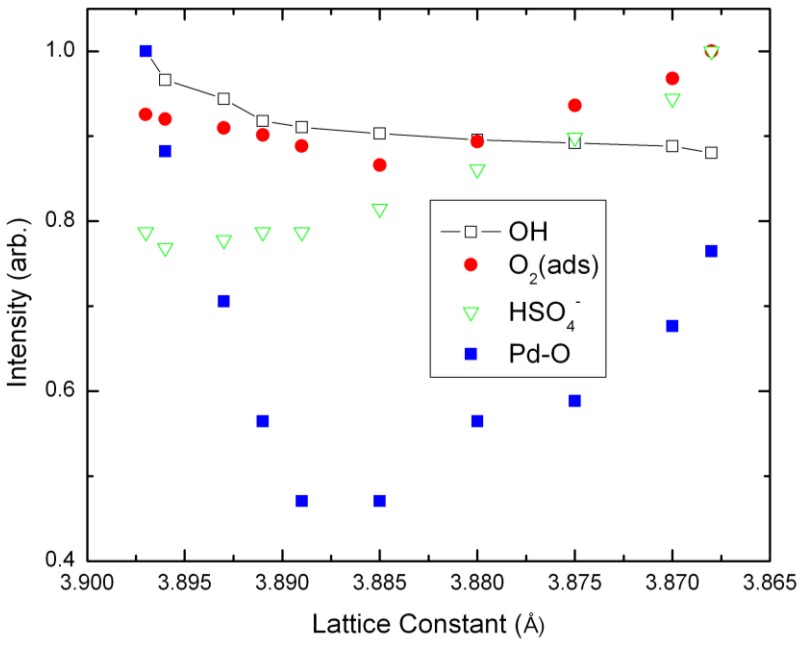

Figure 66. Normalized Raman peak intensities for molecules on $Pd_{90}W_{10}$ surface after ex-situ scan to 850 mV RHE.

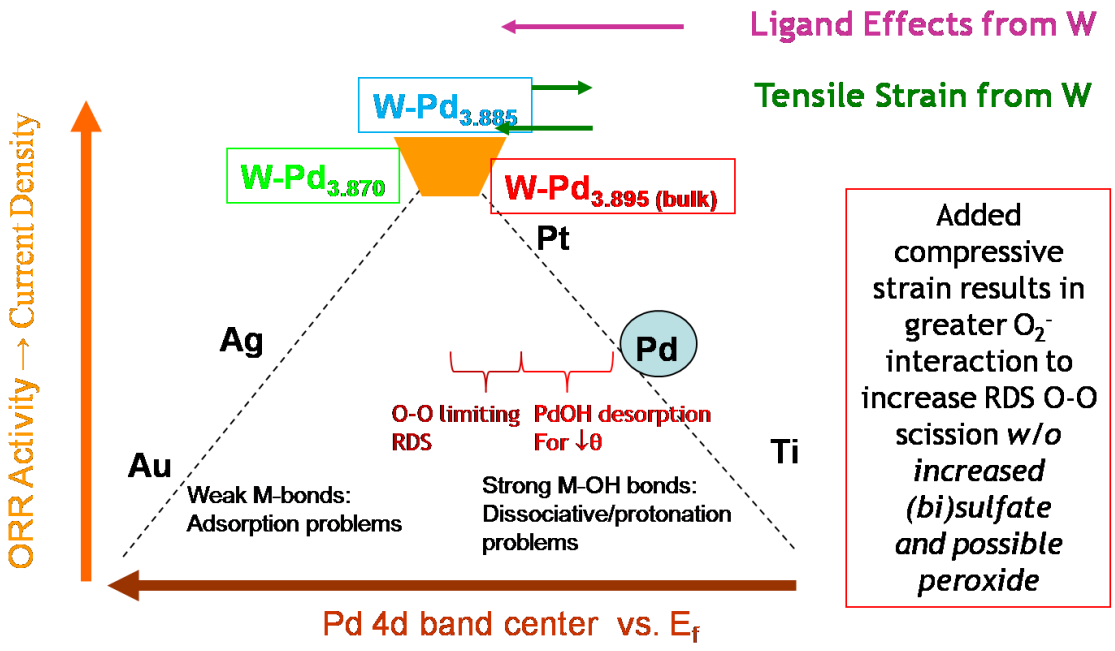

Figure 67. Pictorial representation of RT strained W-Pd ORR activity hypothesis for a Sabatier 'volcano curve' model.

4.3 Ir-W Spread

The W-Pd worked so well that the author decided to branch out with this technique into other Platinum Group Metals (PGM), which would likely form skin or skeletal layers that would not dissolve in acidic environments. One of these was Iridium (Ir), which has similar properties to Pd with a lattice constant of 3.840 Å and a higher binding energy with adsorbed oxygen species to slow down the kinetics of ORR. For example, when looking at the Gibbs free energy of oxide formation at room temperature, PdO ~ -43 KJ/mole while IrO_2 ~ -61 KJ/mole [115]. Thus, a binary spread of Ir and W was sputtered at RT and 400°C. This hot-sputtered temperature was not quite the homologous temperature of 450°C that would match that for the Pd, but was judged sufficient for contrasting with the strain gradient from RT sputtering.

In both the RT and 400°C sputtering, the highest onset centered ~95% Ir, or 5%W, as seen in Figure 68. As in the Pd-W spread, the RT substrate had a much larger lattice constant spread along this ~5% W regime, ranging from 3.848 to 3.830 Å, with the highest onset at 3.833 +/- .002 Å. This was close to the minimum lattice constant in the spread, indicating that a large degree of compression was needed to attain the highest onset. Assuming the same 2-3% W at the surface (not tested by XPS yet), such a compressive strain over .18% would be higher than that leading to the maximum ORR activity in the W-Pd. This would not be surprising since the d-band center from the Ir alloy require even farther shifts away from the Fermi level than the Pd alloy, due to its higher reactivity with adsorbed oxygen species. Unfortunately, further testing with even thinner layers of Ir-W than the 1000 Å middle-thickness substrate were not performed to determine if even lower lattice constants could lead to higher onsets. Onsets from the 400°C sample were close to that of pure Ir as tensile

strains from a lattice constant of 3.844 +/- .002 Å offset any positive effects from the W.

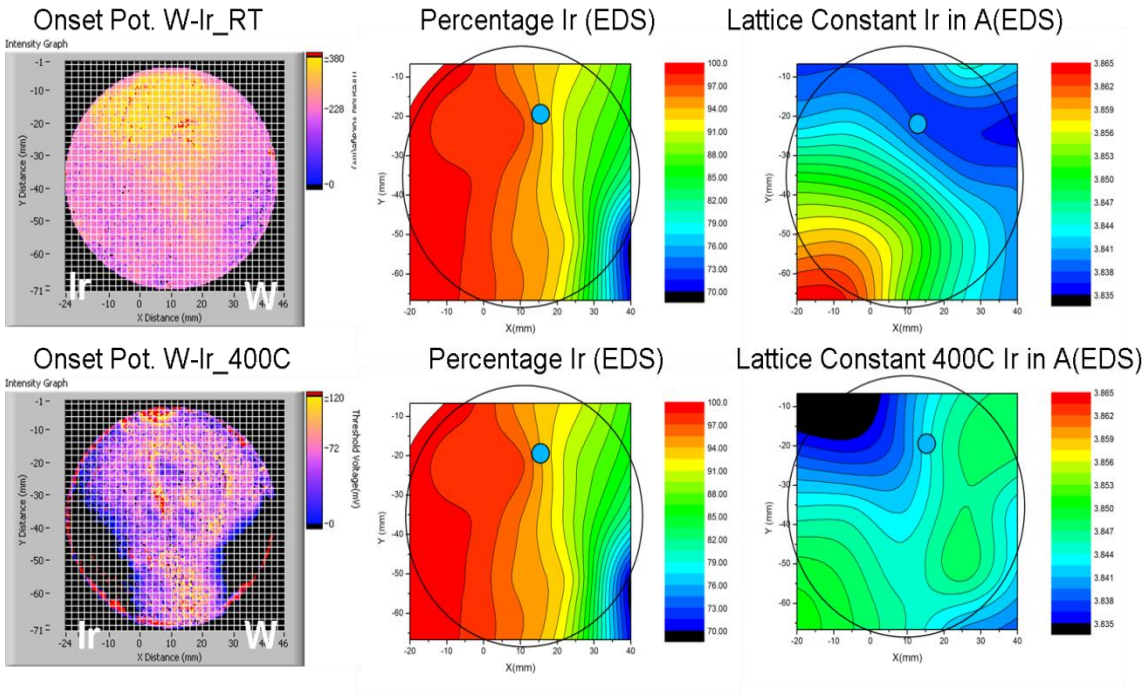

Figure 68. Onset Potentials, bulk Ir percentages, and lattice constants for Ir-W. The first row is for room temperature and the second row for 300°C. The blue dots represent the region of highest onset foe the RT-sputtered substrate.

4.3.1 W-X-Ir Spreads

After this binary spread, a series of W-X-Ir were sputtered at the same conditions as W-X-Pd, with X including all the 3d transition metals. As with the W-X-Pd series, X = V produced the highest current density at 850 mV RHE in aerated 0.05M sulfuric acid, albeit at less than half the value of W-V-Pd, as seen in Figure 69. The EDS spectrum showed a bulk concentration of $W_{.03}V_{.20}Ir_{.77}$, which would translate into a Vegard solid-solution lattice constant of 3.838 Å. However, as seen in

the XRD scans in Figure 47, the bulk lattice constant of this point was experimentally 3.797 +/- .002 Å, a much higher degree of compression than predicted in the binary spread. This may have been due to experimental error in the lattice constant determination (which was calculated from only the (111) peak) or due to alloying between V and W, with a peak seen only in W-V-Ir and in neither of the W-Ir binary spreads. Although the experimental compression was hard to account for, if all the W in the bulk formed a solid solution with V (since they are completely soluble in each other), one could attain a predicted bulk solid solution constant of 3.836 Å between the remaining V and Pd, which would be even closer to the lattice constant of 3.833 +/- .002 Å seen in the binary W-Ir strain spread. Curiously, there was a peak corresponding to W segregation as well in both high temperature spreads, although it signified a β-wolfram structure for the hot-sputtered binary spread (likely formation of slight oxide) and a regular metallic wolfram structure in the W-V-Ir spread in Fenris, which had a higher base pressure. In each case, the broadness of the peak indicated from Scherrer's formulation that it was a nanoparticulate segregation. Without further XRD scans re-taken, all that the author can hypothesize is that some amount of compression is needed for W-Ir to reach a maximum ORR activity, forming a similar model to W-X-Pd, as seen in Figure 70. However, this maximum was still less than that of W-V-Pd, due to either a non-optimal d-band center, too small a lattice constant to efficiently break up O_2 molecules, or some other explanation.

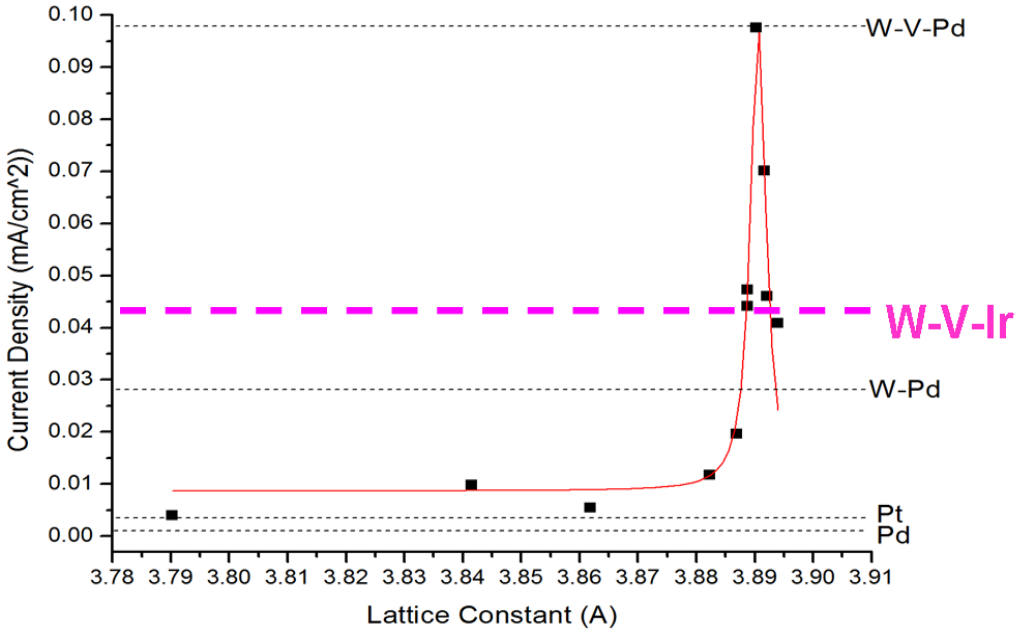

Figure 69. Highest current density line (in purple) at 850 mV RHE in 0.05 M aerated sulfuric acid for W-X-Ir, where X = Ir, as compared to W-X-Pd. Current density levels in plot are ~4.5 times greater than actual values

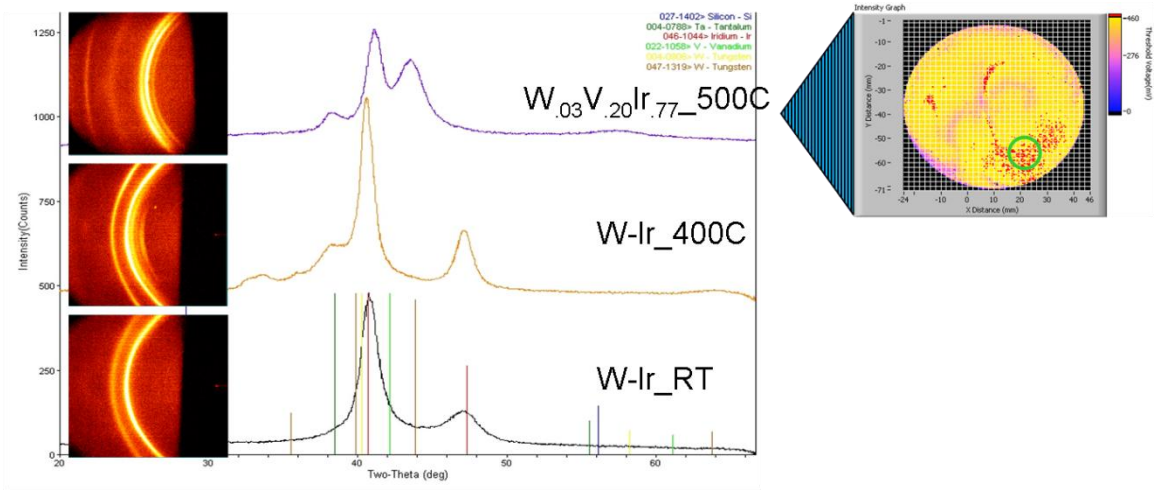

Figure 70. XRD scans from GADDS for the highest onset potential in the Ir-W binary spread at RT and 400°C as compared to the highest onset W-X-Ir alloy, where X = V and the tested region is within the green circle. Chi-arcs are also included for each scan, which show an untextured layer for all scans.

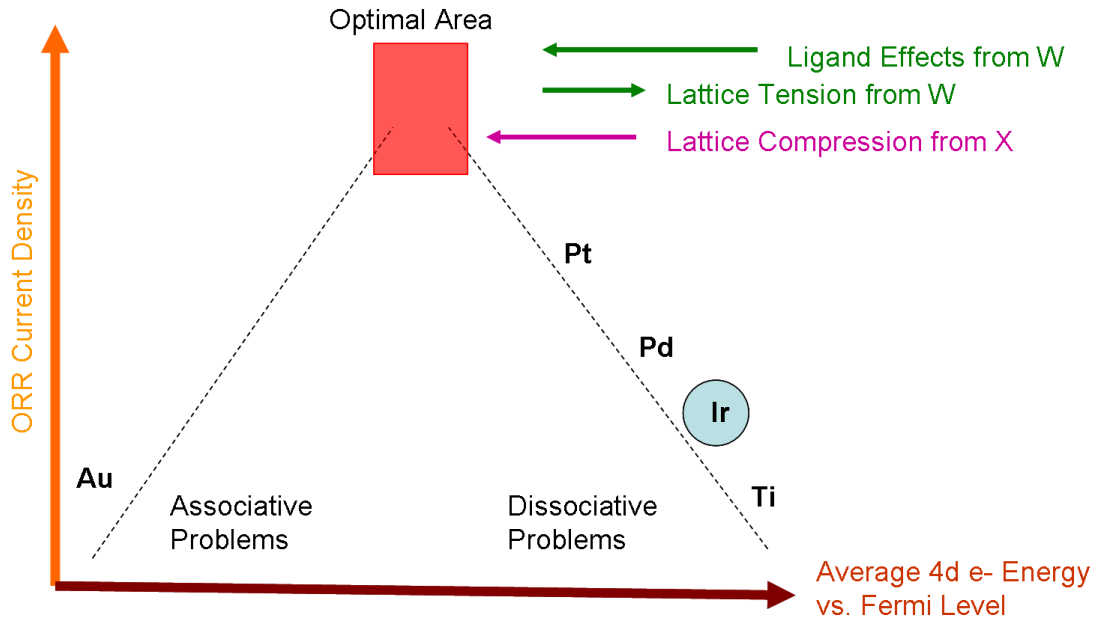

Figure 71. Pictorial representation of ternary W-X-Ir ORR activity hypothesis for a Sabatier 'volcano curve' model.

4.4 Au-Ta Spread

While both Pd and Ir have a problem with oxide formation, Au has the opposite problem, with a Gibbs free energy of oxide formation of ~+15 KJ/mole [115]. The lattice constant of Au is 4.080 Å. A series of Au binary alloys were sputtered at RT with the much more electropositive Ta (revised Pauling electronegativity is 1.5 compared to 2.54 for Au) showing a high onset in some region of the substrate. Like W to Pd, the metallic radius of Ta was only slightly higher than that of Au (1.46 to 1.44 pm). A fortunate result of this relatively small difference in metallic radius was a binary emphasis on ligand effects from the Ta rather than significant contributions from the strain as well, as seen perhaps in Au-Co binary alloys [119].

In the RT-sputtered binary spread map of Figure 72, the region of higher onset seemed centered around 75-85% bulk Au, or 15-25% Ta. There was a higher degree of uncertainty likely arising from the EDS scanning the 100 Å Ta underlayer, even though the author tried to compensate for this by subtracting the underlayer Ta out using the simple relationship that one side of the wafer should be almost pure Au. Other underlayers, including Ti and Nb, are undergoing testing to reduce this problem. The highest onset site seemed to have a lattice constant of 4.075 +/- .002 A, again in compression.

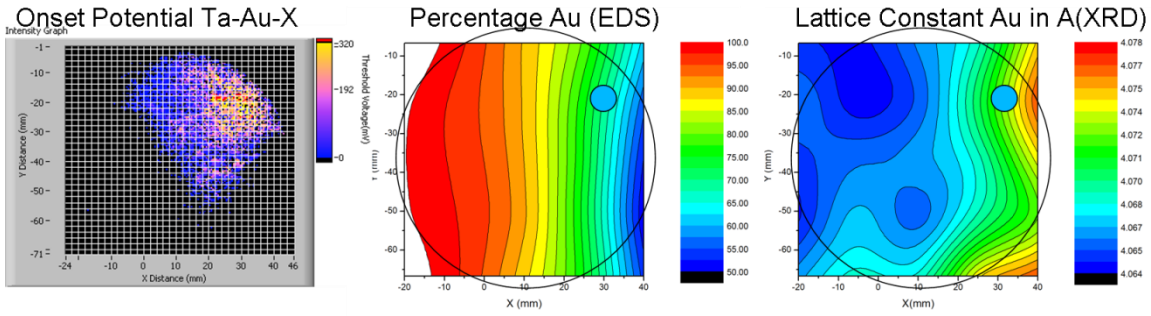

Figure 72. Onset Potentials, bulk Au percentages, and lattice constants for Au-Ta for RT. The blue dots represent the region of highest onset foe the RT-sputtered substrate.

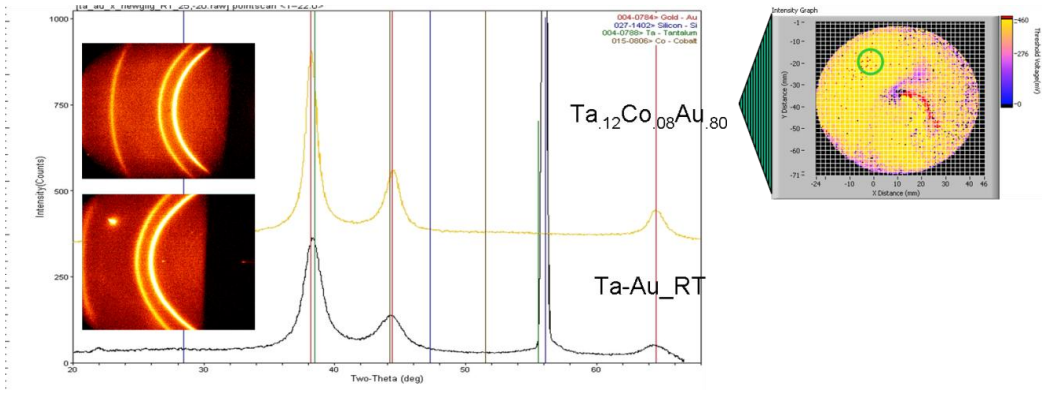

Figure 73. XRD scans from GADDS for the highest onset potential in the Au-Ta binary spread at RT compared to the highest onset Ta-X-Au alloy, where X = Co and the tested region is within the green circle. Chi-arcs are also included for each scan, which show both areas not textured.

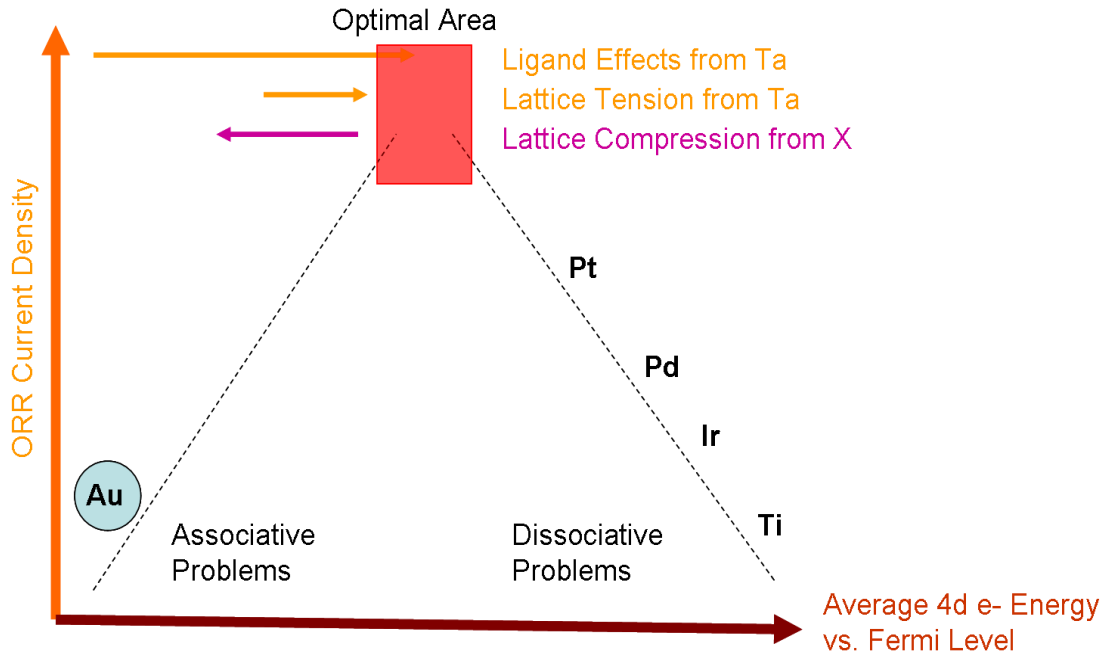

Figure 74. Pictorial representation of RT strained Ta-Au ORR activity hypothesis for a Sabatier 'volcano curve' model.

4.4.1 Ta-X-Au Spreads

A few Ta-X-Au ternary alloys, with X = a smaller element to put the alloy in compression, were sputtered at 400°C, with X = Co showing the highest fluorescent onset; it was not tested for ORR current density. The bulk concentration from EDS was $Ta_{.12}Co_{.08}Au_{.80}$; Vegard's Law for substitutional solid solutions would give a lattice constant of 4.037 Å for the FCC Au alloy. However, when the XRD scans of the binary Au-Ta sputtered at RT were compared to the Ta-Co-Au alloy in Figure 50, they almost matched, with an additional peak from the silicon substrate for the former. Using a Cohen analysis of all three main FCC peaks, this alloy gave an experimental lattice constant of 4.079 +/- .002 Å. Surprisingly, both Co and Ta appeared to fully dissolve into this solid solution, something not apparent from Au-Co, Au-Ta, and Co-Ta binary phase diagrams [120]. Perhaps the Co, instead of substitutionally dissolving

into the solution, was small enough to occupy interstitial sites, something that may not have been predicted without actually sputtering the alloy. This would lead to a higher lattice constant than expected, although still keeping the alloy in compression and almost matching the optimal compression from the binary Ta-Au alloy. A simple Nørskov model, seen in Figure 73, would show the Ta shifting the d-band center of the Au towards the Fermi level transferring electron density to the more electronegative Au combined with a small tensile strain effect. The d-band center would overshoot the optimal energy of the d-band electrons and would need the small compression from the Co to return to the optimal binding energy for oxygen species to have a high ORR activity. There is still some question as to whether the Ta might become oxidized and, as an electron-deficient support, result in greater ORR activity [121]. Further research is required to determine the rationale behind this.

CHAPTER 5

5 PB-RU PYROCHLORES

5.1 Introduction to Pyrochlores

Another set of materials that have shown promise towards the ORR reaction are pyrochlores [122]. This type of oxide has the ideal formula $A_2B_2O_7$, where A and B are rare-earth or transition ions of typical radii ~1 Å for A and ~0.6 - 0.8 Å for B, with the most common oxidation states from +2 through +5. Its structure is described by the Fd3m space group with eight molecules in each unit cell of lattice constant ~10-11 Å. The formula can also be written as $A_2B_2O_6O'$ to differentiate the two oxygen positions in the cell, with the A cation have eight-fold coordination inside a scalenohedron composed of six equiaxed O and two O' atoms residing slightly closer. Conversely, the smaller B cations are six-fold coordinated within a trigonal antiprism (which can resemble an octahedra) of O atoms.

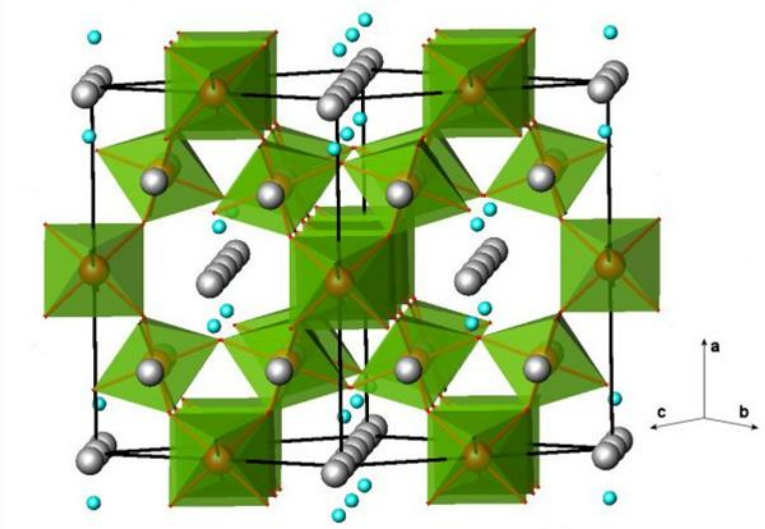

Figure 75. Basic pyrochlore structure consisting of octahedral 'rings' of BO_6 surrounding cuprite-like linear chains of A_20, where the A cations are in grey and the O' in cyan [123].

5.2 Structure

Pyrochlore has a relatively disordered structure that has been described in a few different ways, from an anion-deficient fluorite cell to chains of A_4 and B_4 tetrahedra, but the most easily understood method for this study's purposes was first discussed by Sleigh in the 1960s [124-126]. In it, the pyrochlore is divided into two interpenetrating lattices of BO_6 octahedra and A_2O' chains, as seen in Figure 75. These BO_6 octahedra, which can be distorted, corner-share O atoms to form a B_2O_6, or $(BO_3)_2$, network. As opposed to the octahedral coordination in a perovskite, ABO_3, the octahedra do not stack up on top of each other in a linear fashion, forming a more complex pattern that involves the B-O-B bond buckling from 180° to ~130-140° along the [110] direction. In addition, these octahedra provide most of the structural support for the pyrochlore. As mentioned previously, the A ions have eight-fold coordination, with 6 of those bonds to O atoms from the octahedra, in a 'chair-form' hexagonal arrangement. The remaining two are perpendicular to these, either being located above or below the plane formed by the O atoms. Since the A-O' is shorter than the A-O bond distance, this can be thought of as a separate network of A ions linearly-coordinated to tetrahedrally-shared O' atoms in an A_2O' network; this interpenetrates the $(BO_3)_2$, network, with the closest distance between them at the A-O bond. Each O ends up tetrahedrally-shared between 2 A and 2 B cations. Thus, while the $(BO_3)_2$ network forms the 'back-bone' of the structure, the pyrochlore relies on both the O and O' remaining tetrahedrally-coordinated to A and/or B. Both these cations must not be too electropositive or else the covalent character of the bonding that leads to such tetrahedral coordination will be lost. For instance, $Pb_2Ru_2O_7$ crystallizes into a pyrochlore while $Sr_2Nb_2O_7$ remains a perovskite [127].

5.3 Defects in Pyrochlores

One reason behind the variation in pyrochlore properties is their richness in possible defect states. Two types of defects relevant to this study are anion vacancies and cation substitution. The former can be traced back to the notion of the interpenetrating B_2O_6 and A_2O' networks, in which the B_2O_6 network is responsible for most of the stabilization. Oxygen vacancies can then exist at the O' site, written as $A_2B_2O_6O'_{1-y}$, where $0 \leq y \leq 1$. Such a vacancy can expose two A cations to each other, resulting in electrostatic repulsion. However, the vacancy state can have 'virtual energy levels' which are comparable to the 6s levels of some elements. If the cations are weakly electropositive with a polarizable lone pair of $6s^2$ electrons (.e.g. Pb^{+2}, Bi^{+3}, Tl^{+}), these lone pairs can orient toward the vacancy and hybridize with these virtual levels, in essence bonding across the vacancy in what is called a 'trap-mediated bond' to stabilize any repulsion [128]. As before, if y = 1, for the $A_2B_2O_6$ to remain a pyrochlore and not a perovskite, both cations must be electronegative enough to allow for a degree of covalency with the tetrahedrally-bound O atoms, with $Tl_2Nb_2O_6$ remaining a pyrochlore while $Pb_2Ti_2O_6$ becomes a perovskite at normal pressures [129].

The other defect type involves replacing some or both of the A and B sites with other cations. As long as there are (1) enough of the original cations to stabilize the structure, (2) these substituted cations are not grossly size-mismatched, and (3) the charge can balance through either O' vacancies or multi-valencies of the other cations, this is possible. Due to their less rigidly-structured character, cubic pyrochlores do not have any strict rules for cation size to retain their structure, such as the A, B, and O radii for perovskites: $0.75 \leq (r_A + r_B)/(r_B + r_O)^{1/2} \leq 1.00$. However, since pyrochlores are less dense than their close cousin perovskites, applying pressure through external

means, or in some cases doping cations that have too large a size difference from the original, can transform a nonstoichiometric ABO_3 pyrochlore to an ABO_3 perovskite, such as $Bi_2Rh_2O_6$ [130]. Another example is nonstoichiometric $Gd_{1.9}\ Ca_{0.1}\ Ti_2O_6O'_{0.9}$ [131].

5.4 $Pb_2(Ru_{2-x}Pb_x)O_6O'_{1-y}$

The pyrochlore of interest to this study, $Pb_2(Ru_{2-x}Pb_x)O_6O'_{1-y}$, with $0 \leq x \leq 1$ and $0 \leq y \leq 1$, can have both the anion and cation defects. The stoichiometric $Pb_2(Ru_2Pb_2)O_7$ was first prepared in the early 1970s by Bouchard and Gillson [132]. Since the large 8-fold coordinated Pb^{2+} cation (1.29 Å) is most stable in the A site, charge balance requires 6-fold B-site Ru to be Ru^{+5} (0.565 Å), resulting in a +2/+5 pyrochlore. As the O' is decreased, the size of the cubic pyrochlore unit cell increases from 10.252 Å at y = .5 to 10.271 Å at y = 1. This anion defect likely leads to its primary use as a stable conductive oxide for devices from thin-film resistors to electrodes for dielectrics [133, 134]. RuO_2 is a metallic oxide conductor with a low resistivity of ~3 x 10^{-5} Ωcm due to the overlap between Ru 4d t_{2g} levels and O p_π through Ru-O-Ru 180° bonds. However, in the pyrochlore $Pb_2Ru_2O_7$, the Ru-O-Ru bond is ~135°, which limits the overlap and hence the conductivity. As the O' vacancies are increased, the conductivity increases as well, explained by Goodenough and coworkers as due to the 6s orbitals changed by the trap-mediated states approximating the energy level of the Ru 4d band, which broadens the conduction band [135]. Even at a bond angle of ~135°, $Pb_2Ru_2O_{6.5}$ still reaches resistivities of only ~3 x10^{-4} Ωcm [136].

In addition, these trap-mediated states make the pyrochlore more stable at higher temperatures and pressures similar non-defect pyrochlores. Indeed, Kafalas and coworkers were only able to transition $Pb_2Ru_2O_6$ to the perovskite phase by applying 90 Kbar of pressure in a reduced atmosphere at 1400°C [137]. Due to this stability at higher temperatures, these pyrochlores were mainly synthesized at higher temperatures using powder-processing methods [138]. All phase diagrams, such as the following (re-drawn from a diagram by Hrovak et al.), employ the sintering of fine powders at high pressure in air. In order to keep charge balance as y = 0.5, half of the Ru changes oxidation states to +4. Since the 6-fold cation size is 0.62 Å compared to 0.565 Å in the previous state, the pyrochlore is able to easily accommodate this [139].

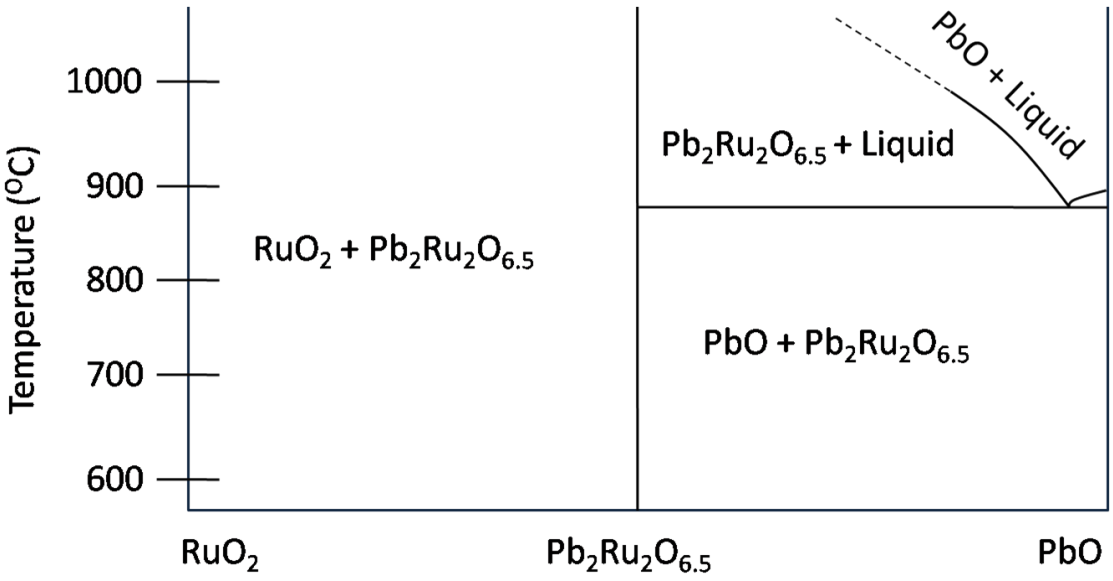

Figure 76. Phase Diagram for Pb-Ru-O phase diagram determined through repeatedly fired pelletized powders [140].

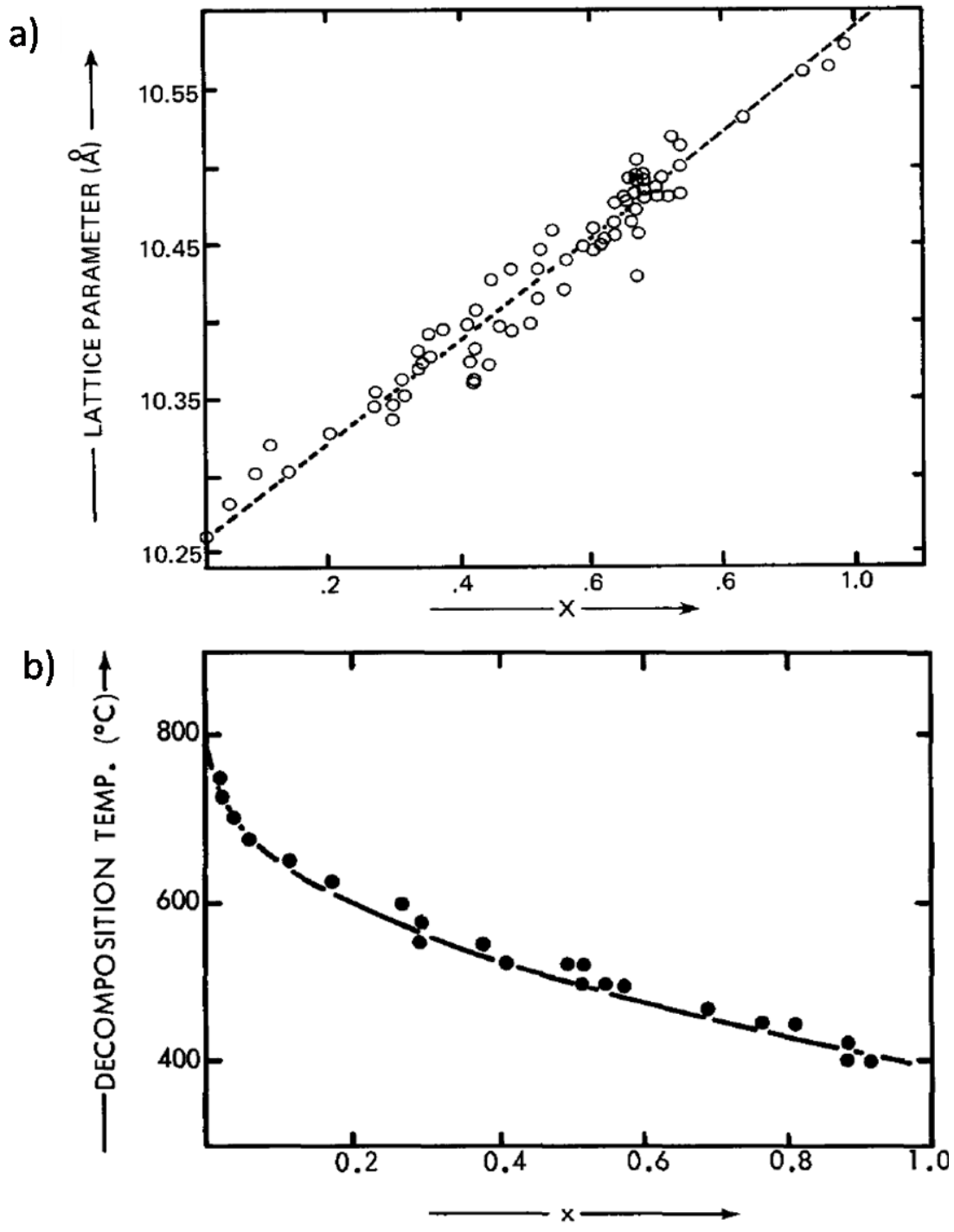

Figure 77. Data points in the Horowitz study on the $Pb_2(Ru_{2-x}Pb_x)O_{6.5}$ a) lattice expansion with increase in substituted Pb and b) the maximum temperatures where such substitution is stable.

However, as may be seen in the phase diagram in Figure 76, while these conditions may allow for the partial cation substitution of Pb^{2+} from the larger A-site, it introduces too much energy into the system for the B-site to be occupied by anything else but noble metals, such as Ru [141, 142]. Hence, in 1981, when Horowitz and his group started preparing nonstoichiometric $Pb_2(Ru_{2-x}Pb_x)O_6O'_{1-y}$ using an aqueous synthesis method involving precipitation and heating at a much lower 300 to 700°C, they found that as the percentage of Pb to Ru increased over 50%, Pb did in fact substitute into the B-sites [34, 128]. The smaller size of the B-site could not accommodate 6-fold coordinated Pb^{2+} (1.19 Å), so the Pb transitions to a +4 oxidation state with a more manageable ionic radius of .775 Å. In fact, as seen in Figure 77, Horowitz et al. found that by substituting Pb^{4+} into the Ru^{4+} site, they could approximate their experimental results showing a linear expansion in the lattice constant with increasing x in $Pb_2(Ru_{2-x}Pb_x)O_6O'_{1-y}$, where $0 \leq x \leq 1$ and $y \sim 0.5$ [35]. Using thermogravimetric analysis in hydrogen, they were able to ascertain that $y \sim 0.5+/-0.1$, regardless of cation substitution. With evidence of vacancy ordering when half the O' sites are vacant, this vacancy concentration appeared highly stable [143]. Above $x \sim 1$, they were unable to obtain a stable crystalline pyrochlore, which was consistent with a $Pb_2(Ru_{2-x}^{5+}Pb_x^{4+})O_{6.5}$ model. If more than $x > 1$, the only way to retain charge balance would involve increasing the oxygen vacancies, which was apparently difficult to achieve at these low temperatures. In addition, they found that amount of Pb^{4+} that could substitute into the B-site decreased with temperature. Others have tried putting the Pb^{4+} cation into the B-site of a pyrochlore and found that it was extremely difficult at normal pressures, attributed to both size limitations and the instability of Pb^{4+} at higher temperatures [144, 145]'. Both the linear substitution and temperature destabilization curve from Horowitz's study appear in the following

figure. By following the lattice parameter a_0, one could use the linear relationship to determine either the stable:

$$x = 2.96 * a_0 - 31.14 \quad (4.1)$$

$$\% Ru = -74 * a_0 + 808.6 \quad (4.2)$$

Notice that since these were based on two significant digits, one cannot expect values with greater precision. These equations should also give approximate values for $0 \leq x \leq 1$ and $\%Ru \geq 25\%$ in the Pb/Ru composition space as long as the temperature is kept below the destabilization threshold for that Pb substitution concentration.

5.5 ORR Catalysis of $Pb_2(Ru_{2-x}Pb_x)O_6O'_{1-y}$

Horowitz and his group, taking advantage of their patented synthesis procedure, discovered the relatively high ORR of this material in acidic and basic media [35]. While not comparable to that of platinum, it was resistant to methanol oxidation. They proposed it was due to surface vacancies and disorder on the surface of the complex oxide that was able to help oxygen gas better penetrate the hydroxylated barrier covering the oxide. By doping increasing amounts of Pb^{4+} on the Ru B-site of the pyrochlore to form $Pb_2(Ru_{2-x}Pb_x)O_{7-y}$ with increased surface Pb and likely oxygen vacancies, Goodenough and his group were able to increase the catalytic activity, although they found it became unstable under high cathodic loads [36]. Of at least four Pb dopant concentrations tried in 2.5 M H_2SO_4, they found the greatest catalytic activity in decreasing order of x = 0.26, 0.17, 0.05, and 0.40. They also tried binding it

to Vulcan-72 and sulfonated DOW membrane gel to increase activity and stability, which occurred, but the activity still remained below that of Platinum [37]. Raghuveer was able to fabricate nanoparticles of this pyrochlore and reached even higher activities comparable with that of Pt, perhaps through differing defect states on the nanoparticulate surface [38].

5.6 ORR Mechanism on Pyrochlore Surface

Unlike the noble metal surface discussed earlier, hydroxide ions form from the dangling bonds of an oxide surface almost immediately after being placed in solution. Oxygen molecules have a much more difficult time penetrating this surface layer for the oxygen reduction to take place. Thus, the most likely initial mechanism is an outer-electron transfer across the hydroxylated surface to an oxygen molecule, forming a superoxide radical that becomes protonated, as seen in Figure 78 [146]. This more polar molecule must then be able to displace a bound hydroxide on the pyrochlore surface. Such a displacement reaction is almost definitely the rate-determining step of the reaction. The rest of the mechanism should parallel the acidic 4-electron reaction for the Griffith 'side-on' adsorption of oxygen, with the exception that only one hydroxide dissociates while the other remains to hydroxylate the surface. This means that the O-O bond-breaking of the superoxide is likely not part of the RDS, as opposed to the noble metal analysis. However, the 1st electron transfer to form superoxide before the displacement may still occur in the RDS and slope of the Tafel plot.

Most mechanisms concerning the pyrochlore oxygen reduction focus on it occurring at either the Pb-O' or the Ru-O sites [37]. There are six candidates that

become hydroxylated on the surface and might be able to reduce oxygen. These include Pb-0_t, Pb-O'_t, Pb-O_b-Pb, Ru-O_t, Pb-O_b-Pb, and Pb-O_b-Ru, where t = terminal oxygen and b = bridging oxygen. Goodenough and Zen, in the aforementioned work involving different levels of Pb doping, have determined a plausible scenario. The strong π-bonding between Ru and O in Ru-O_t and Ru-O_b-Ru made it unlikely that the surface hydroxide would easily dissociate. In addition, such bonding in the RuO_2 did not show high ORR activity. By applying similar rationale, Pb-O_b-Pb and Pb-0_t were ruled out. This left Pb-0_t and Pb-O_b-Ru. The Pb-0_tH bond was known to reduce oxygen well at high pH, but not at low pH. To discover what was occurring, they derived the overpotential of $Pb_2(Ru_{2-x}Pb_x)O_{6.5}$ at a constant current density of 5 mA/cm^2 in different pH solutions. The result showed low overpotentials in highly alkaline solutions that increased to a maximum at pH ~ 2 and then rapidly decreased again. The mean surface charge density, which becomes more positive as protons in solution bind to surface hydroxide, increased exponentially for these pyrochlores right after the point of zero charge, where it is zero. It then leveled off before spiking again at pH ~ 2. The explanation for this was that there are two sites in acidic solutions competing for the ORR, the poorly-catalytic (in acid) Pb-0_tH, and the more highly catalytic Pb-O_b-Ru. The primary reasons behind the reduced activity of the Pb-0_tH stemmed from the increasingly full protonation of this more basic site in acid to Pb-0_tH_2, rendering it unavailable for the ORR displacement However, above a pH ~ 2, the more acidic Pb-O_b-Ru site was not protonated much, if at all, also eliminating it from the reaction. After the pH dropped below ~2, the Pb-O_b-Ru sites started becoming protonated to Pb-HO_b-Ru.

The explanation behind the activity of Pb-O_b-Ru is still unclear. Most theories attribute it to the stronger interaction between the O-Ru compared to Pb-O, with the O-Ru having a strong π-bond component and the Pb a weaker σ-bond. This

asymmetry would make it easier to begin the displacement of OH from the Pb. However, the temporary Pb- -O_b-Ru bond would still be weaker (less acidic) than a regular O-Ru bond, allowing the O_bH to displace with less energy. In addition, once the hydroxide was detached from Pb, the more conductive bond would make the e^- transfer to the peroxide easier.

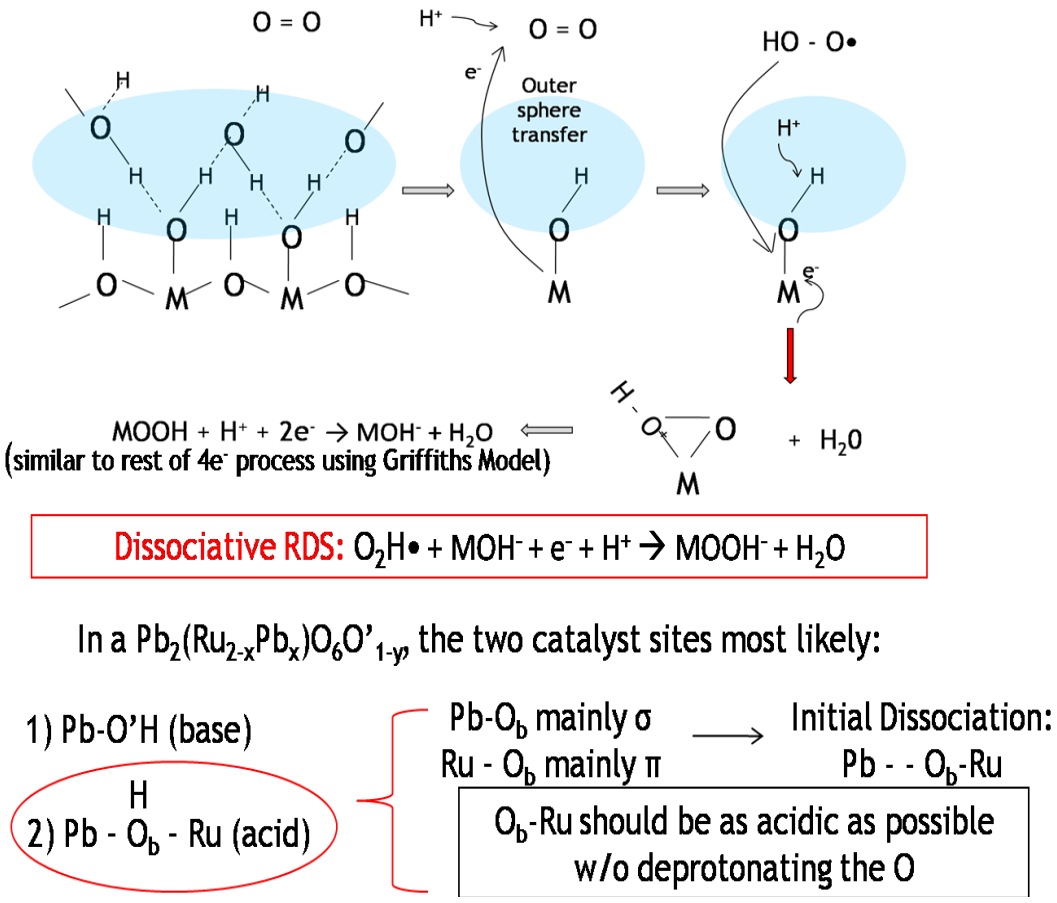

Figure 78. Proposed mechanism for oxygen reduction in Pb-Ru pyrochlore and catalytic sites where it is most likely to occur.

5.7 Pyrochlore Synthesis

As mentioned in 5.4, the most common methods to produce $Pb_2(Ru_{2-x}Pb_x)O_{7-y}$ have involved either powder processing at temperature > ~800°C, where $x \rightarrow 0$, or precipitation in alkaline solution followed by curing up < ~700°C, as first done by Horowitz [147]. In this study, Pb and Ru were DC-sputtered on-axis from separate sputter guns onto a 3" silicon wafer, similar to the noble metal research. However, a 30 nm Ir underlayer was used to insure conductivity across the entire substrate at elevated processing temperatures, as well as providing a diffusion barrier to the silicon substrate. The sputtering was performed in 10 mtorr Ar with 1.1 mtorr O_2 at room temperature. They were then 'flash-annealed' (taken in and out immediately) for one hour in an air furnace for pyrochlore crystallization and growth. Elimination of the O_2 in the sputtering process led to crack propagation and delamination of the Ru and Pb oxides upon oxidation. More than ~10% O_2 led to significant poisoning of the Ru and Pb targets, which were current-controlled. Such poisoning of the Pb to a non-conductive PbO surface layer would block the negative potential required to attract Ar^+ for sputtering. As it was, the voltage of both the Pb and Ru (with a more conductive oxide) increased significantly at 10% O_2. The samples were post-processed rather than hot-sputtered since the Ru had a tendency to form volatile RuO_4 at these conditions, reducing the expected value of Ru in the film significantly.

The fabricated films were subjugated to the same testing procedures as for the noble metal work. To ensure stability during the electrochemical testing, all films were left in constantly stirred 1 M HNO_3 for at least 24 hours. They were subsequently washed with deionized water and dried before any measurements were taken.

5.8 Composition/Temperature Gradient for Pb-Ru Pyrochlores

In Section 5.4, it was seen that Pb substitution into the B-site of $Pb_2(Ru_{2-x}Pb_x)O_{7-y}$ is dependent not only on the initial Pb:Ru ratio, but also upon the annealing temperature. Thus, the initial experiment attempted to combine the two variables. After Ir was deposited, Pb and Ru were sputtered from two guns on opposite sides of the center of the wafer. As opposed to the thickness gradient established in the Pd-W strain tests, this was meant to ensure an initial thickness of ~200 nm across the entire wafer. After sputtering, they were then placed onto a holder made of Si and situated halfway into an open-air tube furnace Thermocouples were attached to the underside of the holder to allow for temperature readings. The initial atomic concentrations (discounting O) and temperature can gradient can be seen in Figure 79 with the fluorescent test results.

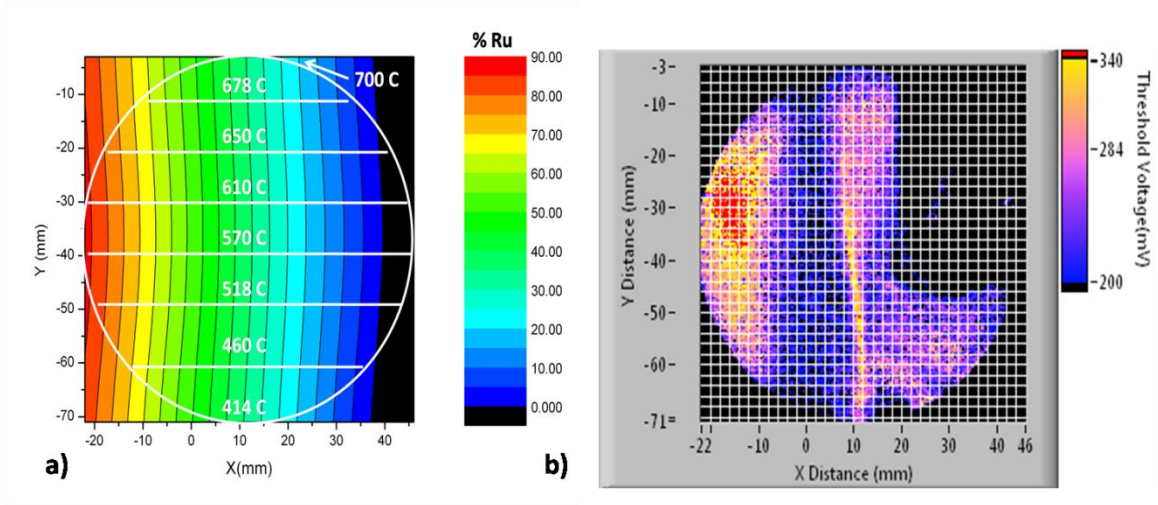

Figure 79. Sample was a) sputtered with a Ru/Pb composition gradient before annealing in air along a perpendicular temperature gradient. It was then b) subjected to the fluorescence test in 0.1M Na_2So_4 to produce an onset potential map.

Enhanced areas of fluorescence, signifying the localized ORR, occurred in two separate composition/temperature spaces on the sample. Both were higher than the typical Pt onset potential from 280-320 mV. Keeping in mind the +/5% error in EDS measurements, one occurred from 70 to 80% Ru, with increasing amounts of Ru in the Pb-Ru pyrochlore at maximum fluorescence. The second also slightly increased Ru percentage in the bulk from 32 to 39%, with an optimal at ~38+/- 5% Ru. These two bands have respectable optimal temperature bands of 575 - 650°C and 575 – 500°C. Some interesting contrasts stood out between them in the XRD measurements analyzed in Figure 80. For the 38% Ru stripe, the lattice constant almost matched the Horowitz linear prediction of Section 5.4, decreasing only after the temperature was raised over what was likely the destabilization temperature for Pb^{4+} at this concentration (~500-550°C). The grain size increased with temperature, either because of the added energy, elimination of slower-diffusing lead for coarsening, or a combination of both. The peak intensity maxima of the even peaks for this pyrochlore, represented by (222) in the following figure, occur at ~525-575°C, where the maximum amount of Pb has been incorporated into the sample. Conversely, in the 70-80% Ruthenia band, the peak intensities decreased much more slowly and the grain size increases. In both cases, an Ir underlayer was used that does not indicate any oxidation at XRD until ~610°C. The IrO_2 intensity measurement for 70-80% Ru was not reported due to the peak similarities between Ir and Ru oxides, which were both present.

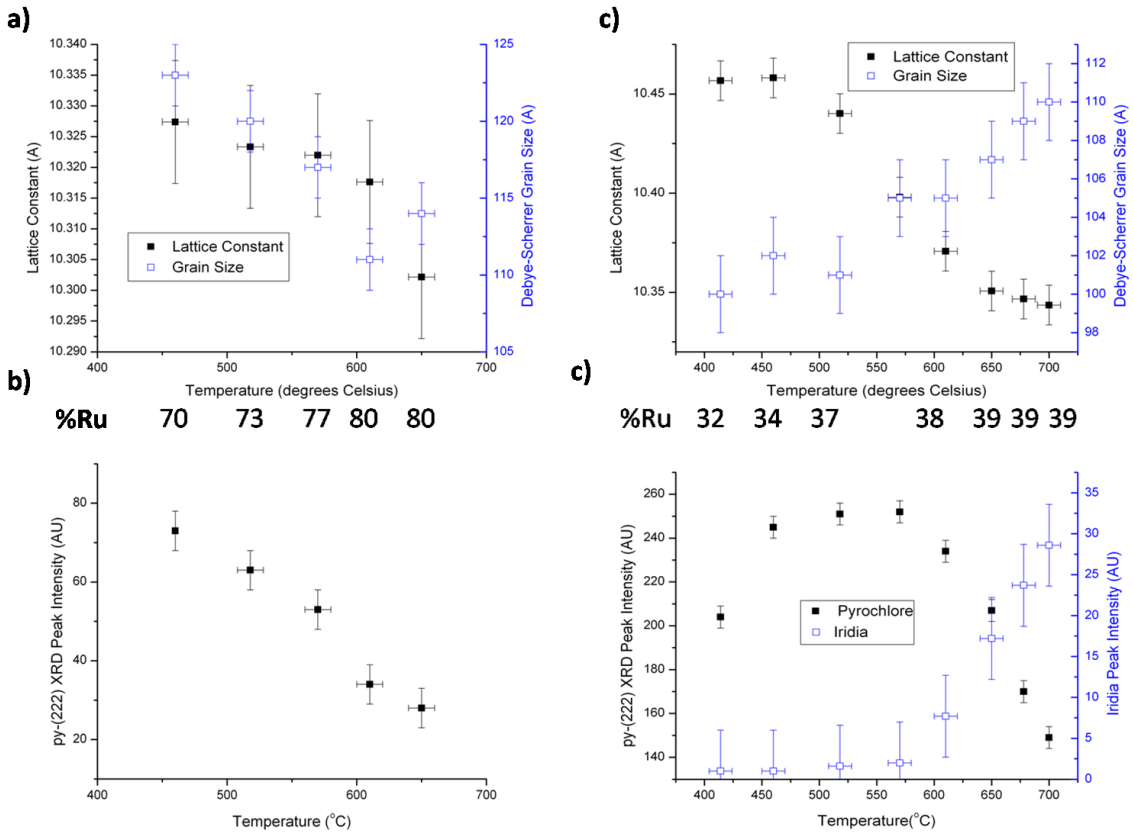

Figure 80. XRD Analysis of a), b) the high Ru concentration region and c), d) the low Ru concentration region. Iridia peak intensity for the high Ru concentration could not be determined due to the similarity between Iridia and Ruthenia peaks. Filled squares correspond to left ordinate.

Figure 81 incorporated both the EDS and lattice constant measurements by using equation (1) in this section to determine the theoretical lattice constant and subtracting it from the experimental. A perfect match would indicate that all the available Pb was incorporated into B-sites. A negative value would imply that some of the Pb was rejected (e.g. above the Pd destabilization temperature) and a positive that the prediction was overestimating the percentage of ruthenium involved in pyrochlore formation, which usually meant that formation of RuO_2 or the volatile RuO_4. Since post-EDS and SEM analysis showed evidence of Ruthenia, it is assumed that the majority of excess Ru all formed the oxide. There appeared to be an inflection point at

~550°C, at which the formation of Ruthenia increased. This formation was coincident with the abrupt rise in the onset potential at ~77% Ru, even though the pyrochlore peak intensities were decreasing. To investigate these two regions of high activity in more detail, a binary spread was prepared at 575°C, which overlapped these two high ORR potentials at different concentrations.

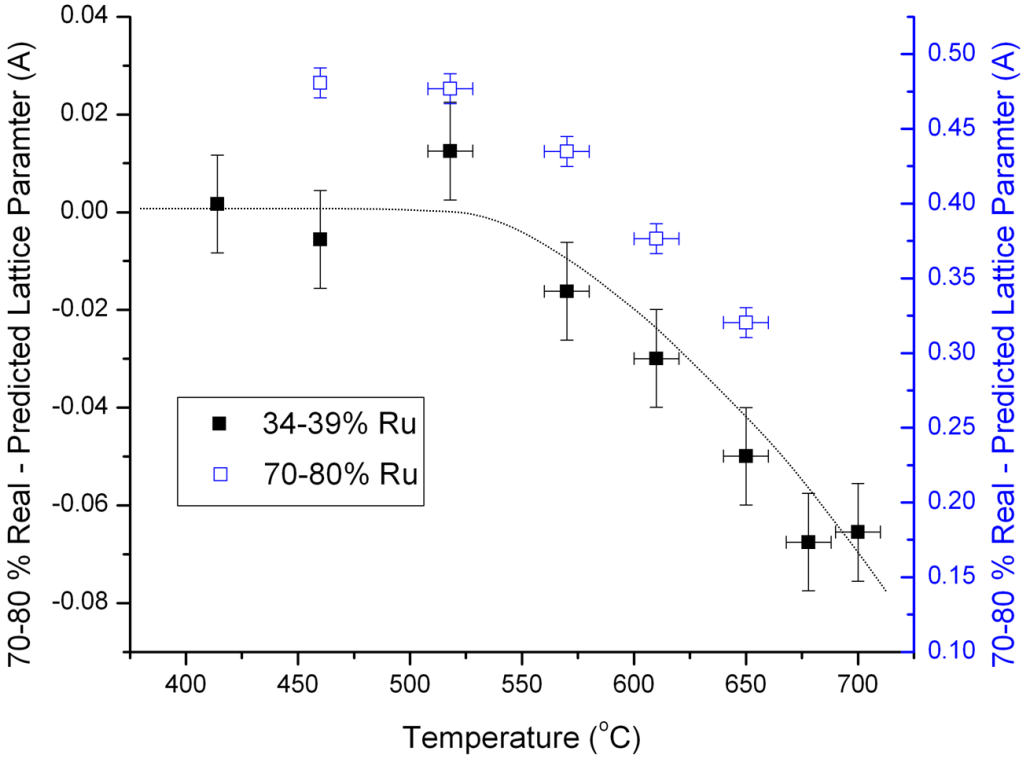

Figure 81. Difference between experimental and predicted lattice constants for the two reactive bands of the Pb-Ru Pyrochlore. Filled squares correspond to left ordinate.

5.9 Binary Pb-Ru Pyrochlore Combinatorial Spread

The binary spread was sputtered from guns that were still on-axis but directed from the bottom of the wafer, which resulted in a slightly different concentration gradient and thickness gradient from ~250 to 70nm. As expected, similar concentrations demonstrated high onset potentials, with activity occurring in the 70-80% and 35-40% Ru concentrations relative to itself and Pb. A slice of this fluorescence map taken along the Y = 37 mm line (~170 nm along the span) is plotted in Figure 82, displaying these dual peaks.

The XRD data in Figure 83 indicated a preponderance of PbO formation in the bulk below 50% Ru and RuO_2 above 50% Ru, in accordance with the Pb-Ru pyrochlore phase diagram [141]. As seen in Figure 84, here was a slight decrease in the lattice constant up to ~50%, where there must have been a significant increase for Pb incorporated into the B-sites of the pyrochlore. A decrease in the grain size supports this explanation, as it is less energetically favorable to dope the Ru^{+4} sites with the larger Pb^{+4}. The highest pyrochlore intensity occurred at the concentration where there was the most activity at % Ru ~ 38%, as expected.

As measured by a 4-point probe in Figure 85, this film, as sputtered on a tantala substrate, showed the lowest resistivity where it was least catalytic. Since a decrease in resistivity is correlated in pyrochlores to loss of the O', allowing for increased σ-bonding of the Pb, the most likely scenario here was $y > 0.5$ for $Pb_2(Ru_{2-x}Pb_x)O_{7-y}$ where the bulk concentration of Ru was ~65-40% [148]. Above 65%, the resistivity corresponded with that of RuO2 and below 40% supported $y \leq 0.5$ for $Pb_2(Ru_{2-x}Pb_x)O_{7-y}$ [149].

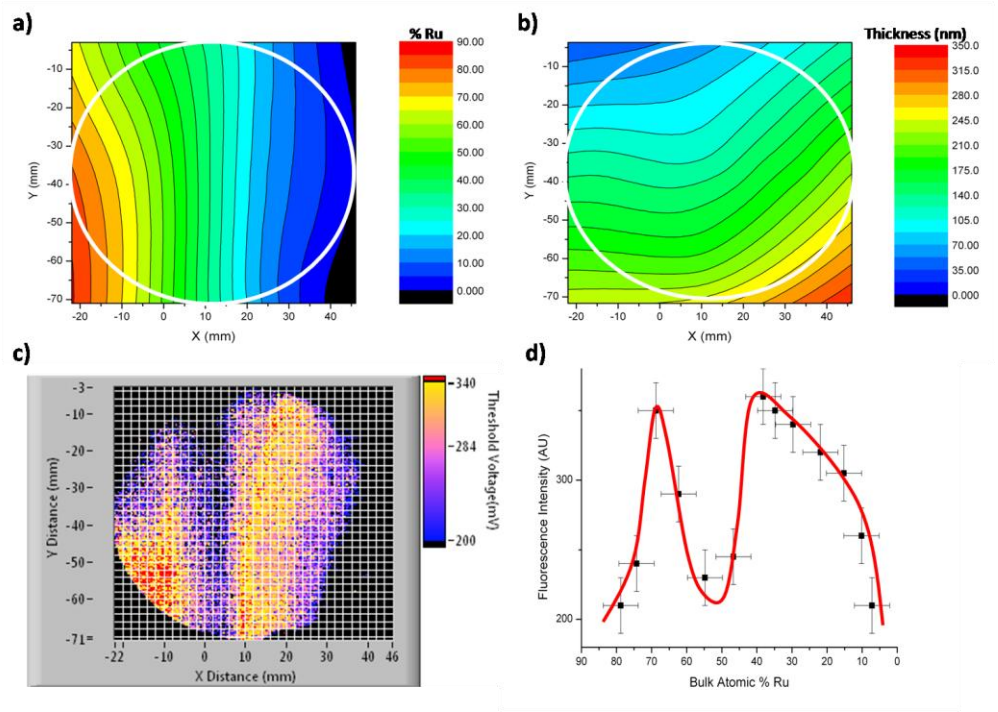

Figure 82. Binary Pb-Ru spread consisted of Pb and Ru forming an a) composition gradient in one direction and b) a thickness gradient in the other. The onset potential map is shown in c) with d) the onset potential across the middle of the wafer at Y = 37mm.

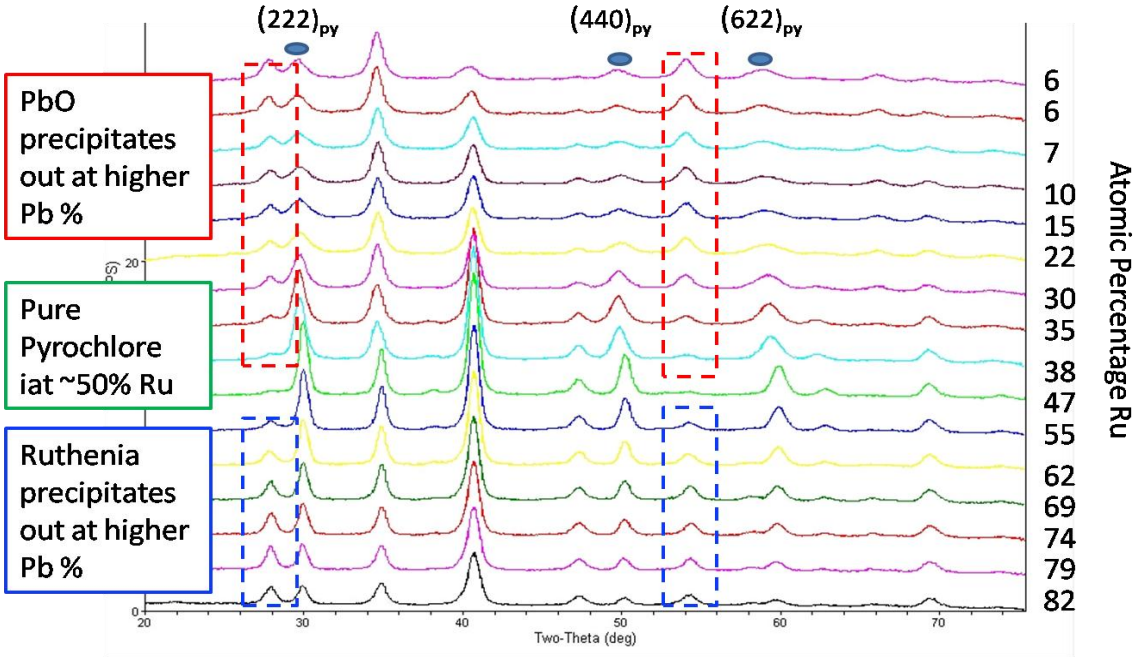

Figure 83. XRD scans of bulk film with varying atomic % Ru compared to Pb/Ru binary. A majority PbO peak was observed before 50% Ru and RuO_2 after 50% Ru.

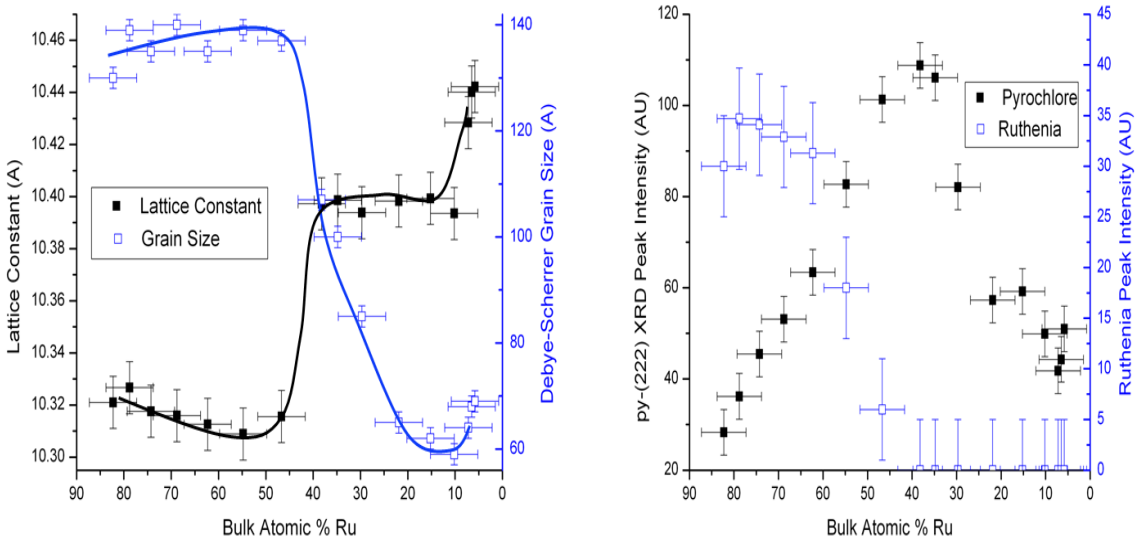

Figure 84. XRD data on the binary pyrochlore with lattice parameter/grain size in a) and pyrochlore/ruthenia peak intensity in b). Filled squares correspond to left ordinate.

SEM pictures (Figure 86) confirmed what was hypothesized from XRD and other data. Above 50% bulk Ru, RuO_2 precipitated out. Since Ruthenia is one of the more active oxides with a free energy of formation at 575°C of -29.5 KJ/mol, it quickly crystallized, using up oxygen that may have gone into the pyrochlore formation. In essence, it may have been acting as a localized 'getterer' for oxygen. Above 50% bulk Pb, surface PbO with a free energy of formation in the -204 KJ/mol likely nucleated. The PbO was dissolved out from the Nitric acid wash before this characterization, leaving the more resistant pyrochlore surface, which had a constant 50/50 surface ratio of Pb/Ru for the fluorescence test.

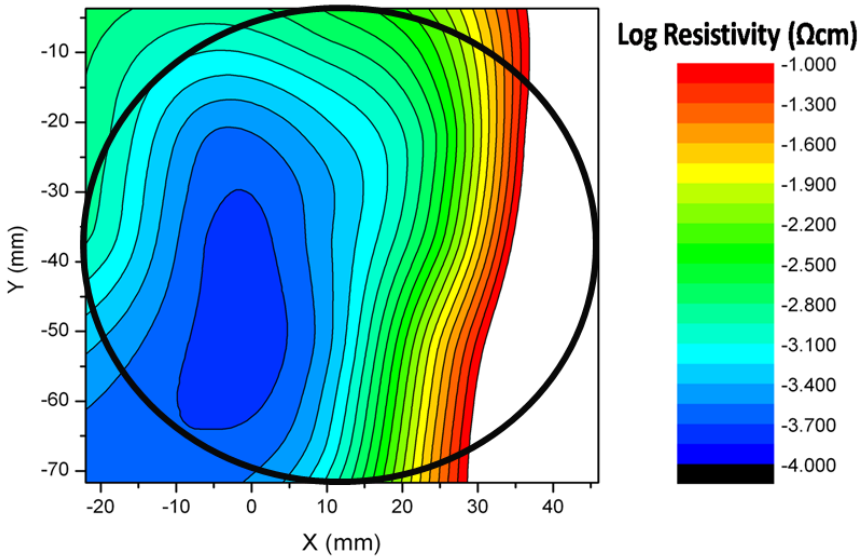

Figure 85. Evidence for the $Pb_2(Ru_{2-x}Pb_x)O_6$ structure at Ru percentages from 45-60%, from the correlation consistent with Pb-substitution and b) resitivity.

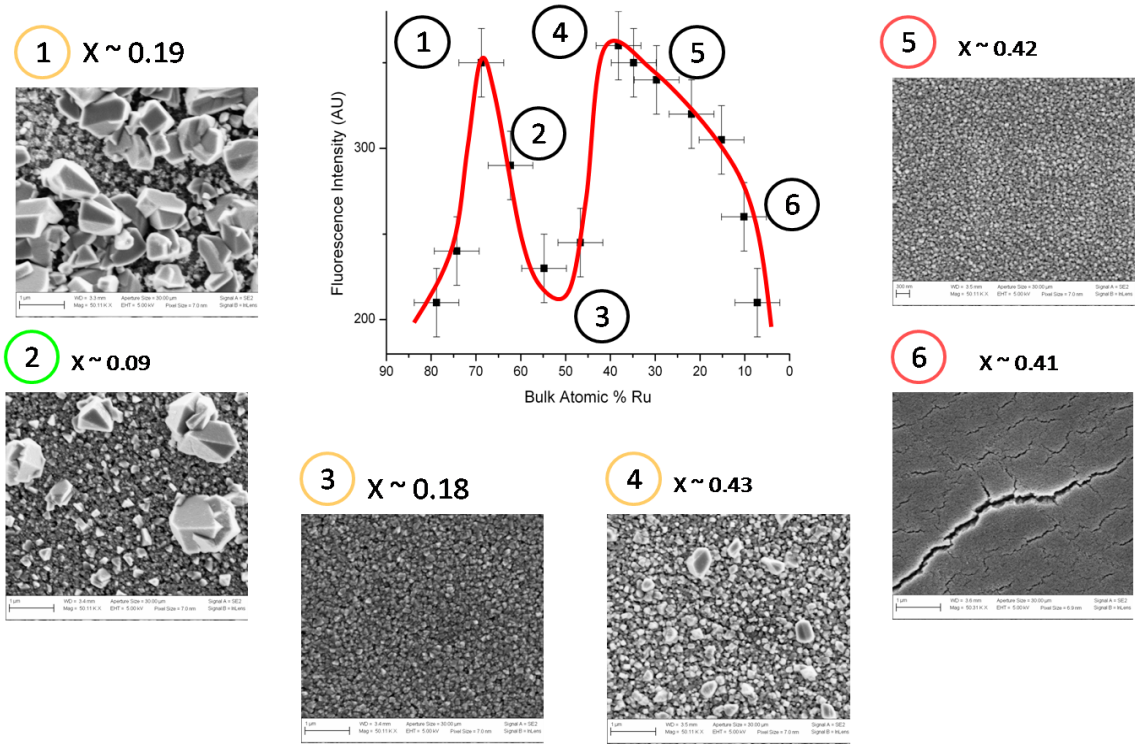

Figure 86. SEM pictures of the pyrochlore at a 50,000x magnification. X-values represent the extra Pb doping in $Pb_2(Ru2\text{-}xPbx)O_{1\text{-}y}$.

When analyzing the XPS in Figure 87, one could quantitatively see what the SEM and XRD analysis had shown. At the pyrochlore surface, unstable lead leached out to form a stable 50% Pb and Ru surface. Before ~45% Ru, the O 1s peak compatible with RuO_2 (529.2 eV) dominated. In the pre-tested film after 45% Ru, the majority O 1s peak corresponded to PbO/PbO2 (~528.8 ev). However, the post-tested film had its largest O 1s peak at approximately 530 eV, which previous studies have associated with a $Pb_2(Ru_{2-x}Pb_x)O_{6.5}$ surface [150]. The higher binding energy could have been due to the lower shielding afforded by the more asymmetric Pb-O_b-Ru bond as electron density was shifted to the Ru atom. Below 20% Ru, the principal peak value shifted closer to 531.5 eV, a sign of $PbSO_4$ formation from either sulfate or sulfuric acid. The film surface appeared to have excess oxygen where there should have been vacancies in the 60-45% Ru non-catalytic region. This was likely due to adsorbed water at acidic pH interfering with the ORR displacement reaction.

In Figure 88, the surface Ru^{+4}/Ru^{+5} ratio reached a minimum of ~0.5 at ~38% bulk Ru before rising with again with either more or less Ru. The correlation to the high activity region seemed to imply that this couple was important to the ORR. The Pb^{+4}/Pb^{+2} ratio also fell to ~1.0 at 39% bulk Ru. It remained at this level as the amount of Pb increased, suggesting a role in the ORR below ~38% bulk Ru. As discussed in the theory section, the two major options for catalytic sites were Pb-O and Pb-O-Ru, with some protonation. Both oxidation couples dropped to minimums ~38% bulk Ru, but only the Ru couple changed with greater bulk Pb. Since the high ORR activity also changed, this activity was more likely due to the site involving Ru, Pb-O-Ru. Enhanced ORR may have occurred through the Pb-O site below 38% Ru, as suggested by the gradual decline in fluorescence to ~15% bulk Ru. The Pb^{+4}/Pb^{+2} couple also appeared to decrease at ~75% Ru, suggesting enhanced ORR from Pb-O sites. A

possible rationale was that there was just enough Ru to grow into large RuO_2 particles but not enough RuO_2 to cover free Pb-O sites.

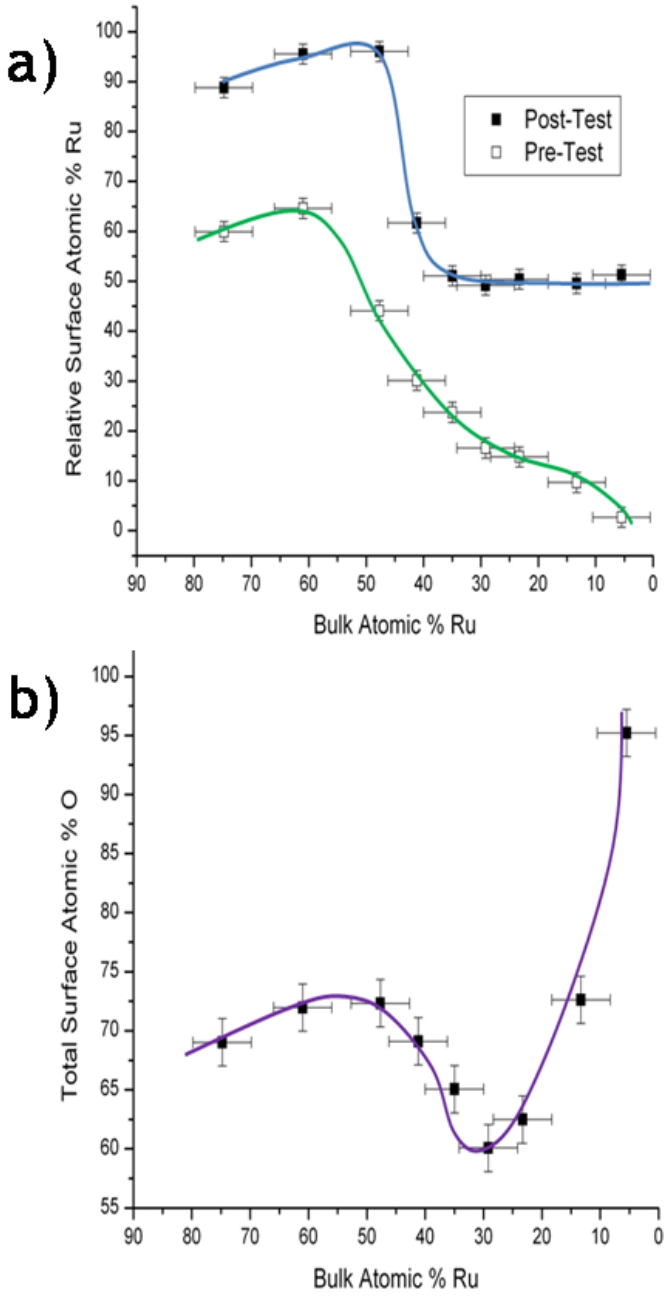

Figure 87. XPS measurements of a) relative Ru surface concentration and b) total O surface concentration after solution testing.

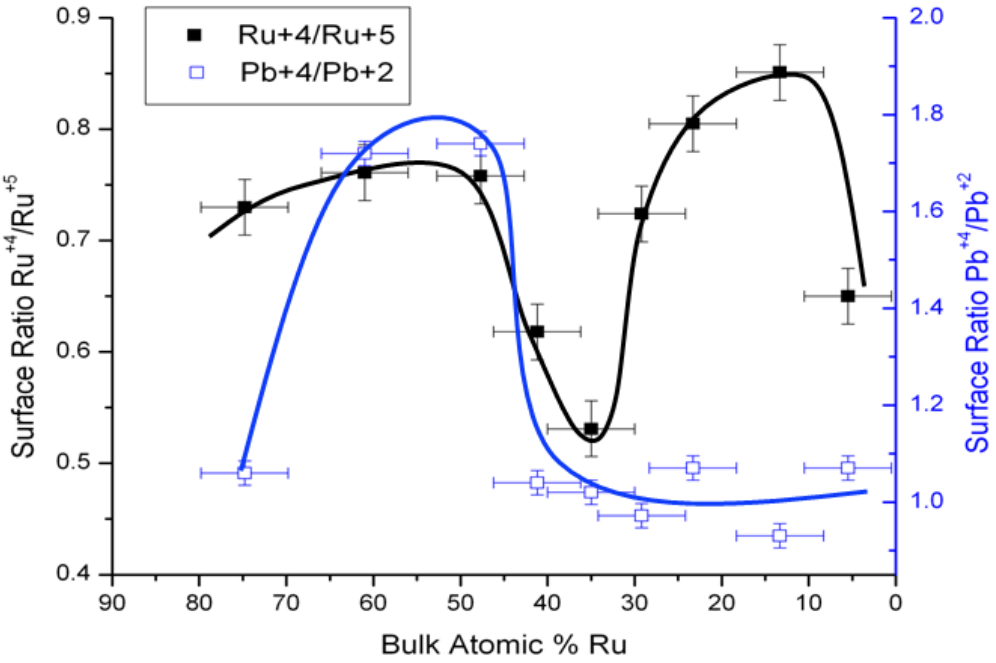

Figure 88. XPS measurement of cation valence coupling after solution testing. The low Ru^{4+}/Ru^{+5} ratio at the highly active catalyst composition supports the notion of the Pb-O-Ru bond. Filled squares correspond to left ordinate.

Raman characterization was used to determine bonding strengths and intensities in active pyrochlore sites. Scans such as the one in Figure 89a) could identify at least 3 main peaks ~137-145 cm^{-1}, 247-253 cm^{-1}, and 669-675 cm^{-1}, belonging respectively to the O-Pb-O bending, Pb-O' stretching, and Ru-O stretching phonons. The first peak was related to Pb replacing Ru in a B-site to form the Pb-O_b-Ru catalytic site. A weaker Pb-O_b bond implied easier displacement of the O_bH hydroxide from Pb-O_b-Ru in the dissociation reaction. To determine the strength of the Pb-O_b bond, the O-Pb-O bending peak was mapped onto the composition spread wafer. Much like a 'taut string', a higher wavenumber implied a stronger bond, higher energy bond, and vice versa for a lower wavenumber. In the ~38% bulk Ru region, the wavenumber was ~141 cm^{-1}. Above 38% Ru, it had a larger wavenumber, or stronger,

less Pb-O_b bond, increasing the energy needed for the displacement reaction. Below ~38% bulk Ru, the wavenumber and reactivity decreased. This may have been due to either a dearth of pyrochlore or a Pb-O_b bond that was so weak that the Pb-O_b-Ru was essentially an O_b-Ru site with a strongly bound O_bH.

When comparing the cyclic voltammograms in Figure 90 of the two most active sites in aerated sulfate solutions at a pH both above and below the PZC of Pb-O_b-Ru (pH~2), a few differences were apparent. First, the $Ru^{+2/+3}$ oxidation peak ~400 mV was similar at the two different pH's the 75% Ru region but different in the 38% Ru region. For Ru to oxidize to a higher state and conserve charge at the surface, the oxide had to release H^+ into the solution. Above a pH ~ 2, the main source of protons from the pyrochlore should have been from Pb-0_tH as Pb-O_b-Ru was deprotonated. Below pH~2, the main source of protons for the pyrochlore should have been from the more acidic O_b in Pb- O_bH-Ru. Since the 38% Ru was the only point that changed intensities to the more acidic O_bH site, this, and not 75% Ru, appeared to be the site with catalytic Pb-O_bH-Ru. The ORR currents of the two points appeared about equal for the pH = 5.6 solution, but the 38% Ru point had a dramatically higher onset potential at pH = 1. Again, this pointed to the continued protonation and activation of the asymmetric Pb-O_bH-Ru site for the 38% Ru in increasingly acidic solutions. The 75% Ru site had a much lower onset potential at a acidic enough pH that the other catalytic site Pb_t-O was likely fully protonated to Pb_t-OH_2 and not particularly active to the displacement reaction. This low onset potential could then be attributed to some RuO_2-based oxygen reduction that was not significantly catalytic for the ORR

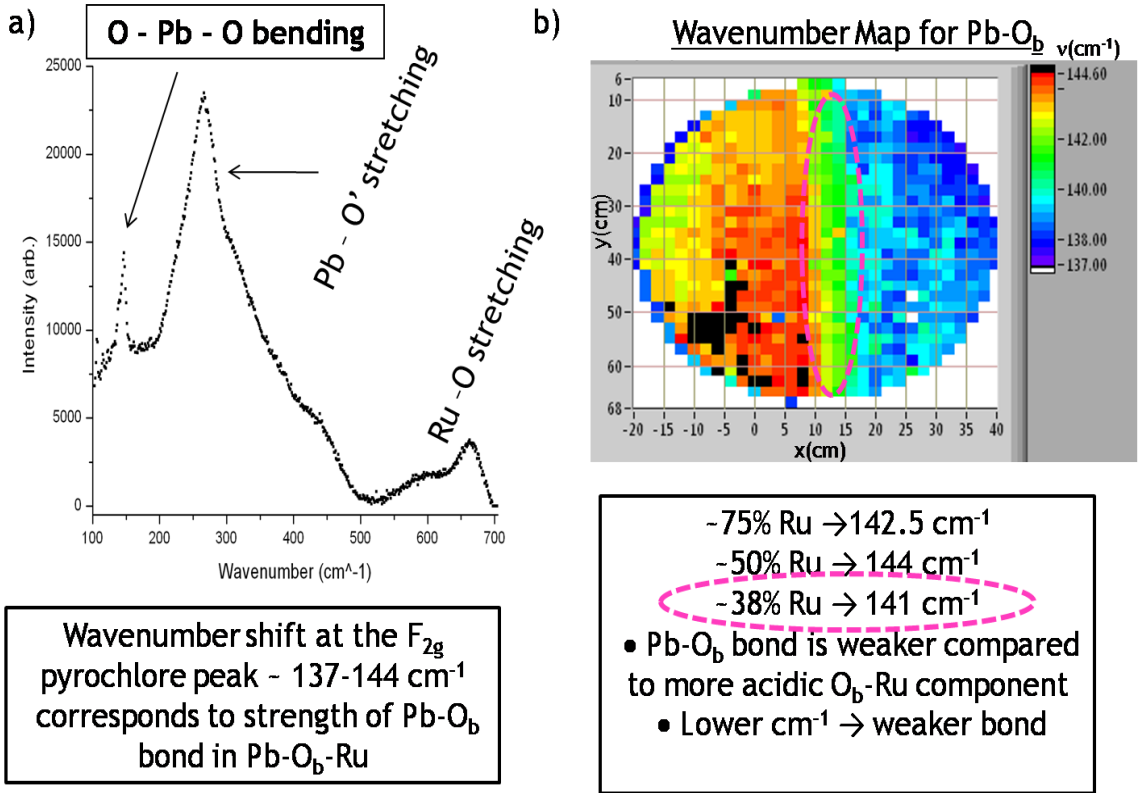

Figure 89. Raman characterization of Pb-Ru pyrochlore showing an a) generic scan from 100 cm^{-1} to 700 cm^{-1} and b) a wavenumber map of the Pb-O_b bend from the Pb-O_b-Ru catalytic site.

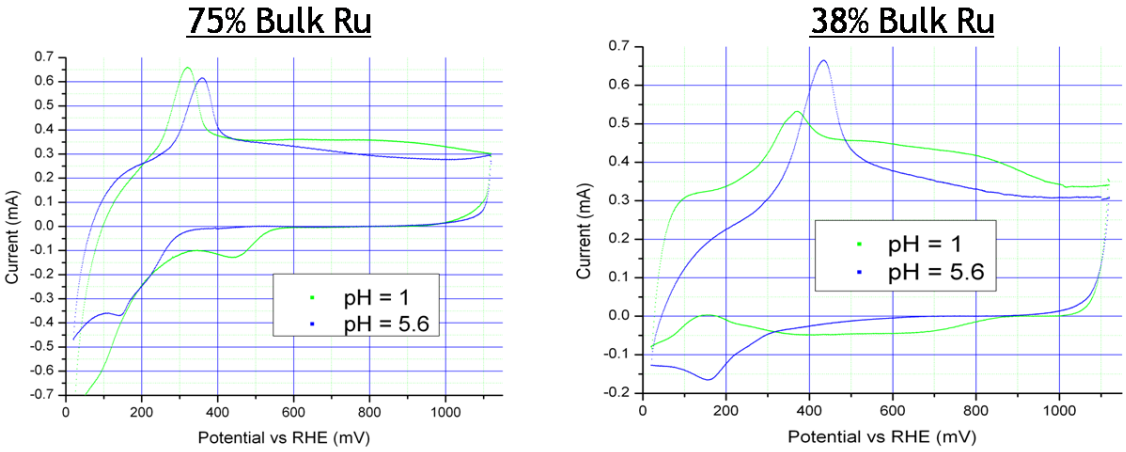

Figure 90. Cyclic voltammograms of Pb-Ru spreads at 75% and 38% bulk Ru in pH = 1 and 5.6 aerated sulfate solutions.

5.10 Pb-Ru-Pd Ternary Pyrochlore

While the binary pyrochlore approaches the activity of Pt, it would be desirable to increase that level even higher through doping either the A or B-site with a third cation. The difference in reduction potential and/or valency has been thought to stimulate charge transfer in metal electrodes [151]. Other groups have doped various 3d transition metal elements and Lanthanides into the Pb-Ru pyrochlores, with mixed results that have not been sufficiently explained [152-154]. This cation would have to satisfy mass, site, and charge balance rules unique to different processing conditions as well as the pyrochlore itself [155]. A high-throughput way to approach this process was to pick elements with similar ionic radii to the A and B sites that had some degree of multi-valency. While the early transition metals Mn, Co, and Cr showed some promise, the highest recorded pyrochlore potential was obtained on a Pb-Ru-Pd composition spread.

In the Figure 91, the greatest activity occurred over a bulk range of 52-56% Pb, 22-32% Ru, and 30-14% Pd. These bulk values translated into a surface concentration that approximated 25% Pb, 50% Ru, and 25% Pd. As ascertained from the Pb-Ru spread, this 50% Ru concentration at bulk Ru levels below 70% was essential because of the Pb-O_bH-Ru mechanism for the initial hydroxide displacement reaction. Instead of substituting in the place of Ru on the surface, the highest activity occurred on replacing the Pb. This makes phenomenological sense when it is considered they both share the +2/+4 couple reaction and that the size of the tetravalent Pd cation is only 0.62 Å, much closer to that of the Ru cation than the .77 Å of Pb.

As can be seen in the XRD data in Figure 92, there was some concern with $PbPdO_2$ precipitating out of the oxide. To test whether it itself was involved in any catalysis, a thin film nanoparticular Pb-Pd spread was sputtered onto a RuO_2 substrate

with little catalytic results. As such, the Pb-Pd oxide most likely blocked the more active pyrochlore from reactants for the ORR. A decrease in the lattice parameter at the most active site seemed to confirm that Pd^{+4} was substituting for Pb^{+4} over a certain compositional range. From ~10 - 25% Pd in Figure 93, the lattice constant of the pyrochlore was ~10.36 compared to the usual 10.40 Å for the binary Pb-Ru pyrochlore. Since the +4 state of both Ru and Pd had a radius of about .62 Å while that of Pb was .775 Å, the only way the lattice constant could have decreased that much was for Pd to replace Pb in the B-site of the pyrochlore. With either more or less Pd, its lattice constant trended upwards towards the 10.40 Å seen in the binary Pb-Ru defect pyrochlore. The intensity of the (222) peak implied that more binary pyrochlore was forming with Pd below ~10% and that less pyrochlore was forming above ~25% Pd; most likely, it was incorporated in the growing $PbPdO_2$ seen in the XRD peaks.

By examining the composition spread in Figure 94 for the O-Pb-O bending peak at ~137-145 cm^{-1}, the optimal Pb-O_b binding strength at ~141 cm^{-1} was found in the same 10-25% Pd location where the ORR activity was highest. Above ~25% Pd, the wavenumber shifted to greater than 146 cm^{-1}, implying that O-Pb-O with a stronger Pb-O bond was being included in some other structure, possibly $PbPdO_2$. With Pd reacting less strongly than Ru to oxygen (hence the Pd alloy catalysts in the previous section), a less asymmetric bond between Pb on one side of an oxygen and Pd on the other was probable. The moderately fluorescent active area in the Ru-rich region had a similar ~144 cm^{-1} to the 75 % bulk Ru in the binary, suggesting the same mixture of RuO_2 and PbO.

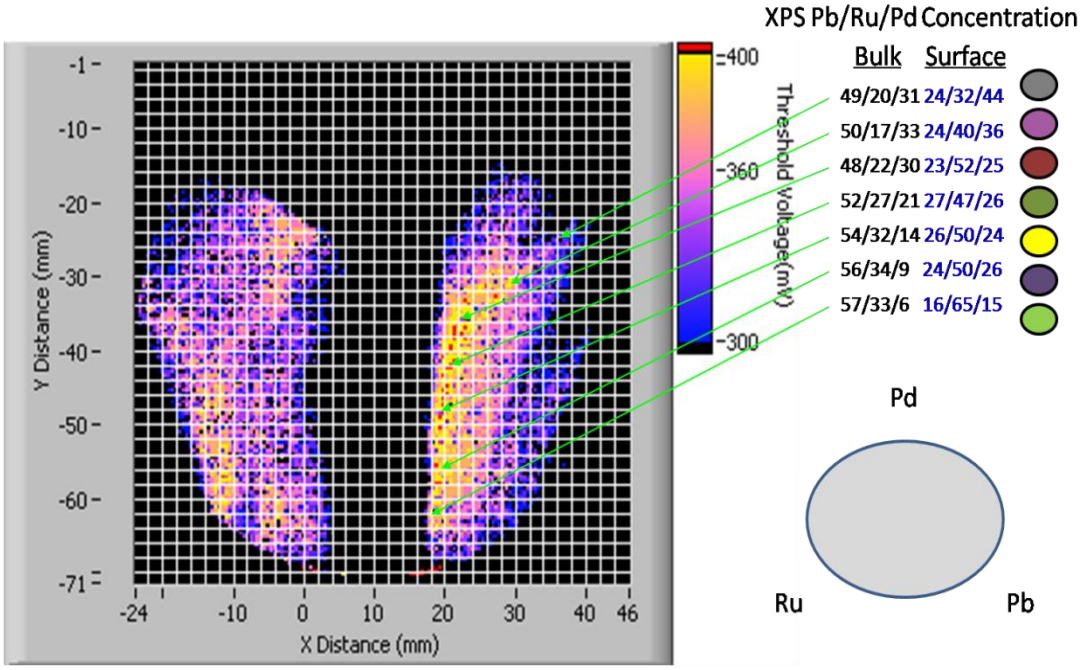

Figure 91. Fluorescent map of the Pb-Ru-Pd oxide spread along with surface and bulk compositions.

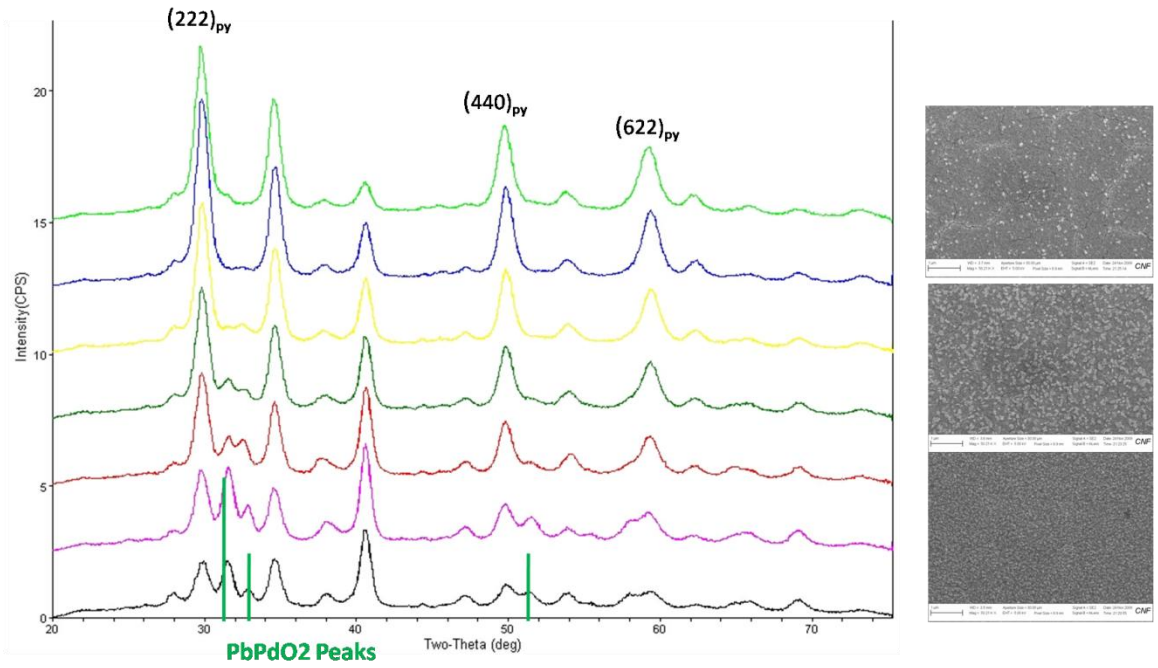

Figure 92. XRD of points color-coded to their compositions in the previous figure. Representative SEM picture of the surface at 50000x are included.

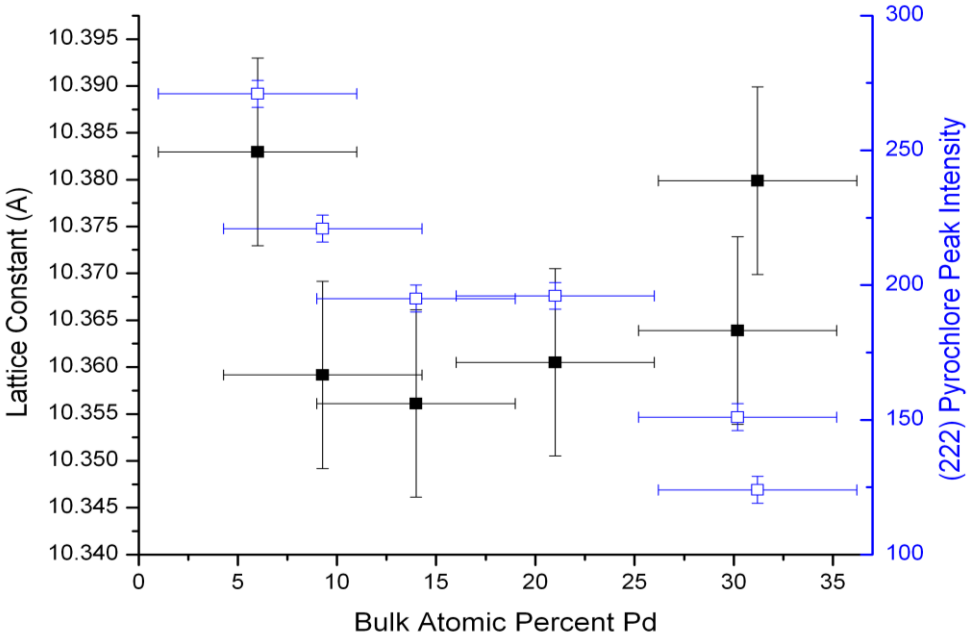

Figure 93. Lattice Parameter change as substitute smaller Pd cation into pyrochlore. Filled squares correspond to left ordinate.

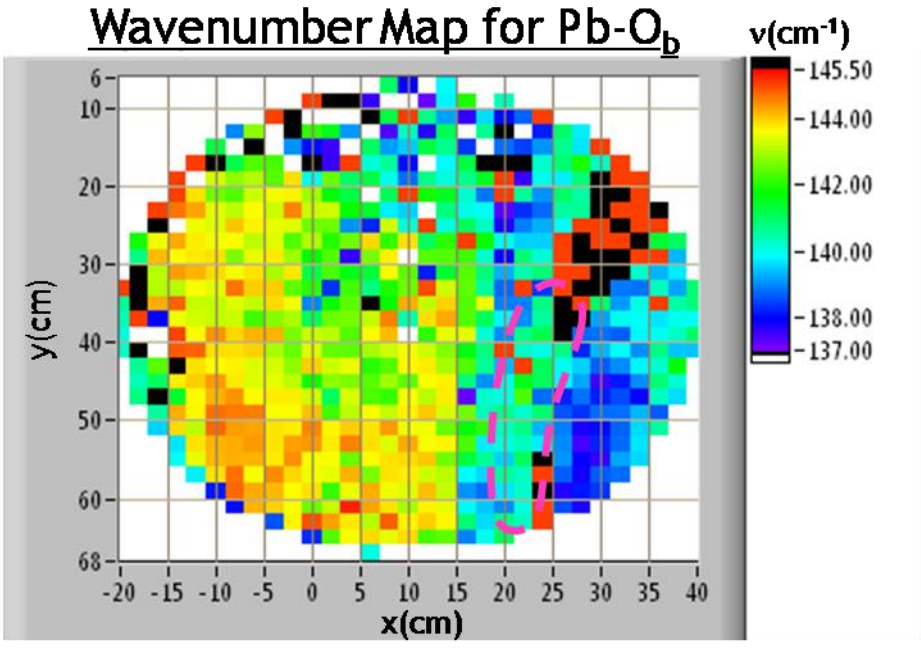

Figure 94. Raman characterization of Pb-Ru-Pd pyrochlore showing a wavenumber map of the Pb-O_b bend from the Pb-Ob-Ru catalytic site. Dashed purple line in bottom right corner of wafer shows region with high fluorescent onset potential.

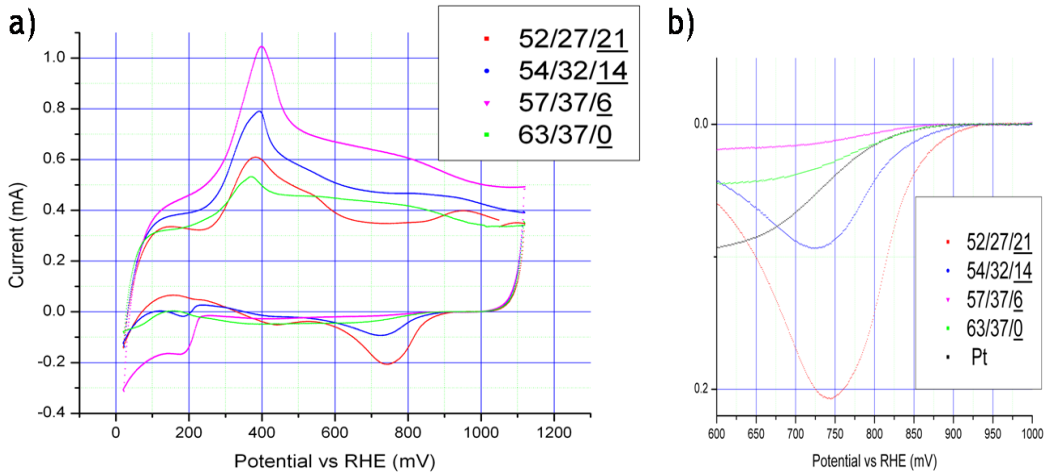

Figure 95. Cyclic voltammograms of Pb-Ru-Pd spreads in their a) entirety and b) focused on the potential region of ORR in aerated 0.05 M sulfuric acid.

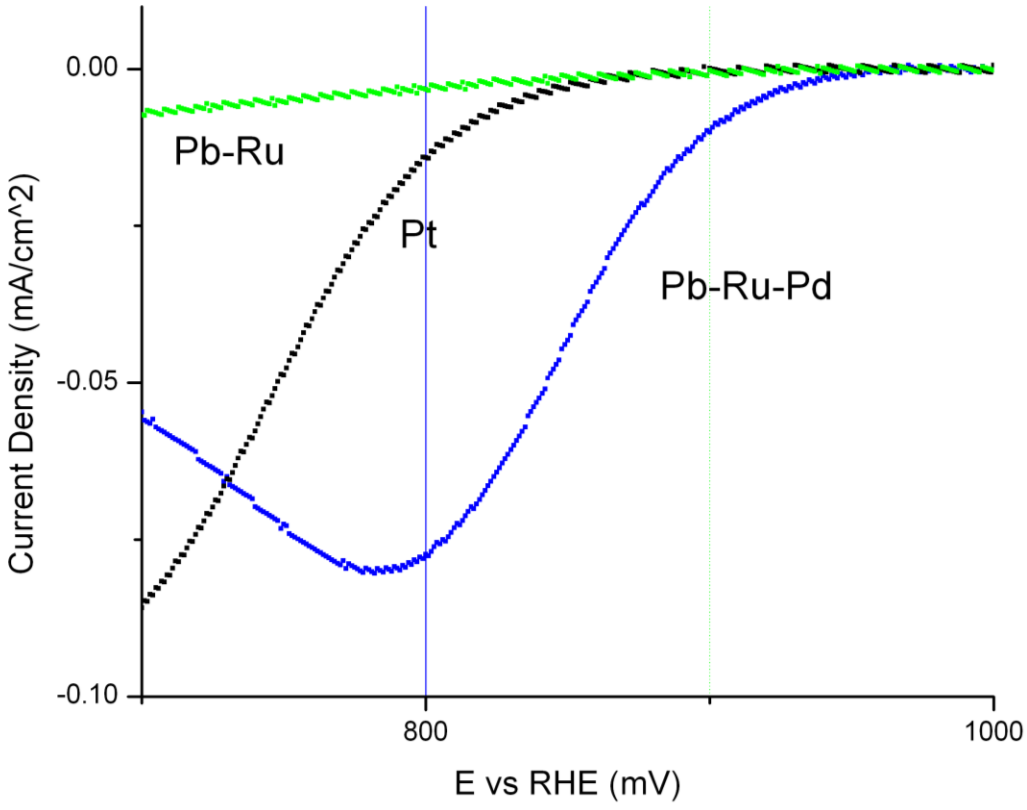

Figure 96. Cyclic voltammetry comparing the most active Pb-Ru pyrochlore and ternary Pb-Ru-Pd pyrochlore to Pt in aerated 0.05 M sulfuric acid.

The cyclic voltammograms (Figure 95) in aerated 0.05 M sulfuric acid confirmed the activity of the 10-25% Pd in Pb-Ru pyrochlore. Both the sites with 14% and 21% Pd had higher ORR onsets and activity at 850 mV vs. RHE. A $Pd^{0/+2}$ oxidation peak began to appear near 1000 mV and a $Ru^{+3/+4}$ peak close to 550 mV with increasing Pd, suggesting Pd was involved in some redox reaction that may have been associated with the ORR. Interestingly, the acidity trend of the O_b from the $Ru^{+2/+3}$ couple at ~400 mV increased to its highest level when Pd was first added at 6% before declining again to the binary Pb-Ru level with increasing amounts of Pd. From the XPS, the Pb/Ru/Pd percentages at 6% bulk Pd were 16/65/15 while the surface percentages for the other two compositions were close to 25/50/25, implying excess RuO_2 at the 6% Pd which may have helped change the acidity. The acidity may have then decreased as more $PbPdO_2$ formed.

Similar results were given after the sample was kept in 1 M constantly-stirred Nitric Acid for 2 weeks, demonstrating a degree of robustness. In Figure 96, one of the ~20% Pd compositions is compared to both the optimal binary Pb-Ru pyrochlore and Pt potential sweeps in aerated 0.05 M H_2SO_4, demonstrating its high ORR activity. The rationale behind the increased activity remains unknown. Possible explanations include Pd replacing Pb to form Pd-O_b-Ru. Once the initial O_b bond was broken, both the free Pd and Ru might have been able to break the O-O bond of either two superoxides through Griffiths ‘side-on’ adsorption or one from Yeager ‘bridging’ adsorption. However, this still does not explain the importance of Pb on the surface to form a 25/50/25 Pb/Ru/Pd ratio. The Ru-Pd, Pb-Pd, and Pb-Ru rich oxide regions were all reasonably conductive but not particularly catalytic – what was it about all three elements that increased the ORR activity? Further research in this area is required to determine this.

CHAPTER 6

6 CONCLUSIONS

Room temperature PEM fuel cells may yet prove essential as energy storage systems. In order bring this about, efficiencies must be increased and materials expense reduced. Pt has been the prevalent cathode for the past 150 years. Due to its prohibitive cost, tendency for poisoning, and high overpotential from kinetic limitations, Pt is not the ideal cathode in PEM fuel cells. This study has explored the possibility of replacing Pt as the cathodic material with other metallic alloys and oxides, most noticeably that of Pd. It is at least four times less expensive and has a much lower tendency towards poisoning. However, it has an even higher cathodic overpotential to the oxygen reduction reaction (ORR) due to anion species (e.g. OH) blocking catalytic sites.

To examine ORR catalyst candidates, sputtered composition spreads of up to 3 elements were able to cover large portions of binary and ternary phase diagrams. These were examined for ORR activity by the integrative fluorescence of umbelliferone dye under UVA as the applied voltage was swept downward in an aerated 0.1 M sulfate solution. Since the umbelliferone's fluorescence intensity increased with pH from localized ORR on the film, regions in the spread with high catalytic activity could be pinpointed by correlation with high onset potentials for fluorescence. These were further examined in a 1 cm diameter cell for ORR current density.

By alloying Pd with the more electronegative W in bulk $W_{10}Pd_{90}$, ligand effects on the d-band from 3-5% W trapped near the surface in a Pd skin/skeletal structure could decrease the oxygen binding energy. The result was fewer O species (e.g. OH)

bound too tightly to catalytic sites at high potentials, especially from the interaction of water (H_2O) with Pd. This was reflected in a lower overpotential, a higher fluorescent onset potential, and ORR current densities at 850 mV vs. RHE an order of magnitude greater than that of Pt in aerated 0.05 M H_2SO_4 acid. Increasing amounts of W could increase the kinetics of the rate-determining step (RDS) by increasing the oxygen bond-breaking of the superoxide (HO_2^-); however, these ligand effects also increased interaction with (bi)sulfate, raising the possibility of 2-electron peroxide production. The fluorescence test revealed the highest onset in W-Pd at Tafel slopes approximating the desired 4-electron production of H_2O, indicating a potential in this test to discriminate between the two main oxygen reduction pathways.

When a 3rd element with a radius smaller than Pd, such as V, was introduced into a bulk $W_{.06}V_{.06}Pd_{.88}$ alloy, compressive strains below 0.1% could increase the rate of superoxide O-O scission without large amounts of (bi)sulfate bonding. Current densities at 850 mV in the same sulfuric acid solution were approximately 30 times greater than that of pure Pt, with limited decreases in current density from the introduction of 0.1 M methanol. Too great a strain shifted the d-band center too far to optimally participate in the initial O_2 interaction, decreasing the rate of the RDS and the ORR. This balancing act of strain effects influenced the development of a novel binary composition/strain spread, which could predict what compositions and strains in other binary spreads could result in high ORR activities. From this, bulk ternary spreads of $W_{.03}V_{.20}Ir_{.77}$ and $Ta_{.12}Co_{.08}Au_{.80}$ were expected to be more catalytic to ORR than Pt at low overpotentials.

Certain concentrations of Pb-Ru pyrochlores were stable and catalytic towards oxygen reduction. $Pb_2(Ru_{1.5}Pb_{0.5})O_{6.5}$ was found to be comparable to Pt as a catalyst at low overpotentials. This defect pyrochlore had Pb^{+4} substituted into Ru^{+4} sites to form a conductive oxide with 50% Pb and 50% Ru on the surface. The displacement

of O_bH, bounded by asymmetric bonding between Pb and Ru (i.e. Pb-O_bH-Ru), for a superoxide was the most likely RDS on the catalytic pyrochlore. By substituting Pd into the Pb^{+4} B-sites of the structure, an even higher catalytic activity was seen, although the rationale behind this remains unclear. A comparison of the most active catalysts discovered in this study is seen in Figure 97.

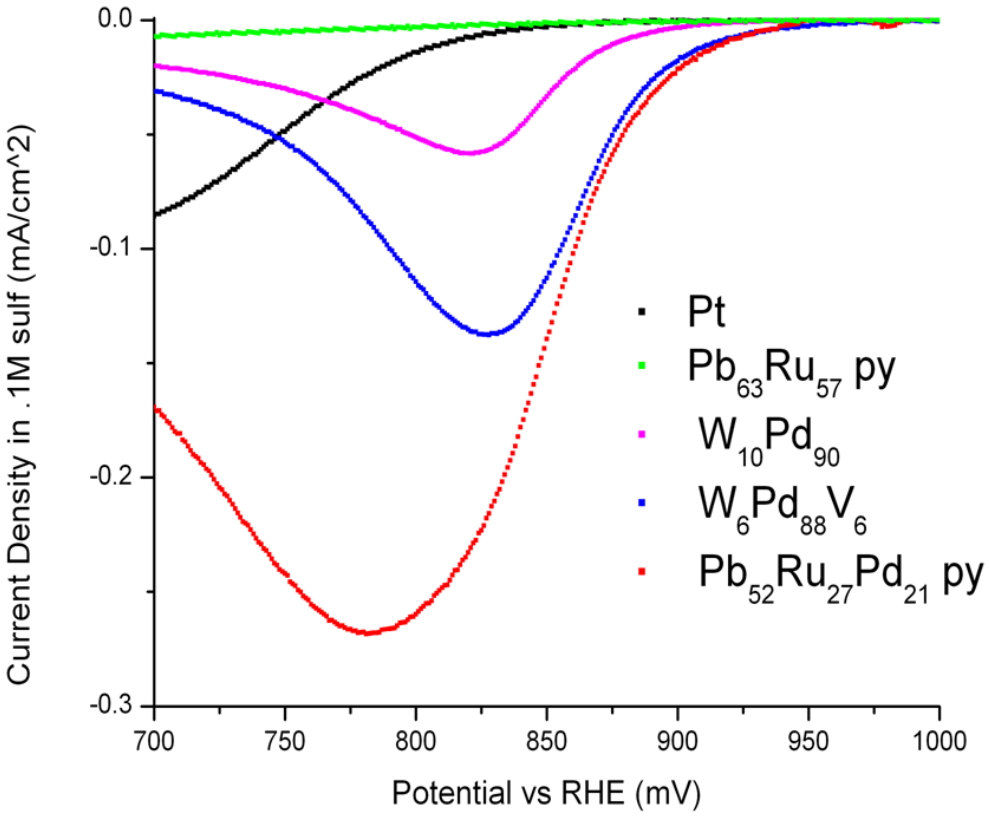

Figure 97. Materials with the highest ORR activity discovered by combinatorial synthesis. Current densities in aerated 0.05 M sulfuric acid valid for relative comparison only.

6.1 Future Work

The following steps could provide further information related to this study:

1) Glancing-angle XRD studies on PGM alloy thin films would determine if the lattice strain in the bulk is indeed transferred to the surface.
2) Rotating ring-disk electrode (RRDE) studies on conductive leads (e.g. TiN or C) could clarify the kinetics and number of electrons involved in the ORR reaction. This would include an estimate of any possible peroxide produced through the 2-electron ORR process. Based on preliminary information, it is believed that significant peroxide may be generated at bulk atomic percentages of W greater than 10%.
3) Simple computer modeling (such as VASP) may provide additional evidence to support the alloying models proposed.
4) Continued sputtering on Ir, Au, Ru, and other PGM-based alloys scanned with the binary composition/strain maps could identify new catalytic materials.
5) The sputtered texture appeared to have some influence on the catalytic properties of Pd. The author noted that he was able to lock-in certain textures by reactive oxide sputtering to form PdO_{2-x} at an angle to the substrate before post-processing reduction back towards the pure metal. Perhaps this could be used to study different facets of Pd.
6) A combinatorial exploration of carbides and nitrides that shift the d-band of other transition metals may prove fruitful. The author has found interesting effects concerning both the electron-donating inside and electron-withdrawing outside of a CNT.
7) Application on the nanoscale (e.g. strained W-Pd nanoparticles) may also increase the reactivity through surface area augmentation. In addition to

studies done by Mark Dreibelbis, recently published work has shown promise [156].

8) More study of Pd in Pb-Ru pyrochlore could provide insight into a new class of highly catalytic pyrochlores that are stable in acidic solutions. Other 3rd elements that provided high fluorescent onsets in near-neutral pH include Cr, Mo, and Sb.
9) A high-throughput technique to discover stable catalysts at lower acidities than pH ~ 6 would be useful. It may not make a significant different in noble metals (e.g. Pt and Pd), but certainly does when examining oxides where the point of zero charge has a noticeable effect on surface adsorbates.
10) The study has concerned catalyst primarily in acidic solutions. More basic solutions may yield further new catalysts (e.g. spinels and perovskites).

Nevertheless, this innovative combinatorial sputtering/optical screening technique to uncover previously unknown ORR catalysts has and will remain ready ‘to strive, to seek, to find, and not to yield’ [157].

REFERENCES

1. Heinlein, R.A., *Friday*. 1st ed. 1982, New York: Holt, Rinehart and Winston. 368 p.

2. Winter, M. and R.J. Brodd, *What are batteries, fuel cells, and supercapacitors? (vol 104, pg 4245, 2003).* Chemical Reviews, 2005. **105**(3): p. 1021-1021.

3. Jarvis, L.P., T.B. Atwater, and P. J. Cygan, *Fuel cell/electrochemical capacitor hybrid for intermittent high power applications.* Journal of Power Sources, 1999. **79**(1): p. 60-63.

4. Grove, W., *On the Gas Voltaic Battery.* Philosophical Magazine and Journal of Science, 1843. **24**: p. 276.

5. Borroni-Bird, C.E. *Fuel cell commercialization issues for light-duty vehicle applications*. 1996. Switzerland: Elsevier.

6. Prochaska, M.D., *Use of combinatorial search for the discovery of new fuel cell anode electrocatalysts*. 2007.

7. Gasteiger, H.A., et al., *Activity benchmarks and requirements for Pt, Pt-alloy, and non-Pt oxygen reduction catalysts for PEMFCs.* Applied Catalysis B-Environmental, 2005. **56**(1-2): p. 9-35.

8. Mukerjee, S. and S. Srinivasan, *Enhanced electrocatalysis of oxygen reduction on platinum alloys in proton exchange membrane fuel cells.* Journal of Electroanalytical Chemistry, 1993. **357**(1-2): p. 201-224.

9. Toda, T., et al., *Enhancement of the Electroreduction of Oxygen on Pt Alloys with Fe, Ni, and Co.* Journal of The Electrochemical Society, 1999. **146**(10): p. 3750-3756.

10. Markovic, N., H. Gasteiger, and P.N. Ross, *Kinetics of Oxygen Reduction on Pt(hkl) Electrodes: Implications for the Crystallite Size Effect with Supported Pt Electrocatalysts.* Journal of The Electrochemical Society, 1997. **144**(5): p. 1591-1597.

11. Paulus, U.A., et al., *Oxygen reduction on high surface area Pt-based alloy catalysts in comparison to well defined smooth bulk alloy electrodes.* Electrochimica Acta, 2002. **47**(22-23): p. 3787-3798.

12. Castro Luna, A., et al., *Pt–Fe cathode catalysts to improve the oxygen reduction reaction and methanol tolerance in direct methanol fuel cells.* Journal of Solid State Electrochemistry, 2008. **12**(5): p. 643-649.

13. Shukla, A.K., et al., *Carbon-supported Pt-Fe alloy as a methanol-resistant oxygen-reduction catalyst for direct methanol fuel cells.* Journal of Electroanalytical Chemistry, 2004. **563**(2): p. 181-90.

14. Paulus, U.A., et al., *Oxygen Reduction on Carbon-Supported Ptâˆ’Ni and Ptâˆ’Co Alloy Catalysts.* The Journal of Physical Chemistry B, 2002. **106**(16): p. 4181-4191.

15. Neergat, M., A.K. Shukla, and K.S. Gandhi, *Platinum-based Alloys as oxygen-reduction Catalysts for Solid-Polymer-Electrolyte Direct Methanol Fuel Cells.* Journal of Applied Electrochemistry, 2001. **31**: p. 373-378.

16. Salgado, J.R.C., E. Antolini, and E.R. Gonzalez, *Carbon supported Pt-Co alloys as methanol-resistant oxygen-reduction electrocatalysts for direct methanol fuel cells.* Applied Catalysis B: Environmental, 2005. **57**(4): p. 283-290.

17. Jalan, V. and E.J. Taylor, *Important of interatomic spacing in catalytic reduction of oxygen in phosphoric-acid.* Journal of The Electrochemical Society, 1983. **130**(11): p. 2299-2301.

18. Paffett, M.T. and S. Gottesfeld, *Dealloying of Pt alloy fuel-cell electrocatalysts.* Journal of The Electrochemical Society, 1988. **135**(8): p. C348-C348.

19. Stamenkovic, V.R., et al., *Trends in electrocatalysis on extended and nanoscale Pt-bimetallic alloy surfaces.* Nat Mater, 2007. **6**(3): p. 241-247.

20. Mukerjee, S., et al., *Role of Structural and Electronic Properties of Pt and Pt Alloys on Electrocatalysis of Oxygen Reduction.* Journal of The Electrochemical Society, 1995. **142**(5): p. 1409-1422.

21. Vukmirovic, M.B., et al., *Platinum monolayer electrocatalysts for oxygen reduction.* Electrochimica Acta, 2007. **52**(6): p. 2257-2263.

22. Heck, R.M., R.J. Farrauto, and S.T. Gulati, *Catalytic air pollution control : commercial technology*. 3rd ed. 2009, Hoboken, N.J.: John Wiley. xxi, 522 p.

23. Li, H., et al., *Design and Preparation of Highly Active Pt-'Pd/C Catalyst for the Oxygen Reduction Reaction.* The Journal of Physical Chemistry C, 2007. **111**(15): p. 5605-5617.

24. Wang, B., *Recent development of non-platinum catalysts for oxygen reduction reaction.* Journal of Power Sources, 2005. **152**: p. 1-15.

25. Shao, M., et al., *Origin of Enhanced Activity in Palladium Alloy Electrocatalysts for Oxygen Reduction Reactionâ€* The Journal of Physical Chemistry B, 2007. **111**(24): p. 6772-6775.

26. Tarasevich, M., et al., *Development of platinum-free catalyst and catalyst with low platinum content for cathodic oxygen reduction in acidic electrolytes.* Journal of Applied Electrochemistry, 2007. **37**(12): p. 1503-1513.

27. Raghuveer, V., A. Manthiram, and A.J. Bard, *Pd-Co-Mo electrocatalyst for the oxygen reduction reaction in proton exchange membrane fuel cells.* Journal of Physical Chemistry B, 2005. **109**(48): p. 22909-12.

28. Fernandez, J.L., D.A. Walsh, and A.J. Bard, *Thermodynamic guidelines for the design of bimetallic catalysts for oxygen electroreduction and rapid screening by scanning electrochemical microscopy. M-Co (M: Pd, Ag, Au).* Journal of the American Chemical Society, 2005. **127**(1): p. 357-365.

29. Jonhson-Matthey, *The Platinum Metals Report*. 2010: London.

30. Pourbaix, M.J.N., J.V. Muylder, and N. de Zoubov, *Electrochemical Properties of the Platinum Metals.* Platinum Metals Review, 1959. **3**(2): p. 47-53.

31. Hibbert, D.B. and A.C.C. Tseung, *Homomolecular Oxygen Exchange and the Electrochemical Reduction of Oxygen on Semiconducting Oxides.* Journal of The Electrochemical Society, 1978. **125**(1): p. 74-78.

32. Nemudry, A., P. Rudolf, and R. Schöllhorn, *Room temperature topotactic oxidation of lanthanum cobalt oxide La2CoO4.0.* Solid State Ionics, 1998. **109**(3-4): p. 213-222.

33. Hayashi, M., et al., *Electrochemical oxygen reduction properties of perovskite-type oxides La(1-x)A(x)MnO(3) (A = Na, K, Rb) in concentrated alkaline solution.* Electrochemistry, 2000. **68**(2): p. 112-118.

34. Horowitz, H.S., J.M. Longo, and J.T. Lewandowski, *Method of making lead-rich and bismuth-rich pyrochlore compounds using an alkaline medium*, USPTO, Editor. 1978, Exxon Research & Engineering Co.: USA.

35. Horowitz, H.S., J.M. Longo, and H.H. Horowitz, *Oxygen Electrocatalysis on Some Oxide Pyrochlores.* Journal of The Electrochemical Society, 1983. **130**(9): p. 1851-1859.

36. Goodenough, J.B., R. Manoharan, and M. Paranthaman, *Surface protonation and electrochemical activity of oxides in aqueous solution.* Journal of the American Chemical Society, 1990. **112**(6): p. 2076-2082.

37. Zen, J.M., R. Manoharan, and J.B. Goodenough, *Oxygen reduction on Ru-oxide pyrochlores bonded to a proton-exchange membrane.* Journal of Applied Electrochemistry, 1992. **22**(2): p. 140-150.

38. Raghuveer, V. and B. Viswanathan, *Nanocrystalline pyrochlore bonded to proton exchange membrane electrolyte as electrode material for oxygen reduction.* Journal of Materials Science, 2005. **40**(23): p. 6249-6255.

39. Yoshihara, K., et al., *Ionic Conductors and Battery Related Materials - Effects of the Substitution of the B-Site Ion on Oxygen Reduction Electrode Properties of the Pyrochlore $Pb_2Ru_2O_{7-y}$ at Low Temperatures.* Key engineering materials., 2006. **320**: p. 235.

40. Kawai, H., et al., *Oxygen Reduction Reaction Activity of Pyrochlore Oxide Electrocatalysts Prepared by Precipitation Method.* Key Engineering Materials., 2010. **421-422**: p. 479-482.

41. Bezerra, C.W.B., et al., *A review of Fe-N/C and Co-N/C catalysts for the oxygen reduction reaction.* Electrochimica Acta, 2008. **53**(15): p. 4937-4951.

42. Lefevre, M., J.P. Dodelet, and P. Bertrand, *Molecular oxygen reduction in PEM fuel cell conditions: ToF-SIMS analysis of Co-based electrocatalysts.* Journal of Physical Chemistry B, 2005. **109**(35): p. 16718-16724.

43. Nagai, M., M. Yoshida, and H. Tominaga, *Reprint of "Tungsten and nickel tungsten carbides as anode electrocatalysts".* Electrochimica Acta, 2007. **53**(2): p. 1030-1036.

44. Hsu, M.-F., et al., *Solid oxide fuel cell fabricated using all-perovskite materials.* Electrochemical and Solid-State Letters, 2006. **9**(4): p. A193-A195.

45. Kinoshita, K. and Electrochemical Society., *Electrochemical oxygen technology*. Electrochemical Society series. 1992, New York: Wiley. xiv, 431 p.

46. Sidik, R.A. and A.B. Anderson, *Density functional theory study of O2 electroreduction when bonded to a Pt dual site.* Journal of Electroanalytical Chemistry, 2002. **528**(1-2): p. 69-76.

47. Shao, M.H., et al., *Palladium Monolayer and Palladium Alloy Electrocatalysts for Oxygen Reduction* Langmuir, 2006. **22**(25): p. 10409-10415.

48. Hyman, M.P. and J.W. Medlin, *Mechanistic study of the electrochemical oxygen reduction reaction on Pt(111) using density functional theory.* Journal of Physical Chemistry B, 2006. **110**(31): p. 15338-15344.

49. Hyman, M.P. and J.W. Medlin, *Effects of Electronic Structure Modifications on the Adsorption of Oxygen Reduction Reaction Intermediates on Model Pt(111)-Alloy Surfaces.* The Journal of Physical Chemistry C, 2007. **111**(45): p. 17052-17060.

50. Hammer, B. and J.K. Norskov, *Theoretical Surface Science and Catalysis -- Calculations and Concepts.* Advances in catalysis., 2000. **45**: p. 71.

51. van Dover, R.B. and L.F. Schneemeyer, *The codeposited composition spread approach to high-throughput discovery/exploration of inorganic materials.* Macromolecular Rapid Communications, 2004. **25**(1): p. 150-157.

52. van Dover, R.B., L.F. Schneemeyer, and R.M. Fleming, *Discovery of a useful thin-film dielectric using a composition-spread approach.* Nature, 1998. **392**(6672): p. 162-164.

53. Löbel, R., et al., *Combinatorial fabrication and high-throughput characterization of a Ti-Ni-Cu shape memory thin film composition spread.* Materials Science and Engineering: A, 2008. **481-482**: p. 151-155.

54. Stuart, R.V., *Vacuum technology, thin films, and sputtering : an introduction*. 1983, New York: Academic Press.

55. Mahan, J.E., *Physical vapor deposition of thin films*. 2000, New York: Wiley. xiii, 312 p.

56. Ohring, M., *Materials science of thin films : deposition and structure*. 2002, San Diego, CA: Academic Press.

57. Downey, K.E., *A continuous composition spread approach to synthesizing and screening Er3+ oxide host materials suitable for use as planar optical amplifiers*. 2008.

58. Gregoire, J.M., et al., *Resputtering phenomena and determination of composition in codeposited films.* Physical Review B, 2007. **76**(19): p. 195437.

59. Hine, K., et al., *Experimental evaluation of MgO sputtering yields by monochromatic Ne, Kr, or Xe ion beams.* Thin Solid Films, 2008. **517**(2): p. 835-840.

60. Reddington, E., et al., *Combinatorial Electrochemistry: A Highly Parallel, Optical Screening Method for Discovery of Better Electrocatalysts.* Science, 1998. **280**(5370): p. 1735-1737.

61. Nizomov, N., et al., *Electronic structure and spectral fluorescence properties of umbelliferone and herniarin.* Journal of Applied Spectroscopy, 2007. **74**(5): p. 626-634.

62. Gregoire, J.M., et al., *High-Throughput Evaluation of Dealloyed Pt--Zn Composition-Spread Thin Film for Methanol-Oxidation Catalysis.* Journal of The Electrochemical Society, 2009. **156**(1): p. B160-B166.

63. Brace, K.M., et al., *A Parallel Optical Screen for the Rapid Combinatorial Electrochromic Analysis of Electrochemical Materials.* Advanced Materials, 2006. **18**(24): p. 3253-3257.

64. Perez, J., et al., *Application of the Flooded-Agglomerate Model to Study Oxygen Reduction on Thin Porous Coating Rotating Disk Electrode.* Journal of The Electrochemical Society, 1994. **141**(2): p. 431-436.

65. Antolini, E., et al., *Carbon supported PtCr alloys as oxygen-reduction catalysts for direct methanol fuel cells.* Journal of Applied Electrochemistry, 2006. **36**: p. 355-362.

66. Parthasarathy, A., et al., *Pressure Dependence of the Oxygen Reduction Reaction at the Platinum Microelectrode/Nafion Interface: Electrode Kinetics and Mass Transport.* Journal of The Electrochemical Society, 1992. **139**(10): p. 2856-2862.

67. Grochala, W. and P.P. Edwards, *Thermal Decomposition of the Non-Interstitial Hydrides for the Storage and Production of Hydrogen.* Chemical Reviews, 2004. **104**(3): p. 1283-1316.

68. Markovic, N.M., et al., *Oxygen reduction reaction on Pt(111): effects of bromide.* Journal of Electroanalytical Chemistry, 1999. **467**(1): p. 157-163.

69. Damjanovic, A., V. Brusic, and J.O.M. Bockris, *Mechanism of oxygen reduction related to electronic structure of gold-palladium alloy.* The Journal of Physical Chemistry, 1967. **71**(8): p. 2741-2742.

70. Yeager, E., et al., *Dioxygen reduction in various acid electrolytes.* Journal of the Serbian Chemical Society, 1992. **57**(12): p. 819-833.

71. Wang, J.X., N.M. Markovic, and R.R. Adzic, *Kinetic Analysis of Oxygen Reduction on Pt(111) in Acid Solutions: Intrinsic Kinetic Parameters and Anion Adsorption Effects.* Journal of Physical Chemistry B, 2004. **108**(13): p. 4127-4133.

72. Uribe, F.A., et al., *Practical aspects of the oxygen reduction reaction (ORR).* 1995: United States. p. 12p.

73. Viswanathan, B., C.V. Rao, and U.V. Varadaraju, *On the Search for Non-Noble Metal Based Electrodes for Oxygen Reduction Reaction.* ChemInform, 2007. **38**(8).

74. Cobley, C.M., D.J. Campbell, and Y. Xia, *Tailoring the Optical and Catalytic Properties of Gold-Silver Nanoboxes and Nanocages by Introducing Palladium.* Advanced Materials, 2008. **20**(4): p. 748-752.

75. Kay, B.D., C.H.F. Peden, and D.W. Goodman, *Kinetics of hydrogen absorption by Pd(110).* Physical Review B (Condensed Matter), 1986. **34**(2): p. 817-22.

76. Cohen, J.B., *Diffraction methods in materials science*. Macmillan series in materials science. 1966, New York: Macmillan.

77. Klug, H.P. and L.E. Alexander, *X-ray diffraction procedures for polycrystalline and amorphous materials*. 1974, New York: Wiley.

78. Thornton, J.A., *High rate thick film growth*, in *Annual review of materials science, vol.7*. 1977, Annual Reviews: Palo Alto, CA, USA. p. 239-60.

79. Yeager, E., D. Scherson, and B. Simic-Glavaski. *Mechanistic aspects of oxygen electrochemistry*. 1984. San Francisco, CA, USA: Electrochemical Soc Inc.

80. Wang, W., et al., *Carbon-supported Pd-Co bimetallic nanoparticles as electrocatalysts for the oxygen reduction reaction.* Journal of Power Sources, 2007. **167**(2): p. 243-249.

81. Sales, B.C., J.E. Turner, and M.B. Maple, *Oscillatory oxidation of CO over Pt, Pd and Ir catalysts: Theory.* Surface Science, 1982. **114**(2-3): p. 381-394.

82. Arenz, M., et al., *The Oxygen Reduction Reaction on Thin Palladium Films Supported on a Pt(111) Electrode.* Journal of Physical Chemistry B, 2003. **107**(36): p. 9813-9819.

83. Bozzolo, G. and J. Ferrante, *Composition dependence of bulk alloy properties.* Physical Review B, 1994. **50**(9): p. 5971.

84. Raghuveer, V., P.J. Ferreira, and A. Manthiram, *Comparison of Pd-Co-Au electrocatalysts prepared by conventional borohydride and microemulsion methods for oxygen reduction in fuel cells.* Electrochemistry Communications, 2006. **8**(5): p. 807-814.

85. Watanabe, D., *Study on ordered alloys of Gold-Manganese system by electron diffraction - 3. Lattice MOdulation in ordered Au_3Mn.* Journal of the Physical Society of Japan, 1961. **16**(3): p. 469-&.

86. Kawasaki, Y., S. Ino, and S. Ogawa, *Electron diffraction study on superlattice formation in Gold-Palladium alloy system.* Journal of the Physical Society of Japan, 1971. **30**(6): p. 1758-&.

87. Zhang, J.-M., F. Ma, and K.-W. Xu, *Calculation of the surface energy of fee metals with modified embedded-atom method.* Chinese Physics, 2004. **13**(7): p. 1082-1090.

88. Zhang, J., et al., *Platinum Monolayer on Nonnoble Metalâ^'Noble Metal Coreâ^'Shell Nanoparticle Electrocatalysts for O2 Reduction.* The Journal of Physical Chemistry B, 2005. **109**(48): p. 22701-22704.

89. Lee, K., et al., *Methanol-tolerant oxygen reduction electrocatalysts based on Pd-3D transition metal alloys for direct methanol fuel cells.* Journal of The Electrochemical Society, 2006. **153**(1): p. 20-4.

90. *CRC Handbook of Chemistry and Physics. 81st Edition.* Journal for American Chemical Society, 2000. **122**: p. 12614.

91. Fernandez, J.L., D.A. Walsh, and A.J. Bard, *Thermodynamic Guidelines for the Design of Bimetallic Catalysts for Oxygen Electroreduction and Rapid Screening by Scanning Electrochemical Microscopy. M-Co (M: Pd, Ag, Au).* Journal of the American Chemical Society, 2004. **127**(1): p. 357-365.

92. Meschter, P.J. *Phase Boundary-Thermodynamics Correlation in Binary Nickel-Transition Metal Systems*. in *Chemical Metallurgy - A Tribute to Carl Wagner*. 1981. Chicago, Ill: ACS.

93. Tarasevich, M.R., et al., *Oxygen kinetics and mechanism at electrocatalysts on the base of palladium-iron system.* Electrochimica Acta, 2007. **52**(15): p. 5108-5118.

94. Uchimura, M. and S.S. Kocha, *The Impact of Pt Oxide Coverage on the Measurement of Durability Diagnostic Parameters*, in *2007 Aiche Meeting*, AiChe, Editor. 2007: Salt Lake City, UT. p. Extended Abstract 295b.

95. Brace, K., et al., *Palladium Allloy Catalysts for Fuel Cell Cathodes*, in *WIPO IP Services*, W.I.P. Organization, Editor. 2007, Ilika Technologies Ltd.: World.

96. Bussayajarn, N., et al. *The cathodic polarization prediction of H2 H2O2 fuel cells by using EIS spectra*. in *30th Congress on Science & Technology of Thailand*. 2004. Bangkok, Thailand.

97. Thomas, S., et al., *Specific adsorption of a bisulfate anion on a Pt(111) electrode ultrahigh vacuum spectroscopic and cyclic voltammetric study.* Journal of physical chemistry, 1996. **100**(28): p. 11726-11735.

98. Yeager, J., *Ernest Yeager.* Journal of The Electrochemical Society, 1981. **128**(4): p. 159C-160C.

99. Pauling, L., *Nature of the Iron-Oxygen Bond in Oxyhaemoglobin.* Nature, 1964. **203**(4941): p. 182-183.

100. Lipkowski, J. and P.N. Ross, *Electrocatalysis*. Frontiers of electrochemistry. 1998, New York: Wiley-VCH.

101. Waterstrat, R., *Binary phase diagrams of transition elements.* Journal of Phase Equilibria, 1981. **2**(1): p. 35-38.

102. Weinert, M. and R.E. Watson, *Core-level shifts in bulk alloys and surface adlayers.* Physical Review B (Condensed Matter), 1995. **51**(23): p. 17168-80.

103. Solomun, T., *The role of the electrolyte anion in anodic dissolution of the Pd(100) surface.* Journal of Electroanalytical Chemistry, 1991. **302**(1-2): p. 31-46.

104. Grden, M., et al., *Electrochemical behaviour of palladium electrode: Oxidation, electrodissolution and ionic adsorption.* Electrochimica Acta, 2008. **53**(26): p. 7583-7598.

105. Kunimatsu, K., et al., *In situ ATR-FTIR study of oxygen reduction at the Pt/Nafion interface.* Physical Chemistry Chemical Physics, 2010. **12**: p. 621-629.

106. Gregoire, J.M. and F.B. van Dover, *A model for calculating resputter rates in codeposition.* Journal of Vacuum Science & Technology A (Vacuum, Surfaces, and Films), 2008. **26**(4): p. 1030-6.

107. Holze, R., I. Vogel, and W. Vielstich, *New oxygen cathodes for fuel cells with organic fuels.* Journal of electroanalytical chemistry and interfacial electrochemistry, 1986. **210**(2): p. 277-286.

108. Matolin, V., et al., *XPS and TPD study of CO interaction with Pd-Al and Pd-Al2O3 systems.* Journal of Electron Spectroscopy and Related Phenomena, 2001. **114-116**: p. 327-332.

109. Mentus, S.V., *Oxygen reduction on anodically formed titanium dioxide.* Electrochimica Acta, 2004. **50**(1): p. 27-32.

110. Suo, Y., L. Zhuang, and J. Lu, *First-Principles Considerations in the Design of Pd-Alloy Catalysts for Oxygen Reduction13.* Angewandte Chemie International Edition, 2007. **46**(16): p. 2862-2864.

111. Norskov, J.K., et al., *Origin of the Overpotential for Oxygen Reduction at a Fuel-Cell Cathode.* The Journal of Physical Chemistry B, 2004. **108**(46): p. 17886-17892.

112. Pourbaix, M., *Atlas of electrochemical equilibria in aqueous solutions*. 1974, [S.l.]: Nat'L Assoc. Of Corrosion.

113. Stamenkovic, V., et al., *Surface segregation effects in electrocatalysis: Kinetics of oxygen reduction reaction on polycrystalline Pt3Ni alloy surfaces.* Journal of Electroanalytical Chemistry, 2003. **554-555**(1): p. 191-199.

114. Oryshich, I.V. and O.S. Kostyrko, *Influence of molybdenum, tungsten, and cobalt on the corrosion of high-temperature strength nickel alloys in molten salts.* Metal Science and Heat Treatment, 1985. **27**(10): p. 740-746.

115. Boer, F.R.d., *Cohesion in metals : transition metal alloys*. Cohesion and structure, 1. 1989, Amsterdam [u.a.]: North Holland.

116. Tu, K.N., J.W. Mayer, and L.C. Feldman, *Electronic thin film science : for electrical engineers and materials scientists*. 1992, New York; Toronto; New York: Macmillan ; Maxwell Macmillan Canada ; Maxwell Macmillan International.

117. Zhou, W.-P., et al., *Improving Electrocatalysts for O_2 Reduction by Fine-Tuning the Ptâˆ'Support Interaction: Pt Monolayer on the Surfaces of a Pd_3Fe (111) Single-Crystal Alloy.* Journal of the American Chemical Society, 2009. **131**(35): p. 12755-12762.

118. Kibler, L.A., et al., *Tuning Reaction Rates by Lateral Strain in a Palladium Monolayer13.* Angewandte Chemie International Edition, 2005. **44**(14): p. 2080-2084.

119. Lin, H., et al., *Oxygen Electroreduction on Gold-Cobalt Oxide Binary Nanocluster Catalysts.* Journal of The Electrochemical Society, 2008. **155**(2): p. B200-B206.

120. Massalski, T.B., H. Okamoto, and A.S.M. International, *Binary alloy phase diagrams*. 1990, Materials Park, Ohio: ASM International.

121. Garsany, Y., et al., *High-Activity, Durable Oxygen Reduction Electrocatalyst: Nanoscale Composite of Platinumâˆ'Tantalum Oxyphosphate on Vulcan Carbon.* The Journal of Physical Chemistry Letters: p. 1977-1981.

122. Manoharan, R., M. Paranthaman, and J.B. Goodenough, *Electrocatalysis on $Pb_2Ir_{(2-x)}Pb_{(x)}O_{(7-y)}$.* European Journal of Solid State and Inorganic Chemistry, 1989. **26**(2): p. 155-174.

123. Weller, M.T., et al., *The pyrochlore family -- a potential panacea for the frustrated perovskite chemist.* Dalton transactions (Cambridge, England : 2003), 2004. **2004**(19): p. 3032-41.

124. Nyman, H., et al., *The pyrochlore structure and its relatives.* Journal of Solid State Chemistry, 1978. **26**(2): p. 123-131.

125. Pannetier, J. and J. Lucas, *New description of the pyrochlore structure composed of Cd2Nb2O6S.* Materials Research Bulletin, 1970. **5**(9): p. 797-805.

126. Sleight, A.W., *New ternary oxides of mercury with the pyrochlore structure.* Inorganic Chemistry, 1968. **7**(9): p. 1704-1708.

127. Sleight, A.W., *$AgSbO_3$: Chemical characterization and structural considerations.* Materials Research Bulletin, 1969. **4**(6): p. 377-380.

128. Horowitz, H.S., J.M. Longo, and J.T. Lewandowski, *Method of making lead and bismuth pyrochlore compounds using an alkaline medium and at least one solid reactant source*, USPTO, Editor. 1980, Exxon Research & Engineering Co.: USA.

129. Hagenmuller, P., *Preparative methods in solid state chemistry*. 1972, New York: Academic Press.

130. Longo, J.M., et al., *Preparation and structure of a pyrochlore and perovskite in the BiRhO3+x system.* Materials Research Bulletin, 1972. **7**(2): p. 137-146.

131. Volkov†, Y.F., et al., *Titanate Ceramics with Pyrochlore Structure as a Matrix for Immobilization of Excess Weapons-Grade Plutonium: II. Hydrolytic Resistance.* Radiochemistry, 2004. **46**(4): p. 358-363.

132. Bouchard, R.J. and J.L. Gillson, *A new family of bismuth -- Precious metal pyrochlores.* Materials Research Bulletin, 1971. **6**(8): p. 669-679.

133. Vetter, G., F. Queyroux, and J.-C. Gilles, *Preparation, stabilite et etude cristallographique preliminaire du compose $Bi_2Sn_2O_7$.* Materials Research Bulletin, 1978. **13**(3): p. 211-216.

134. Shah, J. and W. Hahn, *Material Characterization of Thick Film Resistor Pastes.* Components, Hybrids, and Manufacturing Technology, IEEE Transactions on, 1978. **1**(4): p. 383-392.

135. Kennedy, B.J., *Oxygen Vacancies in Pyrochlore Oxides: Powder Neutron Diffraction Study of $Pb_2Ir_2O_{6.5}$ and $Bi_2Ir_2O_{7-y}$.* Journal of Solid State Chemistry, 1996. **123**: p. 14-20.

136. Sleight, A.W., *High pressure synthesis of platinum metal pyrochlores of the type $Pb_2M_2O_{6-7}$.* Materials Research Bulletin, 1971. **6**(8): p. 775-780.

137. Kafalas, J.A. and J.M. Longo, *Pressure-induced pyrochlore to perovskite transformations in the Sr1-xPbxRuO3 system.* Materials Research Bulletin, 1970. **5**(3): p. 193-198.

138. Randall, J.J. and R. Ward, *The Preparation of Some Ternary Oxides of the Platinum Metals1,2.* Journal of the American Chemical Society, 1959. **81**(11): p. 2629-2631.

139. Shannon, R.D. and C.T. Prewitt, *Effective ionic radii and crystal chemistry.* Journal of Inorganic and Nuclear Chemistry, 1970. **32**(5): p. 1427-1441.

140. Hrovat, M., S. Bernik, and D. Kolar, *Phase equilibria in the RuO2-PbO-Al2O3 and RuO2-PbO-CuO systems.* Journal of Materials Science Letters, 1993. **12**(23): p. 1848-1850.

141. Hrovat, M., et al., *The influence of firing temperature on gauge factors and the electrical and microstructural characteristics of thick-film resistors.* Journal of Materials Science Letters, 2001. **20**(8): p. 701-705.

142. Jacob, K.T., V.S. Saji, and Y. Waseda, *Standard Gibbs energy of formation of $Pb_2Ru_2O_{6.5}$.* 2007.

143. Longo, J.M., P.M. Raccah, and J.B. Goodenough, *$Pb_2M_2O_{7-x}$ (M = Ru, Ir, Re) -- Preparation and properties of oxygen deficient pyrochlores.* Materials Research Bulletin, 1969. **4**(3): p. 191-202.

144. Brisse, F., *Para: Studies on II-V Pyrochlores through Neutron Diffraction*, in *Chemistry*. 1967, Dalhousie: Halifax.

145. Sleight, A.W., *Rare earth plumbates with pyrochlore structure.* Inorganic Chemistry, 1969. **8**(8): p. 1807-1808.

146. Edgell, R.G., et al., *Electrochemistry of ruthenates. Part 1.-Oxygen reduction on pyrochlore ruthenates.* Journal of the Chemical Society, Faraday Transactions 1, 1983. **79**: p. 893-912.

147. Shukla, A.K., R. Manoharan, and J.B. Goodenough, *Enhancement of ionic conductivity by dispersed oxide inclusions: Influence of oxide isoelectric point and cation size.* Solid State Ionics, 1988. **26**(1): p. 5-10.

148. Hrovat, M., et al., *Microstructural and electrical characteristics of some "overfired" thick-film resistors.* Journal of Materials Science Letters, 2001. **20**(4): p. 347-351.

149. Yamaguchi, T. and K. Iizuka, *Microstructure Development in RuO_2-Glass Thick-Film Resistors and Its Effect on the Electrical Resistivity.* Journal of the American Ceramic Society, 1990. **73**(7): p. 1953-1957.

150. Felthouse, T.R., et al., *Expanded lattice ruthenium pyrochlore oxide catalysts II. Catalyst surface investigations by electron microscopy, X-ray photoelectron spectroscopy, and temperature-programmed reduction and oxidation.* Journal of Catalysis, 1991. **127**(1): p. 421-444.

151. Trasatti, S., *Electrodes of conductive metallic oxides. Part A, Part B*. Studies in physical and theoretical chemistry, 11. 1980, Amsterdam: Elsevier Scientific.

152. Saito, Y., et al. *Oxygen reduction electrode properties of pyrochlores $Ln_2Ru_2O_7$-(Ln=Pr,Nd,Sm) in aqueous solutions*. 2007. Laubisrutistr.24, Stafa-Zuerich, CH-8712, Switzerland: Trans Tech Publications Ltd.

153. Yoshihara, K., et al. *Effects of the substitution of B-site ion on oxygen reduction electrode properties of $Pb_2Ru_2O_7$- in aqueous solutions*. 2007. Laubisrutistr.24, Stafa-Zuerich, CH-8712, Switzerland: Trans Tech Publications Ltd.

154. Toda, H., et al., *Ionic Conductors and Battery Related Materials - Oxygen Reduction Electrode Properties of the Ba(Ce,Gd,Ru)O_3-d Oxides at Low Temperatures.* Key engineering materials., 2006. **320**: p. 247.

155. Abe, O. and Y. Taketa, *Mathematical relation between RuO_2 volume fraction and resistance of thick-film resistors.* Journal of Physics D: Applied Physics, 1989. **22**(11): p. 1777.

156. Sarkar, A., A.V. Murugan, and A. Manthiram, *Low cost Pd-W nanoalloy electrocatalysts for oxygen reduction reaction in fuel cells.* Journal of Materials Chemistry, 2009. **19**(1): p. 159-165.

157. Tennyson, A.T., *Poems and plays*. 1967, London; New York: Oxford University Press.